Smart Dispersion of Carbon Nanoparticle Epoxy Composites: From Nano to Application

Vom Promotionsausschuss der
Technischen Universität Hamburg
zur Erlangung des akademischen Grades
Doktor-Ingenieur (Dr.-Ing.)

genehmigte Dissertation

von
Hauke Voormann, geb. Meeuw

aus
Oldenburg

2020

Gutachter:	Prof. Dr.-Ing. habil. Bodo Fiedler Prof. Dr. rer. nat. Gerold Schneider
Vorsitzender des Prüfungsausschusses:	Prof. Dr.-Ing. Otto von Estorff
Tag der mündlichen Prüfung:	29. Oktober 2020

Technisch-Wissenschaftliche Schriftenreihe

Herausgeber:

Prof. Dr.-Ing. habil. Bodo Fiedler

Anschrift:

Technische Universität Hamburg
Institut für Kunststoffe und Verbundwerkstoffe
Denickestraße 15
21073 Hamburg

Band 39:

Smart Dispersion of Carbon Nanoparticle Epoxy Composites: From Nano to Application

Hauke Voormann, geb. Meeuw

1. Auflage

Hamburg 2021

ISSN 2625-6029

DOI: 10.15480/882.3483
ORCID: 0000-0002-7031-3577

Copyright Hauke Voormann 2021

Bibliographische Information der Deutschen Nationalbibliothek:

Die deutsche Nationalbibliothek verzeichnet diese Publikation in der Deutschen Nationalbibliothek; detaillierte Informationen sind im Internet über http://www.dnb.de abrufbar.

This thesis is licensed under:
Creative Commons Attribution-NonCommercial-ShareAlike 4.0 International (CC BY-NC-SA 4.0) Unported License.



CC BY-NC-SA includes the following elements:
BY: Credit must be given to the creator
NC: Only noncommercial uses of the work are permitted
SA: Adaptations must be shared under the same terms

This license allows reusers to distribute, remix, adapt, and build upon the material in any medium or format for noncommercial purposes only, and only so long as attribution is given to the creator. If you remix, adapt, or build upon the material, you must license the modified material under identical terms.

Acknowledgements

At the outset, I wish to express my profound gratitude to Prof. Dr.-Ing. habil. Bodo Fiedler for his guidance, encouragement and support, which he provided as mentor and supervisor of this thesis.

Furthermore, I would like to thank Prof. Dr. rer. nat. Gerold Schneider for being the examiner of my thesis and Prof. Dr.-Ing. Otto von Estorff for being the chairman of my doctoral examination committee.

Special thanks go to my collegue and friend Daniel von Bernstorff for being an outstanding discussion partner at every moment.

I would like to acknowledge my collegues Johann Körbelin and Sven Drücker for all the support they provided to conduct the experimental work.

I am extremely grateful to Prof. Dr.-Ing. Karl Schulte for arousing my passion and enthusiasm for carbon composites from the very beginning of my studies and the guidance through my studies to build up a solid basis for the challenges of this thesis.

Additional thanks go to all the industrial and academical supporters, who provided most of the materials and special measurement equipment. These are namely: Malte Wichmann (Hexion), Andreas Kehne (Ludeko), Ivonne Gräflich (Altropol), Jens Schneider (OCSiAl), Walter Schütz (Future Carbon), Martin Lohe (cfaed), Jakob Marbach (UHH), Anja Borchert (TUHH), Sebastian Schäfer (Thorlabs). My sincere thank goes to the company Exakt Advance Technologies and Ulf Köpke for providing me a prototype of the next generation three roll mill 80E-Plus^{+}.

Furthermore, I thank all my collegues from the Institute of Polymer and Composites, especially Hans Wittich and Inga Sellenschloh for managing the team.

I wish to extend my special thanks to Valea Kim Wisniewski for all the time, work and reviewing she offered to support my work, aswell for being a great co-author for our publications. I wish her good luck to continue this research subject.

I would like to acknowledge the Federal Ministry of Education and Research (BMBF), the German Research Foundation (DFG) and the Departmental Authority for Science, Research and Gender Equality Hamburg (BWFG) for the funding.

Last but not least, I would like to thank my beloved wife Lilli for her tremendous support during the time of experimental work, writing and all the lost weekends. Just your help, understanding and acceptance put me in a position to prepare and write this thesis as it is.

Linden, April 2021 Hauke Voormann

„ *Why do we fall sir?*
So that we can learn to pick ourselves up. “

Alfred Pennyworth

Contents

Abstract i

Kurzfassung ii

List of Symbols, Indices and Abbreviations iii

1 Introduction 1
1.1 Objectives and Scope . . . 2

2 Theoretical Background and State of the Art 3
2.1 Epoxy Resins . . . 3
2.2 Carbon Nanoparticles . . . 6
2.2.1 Carbon Blacks . . . 7
2.2.2 Carbon Nanotubes . . . 7
2.2.3 Graphenes . . . 8
2.2.4 Surface Modification of Carbon Nanoparticles . . . 9
2.3 Electrical Properties of Carbon Nanoparticle/Polymer Composites . . . 10
2.4 Colloidal Dispersions . . . 13
2.5 Dispersion Processes for Carbon Nanoparticle/Polymer Composites . . . 15
2.5.1 Three Roll Milling . . . 17
2.6 Methods for Dispersion Quality Control . . . 18
2.6.1 Optical Coherence Tomography . . . 19
2.6.2 Impedance Spectroscopy . . . 20
2.7 Basics of Rheology - A Literature Overview . . . 21
2.7.1 Rheological Behavior of Carbon Nanoparticle Filled Polymers . . . 23
2.8 Enhancement of Polymers' Fracture Toughness by CNP Modification . . . 26

3 Research Hypotheses and Structure 31

4 Applied Methods 33
4.1 Rheometry . . . 33
4.2 Differential Scanning Calorimetry (DSC) . . . 34
4.3 Fourier-Transform Infrared Spectroscopy (FTIR) . . . 34
4.4 Size Exclusion Chromatography (SEC) . . . 34
4.5 Scanning Electron Microscopy (SEM) . . . 34
4.6 Energy Dispersive X-Ray Spectroscopy (EDX) . . . 35
4.7 Transmission Electron Microscopy (TEM) . . . 35

4.8 Determination of Specific Surface Area (SSA) . . . 35
4.9 Thermo Gravimetric Analysis (TGA) . . . 35
4.10 Raman Spectroscopy . . . 35
4.11 Dispersion via Three Roll Milling . . . 36
4.12 Infrared Thermography . . . 37
4.13 Light Microscopy (LM) . . . 37
4.14 Grindometry . . . 37
4.15 Optical Coherence Tomography (OCT) . . . 37
4.16 Determination of Electrical Conductivity . . . 38
4.17 Impedance Spectroscopy . . . 39
4.18 Dynamic Mechanical Thermal Analysis (DMTA) . . . 39
4.19 Determination of Fracture Toughness in Mode I and II . . . 39

5 Materials 41
5.1 Epoxy Resins . . . 41
5.1.1 Characterization of Uncured Epoxy Resins . . . 43
5.1.2 Properties of Cured Epoxy Resins . . . 46
5.2 Carbon Nanoparticles . . . 49

6 Dispersion of Carbon Nanoparticles in Epoxy Resins via Three Roll Mills 52
6.1 Rheo-Electrical Characterization of Carbon Nanoparticle/Epoxy Composites - Revealing the Driving Force for Dispersion . . . 52
6.1.1 Strain and Frequency Dependent Behavior of Nanocomposites . . . 52
6.1.2 Rheological Properties of Neat Resins . . . 53
6.1.3 Time Dependent Behavior of Nanocomposites . . . 53
6.1.4 Strain Dependency of Nanocomposites . . . 54
6.1.5 Frequency Dependency of Nanocomposites . . . 56
6.2 Online Monitoring of Carbon Nanoparticle Dispersion Processes via Three Roll Mills . 60
6.2.1 Particle Size Evaluation by Optical Coherence Tomography . . . 61
6.2.2 Impedance Spectroscopy . . . 62
6.2.3 Evaluation of Process Data from Three Roll Milling Processes . . . 67
6.3 Monitoring of Three Roll Milling Processes - Variation of Machine, Particle Type and Epoxy Resin . . . 68
6.3.1 Three Roll Milling - Viscosity Dependency . . . 68
6.3.2 Influence of Processing Machine . . . 70
6.3.3 Influence of Resins' Viscosity . . . 72
6.3.4 Temperature Dependency of Dispersion Process . . . 74
6.3.5 Dispersion of Carbon Black - Orion Engineered Carbons Printex L . . . 77
6.3.6 Dispersion of Multi-Walled Carbon Nanotubes . . . 81
6.3.6.1 Nanocyl NC7000 . . . 81
6.3.6.2 Future Carbon CNTB . . . 83
6.3.6.3 Future Carbon CNTA . . . 86
6.3.6.4 Future Carbon CNTP . . . 88
6.3.6.5 Future Carbon CNTN . . . 90
6.3.7 Dispersion of Planar Particles . . . 93
6.3.7.1 Few-Layered Graphene - Avanzare Innovación Tecnológica Avan2 . 93
6.3.7.2 Electro-Chemically Expanded Graphite . . . 95

6.3.7.3 Functionalized Electro-Chemically Expanded Graphite 99
6.3.8 Dispersion of Single-Walled Carbon Nanotubes 101
6.3.8.1 OCSiAl Tuball 75 101
6.3.8.2 OCSiAl Tuball purified 104
6.4 Optimization of Heat Dissipation 106

7 Carbon Nanoparticle/Epoxy Composites - Resulting Physical Properties 108
7.1 Characterization Subsequent to Curing Agent Addition 108
7.1.1 Rheology 108
7.1.2 Impedance Analysis 112
7.2 Characterization in Cured State 116
7.2.1 Impedance Analyses 116
7.2.2 DC Conductivity 119
7.2.3 Dynamic Mechanical Thermal Analysis 121
7.2.4 Fracture Toughness Mode I and II 123
7.2.4.1 Mode I 123
7.2.4.2 Mode II 124
7.3 Conflict of Objective - Enhancement of Physical Properties and Loss of Processibility? . 127

8 Demonstration of Industrial Scale Masterbatch Production (10 kg) 129

9 Application of SWCNT in a Colored GFRP with Antistatic Properties 134

10 Conclusion and Future Prospects 138

References 139

A Programmed Applications 173
A.1 OCT Evaluation via Matlab 173
A.1.1 Main.m 173
A.1.2 Thresh_tool.m 175

B Additional Material Characterization 181
B.1 Additional Characterization of CNP 181
B.1.1 Energy Dispersive X-Ray Spectroscopy 181
B.1.2 Raman Spectroscopy 182
B.1.3 Thermo Gravimetric Analysis 183
B.1.4 Scanning Electron Microscopy 187
B.1.5 Transmission Electron Microscopy 191
B.2 Dynamic Mechanical Thermal Analysis of CNP/EP Composites 195
B.3 Final comparison of Impedance Spectroscopy Results 198

Abstract

Incorporation of carbon nanoparticles in high performance polymer composites promises extensive potential for enhancement of their physical properties. Here the dispersion of the particles is the crucial factor. Only a defined dispersion results in the desired adjustment of properties. On the one hand, the market offers a high variety of industrially available carbon based nanoparticles. These are: Carbon blacks (CB), multi-walled carbon nanotubes (MWCNT), single-walled carbon nanotubes (SWCNT) and graphenes. On the other hand, the demand for nano-enabled products is given. Unfortunately, the bottleneck lies within the incorporation of these particles into the polymer, namely the carbon intermediate production. A commonly used effective technique for the dispersion of carbon-based nanoparticles into high performance epoxy resins (EP), in their liquid state, is the three roll milling (TRM) process. However, it is time consuming and requires a lot of manual handling of the material. In-line analysis enables the expansion of the technological bottleneck and leads to a cost-efficient and quality-controlled dispersion process for the future industrial application.

In a first step, the carbon nanoparticles were characterized regarding their geometry, specific surface area and elementary composition. Rheological characterization of the different molecular weight epoxy resins built a starting point for further investigations. Rheo-electrical characterization of the nanocomposites revealed the applied strain amplitude as predominant driving force for dispersion and not the shear rate. Optical coherence tomography (OCT) allowed the direct evaluation of the particle size distribution over the dispersion process. Analysis of the dependency of the complex impedance on the frequency via impedance spectroscopy revealed the network formation on macro and even on micro scale. Next generation three roll mills are enabled to monitor occurring process forces. The analysis of the line forces during processing allows an assessment of the homogeneity of dispersion.

The combination of these in-line quality-monitoring methods enables a process time reduction of 70 % for a demonstrator masterbatch production of typical batch size. The evaluated impact of the particle type, filler loading and epoxy resin on the viscosity during processing and the resulting thermo-mechanical, electrical and fracture behavior (mode I and II) revealed the potential for industrial applications. Here, SWCNT showed the best property enhancement regarding the electrical conductivity and fracture toughness without increase of viscosity at ultra-low filler loading of 0.01 wt.%. This allowed the manufacturing of a bright colored glass fiber reinforced polymer (GFRP) with antistatic discharge protection. Subsequently, the presented results enable the manufacturing of nano-intermediates in an efficient way with controllable dispersion quality.

Kurzfassung

Die Einarbeitung von Kohlenstoffnanopartikeln in Hochleistungskomposite auf Polymerbasis verspricht ein hohes Potential zur Verbesserung ihrer physikalischen Eigenschaften. Für die gezielte Anpassung der gewünschten Eigenschaften ist die Einstellung des Dispersionszustandes der wichtigste Faktor. Die Vielfalt der an in industriellen Mengen zur Verfügung stehenden Nanopartikeln ist in den letzten Jahren stark gestiegen. Diese sind vor Allem: Ruße (CB), mehrwandige Kohlenstoffnanoröhren (MWCNT), einwandige Kohlenstoffnanoröhren (SWCNT) und Graphene. Auch der Bedarf an nanomodifizierten Produkten hat stark zugenommen. Den Engpass in der Wertschöpfungskette stellt hierbei die Einarbeitung dieser Partikel in das Polymer, zur Produktion von Nano-Intermediates, dar. Stand der Technik ist die Verwendung eines Dreiwalzwerkprozesses (TRM) zur Dispersion von Kohlenstoffnanopartikeln in flüssige Polymere, wie Hochleistungsepoxidharze (EP). Dieser ist jedoch zeitaufwändig und wenig automatisiert. Die Handhabung des Materials erfolgt zu großem Anteil manuell. Ziel dieser Arbeit ist die Aufweitung des Engpasses zur Realisierung eines kosteneffizienten Dispergierprozesses mittels einer in-line Qualitätskontrolle zur zukünftigen industiellen Applikation.

In einem ersten Schritt werden die Morphologie, spezifische Oberfläche und elementare Zusammensetzung der verwendeten Nanopartikel charakterisiert. Die rheologische Charakterisierung der Epoxidharze mit verschiedenen Molekulargewichten bildet die Basis für weitere Untersuchungen. Die rheo-elektrischen Untersuchungen zeigten, dass die Dehnungsamplitude, und nicht wie bisher angenommen die Scherrate, die Hauptursächlichkeit für die Separation der Partikel während des Dispersionsprozesses ist. Die Verwendung der optischen Koheränztomographie (OCT) erlaubte die direkte Evaluation der Partikelgrößenverteilung zwischen den einzelnen Dispergierschritten. Weiterhin zeigte die Anwendung der Impedanzspektroskopie zur Charakterisierung des Verhaltens der komplexen Impedanz, in Abhängigkeit der Frequenz, die Ausbildung des Partikelnetzwerkes auf Makro- wie auch auf Mikroebene. Die neue Generation der Dreiwalzwerke ist mit einer Technologie ausgestattet, die es ermöglicht die auftretenden Kräfte zwischen den Walzen während des Dispergiervorgangs aufzuzeichnen. Die Analyse der Linienkräfte lässt eine Beurteilung der Homogenität der Dispersion zu.

Die Kombination dieser in-line Methoden zur Qualitätskontrolle führte zu einer Prozesszeitreduktion von 70 %, validiert anhand einer Produktion eines typischen Demonstratormasterbatches. Die Evaluation des Einflusses des Partikeltyps, Füllstoffgehalts und des verwendeten Epoxidharzes auf die Viskosität während der Verarbeitung und der resultierenden thermo-mechanischen und elektrischen Eigenschaften sowie der Bruchzähigkeit in Mode I und II demonstrierte das Potential für industrielle Anwendungen. Die verwendeten SWCNT führten zur höchsten Steigerung der elektrischen Leitfähigkeit und Bruchzähigkeit ohne dabei die Viskosität zu erhöhen. Für diese Verbesserung ist ein sehr geringer Füllstoffgehalt von nur 0,01 wt.% notwendig. Dies erlaubte die Herstellung eines signalfarbigen Glasfaserverbundwerkstoffes (GFRP) mit antistatischen Eigenschaften. Die Ergebnisse dieser Arbeit ermöglichen zusammenfassend eine zukünftige effiziente Herstellung von Nano-Intermediates mit kontrollierbarer Dispersionsqualität.

List of Abbreviations, Symbols and Indices

Abbreviations

Abbreviation	Description
2D	Two dimensional
3D	Three dimensional
3PBT	Three-point-bending-test
4PBT	Four-point-bending-test
A	Acid
AC	Alternating current
AHEW	Amine hydrogen equivalent weight
ATR	Attenuated total reflection
B	Base
BADGE	Bisphenol A diglycidyl ether, same as DGEBA
BET	Brunauer-Emmett-Teller theory
BMBF	Federal Ministry of Education and Research
BWFG	Departmental Authority for Science, Research and Gender Equality Hamburg
C	Carbon
C_{20}	Dodecahedral fullerene, with 20 C-atoms
C_{60}	Buckminsterfullerene
C_{80}	Fullerene, offering 80 C-atoms
CAGR	Compound annual growth rate
CB	Carbon black
CNF	Narbon nanofiber
CNT	Carbon nanotube
CNTA	Argon plasma treated CNTB
CNP	Carbon-based nanoparticle
CNTB	Reference MWCNT supplied by Future Carbon
CNTN	CNTB equipped with elastomer side chain, offering amino-functionalization
CNTP	Atmospheric plasma treated CNTB
CPE	Constant phase element
CVD	Chemical vapor deposition
DC	Direct current
DCPD	Dicyclopentadiene
DFG	German Research Foundation
DGEBA	Diglycidyl ether of bisphenol A, same as BADGE
DLS	Dynamic light scattering
DMTA	Dynamic mechanical thermal analysis
DSC	Differential scanning calorimetry
EDX	Energy dispersive X-ray spectroscopy
EEW	Epoxy equivalent weight
EP	Epoxy resin

Abbreviation	Description
ESD	Electro static discharge
ExG	Electro-chemically expanded graphite
fExG	Functionalized electro-chemically expanded graphite
FLG	Few-layered graphene
FTIR	Fourier-transform infrared spectroscopy
GFRP	Glass fiber reinforced plastic
GO	Graphene oxide
H	Hydrogen
HCl	Hydrochloric acid
He	Helium
LM	Light microscopy
MLG	Multi-layer graphene
MW	Molecular weight
MWCNT	Multi-walled carbon nanotube
MWD	Molecular weight distribution
NC	Nanoclay
ND	Nanodiamond
Ne	Neon
NaOH	Sodium hydroxide
O	Oxygen
OCT	Optical coherence tomography
OH	Hydroxy bond
QA	Quality assurance
PC	Polycarbonate
PMMA	Poly(methyl methacrylate)
PP	Polypropylene
PS	Polystyrene
REACH	Registration, evaluation, authorization and restriction of chemicals
rGO	Reduced graphene oxide
RT	Room temperature
SAOS	Small amplitude oscillation shear
SEC	Size exclusion chromatography
SEM	Scanning electron microscopy
SENB	Single-edge notched bending
SHM	Structural health monitoring
SiC	Silicon carbide
SSA	Specific surface area
SWCNT	Single-walled carbon nanotube
TEM	Transmission electron microscopy
TGA	Thermo gravimetric analysis
TiO_2	Titania
TPU	Thermoplastic polyurethane
TRM	Three roll milling
UP	Unsaturated polyester resin
USA	United States of America

Abbreviation	Description
VdW	Van-der-Waals forces
VOC	Volatile orcanic content
XRD	X-Ray diffraction

Symbols

Symbol	Unit	Description
a	µm	Crack length
A	mol^{-1}	Avogadro's number ($6.022140923\ 10^{23}\ mol^{-1}$)
$A_{\alpha\beta}$	Without unit	Tabulated coefficient (fracture toughness)
b	Without unit	Dimension dependent critical exponent
B	mm	Sample thickness in 3PBT and 4PBT
C	pF	Capacity
d	mm	Asymmetric distance in 4PBT
d_i	mm	Diameter of TRM roller
De	Without unit	Deborah number
e	C	Electron charge ($1.60217662\ 10^{-19}$ C)
E	MPa	Young's moudulus
E'	MPa	Storage modulus
E''	MPa	Loss modulus
E^*	MPa	Complex modulus
f	s^{-1}	Frequency
F_I	Without unit	Geometric factor for mode I
F_{II}	Without unit	Geometric factor for mode II
G	MPa	Shear modulus
G_R	%	Degree of graphitization
G'	MPa	Shear storage modulus
G''	MPa	Shear loss modulus
G^*	MPa	Complex shear modulus
h	µm	Spacing shear gap
h_I	Without unit	Weight function for mode I
h_I	Without unit	Weight function for mode II
$\hbar$	Js	Reduced Planck constant (1.054571817 Js)
I	A	Output current
I_D	Without unit	Intensity of D-band
I_G	Without unit	Intensity of G-band
j	Without unit	Unit imaginary number
k	Without unit	Factor
K	K kg mol^{-1}	Empirical parameter
K_I	MPa $\sqrt{\text{m}}$	Stress intensity factor in mode I
K_{IC}	MPa $\sqrt{\text{m}}$	Critical stress intensity factor in mode I
K_{II}	MPa $\sqrt{\text{m}}$	Stress intensity factor in mode II
K_{IIC}	MPa $\sqrt{\text{m}}$	Critical stress intensity factor in mode II
l	mm	Friction width
l_c	µm	Penetration depth
L	mm	Distance from support to crack mode II (in 4PBT)
L_a	Å	Crystalline width
L_{el}	H	Inductivity
m	Without unit	Exponential parameter for CPE
m_e	kg	Mass of an electron ($9.1093837015\ 10^{-31}$ kg)

Symbol	Unit	Description
M_n	kg mol^{-1}	Number average molecular weight
M_c	kg mol^{-1}	Molecular weight of chain segments between cross-links
n	Without unit	Polymerization degree of EP
n_i	Rpm	Revolution speed of roller of TRM
o	Without unit	Amount of required dispersion cycles
p	N	Load in 3PBT and 4PBT
q	Å	Distance of atoms
Q	pF	Capacity of CPE
r	mm	Radius
R	J mol^{-1} K^{-1}	Universal gas constant (8.314462618 J mol^{-1} K^{-1})
R_{el}	Ω	Ohmic resistance
s	nm	Stack thickness of multi-layer graphene
t	s	Time
T	K or °C	Temperature
T_i	°C	Temperature inside TRM roller
T_G	K or °C	Glass transition temperature
T_S	°C	Sample temperature
U	V	Electric potential
v	m s^{-1}	Angular velocity
V	V	Input voltage
$\dot{V}$	cm^3 s^{-1}	Volume flow in TRM
W	mm	Sample height in 3PBT and 4PBT
W_d	mJ	Discharge energy
X_C	Ω	Capacitive part of reactance
X_L	Ω	Inductive part of reactance
Z_{CPE}	Ω	Impedance of a CPE
Z^*	Ω	Complex impedance
Z'	Ω	Real part of complex impedance
Z''	Ω	Imaginary part of complex impedance
δ	rad or °	Phase difference
ΔL	mm	Lenght addition to specimen
$\Delta\lambda$	nm	Spectral width
γ	%	Shear deformation
$\dot{\gamma}$	s^{-1}	Shear rate
η	Pa s	Viscosity
η^*	Pa s	Complex viscosity
θ	°	Rotational angle
Θ	Without unit	Aspect ratio
κ	Without unit	Empirical factor
λ	s	Relaxation time
λ_0	nm	Central wavelength
λ_B	eV	Height of energy barrier
λ_c	s	Characteristic time
λ_l	nm	Wavelength
λ_s	s	Scale of deformation

Symbol	Unit	Description
μ	cm^{-3}	Cross-link density
ρ	$g\,cm^{-3}$	Density
σ_{el}	$S\,m^{-1}$	Electrical conductivity
σ_{yield}	MPa	Yield stress
τ	Pa	Shear stress
υ	nm	Distance at double layer
υ_{Stern}	nm	Thickness of Stern-layer
ϕ	wt.%	Filler loading
φ	rad or °	Phase angle
ψ	mV	Stern-layer potential
ω	$rad\,s^{-1}$	Circular frequency
ω_c	$rad\,s^{-1}$	Cross-over frequency

Indices

Index	Description
$()_0$	Initial
$()_{Agg}$	Corresponding to agglomerates
$()_{Bulk}$	Corresponding to bulk material
$()_c$	Critical
$()_{CNT}$	Corresponding to CNT network
$()_e$	Electron
$()_{elastic}$	Corresponding to elastic behavior
$()_{HB}$	Human body
$()_i$	Number of corresponding TRM roller
$()_{max}$	Maximum value
$()_{onset}$	Onset value
$()_{polymer}$	Corresponding to polymer
$()_{peak}$	Peak value
$()_T$	Evaluation at temperature T
$()_{tot}$	Total value
$()_{viscous}$	Corresponding to viscous behavior
$()_x$	Direction of x
$()_{xy}$	Direction of x and y plane
$()_y$	Direction of y
$()_\upsilon$	Value at distance υ
$()_\infty$	Final property of the material

1 Introduction

The addition of electrically conductive fillers like metal particles, carbon black, graphite or carbon fibers is a common method to provide electrical conductivity in intrinsically isolating polymers. The necessary filler content, depending on particle type, usually lays in the range of 5 wt.% to 15 wt.%. These high filler loadings have a significant detrimental impact on the processing properties. Especially the viscosity increases with increased filler content [1, 2]. Additionally, high concentrations of fillers have a negative impact on the mechanical properties [3], as well as chemical resistance, where low filler loadings are favorable [4, 5]. Furthermore, a customization of the products is limited with regard to coloring for high filler loadings. The allotropes of carbon based nanomaterials (e.g. carbon nanotubes (CNT) and graphene) are considered as the most promising materials of the last decade. An incorporation of these materials leads to outstanding properties of these nanocomposites and even results in additional functional properties. Due to their nanoscale diameter and extreme high aspect ratio (>1000), filler concentrations of even less than 0.01 wt.%, in case of electrical conductivity, are sufficient [6]. Their unique physical properties attract attention - electrical conductivity comparable to copper, thermal conductivity in the magnitude of diamond and Young's modulus ten times higher than steel [7]. Although they own these outstanding physical properties, a transfer to macroscopic scale and commercialization is still limited [8]. In the past the addition of carbon-based nanoparticles (CNP) was intensively investigated as an economic alternative [9]. Incorporation of CNP into a polymeric matrix leads to improvement of the physical properties of produced CNP/polymer composites. The electrical insulating polymer becomes conductive, which makes it a favorable alternative for electrostatic discharge (ESD) protective applications [10, 11]. The electrical conductivity can be adjusted well with variations of aspect ratio or filler loading and the mechanical properties of the composites are enhanced, too [12–14]. Promising applications for carbon-based nanoparticles are in composite materials, electro-chemistry, nanometer-sized electronic devices, electrode and separator materials for fuel cells and printed electronics [9, 15–17] and there are many other fields of application for carbon based materials such as supercapacitors, batteries, water filters, anti biofouling coatings and microelectronics [18, 19]. Hyperion Catalysis International, Inc., were the first to produce MWCNT in multiton scale since the 1990s [9]. Conductivities up to 10^4 S/m can be achieved with 10 wt.% filler concentration [20]. For single-walled carbon nanotubes thresholds for electrical percolation lay in the order of $5{\cdot}10^{-5}$ wt.% up to the percentage range [21–23]. In the past, lack of scaleable production processes and high prizes of about 1000 $/kg prevented the establishment of SWCNT, although their resulting properties in polymer composites are superior to multi-walled carbon nanotube reinforced composites [24].
Nowadays, carbon-based nanoparticles are becoming available at industrial scale [25] at affordable prices. Furthermore, they will exhibit remaining high compound annual growth rates (CAGR) in the next few years [26, 27], which are predicted to be 18 % and 30 % to 40 % for the carbon nanotube [28] and the graphene market [29, 30], respectively. The manufacturer OCSiAl predicted the annual production capacity of Tuball SWCNT with 1000 t/y in 2018 [31]. Graphene supplier The Sixth Element Materials Technology gives their production capacity of graphene oxide with 260 t/y and graphene with 130 t/y [32], respectively, while MWCNT manufacturer Nanocyl gives their production capacity with 460 t/y [33]. A demand for standardized declarations of these materials has been claimed from early on and is still remaining crucial [34]. The recent REACH[1] registration for the ton scale commercialization of carbon nanotubes and graphene [35–37] makes certified particles available for industrial scale and manifold applications.

[1] **R**egistration, **E**valuation, **A**uthorisation and Restriction of **CH**emicals

The dispersion process is the key limiting factor to overcome for application of carbon-based nanoparticles at industrial scale [38]. Separation and dispersion of carbon-based nanoparticles is time-consuming and generates high costs in the value chain. Today's approaches for industrial processing are not economic and exhibit a low degree of automation [27]. The far lower required filler loading results in a cost saving at the material site. Due to inefficient processes for filler incorporation, the production of nano-enabled products generates high costs. Therefore, the cost advantage on materials site, generated by the required low filler loading, gets lost throughout the value chain. This contributes to the lack of manufacturers of nano-intermediates (e.g. concentrated masterbatches, dispersions and inks). For industrial application safety, issues regarding the handling of the dry nanoparticles are an intensive problem, too [26, 39]. In nano-intermediate products the nanoparticle powders are bound in a liquid matrix. This prevents the release of these particles and hence, exposure to human beings is prevented. Figure 1.1 shows the value chain to produce carbon nanoparticle enabled materials from the raw material to the final product.

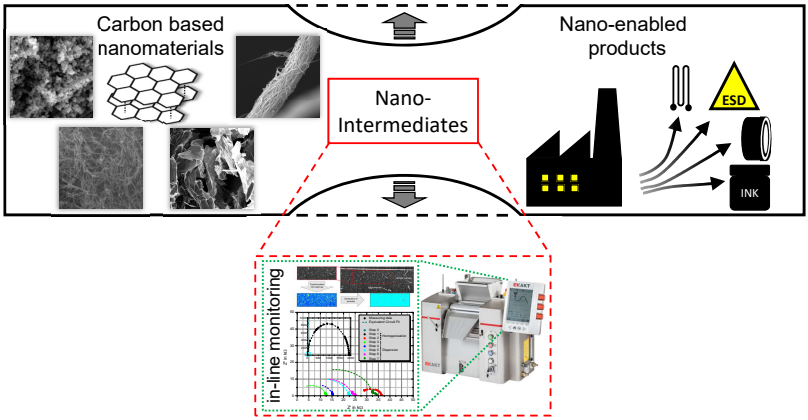


Figure 1.1: Value chain CNP-production according to Fullerex Ldt. [26]

1.1 Objectives and Scope

This thesis addresses the existing bottleneck in the value chain via in-line monitoring of the dispersion process for carbon nanoparticle/polymer composite manufacturing from the nanoparticle to the final application. The following questions will be addressed:

1) What is the driving force for particle separation in dispersion processes?
2) What are scalable dispersion processes for carbon nanoparticle/polymer production?
3) What are suitable in-line monitoring methods to assess the quality of the dispersion?
4) Are there criteria for an optimum dispersion, depending on material properties?
5) Which mechanisms dominate the dispersion process for different carbon based nanoparticles and polymer properties?
6) Is there an optimum particle concentration for enhancement of physical properties with regard to technical application in dependency of the processibility?

Parts of this thesis are published in peer-reviewed journal articles, listed in reference [40].

2 Theoretical Background and State of the Art

2.1 Epoxy Resins

Polymers, in general, offer, compared to classical metal materials, the advantages of low costs and more degrees of freedom in case of molding into complex shapes. Thermoplastic polymers have their limitation in case of the production of large-scale parts. This derives from the necessity to melt them for shaping and cool them down to provide sufficient mechanical properties. This requires an enormous amount of thermal energy and the processing time scales with part size. Most of the thermosetting polymers are in a liquid state at ambient temperature and require a cross-linking process to get in the solid state. Their liquid state, in uncured form, is a huge advantage in case of manufacturing large fiber reinforced composite parts such as wind turbine blades, hulls of ships or toolings [41]. Epoxy resins are one of these high-performance thermosets. They possess outstanding physical properties, namely low cure shrinkage, no volatiles in uncured state and during curing, compatibility to wide set of materials, high strength, durability, corrosion and chemical resistance as well as good electrical insulation [42]. Furthermore, their properties can be well adjusted [43, 44]. Epoxy resin is called any molecule, which offers more than one epoxy group (oxirane ring). A widely used epoxy resin is the diglycidyl ether of bisphenol A (DGEBA or BADGE). The synthesis of DGEBA is shown in Figure 2.1.

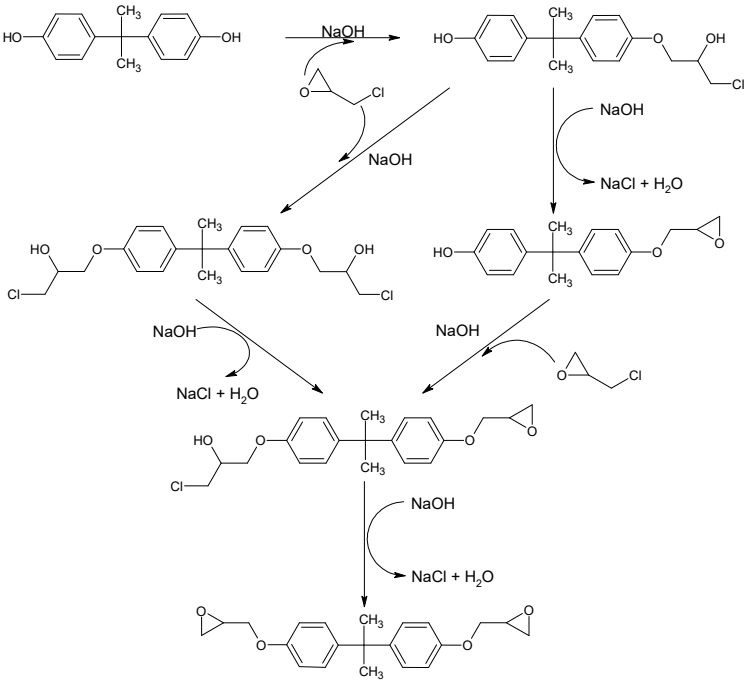


Figure 2.1: Reaction of bisphenol A and epichlorohydrin [45]

Bisphenol A (4,4'-(propane-2,2-diyl)diphenol) reacts in two steps with epichlorohydrin (2-(chloromethyl)oxirane) [46]. The first step is the base-catalized reaction of bisphenol A with epichlorohydrin. NaOH is used as a catalyst to produce chlorohydrin and neutralizes at the same time as forming HCl. Neat DGEBA is a crystallin solid at room temperature. This makes it difficult to process. Higher molecular weight (MW) epoxies are liquid and their viscosity rises with increasing molecular weight [47]. The variation of the bisphenol A to epichlorohydrin ratio results in different polymerization degrees n, leading to higher amounts of repeating groups in the mid part of the molecule. The polymerization degree can be well adjusted (see Figure 2.2). This leads to a variation in chain

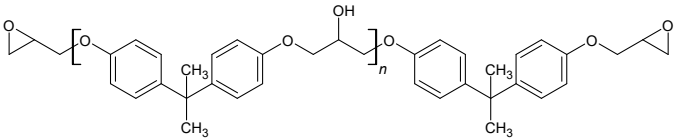


Figure 2.2: Molecular structure of DGEBA with repeating groups

length and therefore, directly affects the molecular weight distribution (MWD), which has high impact on the resulting physical properties. For most applications a n between 0 and 1 is desireable for liquid to semi-solid epoxy resins [43]. Terminating epoxy groups as well as the hydroxyl groups in the middle of the molecule are highly reactive. The aromatic backbone provides a high degree of heat and chemical resistance. Aliphatic sequences in between ether linkages grant chemical resistance and flexibility [48]. The unmodified state of epoxy resins is rarely used in industrial applications [41]. This is caused, on the one hand, by the high viscosity in liquid state and on the other hand by the brittleness of the cured resin. In order to reduce production costs, the material costs need to be kept as low as possible and furthermore, it requires the adjustment of rheolocical and physical properties as well as an improvement of cure kinetics (time and temperature) is necessary [43, 49]. To prevent crystallization, an addition of bisphenol F digycidyl ether is commonly utilized in industrial application [50]. Hereby, bisphenol F digycidyl ether offers a lower tendency to form crystals and offers a much lower viscosity, caused by the absence methyl groups between the aromatic rings. This makes the molecule less rigid and allows lower attractive Van-der-Waals (VdW) forces [51]. Figure 2.3 gives its molecular structure. Applications

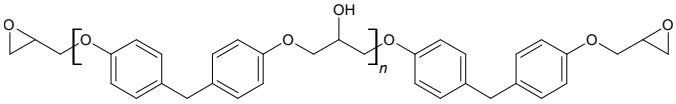


Figure 2.3: Molecular structure of bisphenol-F-diglycidyl ether with repeating groups

like infusion processes, paints or adhesives require extreme low viscosities, which cannot be obtained with neat epoxy resins. Addition of aliphatic or aromatic reactive as well as non-reactive diluents or solvents leads to a required decrease in viscosity [52, 53]. Figure 2.4 gives the molecular structure of the widely used reactive diluent 1,6-hexanediol diglycidyl ether. The formation of a cross-linked network of

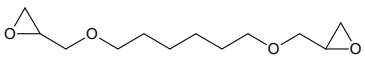


Figure 2.4: Molecular structure of the reactive diluent 1,6-hexanediol diglycidyl ether

a thermoset requires the addition of curing agents [54].

Curing agents possess terminating multi-functional groups, like amino-groups. These react with the oxirane rings as well as the hydroxyl groups. Curing agents can be liquid, mostly offering an aliphatic backbone, or are solids in case of most aromatic curing agents [44]. Utilization of aromatic diamines results in high oxidative resistance and flexural modulus [55]. The ratio of required curing agent to epoxy resin can be calculated from their epoxy equivalent weight (EEW) and amine hydrogen equivalent weight (AHEW), respectively. The EEW is given by grams of epoxy resin containing one equivalent of epoxy groups. The AHEW is obtained by grams of curing agent containing one equivalent of amine groups. The mixing ratio can be calculated by following equation [43]:

$$\text{Parts by weight of amine to be used with 100 parts by weight of epoxy resin} = \frac{AHEW}{EEW} \tag{2.1}$$

During the curing reaction, the material starts to vitrify at a certain degree of cross-linking. The progress of gelation, reaching a glassy state, slows down the cure kinetics dramatically [56]. This is the case if the glass transition temperature T_G reaches the ambient curing temperature. Amine based curing agents react with the DGEBA in the three ways [57], presented in Figure 2.5.

1) The addition reaction of primary amines leads to a β -hydroxylamine
2) The reaction of the extant hydrogen of the now secondary amine leads to the formation of a tertiary amine [58]
3) Elevated curing temperatures trigger the formation of ethers

Homopolymerization occurs at the presence of lewis acids or strong lyes acting as catalyst [59].

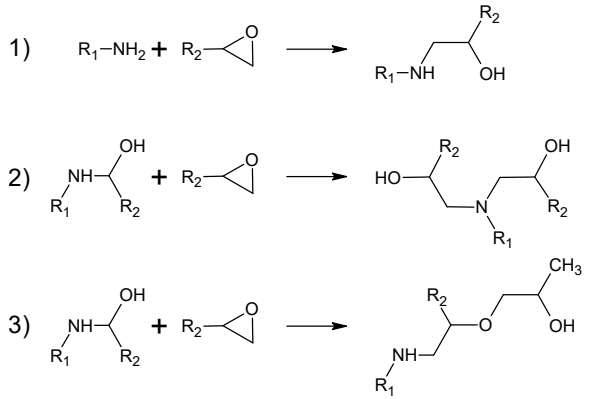


Figure 2.5: Reaction mechanisms of epoxies with primary amines - adapted from [46, 60, 61]

By utilization of the Flory–Fox equation, which is a simple empirical formula, the correlation of the number average molecular weight M_n to the glass transition temperature T_G of a polymer system is possible [62].

$$T_G = T_{G,\infty} - \frac{K}{M_n} \tag{2.2}$$

K is an empirical parameter regarding to the free volume. The research works of Flory gave the fundamentals to correlate the modulus in the rubbery state with the cross-linking density of polymers [62–64].

This correlation was further developed by Tobolsky et al. [65–68]. They derived following equation to determine the average molecular weight of chain segments between cross-link points M_c:

$$M_c = \frac{3 \cdot \kappa R T \rho(T)}{E'_T} \tag{2.3}$$

In this equation, $\rho(T)$ is the density at a temperature much higher than T_G, E'_T is the corresponding storage modulus at this temperature, κ is an empirical factor, R the universal gas constant and T the temperature of evaluation. Due to volume constancy for deformations with small strain amplitudes, E'_T can be replaced by three times the shear modulus G'_T ($E = 3G$) [69]. This equation was widely used in literature [70–73]. Unfortunately, the value of κ is uncertain. In highly cross-linked polymers, the amount of inactive chains results in a non-Gaussian network. In a first approximation κ can be assumed to be unity for E <10^7 Pa. The significance of the non-Gaussian character increases for E >10^7 Pa with increasing cross-link density [74–76]. Therefore, Equation 2.3 does not longer hold. Nielsen derived following empirical equation for highly cross-linked networks [76]:

$$\log_{10} G'_T = 7 + \frac{293 \cdot \rho(T)}{M_c} \tag{2.4}$$

The cross-link density μ in cm^{-3} can be calculated as follows [74]:

$$\mu = \frac{\rho(T) N}{1.5 \cdot M_c} \tag{2.5}$$

The Avogadro's number is represented by N. Combining Equation 2.4 and 2.5, again taking into account $E = 3G$, leads to following correlation for the cross-link density of highly dense polymer networks like epoxies:

$$\mu = \frac{N(log_{10}(\frac{1}{3} E'_T) - 7)}{439.5} \tag{2.6}$$

2.2 Carbon Nanoparticles

The element carbon consists of six protons and six neutrons and offers an atomic mass of 12.01 g/mol. The electron configuration of this element enables three hybridized energy states of the electrons, leading to a high variety of possible bonds and crystal structures [77]. Until 1985 only the two natural allotropes, beside amorphous carbon black, were discovered, namely graphite and diamond [78]. The discovery of spherical fullerene (C_{60}) drew attention to the field of carbon research. Nowadays, several variants of fullerene were synthesized (C_{20} to C_{80}) [79]. In 1991, the re-discovery of cylindrical carbon nanotubes induced a further hype to the field of carbon nanoparticle research [80]. The first successful exfoliation of single-layer graphene in 2004 revealed the last known allotrope so far [81–83]. Carbon nanomaterials offer the potential to overcome the limitations of silicon to pave the way for the post-silicon era [84, 85]. Figure 2.6 gives the chronological discoveries of carbon allotropes and their structure. Diamond offers a sp^3-hybridized, tetrahedral structure and is well known for its hardness and exceptional Young's modulus. For technical application the most important structure is the hexagonal sp^2-hybridized structure [77]. Graphite is at 20 °C and 1 atm (0.1 MPa) the thermodynamically stable structure of carbon [90]. Graphite is well known for its outstanding electrical conductivity and thermal stability in inert athmosphere [91]. The triple point is at 5000 K [91]. Oxidation resistance is given up to 600 °C [92]. The sp^2-hybridization results in a beneficial energy state, formed by three σ-bonds. These bonds lay in the same plain under the same angle. Normal to this plain the bonds form a π-valence-band. Furthermore, the electrons can occupy a π*-band. The σ- and π- configurations result in high mechanical, chemical and thermal activation energies [86]. For a single-layer hexagonal carbon structure the π*-band results in superior electron mobility.

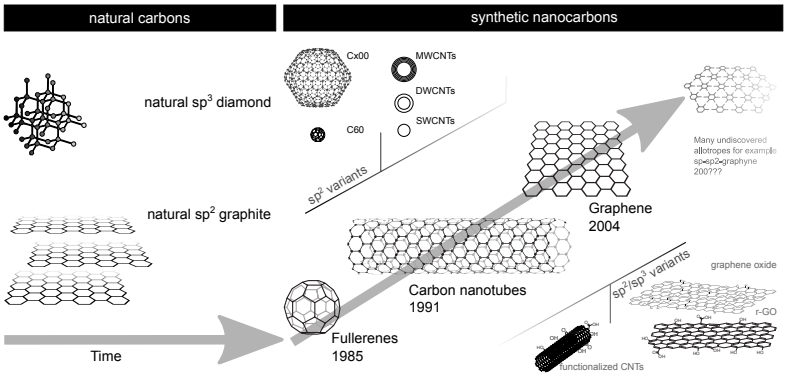


Figure 2.6: Overview over crystalline carbon structures: natural: diamond (sp^3-hybridized) and graphite (sp^2-hybridized); synthetic carbons: fullerene, carbon nanotubes and graphene (all sp^2-hybridized) - reprinted from [86] (adaption: [85, 87–89])

This leads to a touching conduction- and valence-band. The band gap equals 0 eV, which results in exceptional electrical properties. More than 100 solid forms of carbon structures are described in [93, 94]. Recently discovered carbon foams, like aero graphite, consist of rolled graphene layers, wich are organized in tetrapod structure [95].
This research focuses on the 0-dimensional carbon black, 1-dimensional carbon nanotubes and 2-dimensional few layered graphene [89]. These will be introduced in the following.

2.2.1 Carbon Blacks

Carbon black is an industrially produced, fine structured, spherical amorphous carbon. In contrast to common soot, which results from combustion, industrial carbon black is produced by tailored incomplete combustion of hydrocarbons. The resulting carbon offers spherical primary particles, with narrow size distribution, which aggregate and form agglomerates below 1 µm on micro scale [94]. The primary particles constit of fine micro-crystals with dimensions from 8 nm to 400 nm [96]. The size of the primary particles and the geometry and dimension of the aggregates can be well adjusted by variations in the manufacturing process. This allows precise adjustment of the physical properties. Avaiable processes are the furnace black, thermal black, channel black, lamp black and acetylene black process [97, 98]. The specific surface areas (SSA) of industrial carbon black varies from 10 m^2/g to 1000 m^2/g. For comparison, activated carbon provides a specific surface area of 950 m^2/g to 2000 m^2/g [99]. The diameter of CB lays between 10 nm to 300 nm. The aggregated structure leads to high electrical conductivities [100]. CB is mainly used in the tire industry for rubber modification as well as polymer products. Other applications are printing inks and coating, due to the specific surface area, particle dimensions and structure. They feature conductivity and black color, when used as an additive [101].

2.2.2 Carbon Nanotubes

Carbon nanotubes were re-discovered, as already stated, by the Japanese physicist Iijima during an arc-discharge process [80]. They belong to the carbon groups of the fullerenes. Rolled layers of graphene sheets form the cylindrical structure of CNT. The carbon atoms form a hexagonal sp^2-structure within the rolled layer [102]. They are classified by the amount of rolled layers as well as their chirality [103]. In

case of only one rolled graphene layer, the CNT is called single-walled carbon nanotube. They offer a diameter of 0.4 nm to 3 nm. Multi-walled carbon nanotubes in contrast consist of up to 40 layers. Their diameters vary from 25 nm to 60 nm. Depending on the manufacturing method, the resulting lengths differ from few µm to several mm. This leads to high aspect ratios (ratio of length to diameter; $\eta_{\text{aspect ratio}}$) and specific surface areas. CNT offer outstanding tensile strength and stiffness, at comparable low density. Further remarkable properties are their high thermal and electrical conductivity. The high electrical conductivities result from the de-localized electrons, allowing a movement over the graphene structure. Depending on their chirality the SWCNT are either metallic or semi-conductive. MWCNT are always metallic [104]. Carbon nanotubes can be manufactured by arc-discharge, laser ablation or chemical vapor deposition (CVD) processes [105]. For CVD grown CNT, the nanotubes grow on a substrate, for example a single-crystal silicon wafer, from the gas phase. This phase consists of a hydrocarbon, e.g. toluene. The presence of a metallic catalyst, e.g. iron in form of ferrocene, initializes the growth. In contrast to arc-discharge produced CNT, the CVD-grown CNT offer higher purity, length and alignment. The production rates for laser ablation are given with 0.05 kg/day. Arc-discharge provides an output of 0.12 kg/day and CVD-processes 50 kg/day [106].

2.2.3 Graphenes

Since the demonstration of the successful exfoliation of a single-layer graphene from multi-layer graphite [81], the industry demands for scale-up processes. Table 2.1 lists the available processes for graphene production. McKinsey estimates a 70 billion dollar market for graphene semiconductors in 2030 [107]. In general, there are two possible approaches to synthesize graphene available. The bottom up and the top down approach [108]. The first includes all separation approaches for chemical or mechanical exfoliation. These "peel-off" methods are scalable and therefore mandatory for the industrial application of graphene. The wet chemical approaches utilize strong acids, which damage the sp^2-hybridized structure of the natural graphite. This leads to formation of side-chains at the edges of the graphene sheets, which mainly are oxygen bonds, leading to graphene oxide (GO). That sp^3-hybridization enlarges the spacing between the graphene layers. The inter-layer spacing of natural graphite is given with 3.34 Å and 7.88 Å for GO. This enlargement enables the separation via thermal or mechanical methods. This liquid phase exfoliation approach is called *"modified Hummers' method"* [109]. The following reduction of the GO can be realized by either chemical or thermal treatment to form reduced graphene oxide (rGO). Due to the induced damage of the sp^2-hybridization, the electrical properties of these graphene derivates are poor. In general, addition of GO into polymers enhances the ultimate tensile strength, Young's modulus and fracture toughness, because the structure defects of the layers do not weaken the mechanical properties as much as in terms of electrical conductivity [110, 111]. A further scalable top down method is described by Yang et al. [112, 113]. They utilize alternating current (AC) to exfoliate graphite on both electrodes to increase production capacity.

The bottom up methods base on chemical vapor deposition processes. The sp^2-hybridized carbon layers grow on metal or metal carbide surfaces or by decomposition of metal carbides. Nowadays available CVD processes allow the growth of graphene layers in the lateral size of several centimeters.

The C/O ratio, amount of layers and lateral size classifies the particles [114]. As an example, Bianco et al. consider a layered graphene with two to five layers as few layer graphene (FLG) and two to ten layer graphene as multi-layer graphene (MLG) [115].

Table 2.1: Comparison of the different production methods for graphene - adapted from [84]

	Ref.	Electronic quality of layer	Cost	Number of layers	Productivity	Nature	Lateral size	Precursor
Mechanical exfoliation	[116]	High	Low	Single and multiple	Low	Pristine	10 µm	Graphite
Liquid suspension of graphene oxide followed by chemical reduction	[117]	Low	Low	Single and multiple	High	Chemically modified	Several 100 nm	Graphite oxide
Liquid-phase exfoliation	[118]	High	Low	Single and multiple	High	Pristine	< 0.1 µm	Graphite
Epitaxial growth by thermal desorption of Si atoms from SiC surfaces	[119]	High	Low	Single and multiple	Low	Pristine	$\geq$50 µm	Silicon carbide
Epitaxial growth by CVD on transition metals	[120, 121]	High	High	Single and multiple	Low	Pristine	$\geq$100 µm up to wafer-size	Hydrocarbons
Solvothermal synthesis	[122]	N/A	Low	Single and multiple	High	Chemically modified	< 0.1 µm	Ethanol
Unzipping carbon nanotubes	[123]	High	Low	Single and multiple	High	Chemically modified	4 µm nano ribbons	MWCNT
Electro-chemical exfoliation	[124, 125]	High	Low	≤ 3	High	Pristine or chemically modified	Up to 44 µm	Graphite

2.2.4 Surface Modification of Carbon Nanoparticles

For the incorporation of carbon nanoparticles into a polymeric matrix, the surface of the particles might be modified to ensure optimum adhesion. In case of amine curing epoxy resins an amino-functionalization is suitable [126]. Here two functionalization routes are favorable, the direct side wall and the defect functionalization [38, 127]. In case of defect functionalization, in a first step, the nanoparticles are heated in a mixture of sulphuric and nitric acid in order to remove impurities of carbon black and graphite nanoparticles. Furthermore, this treatment oxidises the surface of the particles [128]. In a second step, the oxidised nanotubes are heated with an excess of e.g. triethylenetetramine to chemically bond amino-groups to the surface. The functionalization is improved by additional in-situ ultrasonication [129]. This leads to a significant increase of the matrix-dominated inter laminar shear strength by 20 % in fiber composite applications [130]. Nevertheless, this functionalization route leads to a reduction of sp^2-hybridization and increase of sp^3-hybridization of the outer walls of CNT [131]. This does not negatively affect the electrical conductivity, which is mainly controlled by the inner metallic tubes of neighboring CNT in the final composite [132]. The thermal treatment with following hydrochloric acid treatment and a further annealing

step leads to purified carbon nanoparticles [106]. The initial thermal treatment leads to oxidization. HCl removes the metallic impurities as well as the amorphous carbon and the final annealing leads to a high degree of graphitization. A further method to achieve an activation of the surface of carbon nanoparticles is the plasma treatment. Plasma treatment creates defect sites on the nanotube surface that are chemically active [133, 134].

2.3 Electrical Properties of Carbon Nanoparticle/Polymer Composites

The development of novel multi-functional materials, in particular by modification of polymers with carbon-based nanoparticles, became one of the main research topics in the last decades. Special interest focuses on SWCNT due to their unique material properties. By adding this filler type, the intrinsic insulating polymer becomes electrically conductive. This modification provides the possibility for industrial applications requiring electrostatic discharge protection. In the 1880s, the topic of electrostatic discharge began to attract attention, when nearly 80 explosions occurred in German laundries due to electric discharge [135]. Recent statistics published in Europe and the USA show that, even today, electric discharges are the cause for explosions in 35 % of all cases [136]. In general, charge formation occurs due to body separation. There are three typical cases to distinguish [137]:

1) Two bodies in contact are separated by sliding each other (e.g. unwinding tape)
2) Repetitive separation (e.g. walking on a carpet)
3) Quasi-continuous contact and separation (e.g. flow of liquids in pipes)

The possibility of static electricity to be a source of ignition rises, if following conditions occur [138]:

- Charge generation is higher than dissipation rate
- Discharge occurs in ignitable atmosphere and exceeds ignition energy

Following equation calculates the discharge energy W_d in dependence of the generated potential U and the capacity C of the material:

$$W_d = \frac{1}{2} C_{HB} U^2 \tag{2.7}$$

A person walking across a carpet generates an electrical potential of about 15 kV. According to the human body model, the capacity of the human body C_{HB} differs between 100 pF to 300 pF [139]. This leads to a generated energy dissipation of 10 mJ up to 35 mJ. Britton et al. classified the discharge energies according to the human reaction, whereby more than 15 mJ lead to an unpleasant shock [138]. In comparison, the generated energy exceeds the lowest minimum ignition energy by a factor of 100 for common vaporous solvents (e.g. 0.19 mJ for acetone at a concentration of 4.97 vol.% in air) [140]. The dissipation of generated charge avoids high charge formations. Antistatic materials provide an electrical conductivity, which is sufficient to dissipate the charge in short time at accompanying hazard-free electrical current flow, preventing a generation of discharge sparks. For handling electrostatic sensitive devices, three types of resistances influence the charge dissipation: The surface resistance, measured between two electrodes, the volume resistance measured between top and bottom surface and the dissipation resistance, measured between top surface and ground. According to ASTM F 150-06 the static dissipative region lays between 1 MΩ (safe dissipation) to 1 GΩ (sufficient fast dissipation) [141]. Nowadays, the possibility to adjust the electrical properties of carbon filled polymer systems is given [14]. Figure 2.7 sums up the classification of conductors and insulators with respect to their surface resistance. To achieve the demanded electrical conductivity of the polymeric matrix, an addition of carbon based nanoparticles is necessary. This even opens the possibility to realize a conductivity in glass fiber reinforced plastics. Furthermore, the addition

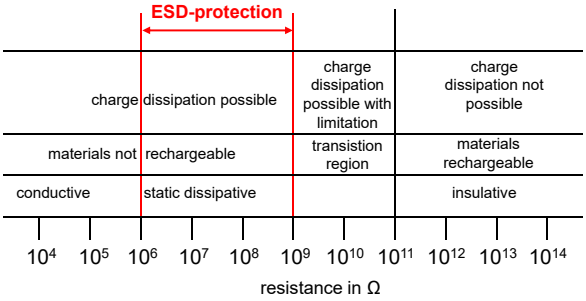


Figure 2.7: Classification of materials in respect to their surface resistance in style of [142]

of carbon nanoparticles adds functional properties to the composites. This can be e.g. self sensing materials for structural health monitoring (SHM). The electrical conductivity of a polymer is in the order of 10^{-8} S/m and can be enhanced by nanoparticle modification up to several S/m [105]. The literature gives three electron conduction mechanisms [143, 144]:

1) Direct particle contacts
2) Tunneling electrons between closely neighboring conductive filler particles
3) Intrinsic conductance of the conductive filler particles

At a certain degree of conductive filler addition, the electrical conductivity of the formerly insulating polymer rises by up to ten decades. This specific filler loading is called the percolation threshold. By reaching this filler content, a fully established electrical conductive network penetrates the polymer [145]. The electrons can move freely through the material. This is enabled by the tunneling effect. For tunneling, the distance between the particles has to be smaller than the material's specific tunneling distance, however a direct contact between the particles is not required [146–148]. Electrical conductance, provided by direct contact of particles, becomes predominant at filler loadings above percolation. The tunnel current density J based on Simmon's theory [149] is given with

$$J = Ue^2 exp(-\frac{2q}{\hbar}\sqrt{2m_e\lambda_B})\sqrt{2m_e\lambda_B} \tag{2.8}$$

where U denotes the electrical potential, e the electron charge, q the distance between particles, $\hbar$ the reduced Planck or also Dirac constant [150], m_e the mass of electron and λ_B the height of the energy barrier. The tunnel effect is a quantum mechanic phenomenon, which bases on the Schrödinger equation [151]. This differential equation of a wave function describes the possible locations of electrons. With a low probability, electrons can occur behind the energy barrier. This enables the electrons to move from particle to particle.

The literature does not give a consistant definition of the of the electrical percolation threshold. One of the definitions states the filler content, which significantly increases the electrical conductivity σ_{el} of the composite. A typical value for that is 10^{-6} S/m, which is the critical value to achieve antistatic properties [152]. Another definition is the point of inflection derived from the S-shaped percolation curve [153, 154]. This definition is easy to apply mathematically. The literature gives several models to describe the mechanisms of percolation for spherical particles. They all have in common that they describe the insulator-conductor transition. Statistical percolation considers a grid model. Particles randomly occupy the grid sites. Transition from a local to an infinite state of particle interaction can be modeled by variation

of the particle amount, which corresponds to the filler content. The percolation threshold separates these two states. Statistical occupation of the grid sites enables the occupation of adjacent sites, forming a cluster. When the cluster reaches macroscopic scale, the percolation threshold is reached and the interconnected electrical network is formed. This model does not consider any diffusion or particle movements. Therefore, it only bases on statistical distribution [155]. The equation to determine the critical filler content is given with

$$\sigma_{el} \sim (\Phi - \Phi_c)^b \tag{2.9}$$

were σ_{el} denotes the electrical conductivity, Φ the filler loading, Φ_c the critical filler loading and b the dimension dependent critical exponent [155–157]. For example, the critical percolation threshold for spherical particles is given with $\Phi_c \approx 16 \pm 2\ vol.\%$ [156]. Description of the percolation behavior of non-spherical particles requires the consideration of colloid dispersions. Celzard et al. describe one of the possible models [158]. They describe a model to determine the percolation threshold of carbon nanoparticle modified polymers, which bases on the determination of displaced volume. Balberg et al. as well as Martin et al. give following equation for the determination of the percolation threshold from the aspect ratio Θ [159, 160]:

$$\Phi_C \approx \frac{1}{\Theta} \tag{2.10}$$

Bauhofer et al. collected experimental data from a wide set of carbon nanotube percolation curves and evaluated the percolation thresholds [20]. They derived following empirical formula for the electrical conductivity:

$$\sigma_{el}(\Phi) = 6 \cdot 10^4 \cdot \Phi^{2.7} \tag{2.11}$$

In a prior study, the impact of a wide set of carbon nanoparticles on the electrical conductivity of CNP/EP composites was investigated [14]. Figure 2.8 shows the filler content dependent electrical conductivity for different carbon fillers in epoxy resin. The spherical carbon black (Printex 300) percolates at highest filler

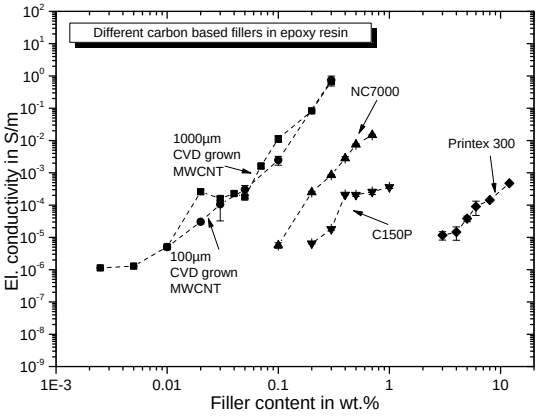


Figure 2.8: Impact of filler content on the electrical conductivity for different carbon fillers [14]

content. The higher aspect ratio MWCNT NC7000 show percolation at lower filler content compared to MWCNT C150P. The lab scale CVD grown MWCNT offer high aspect ratios and show the same percolation behavior, despite their difference in length. The aspect ratio has, as stated in equation 2.10, a high impact on the percolation behavior [14]. For industrial application carbon nanotubes with a length above

100 µm should be used [14, 161]. Models like this become invalid, if the interaction between particle and polymer becomes dominant. For dispersed particles this effect is significant due to the high interface in comparison to the particles' volume. The chemical interactions of particle, like Van-der-Waals and coulomb forces as well as Brownian movement need to be considered. Colloidal theory takes all the mentioned effects into account and describes kinetic percolation effects [162–164].

2.4 Colloidal Dispersions

Fine dispersed solid particles in a surrounding liquid phase, offering molecules with much lower size, form a colloidal dispersion. The particles offer a high specific surface area and therefore, surface to volume ratio [164]. The continuous phase is considered as dispersant. Dispersion of carbon nanoparticles in liquid epoxy resin forms such a colloidal dispersion [165]. Within the dispersion occur diffusion and brownian movement, as well as particle-dispersant and particle-particle interactions. The interaction results from attractive Van-der-Waals forces, attraction of oppositely charged and repulsion of equally charged particles. Surface properties play a dominant role [164]. After dispersion, the system is in a non-stable state and tends to agglomerate through collision and converging. Environmental influences, like changes in temperature or addition of electrolytes, benefit the coagulation. The introduction of shear forces into a dispersion causes collisions, which lead to a higher tendency for coagulation, too [105]. According to Brezesinski following repulsion forces contribute to the energy barrier, stabilizing the dispersion [164]:

1) Born repulsion
2) Short range hydration repulsion
3) Entropic repulsion
4) Electrostatic repulsion

Born repulsion results from incomplete converging of two particles due to their irregular surface structure. Formation of hydration shells in aqueous solution cause short range hydration repulsion. The molecules, surrounding the particles, need to desorb to enable a full contact. For coagulation this energy barrier needs to be overcome. In organic and non-aqueous dispersants this kind of repulsion is called lyosphere repulsion [166]. Entropic repulsion is more dominant for smaller particle size. Absorbed free molecules on the particle's surface take various conformations and vibration states. An entropic loss results from the restraining of the macro molecules. Electrostatic interaction of equally charged particles leads to a repulsion force. This offers the main contribution to the stabilization of a dispersion. Mechanical energy input into the dispersion by stirring or shearing may charge the surfaces of the particles. For carbon nanoparticles the surface mainly consists of carbon. Most carbon nanoparticles offer only a low intrinsic content of reactive surface groups, due to their low defect density. However, their large surface area benefits the adsorption of foreign atoms, which creates reactive groups, and even the storage at ambient environment for a several time span leads to formation of these groups [167]. The resulting content is difficult to identify and quantify. A classification into acids, alkaline and neutral groups is possible. Carbon nanoparticles in epoxy as dispersant show a formation of an acid-base equilibrium between the dispersant and the formation of surface groups of the particles takes place [105]:

$$AH + B \rightleftharpoons A^- + BH^+ \tag{2.12}$$

The proton exchange happens through the formation of conjugate acid-base pairs. This transforms a base (B) into an acid (A) and vice versa. Fowkes et al. demonstrated with their model the chemical interaction between the particles and the dispersant [168]. Figure 2.9 shows schematically the charge formation of a

particle within the dispersion. In a first step, epoxy molecules (B) converge to the surface of the particle (a). At the carbon particle surface, the proton is transferred from the reactive surface groups (AH), to the alkaline groups of the epoxy (B) according to Figure 2.12 (b). The surface charge results from the desorption of the dissociated molecule (BH), compare Figure 2.9 (c) [169]. In this case, the remaining surface charge is negative, caused by the alkaline nature of the dispersant. The dissociated molecules form an electric double layer [105]. Free ions of the dispersant act as compensation of the particles'

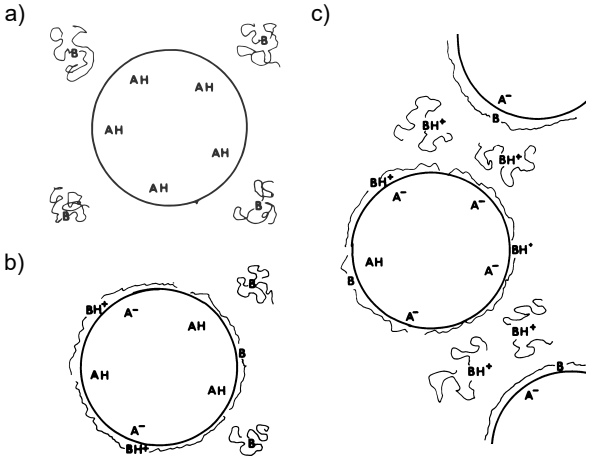


Figure 2.9: Chemical interaction of CNP in EP [168]

surface charges. This leads to a formation of an immobile ion layer near the surface, which neutralizes the excess charges partially. The layer is also called Stern- or Helmholtz-layer. Its thickness is given with υ_{Stern} und lays between 0.1 nm and 1 nm [170, 171]. The potential directly at the surface is given with ψ_0 and linearly decreases up to the distance υ. Here the potential reaches the Stern-potential ψ_υ. With increasing distance, the concentration of cations is still larger compared to the averaged concentration of the dispersion. Brownian movement of molecules and ions leads to the formation of a diffusive layer. The excess charge decreases according to Stern's model exponential. At large distances to the filler particles, the excess charge is fully neutralized [164]. The Zeta-potential gives the most important characteristic value to characterize charged particles within a dispersion. It is defined by the electrical potential at the diffusive layer of a particle. The stability of a dispersion is directly proportional to the thickness of the double-layer as well as the value of the Zeta-potential. Both lead to an improved separation of the particles. The amount of free ions within the dispersion strongly affects the thickness of the double-layer. The addition of an amine based curing agent increases the amount of free ions. This decreases the stability of carbon nanoparticle/epoxy dispersions. Addition of curing agent leads to agglomeration and coagulation [105, 160, 169]. The attractive forces, which act against the repulsive are following [164]:

1) Electrostatic coulomb force of oppositely charged particles
2) Van-der-Waals forces
3) Interface forces while coalescence of surrounding particles
4) Forces, resulting from chemical and physical absorption, while bridging of colloidal particles at molecular scale

Coulomb attractions are the strongest forces responsible in coagulation. Particle coalescence is of minor importance in this work, because of the absence of a third medium, which is insoluble in the dispersant. In the case of an existing third phase, the different surface tensions lead to formation of a shell. This separates the particle and the dispersant. Converging of two covered particles leads to coalescence, which results in coagulation. Van-der-Waals forces take effect on all kinds of particles in a electrolyte. VdW interactions are proportional to the power of six to the reciprocal distance between the particles and therefore, need only to be considered in case of particle collision. Furthermore, reactive groups can form chemical bonds between the particles, leading to coagulation. Due to geometric restrains a coagulation occurs at a certain filler loading. Shear forces above a critical value benefit coagulation. This is called ortho-kinetic coagulation. Coagulation induced by particle collisions, resulting from Brownian movements, is called peri-kinetic coagulation [172]. Figure 2.10 gives an schematic overview of the resulting interaction curve in dependency of the distance by superposing attractive and repulsive forces. The energetic favorable and stable states for the dispersion are the primary and secondary minimum. The

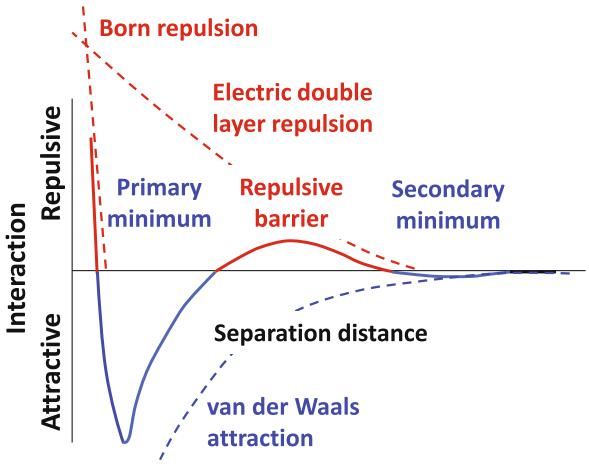


Figure 2.10: Energetic potential of colloidal particles in dependency of the particle distance - adapted from [173]

first minimum offers a low particle spacing degree. VdW forces dominate this state and the particles occur in an agglomerated state. To change the state, the energy barrier (maximum) must be overcome. An energy input into the dispersion enables this. Dispersion processes are utilized to realize the required energy input. A break-down of the agglomerated particles by separation takes them into the secondary minimum. This state is stable, but not the most favorable state. The dispersion can be easily disturbed by shear forces or Brownian movement [11]. Usually, carbon nanoparticle/polymer composites come along in an agglomerated state. To break-down these strongly bonded agglomerates, high energy input into the system is necessary. Available high shear processes are ultrasonication, high speed stirring, ball milling or three roll milling [174, 175].

2.5 Dispersion Processes for Carbon Nanoparticle/Polymer Composites

The addition of filler particles into a polymer matrix enables the adjustment of its physical properties. For instance, the addition of carbon-based nanoparticles leads to the electrical conductivity of the intrinsic

insulating polymer. This is considered to be the most promising application [176]. Furthermore, the addition of this filler type results in an enhancement of mechanical properties, especially the fracture toughness [175]. These properties strongly depend on the distribution of the incorporated particles and the resulting interconnected network [177]. The dispersion process to incorporate nanoparticles into the matrix is, as initially stated, the key limiting factor to overcome [8, 38]. Nanoparticles are available in powder form. These powders consist of macro-scale agglomerates with low interface compatibility to polymers. High aspect ratios lead to enormous specific surface areas, resulting in strong particle interactions [13, 38, 178]. The challenge is the separation of the particles and adjustment of their distribution [179]. Furthermore, there are only few companies available, which incorporate the health risky powders into the polymers [26]. Majidian et al. showed that the polydispersity of CNP/polymer dispersions is crucial for electrical properties [180]. Dispersions consist of agglomerates, which are interlinked with well dispersed nanoparticles. This offers the opportunity to adjust the properties [180]. For adjustment of carbon nanoparticle distribution in the matrix polymer, following parameters need to be considered [181]:

1) Geometry of the particles
2) Initial entanglement
3) Volume fraction
4) Matrix viscosity
5) Particle-particle interactions

For the incorporation and separation high shear forces are necessary [182]. Ma et al. as well as Yoon et al. summed up the main dispersion techniques available for CNP/polymer composites. Ball milling, high speed stirring and extrusion processes were evaluated [38, 174, 176]. High speed stirring and ball milling utilize the steady movement of either a stirring rod or the rotational movement of rigid balls. For low filler concentrations in low viscosity systems ultrasonic technology combined with chemical processes result in required separation, distribution and stabilization [11, 183–185]. Ultrasonication realizes the energy input by a high frequency oscillation vibration. This creates voids in the liquid, which collapse violently, releasing energy. This phenomenon is called cavitation [186]. Particles, accelerated up to 1000 km/h, collide with each other, and the agglomerates break-down. Especially for water based dispersions, the utilization of surfactants as well as ultrasonication lead to efficient results, but they are limited to low viscosity systems [187]. With increasing matrix viscosity the required energy input increases. A local ultrasonication with a horn is much more efficient compared to a ultrasonic bath [188]. The local energy input by ultrasonication leads to damage of the particles [189] and therefore, reduction of electrical properties of the composite [190–192]. A tradeoff with intermediate amplitude and duration leading to required physical properties needs to be found [189]. For some types of CNT the generated shear forces are not strong enough to separate and disperse the particles [193]. For industrial application the dispersion process must be scalable, continuous and the production time is the driving force regarding cost efficiency [27].
A state of the art approach is the masterbatch process. Masterbatches are highly concentrated and therefore high viscous systems. After dispersion a dilution to the desired concentration follows. High viscous masterbatch production is not possible with sonication, because material circulation is hindered. Especially for this high viscous and concentrated type of nano-intermediate, the production is time consuming. The masterbatch dilution approach leads to improved MWCNT macro dispersion compared to direct incorporation [194, 195]. Another advantage of higher viscous dispersions is the longer shelf life by reduced agglomeration rates [196]. The liquid matrix with an enormous filler content shows a solid-viscous behavior, leading to challenging material handling and transportation. Nevertheless, the production of highly concentrated masterbatches with a subsequent dilution to the desired concentration is therefore a cost effective approach to process polymer systems containing nanoparticles. An alternative approach for the

incorporation of particles is three roll milling [175, 197]. TRM-technology is capable of incorporating particles in comparable high-viscous polymer systems, like epoxy resins, and is realizable as a continuous process. By improving the dispersion process the bottleneck in the value chain vanishes and the cost advantage of carbon nanoparticles can be transferred from the raw material into the final product.

2.5.1 Three Roll Milling

Calandering, or commonly three roll milling, processes provide the opportunity for scale-up to mass production [198], although they offer the lowest volumetric flow due to their limited surface area [199]. A three roll mill consists of three adjacent calendars, which rotate in opposite directions with increasing angular velocities and decreasing gap sizes. Figure 2.11 shows the schematic layout of a three roll mill. Revolution speeds of the rollers (n_1, n_2 and n_3) and gap spacing can be adjusted. The material is loaded into the feeding gap and dragged in between the rollers. In the dispersion gap high shear forces occur leading to the separation of the particles [200]. After passing the TRM, the apron blade collects the dispersed material, which is subsequently re-fed into the feeding gap, if necessary. The process zones are in detail:

(I) Material feeding: Mixing of the material occurs. A vortex is formed according to Ancker [201], leading to a rotation of the material that is not dragged into the gap

(II) Film formation: A film forms from the bulk material and is dragged into the gap. The deformation of the material pushes the rolls apart, leading to high line forces in the feeding gap.

(III) Dispersion: The film thickness must be reduced further by one third. The separation of the particles takes place due to the velocity gradient in the gap.

This procedure is repeated until a sufficient dispersion state is achieved. This can be up to 25 steps with variation of revolution speed and gap spacing [202]. The transport of the material through the TRM can

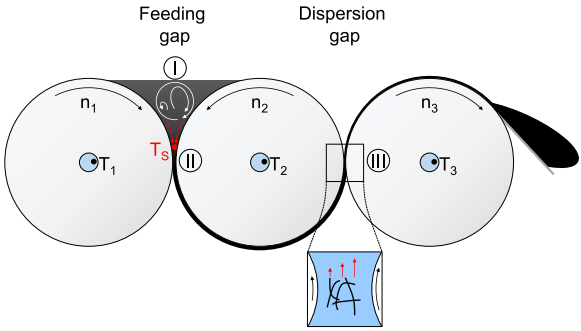


Figure 2.11: Schematic visualization of three roll milling process

be described with a drag and pressure flow [203]. The resulting material flow and line load distribution for $n_2 > n_1$ is shown in Figure 2.12. Magnier et al. simulated the calendaring process with two rolls and thermoplastic materials. They showed that the highest loads occur just before the gap spacing becomes smallest [204]. The condition of $n_2 > n_1$ is necessary to guarantee a transfer of the material through the TRM. As shown in Figure 2.12, the material sticks on the faster roll, thus leaving the gap at minimum roller spacing. For further calculations, the resin is assumed as in-compressible. TRM introduces high shear rates into the material. The gradient of the flow velocity v along the gap spacing h gives the shear

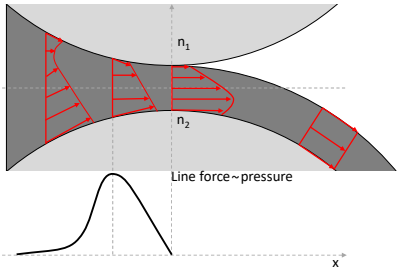


Figure 2.12: Occurring flow velocity profiles and line load distribution - adapted from [203–205]

rate $\dot{\gamma}$.

$$\dot{\gamma} = \frac{\partial v}{\partial h} \tag{2.13}$$

The angular velocity at the surface of the roll is calculated from the roll's diameter d_i and its revolution speed n_i by following formula:

$$v_i = \pi d_i n_i \tag{2.14}$$

The resulting shear rates are highest at the smallest roller spacing h, which is also the gap spacing, and can be calculated as follows

$$\dot{\gamma} = \frac{\pi d(\frac{n_2 - n_1}{60}) \cdot 10^{-3}}{h \cdot 10^{-6}} \tag{2.15}$$

The volume flow $\dot{V}$ can be calculated by following equation, considering the friction width l, given by the layer width, which is limited by the spacing of the brackets.

$$\dot{V} = ((v_1 \cdot h) + \frac{1}{2} h(v_2 - v_1)) \cdot l \tag{2.16}$$

The material flow through the TRM needs to be the same within both gaps. Therefore, the ratio of the revolution speeds determines the ratio of the gap spacings. Summarizing, small gap sizes and high differences in angular velocity generate the enormous shear rates. For high viscous epoxy resin systems TRM processing of CNP leads to the best particle dispersion [175, 198, 206, 207]. High advantage of TRM is the possibility to apply the masterbatch approach. Masterbatch processes offer potential for production time reduction leading to cost reduction [208, 209]. By implementation of an in-line quality assurance (QA) the amount of processing steps can be reduced. This results in an efficiency optimized process applicable for industrial scale production.

2.6 Methods for Dispersion Quality Control

For industrial acceptance, CNP must be available in high amounts and competitive prices. Time and cost effective processes have to be developed. A repeatable and defined dispersion quality for adjustable mechanical and electrical properties must be guaranteed. Depending on application, requirements for particle distributions and dispersion states differ. Well separated and distributed particles lead to mechanical enhancement. For electrical conductivity, interlinked agglomerates forming conductive paths are desirable [180, 210]. Buschhorn et al. reviewed available methods for the characterization and evaluation of dispersion states [211]. The most direct method to evaluate the particle size, without their distribution, is the grindometry. Microscopic methods, like light microscopy (LM), scanning (SEM) and transmission

electron microscopy (TEM) need time-consuming sample preparation and analysis. Furthermore, the investment for SEM and TEM microscopes is high. On nano-scale contrast imaging gives good results for agglomeration size and particle distributions for a small volume [152, 212]. However, the gathered images only show a projection of the particles into the image plane. Thus, depth information gets lost. The limitation for LM is the filler concentration caused by the light absorbing properties of the CNP [211]. A state of the art technology to evaluate particles size distributions is the dynamic light scattering (DLS). Illumination of particles with a laser and analysis of the variation, due to brownian movement, of the back scattered light gives the particle size distribution [196]. Here, the sample preparation is time-consuming, too. This method's limitation also lays in high filler concentrations and low brownian movement in high viscous matrices [196, 213]. A derived method from DLS is an approach to measure the transmittance along sample height over the time [214]. Fourier-transform infrared spectroscopy (FTIR) is capable of revealing chemical interactions between matrix and particle to improve the dispersion quality [215]. A lot of work had been done regarding the correlation of direct current (DC) conductivity of CNP/polymer composites with the particle distribution. Buschhorn et al. concluded that the correlation between the DC conductivity and particle distribution is not possible. Only the electrical percolation can be evaluated [211]. Other indirect methods are rheology, differential scanning caliometry (DSC) and sedimentation analysis. All these methods have in common that they are not applicable for in-line monitoring of the dispersion state [211]. Other approaches basing on circular frequency-dependent alternating current conductivity, also known as electrical impedance, and optical coherence tomography are reported in literature and will be introduced in the following paragraphs.

2.6.1 Optical Coherence Tomography

OCT provides non-invasive structural information in real time, based on back scattered light from different layers within a material. This optical imaging technique offers two dimensional (2D) cross-sectional and three dimensional (3D) volumetric images. The resolution is on micron-scale and provides a penetration depth of few millimeters. Low-coherent light is coupled into a material and scatters. The echo's time delay and the intensity of backscattered light is compared to light that traveled a known distance, after they interfered with each other [216]. The swept source and spectral domain OCT exist in the category of the fourier domain optical coherence tomography. Main difference is the used light source. In swept source OCT, the light source is a short-cavity swept laser and the light is already divided into a spectrum, making a spectroscope unnecessary. This results in high-speed data acquisition and much clearer images. For spectral domain, the light source is a super-luminescent diode laser generating a broad wavelength light [217]. Penetration depth l_c is directly depended on the central wavelength λ_0 and the spectral width $\Delta\lambda$.

$$l_c = \frac{2ln2}{\pi} \frac{\lambda_0^2}{\Delta\lambda} \tag{2.17}$$

For spectral domain systems, the central wavelength is approximately 840 nm and for swept source systems 1050 nm. Shorter wavelength OCT systems are ideal for high resolution requirements. For imaging samples that have higher optical scattering properties, longer wavelengths lead to better results. Longer center wavelengths are not heavily affected by scattering. This leads to improved penetration depths. The non-invasive technique in combination with high resolution makes it suitable for process implementation [218]. There are only few publications available utilizing OCT for dispersion analysis. In principal, OCT provides a quantification of CNP and fibers in composites [219–221]. Schneider et al. demonstrated the applicability for OCT to get information about the dispersion state of CNP in polymer matrices processed with a TRM [222].

2.6.2 Impedance Spectroscopy

Impedance spectroscopy analyses the circular frequency dependent complex electrical behavior of materials. The system is excited by an alternating circular frequency dependent input voltage V and the output current I is measured, were $\omega = 2\pi f$.[1]

$$V = V_0 \cdot e^{j\omega t} \qquad I = I_0 \cdot e^{j(\omega t + \varphi)}$$

The impedance Z can be split into real and imaginary part.

$$Z^* = \frac{V}{I} = \frac{V_0}{I_0} e^{-j\varphi} = Z' - j \cdot Z'' \tag{2.18}$$

The absolute value of the impedance Z is can be calculated by utilization of following equation:

$$|Z^*| = \sqrt{Z'^2 + Z''^2} \tag{2.19}$$

Z' denotes the real part and Z'' the imaginary part.

$$Z' = |Z^*| \cdot cos(\varphi) \qquad Z'' = |Z^*| \cdot sin(\varphi)$$

Z' and Z'' are dependent of the phase angle φ, which is derived by following correlation:

$$\varphi = tan^{-1}\left(\frac{Z''}{Z'}\right) \tag{2.20}$$

The real part is given by

$$Z' = R_{el} \tag{2.21}$$

where R_{el} denotes an ohmic resistance. The imaginary part is the reactance and results from a superposition of capacitive and inductive electrical behavior.

$$Z'' = X_C + X_L \tag{2.22}$$

The capacitive part of the reactance X_C results from a capacitive behavior and is mathematically described by

$$X_C = -\frac{1}{C\omega} \tag{2.23}$$

with the capacity C. The inductive part of the reactance X_L results from an inductive behavior and is mathematically described by

$$X_L = L_{el}\omega \tag{2.24}$$

with the inductivity L_{el}. Figure 2.13 schematically illustrates the dependency of the impedance for (a) a resistor and (b) a capacitor. For CNP/polymer composites the absolute value of Z decreases with increasing circular frequency [223]. At low frequencies the bulk impedance is circular frequency independent, while at higher frequencies the impedance decreases [224]. This behavior is called *Jonscher's "universal dielectric response"* [225]. The impedance can be well described by a model consisting of resistors and capacitors [224, 226]. Where the resistive behavior contributes to interconnected CNP agglomerates and the capacitive behavior the distribution of the particles within the insulating polymer matrix [227]. The impedance spectra shows a clear dependency on filler concentration. With increasing filler concentration the resistive behavior becomes more dominant [228]. Other publications show that constant phase elements (CPE) give better results for describing the non ideal capacitive behavior [229, 230]. CPE describes

[1] ω: circular frequency in rad/s and f: frequency in Hz

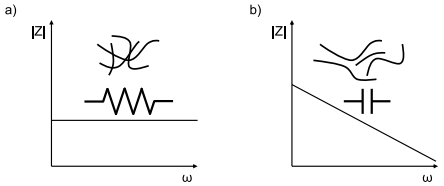


Figure 2.13: Schematic dependency of absolute complex impedance on circular frequency of a filler network with (**a**) agglomerates leading to resistive behavior and (**b**) separated particles leading to capacitive behavior

the AC response of non-homogeneous systems. CPE has two parameters: Q and m. The impedance of this element is given by the formula:

$$Z_{CPE} = \frac{1}{Q \cdot (j\omega)^m} \tag{2.25}$$

Z_{CPE} becomes equal to a capacitance for $m = 1$. Similarly to a capacitor, a CPE keeps the phase constant at variable frequencies, but the phase shift differs from 90 °. CPE represents a non-perfect capacitor.

2.7 Basics of Rheology - A Literature Overview

The TRM drags the material into a micrometer gap between counter rotating rollers to generate high shear forces. Here, the generated shear stress τ depends directly on the liquid's viscosity η and shear rate $\dot{\gamma}$.

$$\tau = \eta\dot{\gamma} \tag{2.26}$$

A rheometer is utilized to measure the material's flow behavior. Hereby, Couette geometries for example offer shear rates of 4000 s^{-1}. Three roll milling and ultrasonication generate high shear rates of 10^5 s^{-1} [231] and 10^9 s^{-1} [192], respectively. Hence, they are attributed to achieve the best dispersion grades [38]. Disregarding high shear rates, a certain time of shear rate application is neccessary to achieve particle separation [232]. The dispersion of CNT into polymers was intensively investigated in numerous publications. Schulz et al. observed superior dispersion results for TRM [233]. Here, high shear mixing and sonication raise unsolved issues, like the fact that the continuous TRM process, offering lower shear rates, leads to better dispersion grades than dispersion by way higher shear rate oscillatory ultrasonication [176]. Despite that, ultrasonication leads to fracture of CNT, which results in lower maximum conductivity at higher filler loading [190]. TRM does not lead to this undesired fracture of CNT according to Gojny et al. [175]. Another disadvantage of ultrasonication is the fast heating up of the material and very local energy input [234]. TRM offers local high shear forces within the gap and a short dwell time, resulting in moderate heat input, as well as controllable and mild dispersion [38]. To address the different dispersion results by steady and oscillating dispersion methods, a profound look at the rheological properties is necessary to identify the shear-induced agglomeration and separation mechanisms in particle filled polymers. The theory of rheology will be introduced and an overview of the research that has been done, regarding rheological characterization of particle filled polymers, will be given.

A material between two parallel plates, which have differential parallel moving velocities, is exposed to shear. The resulting shear stress τ in the material depends on the applied shear deformation γ and shear modulus G. Due to the fact that the values of the shear deformation tend to be small, the value is usually given in %.

$$\tau = G \cdot \gamma \tag{2.27}$$

The viscosity of the material describes its resistance to deform under shear stress, resulting from inner friction of the material and is described by Equation (2.26). For a rheometer consisting of two discs (one stationary and the other rotating) with a radius r, spacing h and rotational angle θ, the shear deformation γ is given by:

$$\gamma = \frac{r}{h} \cdot \theta \tag{2.28}$$

By derivation, $\dot{\gamma}$ is defined as:

$$\dot{\gamma} = \frac{r}{h} \cdot \frac{d\theta}{dt} \tag{2.29}$$

For a sinodial oscillatory excitation, the shear deformation with the constant angular frequency ω and constant shear amplitude γ_0 is given by:

$$\gamma(t) = \gamma_0 \cdot sin(\omega t) \tag{2.30}$$

and consequently, the shear rate $\dot{\gamma}$ is given by:

$$\dot{\gamma}(t) = \gamma_0 \cdot \omega \cdot cos(\omega t) \tag{2.31}$$

Due to the non-ideal viscous behavior of most materials, the resulting shear stress τ is out of phase:

$$\tau(t) = \tau_{max} \cdot sin(\omega t + \delta) \tag{2.32}$$

This shear stress can be split in an in-phase (real) and an out-of-phase (imaginary) part. The in-phase part corresponds to the elastic (energy storing) material characteristic and the out-of-phase viscous (energy dissipating) material characteristic. Following addition theorem enables the segmentation in elastic and viscous contribution:

$$sin(\alpha + \beta) = sin(\alpha)cos(\beta) + cos(\alpha)sin(\beta) \tag{2.33}$$

Taking the stated addition theorem into account, Equation 2.32 gives:

$$\tau(t) = \tau_{max} \cdot cos(\delta)sin(\omega t) + \tau_{max} \cdot sin(\delta)cos(\omega t) \tag{2.34}$$

Whereby $cos(\delta)$ and $sin(\delta)$ are constant values. The stress within the material is the sum of the energy storing (elastic) contribution:

$$\tau_{elastic} = \tau_{max} \cdot cos(\delta)\gamma_0 = G' \cdot \gamma_0 \tag{2.35}$$

and a dissipating contribution (viscous) [235]:

$$\tau_{viscous} = \tau_{max} \cdot sin(\delta)\gamma_0 = G'' \cdot \gamma_0 \tag{2.36}$$

The complex shear modulus G^* consists of an elastic storage modulus G' and viscous loss modulus G''. Whereby the absolute value of the complex shear modulus is given by:

$$|G^*| = \sqrt{G'^2 + G''^2} \tag{2.37}$$

As already stated, a visco-elastic material responds to a sinodial shear strain excitation (refere Equation (2.30)) with a phase shifted stress response. The phase shift is given by δ. Finally, Equation (2.38) correlates the resulting shear stress with the applied shear strain [236]:

$$\tau(t) = \tau_{max} \cdot sin(\omega t + \delta) = \gamma_0(G'(\omega) \cdot sin(\omega t) + G'' \cdot cos(\omega t)) \tag{2.38}$$

For a fully-elastic material, G^* would be equal to G' and for a viscous fluid equal to G''. The phase shift δ can be derived from the following equation:

$$tan(\delta) = \frac{\tau_{max} \cdot sin(\delta)}{\tau_{max} \cdot cos(\delta)} = \frac{G''}{G'} \tag{2.39}$$

$G' > G''$ solid-like $\qquad$ $G'' > G'$ fluid-like $\qquad$ $tan(\delta) = 1$ fluid solid cross-over

This results in a complex viscosity η^*, which is defined as:

$$\eta^* = \frac{G^*}{\omega} \tag{2.40}$$

The field of oscillatory rheology provides two common established test procedures. One is the frequency-sweep and the second one is the strain-amplitude-sweep. For a frequency-sweep the angular frequency ω increases at constant shear strain amplitude γ_0 over the test time. For a strain-amplitude-sweep the shear strain amplitude γ_0 increases at constant angular frequency ω over the test time. Therefore, the shear rate given in Equation 2.31 depends for presented test procedures either on ω or γ_0.
To characterize the behavior of the material, the relaxation time needs to be considered [237, 238]. This can be evaluated by the Deborah number and is also valid for filled polymers [239]. The Deborah number De is defined as the ratio of characteristic time λ_c to the scale of deformation λ_s.

$$De = \frac{\lambda_c}{\lambda_s} \tag{2.41}$$

The characteristic time is defined as the time, which a material requires to reach 63.2% of its ultimate retarded elastic response to a step change [236]. For $De > 1$ elastic effects are dominant, while viscous effects are dominant for $De < 0.5$. For all other Deborah numbers the material exhibits viscoelastic behavior. A high molecular weight polymer exhibits a cross-over of the storage and loss modulus in the frequency-sweep. This is usually not the case for the low molecular weight epoxy resins. Therefore, it can be considered as Newtonian-like fluid [240–243]. The reciprocal value of the cross-over frequency ω_c is considered as relaxation time λ.

$$\lambda = \frac{1}{\omega_c} = \frac{1}{2\pi f_c} \tag{2.42}$$

Cox and Merz postulated that $\eta(\dot{\gamma}) = \eta^*(\omega)$ for simple structured polymers [244].
According to Equation (2.29), the shear rate in steady shear flow increases with increasing angular velocity. For oscillatory flow, according to Equation 2.31, as already stated, $\dot{\gamma}$ increases with higher angular frequency ω or strain amplitude γ_0.

2.7.1 Rheological Behavior of Carbon Nanoparticle Filled Polymers

Addition of particles into polymer may enhance their stiffness, strength, dimensional stability, fracture toughness, impact strength, heat deflection temperature and mechanical damping. Furthermore, the addition may reduce the permeability to gases and fluids and modifies the electrical properties. Undoubtedly, the main reason, besides adding functional properties, is the cost reduction by filler addition, caused by less polymer usage. Best example to mention is the modification of automotive tires with carbon black to enhance their durability and lower the costs [236]. Unfortunately, the rheological properties of a polymer may be affected negatively by particle addition. The particle type needs to be well chosen. Here the costs, availability, compatibility with the polymer, which may change the flow characteristics, physical properties, thermal stability, chemical resistivity, recyclability and toxicity need to be considered. An added filler into a polymer, with the purpose of reinforcement, which is strong and stiff, should bear the main part of

the stress applied to the composite. The polymer which offers low strength, but is tough and flexible should transfer the load into incorporated filler particles [236]. Three configurations of particle-polymer interactions occur [236]. In the first case, the filler is only present physically and exhibits no interaction with the non-polar polymer. In this case, the filler acts as a diluent and weakens the material by low interface strength. In the second case, the filler is physically present, while polymer wets the surface, caused by either the inherent polymer affinity or a surface treatment of the filler. The development of physical bonds leads to an increase of inner friction, which constrains the mobility of the filler. Thereby, this results in an increase in strength and elongation at break. The potential of enhancement of the physical properties depends on the interface strength between filler and polymer. The last case gives the formation of chemical bonds between filler and polymer, offering an exceptional strengthening potential. Well known examples are the carbon black reinforcement of rubber or the incorporation of silanized glass fibers in fiber reinforced epoxy.

Another factor to consider is the required filler loading to achieve the desired enhancement of physical properties. The particle-particle interaction weakly increases at low filler and rather strongly at elevated loadings. A sufficient filler degree is necessary for the beginning of interparticle interactions. This depends strongly on the geometry and surface nature of the incorporated particles as well as their distribution within the matrix [236]. Required filler loadings for particle-particle interaction are much lower for high aspect ratio particles, like fibers, (in the range of 1 vol.%) and non-agglomerated spherical particles, with a large diameter, need a filler concentration of 20 vol.% to 40 vol.% to interact [245]. The specific surface area, which needs to be wetted, is very high for nanoparticles and hence, results in high impact on flow properties [246]. For electrical conductivity a complete network formation has to be given. The network formation is dominated by particle-particle interactions and the required filler loading can be determined by rheological measurements, because of the liquid, dominated by the polymer phase, and rigid (solid), dominated by the particle network, transition [247]. This transition is often considered as rheological percolation. Reaching this percolation threshold, the long range interaction of the fractales form a supermolecular three dimensional nework within the polymer [248]. Their determination is discussed controversially in literature. Utilization of oscillating rheology measurements reveals the elastic part, resulting from particles and dissipative part, resulting from the polymeric phase, of the filled polymer [249]. Penu et al. summarized the available criteria to identify the critical filler content for rheological percolation [247]. Critical parameters to look at are the change of complex viscosity η^* [248], storage modulus G' [250] or the ratio of storage and loss modulus G'/G'' [251] in dependency of the filler loading. At the rheological percolation threshold, a critical filler loading is reached, suddenly raising the viscosity [197, 248] and storage modulus [252–255]. Whereby, the highest sensitivity is shown by the storage modulus [256]. Other indicators are the cross-over of G' and G'' [257] or the evaluation of the inflection point in storage modulus [257]. Frequency dependency of the composite reveals the relaxation processes within the composite, which are highly affected by the filler particles [258]. At low oscillating frequencies the complex viscosity shows a plateau, indicating the rheological percolation [247, 259–261]. For thermoplastic based nanocomposites the polymer entangles with the particles [262]. For low frequencies the particles restrain the long range relaxation of the polymer, which is responsible for the plateau behavior and explains the rise of viscosity with increasing filler loading [263]. At high frequencies the particles have minor impact. They do not affect the short range relaxation of the polymer [134].

The shear rate-dependent network changes of particle-filled polymers were investigated intensively for steady shear flow, and the structure analysis by rheology for MWCNT polymer suspensions was studied widely. The literature gives three types of material behavior of carbon nanoparticle-filled polymers under shear. Figure 2.14 gives a schematic overview of these rheological material behaviors. Their features will be discussed in the following section. Furthermore, unsolved questions will be revealed. Most rheological results in the literature are reported for filled thermoplastic polymers. Figure 2.14 (a) describes a pseu-

doplastic material behavior under increasing steady shear rate. The viscosity is shear rate independent until a yield point and shear-thinning occurs subsequently [233, 236, 264]. In low viscosity systems like unsaturated polyesters, shear-thinning occurs without a yield point [265]. This shear-thinning occurs due to shear alignment of the filler particles during steady shear, which lowers particle-particle interactions within the network [2].

A concurrent measurement of the electrical DC properties reveals deeper structural changes of carbon nanoparticle-filled polymers. This method was firstly reported by Skipia et al. in 2009 [266]. Low steady shear rates lead to carbon nanoparticle agglomeration in epoxy resins [266–273] and thermoplastic polycarbonate (PC) [274, 275]; whereas high shear rates break-down agglomerates and therefore the conductive network [268, 276, 277]. Independent of the initial dispersion state, the final resulting electrical particle network is directly connected to the applied steady shear rate [275, 278, 279]. An increase in viscosity accompanies increased electrical conductivity due to the build-up of the particle network [280]. The shear-thinning and change of the network is due to the rearrangement of particles and the orientation of polymer chains, initiated by the shear rate [270, 280, 281]. Beside the steady shear results, there are data available for oscillatory frequency and strain-sweeps. Oscillatory experiments are most suitable to assess the internal structure of a material.

Figure 2.14 (b) schematically shows the dependency of the complex viscosity of carbon nanoparticle-filled polymers on angular frequency. With increasing angular frequency, the complex viscosity decreases due to increasing shear rate (Equation (2.31)). Shenoy et al. postulated that the results from dynamic experiments would not lead to any new conclusions [236]. Nevertheless, there are few experimental data available for this strong shear-thinning behavior in EP [282, 283], as well as for thermoplastic matrices [284–287]. The storage modulus determined in oscillatory experiments and electrical conductivity are in good accordance. A high storage modulus comes along with a pronounced three-dimensional particle network at low frequencies [250, 275, 288]. Most of the studies focused on the dependency of either the electrical or rheological properties of the filler content. An increasing filler content leads to a higher storage modulus, yield stress and electrical conductivity with occurring pronounced independency of G' for low frequencies independently of the used polymer [265, 270, 283, 285, 287, 289–291]. Chapartegui et al. concluded that higher angular velocities lead to more destruction of the filler network [270].

The dependency of complex viscosity on applied shear strain amplitude is schematically shown in Figure 2.14 (c). A pronounced shear-thinning is observed in this case, as well [292, 293]. The impact of oscillatory strain on particle networks, in the case of viscosity, is higher for low molecular weight polymers [294]. Richter et al. showed by experiments and a theoretical approach that shear amplitude leads to a change of particle clusters [295]. An increase of G' and conductivity at small deformations is reported

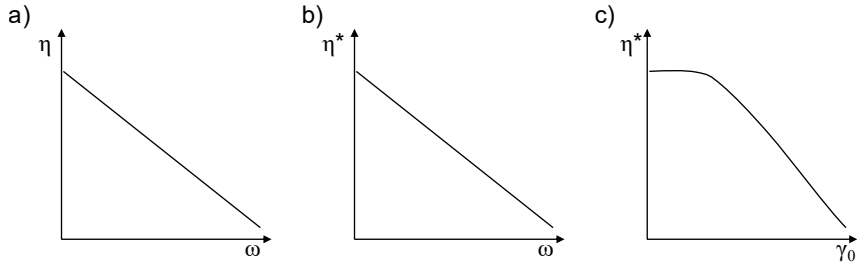


Figure 2.14: Overview of reported rheological behaviors of MWCNT/polymer suspensions: shear-thinning for: (**a**) steady flow with increasing shear rate (rate-sweep), (**b**) oscillatory flow with increasing angular frequency (frequency-sweep) and (**c**) oscillatory flow with increasing strain amplitude (amplitude-sweep or strain-sweep)

by Handge et al. [296] and a decrease of conductivity with accompanying shear-thinning for high strains by Zeiler et al. [297].
The identification of the mechanisms for CNT/polymer is complex, because three types of networks occur [281]:

1) Polymer network, by entanglements of molecule chains
2) Carbon nanotube network, by interconnected CNT
3) Combined nanotube/polymer network

Especially for high molecular weight thermoplastic materials, which show a distinct non-Newtonian viscoelastic behavior, the mechanisms of the network changes strongly interfere [298]. By using low molecular weight polymers, a accentuation of filler network induced effects is possible [270].
Summarizing, an increase in shear rate leads to a structural change of the composite material, independent of increasing angular velocity in steady shear or increasing shear amplitude or angular frequency in oscillatory shear. The mechanisms behind the impact of strain amplitude and angular frequency on the particle network remain unresolved. There are no results regarding oscillatory rheo-electrical characterization of MWCNT/EP composites reported yet to answer this. Dispersion of nanoparticles in polymer matrices is crucial in many areas, the incomplete understanding of fundamental mechanisms of particle network formation is therefore an important field to study.

2.8 Enhancement of Polymers' Fracture Toughness by CNP Modification

Epoxy resins offer high-performance properties, namely light weight potential, improvement of corrosion resistance, barrier properties, fire retardency and good electrical insulation properties [183] for a wide range of adhesive applications, as matrices in fiber reinforced composites or coatings [41]. However, due to their high grade of cross-linking they possess low fracture toughness and therefore, a brittle nature [299]. As already stated, the addition of carbon based nanoparticles leads to an electrical conductivity of the otherwise insulating polymer. The electrical conductivity can be well predicted with regard to particle concentration, their aspect ratio and waviness [300]. By variation of particle type and filler content, the electrical conductivity can be precisely adjusted [14]. Carbon nanoparticles typically lead to a non-favorable enormous increase of the nanocomposite's viscosity in dependency of filler type and loading [1, 2]. The viscosity is a critical parameter regarding the processibility of polymers. Reddy et al. observed that fillers migrate into the free volume and will increase it. This leads to a non-favourable decrease of nanocomposite's glass transition temperature [301]. Contrary, Vivo et al. reported a slight increase of the glass transition temperature for MWCNT addition [302]. Nevertheless, the addition of carbon nanoparticles leads to an enhancement of the mechanical properties of the polymer composite.
The critical value of the crack front stress intensity factor characterizes the resistance of a material against failure by fracture. Figure 2.15 (a) shows the test setup for the determination of critical stress intensity factor K_{IC} in a three-point-bending test (3PBT). The pre-notched rectangular sample is loaded under bending, resulting in a pure tension loading of the crack tip (mode I). For a critical stress value the crack starts to proceed. This results in sudden failure in case of brittle materials like glassy polymers. The determination of the mode II critical stress intensity factor K_{IIC} requires a crack tip loading under nearly pure in-plane shear. Fett suggests a realization in an asymmetric four-point-bending test (4PBT) of a pre-notched sample, shown in Figure 2.15 (b) [303]. He analyzed the crack tip loading and failure with finite element modeling and energy considerations.

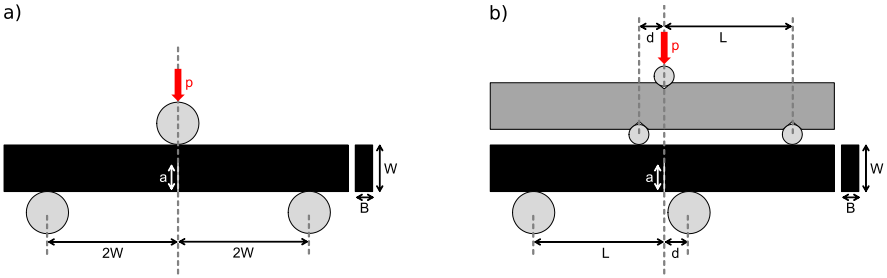


Figure 2.15: Test setup and definitions for determination of (**a**) K_{IC} in a three-point-bending test and (**b**) K_{IIC} in asymmetric four-point-bending test - adapted from [304]

The geometry of the specimen and dimensions of the test setup are given by the height W, thickness B, distance from support to crack L, crack length a and asymmetric distance d. The corresponding applied loads in 3PBT and 4PBT are given by p. Figure 2.16 gives the dimensions of the plastic zones in mode I and II for the condition $K_{IC} = K_{IIC}$, respectively. The determination of stress distributions along

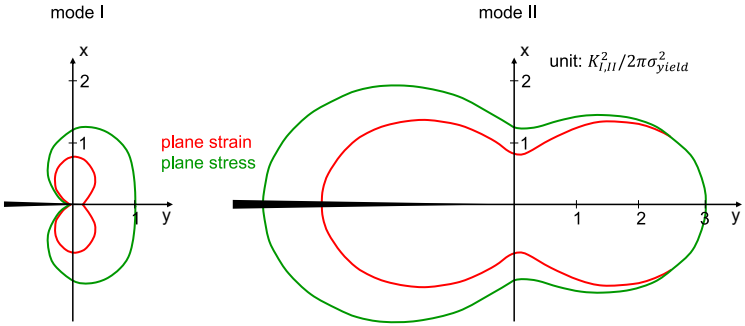


Figure 2.16: Dimensions of the plastic zones for (**left**) mode I and (**right**) mode II crack tip loading - adapted from [305, 306]

the specimen ($\sigma_x(x,y)$, $\tau_{xy}(x,y)$) leads to numerical descriptions of those stresses with endless sum terms. To obtain a reasonable accuracy for the stress distribution, the sums are cut after a certain order of terms. The stress distribution in combination with the geometry of the specimens leads to an integrational description of the stress intensity factors:

$$K_I = \int_0^a h_I(\zeta/a, a/W)\sigma_y(\zeta)d\zeta \tag{2.43}$$

and

$$K_{II} = \int_0^a h_{II}(\zeta/a, a/W)\tau_{xy}(\zeta)d\zeta \tag{2.44}$$

with $\zeta = (W/2) - y$.

By consideration of a boundary-collocation technique, it is possible to find formulas for the weight functions h_I and h_{II}:

$$h_I = \sqrt{\frac{2}{\pi a}}\frac{1}{\sqrt{1-\zeta/a}(1-a/W)^{3/2}}[(1-\frac{a}{W})^{3/2} + \sum A_{\alpha\beta}(1-\zeta/a)^{\alpha+1}(\frac{a}{W})^{\beta}] \tag{2.45}$$

$$h_{II} = \sqrt{\frac{2}{\pi a}} \frac{1}{\sqrt{1-\zeta/a}(1-a/W)^{1/2}} [(1-\frac{a}{W})^{1/2} + \sum A_{\alpha\beta}(1-\zeta/a)^{\alpha+1}(\frac{a}{W})^{\beta}] \quad (2.46)$$

with tabulated coefficients for $A_{\alpha\beta}$. Integrating over the length of the crack the stress intensity factors can be calculated after following equation:

$$K_I = \frac{p}{WB}(1-\frac{d}{L})\sqrt{\pi a} F_I \quad (2.47)$$

$$K_{II} = \frac{p}{WB}(1-\frac{d}{L})\sqrt{\pi a} F_{II} \quad (2.48)$$

The geometric factors F_I and F_{II} can be obtained from tables according to the specimens geometry or can be calculated following the equations stated below:

$$F_{II} = 3.9204\xi - 5.1295\xi^2 + 14.4766\xi^3 - 26.2916\xi^4 + 17.073\xi^5 \quad (2.49)$$

with $\xi = a/W$.

Important ratios to determine the mode II fracture toughness (in plane shear) in an asymmetric 4PBT are the following.
The length to width ratio should be

$$\frac{L}{W} = 2.5, \quad (2.50)$$

so that the distance between supports has a minimized influence on the result.

Other geometry ratios are

$$0.4 < \frac{a}{W} < 0.6 \quad (2.51)$$

so that the influence of K_I becomes small. Ayatollahi et al. investigated different ratios by finite element modeling and concluded that 0.5 is an appropriate value to choose, because it secures the maximum distance to both, the bottom and top edges [307].

$$0.35 < \frac{d}{W} < 0.625 \quad (2.52)$$

leads to an independent factor K_{II} from the ratio d/W.

By choosing following ratios for a given material thickness of W

$$\frac{L}{W} = 2.5, \quad \frac{a}{W} = 0.5, \quad \frac{d}{W} = 0.5 \quad (2.53)$$

following relations can be derived

$$W = \frac{L}{2.5} = 2a \Rightarrow L = 5a = 5d \quad (2.54)$$

The mode II fracture toughness (crack tip loading in in-plane-shear) specimens have to be of a minimum length to ensure the asymmetric bending test configuration without gliding through the supports:

$$L_{total} = 2L + \Delta L = 50\,mm$$

where ΔL denotes the length addition to the minimum required specimen length. According to this geometry with the ratios stated above the geometry factors are the following: $F_I = 0.0806$ and $F_{II} = 1.3661$, so that the stress intensity factors are:

$$K_I = \frac{p}{WB}(1 - \frac{d}{L})\sqrt{\pi a} \cdot 0.0806 \tag{2.55}$$

$$K_{II} = \frac{p}{WB}(1 - \frac{d}{L})\sqrt{\pi a} \cdot 1.3661 \tag{2.56}$$

Since mode II is investigated exclusively in the asymmetric 4PBT and mode I in 3PBT, only the equation for K_{II} has to be considered. This decision contributes to the pure tension loading of the crack tip in 3PBT, which is most desirable for mode I fracture.
The mode I fracture toughness (crack tip loading in tension) is determined in the presented symmetrical three-point-bending-test. Important geometrical ratios for the sample are specified in ASTM D5045-14 [308] with:

$$2 < \frac{W}{B} < 4 \tag{2.57}$$

and

$$0.45 < \frac{a}{W} < 0.55 \tag{2.58}$$

The mode I fracture toughness in 3PBT can be calculated by the following equation, stated in ASTM D5045-14 [308]:

$$K_I = \frac{p}{B\sqrt{W}} f(x) \tag{2.59}$$

with $x = a/W$ and

$$f(x) = 6x^{1/2} \frac{1.99 - x(1-x)(2.15 - 3.93x + 2.7x^2)}{(1+2x)(1-x)^{3/2}} \tag{2.60}$$

It is widley reported, as already stated that the brittleness of epoxy can be overcome by addition of various types of nanoparticles [309, 310]. They promise high potential for fracture toughness improvement without affecting other mechanical properties. This results from improved energy dissipation and internal stress re-allocation. The quality of dispersion is crucial, because the nanoparticles eventually act as defects in case of poor dispersion [311–313]. For instance, the modification of polypropylene (PP) with fillers results in a heterogeneous composite system. The distributed particles induce stress concentrations under an external mechanical load. The magnitude of stress intensification highly depends on the particles' geometry and distribution as well as on the physical properties of the particles and polymer. Also, the interfacial adhesion plays a dominant role [314]. Heterogeneous stress distribution in combination with the developing local stress intensifications around the particles influence the deformation and fracture behavior as well as its overall performance of the composite. Filler addition affects the crystalline structure, too. This results as well in different mechanisms for fracture and deformation of the composite. Especially, rigid particles incorporated in PP lead to enourmos differences in the crack initiation and propagation, showing a completley different fracture behavior. The fracture process initializes with beginning of plastic deformation of the polymer in front of the crack tip. Debonding of particles and polymer (creation of holes) and the subsequent plastic flow of the matrix zones, remaining between the cavities, are the responsible micromechanisms leading to plastic deformation. These generated zones show high plastic deformations until rupture by tearing occurs. Particle-polymer debonding is considered in literature to be the initial damage mechanism [315]. In epoxy composites the nanoparticles lead to plastic deformation of the polymer and nucleation of voids. Also, the particles benefit crack deflection and bifurcation at agglomerates [206].

Nadiv et al. investigated the optimal concentration of nanoparticle filler loading regarding fracture toughness in mode I and correlated it with the electrical and rheological percolation [316, 317]. They concluded that the rheological percolation occurs prior to electrical percolation. The optimal nanoparticle concentration, which gives the best tradeoff between the material's property enhancement, slightly lays below the filler loading leading to rheological percolation. Allaoui et al. underpin the observation that electrical and rheological percolation lay in the same filler loading range [318]. Domun et al. reported this optimal filler content regarding the mode I fracture toughness increase for a wide set of different type of nanoparticles in their review article, as well [310]. Numerous other groups underpinned this observation [307, 310, 319–326]. The fact that the electrical percolation requires a higher filler loading than the rheological percolation leads to a trade-off between the enhancement of physical properties and processibilty of such nanocomposites. The effect of carbon nanoparticles on mode II fracture toughness is discussed controversially in literature. Various groups report an increase of mode II fracture toughness [307, 322, 327, 328]. A continuous decrease with increasing filler loading is reported by Moghadam et. al. [329] and Shadlou et al. [327]. Zappalorto et al. observed a maximum in mode I and mode II fracture toughness by variation of filler content [323]. These enhancements can be even transferred into the fiber composite [330]. Figure 2.17 (a) gives a summary of the reported K_{IC} and K_{IIC} values for polymer nanocomposites with MWCNT, nanoclay (NC), graphene, nanodiamond (ND), carbon nanofiber (CNF) and SWCNT modification.

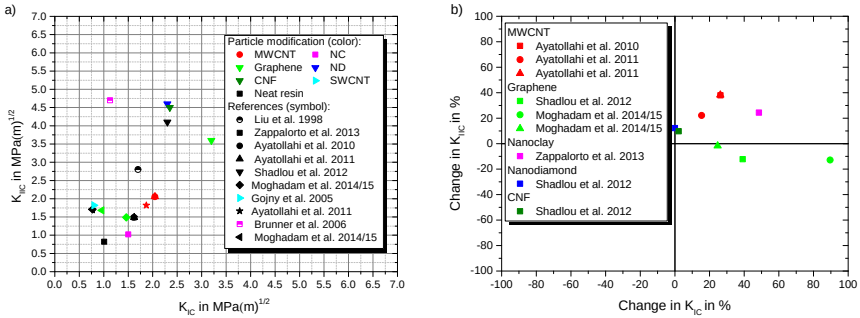


Figure 2.17: Overview of (**a**) K_{IC} and K_{IIC} values for neat polymers and their nanocomposites with different filler types and (**b**) enhancement of fracture toughness normalized to the values of the neat polymer for different particles types [206, 307, 310, 322, 323, 327, 329, 331–334]

The variation in reported values of K_{IC} and K_{IIC} is very high, even for the neat polymer. The enhancements of K_{IC} and K_{IIC} normalized to the values of the neat polymer are given in Figure 2.17 (b). Planar particles, like graphene, improve the fracture toughness in mode I up to 90 %. The opposite is the case for the mode II fracture toughness. Here, they lead to degradation. MWCNT, ND, NC and CNF enhance the fracture toughness in mode I and II.

3 Research Hypotheses and Structure

The main research hypothesis and auxiliary research hypotheses can be derived from the initially stated questions given in Section 1.1 and the issues addressed in the previous section.

Main research hypothesis

The assessment of optimum material properties and dispersion quality out of the process with a resulting cut-down of processing time becomes available by the implementation of in-line monitoring of three roll milling dispersion processes.

Auxilary research hypothesis 1

The predominant factor for particle separation throughout the dispersion process is the applied strain.

Auxilary research hypothesis 2

Line-load evaluation, electrical measurements and optical coherence tomography allow the assessment of dispersion quality.

Auxilary research hypothesis 3

An optimum filler loading exists with regard to processiblity as well as final electrical and mechanical properties of the nanocomposites in dependency of used particle type.

Auxilary research hypothesis 4

Three roll milling is a suitable technology for dispersion production at industrial scale.

Figure 3.1 illustrates the strategy to address the aforementioned hypotheses and gives the structure of this thesis along the value chain from the nanoparticle and polymer to the final application. In a first step the used epoxy resins will be characterized to have reference values for the demonstration of the impact of nanoparticle modification. The second step is the characterization of the different nanoparticles used. Subsequently, the driving force for the particle dispersion will be derived from rheo-electrical measurements of nanoparticle/epoxy composites. Different online-monitoring approaches, namely impedance spectroscopy, optical coherence tomography as well as acquired process data from three roll milling, will be evaluated. Accompanying, the impact of particle type and variation of used epoxy resin will be investigated. Chapter 7 gives the final properties of the nanocomposites in the liquid dispersion, after addition of the curing agent and in the solid cured state. Relevant properties in the liquid state are the rheological behavior, the stability and the electrical properties. In the cured state the electrical and thermo mechanical properties as well as the fracture behavior will be investigated. After that, the scalability of the three roll milling process will be demonstrated and the evaluated online monitoring methods will be validated by highlighting the possible processing time reduction. Finally, the possibility for the realization of a a bright colored glass fiber reinforced structure by SWCNT modification, which fulfills antistatic requirements, will be demonstrated.

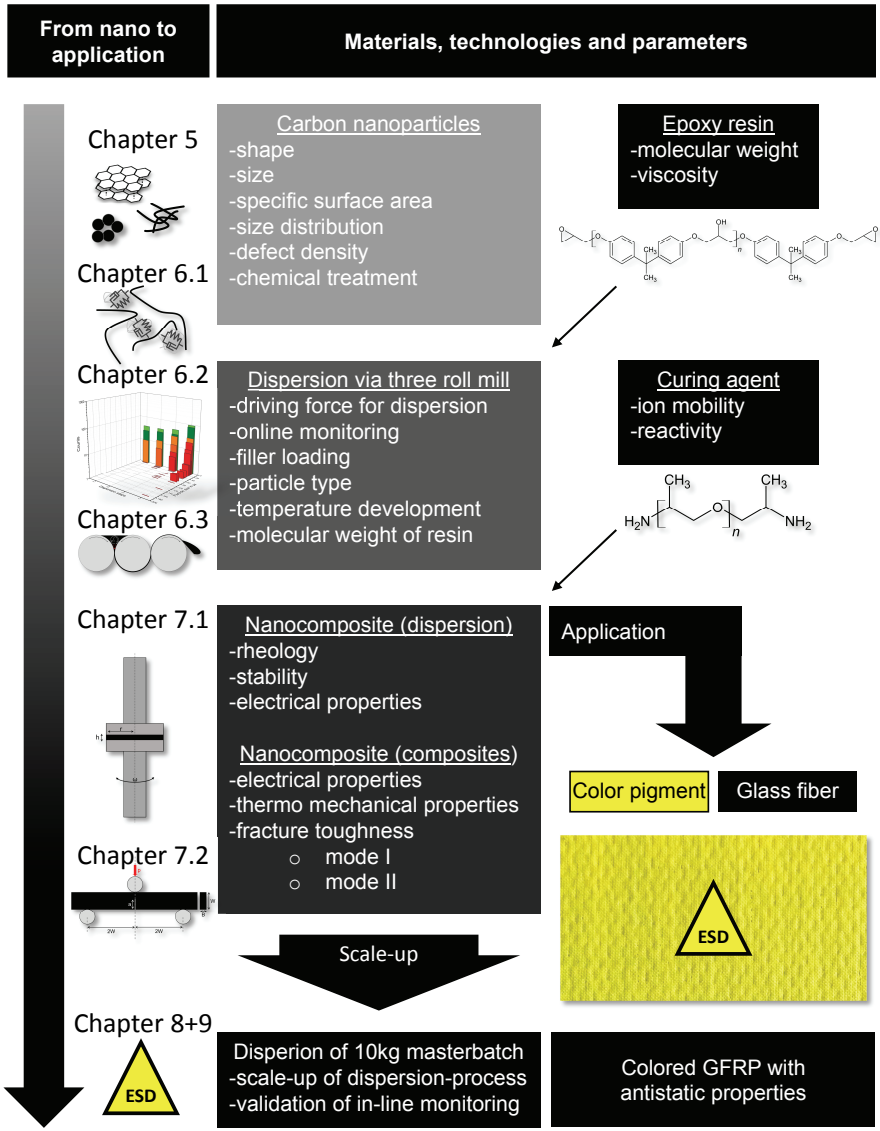


Figure 3.1: Schematical overview of the structure of the thesis - layout adapted from [335]

4 Applied Methods

4.1 Rheometry

A rheometer ARES RDA-III 28 (TA Instruments) was used for rheological characterization. The neat epoxy resins were characterized by strain-sweeps, frequency-sweeps as well as time-sweeps at 30 °C. Additionally, the curing behavior was investigated by time-sweeps. Temperature-sweeps revealed the temperature dependent viscosity of the epoxy resins. Table 4.1 lists the used parameters for the conducted resin characterization.

Table 4.1: Parameters for rheological characterization of epoxy systems

Test method	Plate diameter d	Spacing t	Strain	Frequency	Temperature
	mm	µm	%	Hz	°C
Time-sweep	40	500	10	5	30
Frequency-sweep	40	500	10	0.01 -80	30
Strain-sweep	40	500	0.1 -100	5	30
Curing behavior	40	500	2	5	30
Temperature-sweep	40	500	10	5	RT to 80

To monitor the shear rate-induced changes of the particle network to reveal the driving force for dispersion, a rheo-electrical characterization was carried out. Thereby, the rheometer was enabled to measure, concurrent to the rheological properties, the electrical DC resistance by utilizing a 2601A system source meter (Keithley). The electrical DC resistance was measured with 1 V between the two plates. Strain-sweeps were performed from 0.1 to 100 % at a frequency of 5 Hz. The test setup was a plate-plate configuration with a radius r of 20 mm and a spacing h of 500 µm. This gap spacing ensures that big agglomerates are not trapped between both plates. Figure 4.1 visualizes the test setup. To characterize the morphological changes of the particle network within the uncured resin, strain controlled frequency-sweeps at different strain amplitudes and strain-sweeps with different angular frequencies were carried out. The frequencies for strain-sweeps varied from 0.01 Hz to 80 Hz and the strain amplitude levels for frequency-sweeps from 0.1 % to 20 %. Frequency-sweeps were carried out in a frequency range from 0.01 Hz to 80 Hz and strain-sweeps from 0.1 % to 100 %. Additionally, the time-dependent relaxation of the particle network within the composite material after pre-shearing due to the dispersion process was investigated. This was analyzed by impedance spectroscopy and a long time oscillation rheological test with concurrent measurement of the DC resistance. The test frequency was 5 Hz and the strain amplitude was set to 0.5 %. Spacing and plate diameter were kept constant. For rheological characterization during the dispersion and after addition of the curing agent into the nanocompoiste, strain-sweeps were performed from 0.1 % to 100 % shear strain at a test frequency of 5 Hz to determine the complex viscosity as indicator for the state of the particle network.

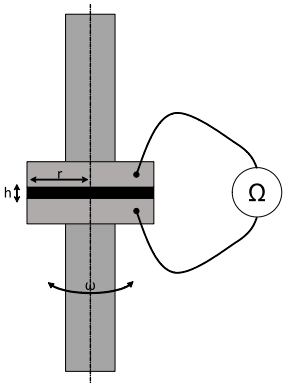


Figure 4.1: Rheo-electrical test setup

4.2 Differential Scanning Calorimetry (DSC)

Differential scanning calorimetry was performed on a 204F1 Phoenix F1 (Netzsch) in a temperature range from 20 °C to 200 °C at a heating rate of 20 K/min. DSC reveals the glass transition temperature T_G as well as endothermal and exothermal processes within the material, like evaporation of residual solvents.

4.3 Fourier-Transform Infrared Spectroscopy (FTIR)

Fourier-transform infrared spectroscopy was performed utilizing a Vertex 70 (Bruker) with a MIRacle attenuated total reflection (ATR)-equipment. The wavenumber range was chosen from 500 cm^{-1} to 4000 cm^{-1}. FTIR was performed to reveal the molecular composition of the different molecular weight epoxy resins.

4.4 Size Exclusion Chromatography (SEC)

Additionally, the molecular weight distributions were obtained using size exclusion chromatography (SEC) (system setup: FLOM Intelligent pump AI12, Schambek SFD RI2012 detector and HP 1050 series UV/Vis detector (λ_l = 256 nm)), using a MZ-gel SDplus linear column (5 μm, 300 x 8 mm) in tetrahydrofuran as solvent. The values were referenced against monodisperse polystyrene (PS) standards (Agilent). The tests were performed at the University of Hamburg.

4.5 Scanning Electron Microscopy (SEM)

Scanning electron microscopy was performed on a Zeiss Supra VP 55 (Zeiss) with an acceleration voltage between 5 kV and 10 kV to analyze the morphologies of the particles and to obtain a visualization of the agglomeration state. A Phenom XL (Thermo Scientific) was used to capture SEM images for crack initiation investigations on the nanocomposites' fracture surfaces. The operating voltage was 5 kV and the detector Topo A was used. Edges of the samples were coated with silver paint to improve the charge dissipation.

4.6 Energy Dispersive X-Ray Spectroscopy (EDX)

During SEM on Zeiss Supra VP 55, energy dispersive X-ray spectroscopy (EDX) was performed, too. EDX was taken at a voltage of 15 kV to reveal impurities and elemental composition of the particles.

4.7 Transmission Electron Microscopy (TEM)

Transmission electron micrographs, taken with FEI Talos F200X (Thermo Scientific) revealed the number of walls and layers as well as the bundle sizes of the particles. An acceleration voltage of 200 kV was used. Carbon particles were ultrasonicated in methanol, placed on a TEM grid and dried at 80 °C for preparation.

4.8 Determination of Specific Surface Area (SSA)

SSA of the particles were determined by a Surfer Gas Adsorption Porosimeter (Thermo Scientific) utilizing nitrogen to point out the particles' surface area, which need to be coated by the epoxy resin. The dertermination was conducted from the acquired adsorbtion-desorption-isothermal curve by utilizing the theory of Brunauer-Emmet-Teller (BET) [336].

4.9 Thermo Gravimetric Analysis (TGA)

Additionally, the impurity content of the nanoparticles was determined with thermo gravimetric analyses utilizing a TGA/DSC 1 - thermo gravimetric analyzer (Mettler-Toledo). Samples were placed in a 70 µl alumina crucible covered with a pierced lid. Temperature cycle started with a heat up from room temperature to 50 °C under nitrogen atmosphere. Afterwards an isothermal step at 50 °C for 10 min in nitrogen atmosphere followed, to keep the sample in steady state. The sample was heated under oxygen atmosphere to 950 °C, was held at this temperature for another 10 min and then cooled down to room temperature. Heating rates were 10 K/min and cooling rate 30 K/min. To evaluate the homogeneity of the CNP gaussian peak fits were applied to the differential curve according to Scheibe et al. [337, 338].

4.10 Raman Spectroscopy

The analysis of the defect density and the graphitization was evaluated via Raman spectroscopy utilizing a Jobin Yvon HR 800 (HORIBA) Japan, with a He-Ne laser offering a wavelength of 633 nm. The Raman spectra were obtained at room temperature (25 °C) with a spectral width of 500 cm^{-1} to 3000 cm^{-1}, an acquisition time of 10 s and a set filter of 0.6 . For evaluating the Raman spectra, in particular the D/G band ratio, the maxima of the individual peaks were correlated with each other. Lorentz fits were applied to evaluate the correct peak height. Carbon nanoparticles were measured without any pre-treatment. The I_D/I_G ratio reveals the quality of the nanoparticles. The degree of graphitization G_R can be calculated by following equation [339]:

$$G_R = \frac{I_G}{I_G + I_D} \cdot 100\% \tag{4.1}$$

The crystalline width L_a can be obtained as well from the I_D/I_G ratio by following empirical equation [340–342], which are in good correlation with the results gathered by X-ray diffraction (XRD) [343, 344]:

$$L_a = \frac{4.4}{I_D/I_G} \tag{4.2}$$

4.11 Dispersion via Three Roll Milling

The carbon nanoparticles were dispersed into the matrix via three roll mills. The process parameters were adapted from previous studies [175, 224, 345]. The particles were mixed manually with the epoxy resins. Filler degrees were chosen along the electrical percolation threshold. The given concentrations are calculated for the final composite, including the curing agent. The mixing ratio by weight of the epoxy systems was 100 parts resin and 28 to 30 parts curing agent, depending on the epoxy equivalent weight. The processed demonstrator masterbatch concentration relates to the neat epoxy system. Dispersion was performed on EXAKT three roll mills 120E-250 and 80E-Plus$^+$ (EXAKT Advanced Technologies) with roll diameters of 120 mm and 80 mm, respectively. The line load measurement was performed for the 120E-250 with a measuring box, supplied by the TRM manufacturer. The box enables to read out the line force data as well as the product temperature T_s (compare Figure 2.11). In the TRM 80E-Plus$^+$ the acquisition of line force data and measurement of the temperatures inside the three rollers (T_1, T_2 and T_3, see Figure 2.11) is directly implemented in the machine. The process parameters for the seven-step dispersion process with decreasing gap spacings were published in several studies [14, 346–350]. Table 4.2 lists the parameter for TRM 120E-250. Taking into account Equation (2.16), considering the fixed gear ratio of $1/3$ between the rollers and the diameter of the rollers, the gap ratio must be as well $1/3$. Figure 4.2 gives the resulting shear rates in dependency of the gap spacings and the chosen

Table 4.2: Process parameters for dispersion on three roll mill 120E-250

Step	Gap_1 in µm	Gap_2 in µm	n_1 in Rpm	n_2 in Rpm	n_3 in Rpm
1	120	40	33	100	300
2	40	13	33	100	300
3-7	13	5	33	100	300

roller speeds for diameters of 120 mm and 80 mm, calculated with Equation (2.15). To keep the shear rates compareable on both TRM a roller speed of 450 RPM was chosen for dispersion on the 80E-Plus$^+$. The rollers temperature was set to 30 °C and friction width l was 85 mm for all dispersion processes on 80E-Plus$^+$ and 145 mm on 120E-250 due constraints given by the machine. Table 4.3 gives processing

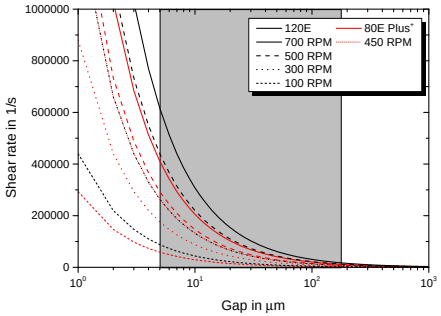


Figure 4.2: Shear rates in TRM in dependency of gap size and revolution speed

parameters on 80E-Plus$^+$.

Table 4.3: Process parameters for dispersion on three roll mill 80E-Plus^{+}, adapted from [350]

Step	Gap_1 in µm	Gap_2 in µm	n_1 in Rpm	n_2 in Rpm	n_3 in Rpm
1	120	40	50	150	450
2	40	13	50	150	450
3-7	13	5	50	150	450

4.12 Infrared Thermography

Infrared thermography images during dispersion were taken with a A640 (FLIR) to reveal the heat input into the material during processing.

4.13 Light Microscopy (LM)

Accompanying analysis of the dispersion quality via transmitted-light microscopy performed with BX-51 (Olympus). The pre-crack length of fracture toughness specimen was measured with same microscope. The averaged value was determined from three measuring points. Furthermore, a digital microscope VHX-6000 (Keyence) was used to reveal the 3D-morphology of the fracture surfaces.

4.14 Grindometry

The particle size analysis was performed by grindometry according to DIN EN ISO 1524 [351] with 25 µm grind gage PD-1510 and 100 µm grind gage PD-1512 (BYK-Gardner). Grindometry identifies the largest particles in the dispersion.

4.15 Optical Coherence Tomography (OCT)

Preliminary, for OCT dispersion analysis, two systems, namely TEL220C1 and GAN210C1 were evaluated. The GAN210C1 offers two light sources to achieve a broad spectrum. Both OCT-devices and the lenses are products of Thorlabs. Table 4.4 lists the specifications of the two systems.

Table 4.4: Specifications of OCT systems evaluated

Specification	Unit of measure	TEL220C1 with LSM03	GAN210C1 with LSM03-BB
Central wavelength	nm	1300	900
Depth resolution	µm	5.5	6.0
Lateral resolution	µm	13	8
Depth range	mm	3.5	2.8
A-Scan Rate	kHz	up to 76	up to 36

Figure 4.3 shows the resulting images recorded by (a) TEL220C1 and (b) GAN210C1

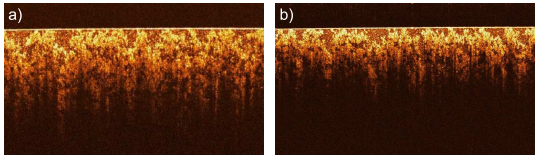


Figure 4.3: OCT image of cured resin containing 0.05 wt.% SWCNT (**a**) TEL220C1 and (**b**) GAN210C1

Both systems are able to detect scattering agglomerates. Penetration depth decreases with increasing filler concentration. The lateral resolution of GAN210C1 is superior to TEL220C1, but the penetration depth for TEL220C1 is 20 % higher. Hence, for further investigations TEL220C1 system with a LSM03 lense was chosen. For the dispersion analysis within this study, the taken OCT images were evaluated by a matlab script. Figure 4.4 illustrates the analysis process schematically. At first, a representative part of the image was cropped manually. The grey values were transformed into a heat map for purpose of improved visualization. Nearby pixels with the same color value were merged and identified as particles or agglomerates by the matlab function *bwconncomp*. The program code is given in Appendix A.

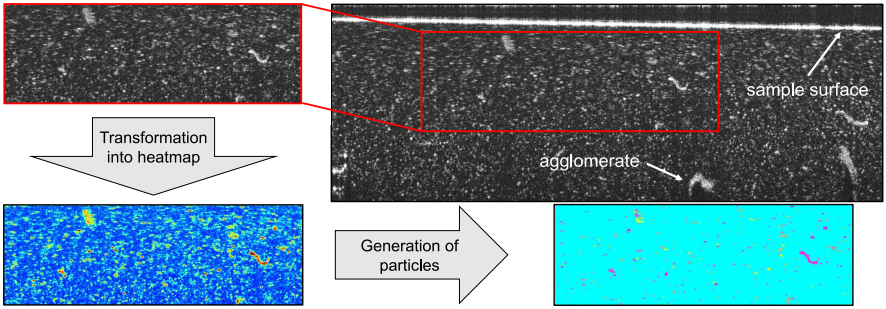


Figure 4.4: Schematic sequence of used matlab script

4.16 Determination of Electrical Conductivity

For plate manufacturing, the materials were infused with vacuum assistance into a closed mold. The post curing cycle to achieve maximum cross-linking was chosen according to the data sheet [352] with 15 h at 80 °C. After demolding, the samples were milled from the plate into the desired geometry. Prior to sawing and notching for fracture toughness sample preparation, the flanks of the manufactured rectangular specimens were covered with silver paint for determination of electrical conductivity. The electrical DC resistance of the cured rectangular specimens was measured at operating voltage of 1 V or 10 V, depending on specific electrical resistance of the material, between the silver paint covered flanks with a Keithley 2601A system source meter. The measurement was according to DIN EN ISO 3915 [353] (referring Figure 4.5 (a)). The volume and surface resistance were determined according to ASTM D257-07 [354] with combination of Keithley resistivity test fixture 8009 and Keithley source meter 2601A [355] (compare Figure 4.5 (b) and (c)). This surface resistance measurement method was adapted from Aurelia et al. [356].

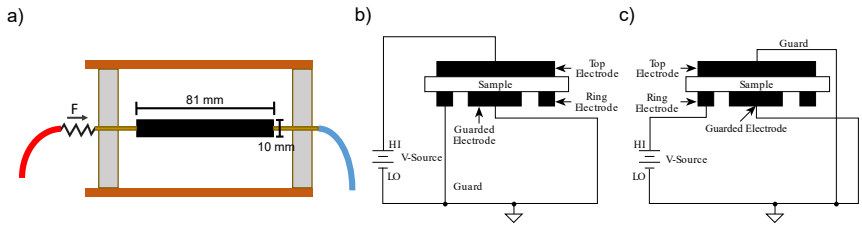


Figure 4.5: Test setups for electrical measurements (**a**) according to DIN EN ISO 3915 [353], (**b**) volume resistivity according to ASTM D257-07 [354] and (**c**) surface resistivity according to ASTM D257-07 [354] - adapted from [355, 357]

4.17 Impedance Spectroscopy

For impedance measurements a HP 4284A precision LCR meter coupled over a GBIB interface into Labview was used. After each dispersion step of the TRM process a small amount of the liquid particle-resin dispersion was inserted into a poly(methyl methacrylate) (PMMA) cylinder with an inner diameter of 12 mm. Two cylindrical aluminum electrodes were inserted from each side into the cylinder. The excess material could leak from the cylinder through a small hole. The final spacing was 10 mm. Additionally, samples were measured in cured solid state, to reveal network changes during the curing. The used samples were the same as used for DC conductivity measurements. Edges were covered with silver paint. The resistive part Z' and capacitive part Z'' were evaluated in a range from 20 Hz to 1 MHz with a voltage of 1 V for all concentrations. For improved understanding of electrical network formation over dispersion process a theoretical equivalent circuit model was developed. It gives the physical explanation for the measured data. The utilized CPE elements represent the non ideal capacitive behavior of the materials. Belhimria described the impedance behavior of CNT epoxy composites with a series of two parallel circuits consisting of a resistor and capacitor [358]. For fitting of the measured data with the model the Software EISAnalyser, which utilizes a Levenberg-Marquardt least squares fitting algorithm, was used.

4.18 Dynamic Mechanical Thermal Analysis (DMTA)

For dynamic mechanical thermal analysis (DMTA) specimens with a thickness of 2 mm were prepared from the manufactured plates. DMTA was performed with a Gabo Eplexor 500N (NETZSCH GABO Instruments). The heating rate was set to 3 K/min, clamping distance 30 mm and test frequency 5 Hz. The temperature range was 20 °C to 180 °C. DMTA was performed to determine the glass transition temperature as well as analysing the damping behavior of the cured composites.

4.19 Determination of Fracture Toughness in Mode I and II

The used geometry for mode II specimens is listed in Table 4.5.

Table 4.5: Required dimensions of mode II specimens

B	W	$a = 0.5W$	$L = 5a = 5d$	$d = 0.5W$
3.9 mm	7.8 mm	3.9 mm	19.5 mm	3.9 mm

Therefore the lower and upper support span length for asymmetric 4PBT to introduce the load is

$$L + d = 19.5\,mm + 3.9\,mm = 23.4\,mm$$

The geometry of the mode I specimen is the same as for the mode II test, only the lower support span and the load introduction differ, refer to Table 4.6. The total crack length a consists of a sawing cut and a

Table 4.6: Required dimensions of mode I specimens

$B = 0.5W$	W	$a = 0.5W$	$L = 2W$	$L_{support} = 4W$
3.9 mm	7.8 mm	3.9 mm	15.6 mm	31.2 mm

sharp pre-notch. This sharp pre-notch should be at least twice as deep as the sawing cuts width to ensure a negligible notch-effect. For the used 150 µm diamond sawing blade, the pre-notch has to be at least 300 µm deep. To ensure this boundary condition the sharp notch a_{blade} is chosen to be 500 µm. Therefore, the sawing cut has to be

$$a_{saw} = 3.9\,mm - 0.5\,mm = 3.4\,mm$$

deep, to reach the total crack length a of 3.9 mm.
The effect of different notching techniques for glassy polymeric single-edge notched bending (SENB) samples has been intensively investigated in literature [359–362]. They all conclude that an infinitesimal sharp notch leads to a homogeneous stress field and no prior plastic deformations in front of the crack tip. To ensure this, a three-step notching procedure was utilized as described in Figure 4.6. The crack consists of three unifying crack fronts. The first two fronts are inserted with a fresh razor blade from the base edges of the machined notch. These cracks stop to propagate at a certain point due to increasing cross-section in front of the crack tip. A triangular cross-section remains in the middle of the machined notch base. In this the third crack front is initiated with the razor blade and the combined crack fronts form one very sharp notch with a defined length.

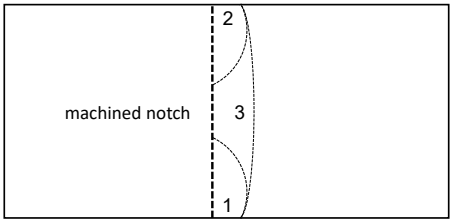


Figure 4.6: Visualization of novel notching technique for pre-crack insertion

The 3PBT and asymmetric 4PBT were conducted with a Zwick/Roell Z2.5 universal testing machine with a cross-head speed of 10 mm/min. The diameter of the support rollers was 6 mm. 3PBT was perfomed according to ASTM D5045-14 [308] and the asymmetric 4PBT was performed according to the setup of Fett [303].

5 Materials

5.1 Epoxy Resins

Used polymers for the dispersion process were epoxy resins with different molecular weight distributions. This allows to determine the influence of increasing viscosity on the dispersion process at constant processing temperatures. Furthermore, the epoxy resins were analyzed in the liquid and cured state to reveal the impact of the different molecular weights on the physical properties. Moreover, the results are the reference values for the nanoparticle modified epoxies. All used epoxy resins base on bisphenol A-diglycidyl-ether or bisphenol F-diglycidyl-ether. Table 5.1 lists the properties of the resins according to the suppliers product data [363]. Epikote 162 offers the lowest viscosity, which increases with 827, 828LVEL, 828 and 834, respectively.

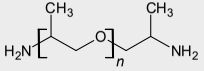
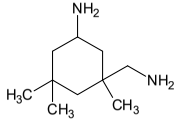
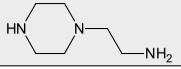
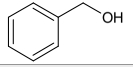
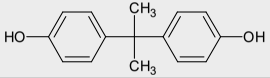
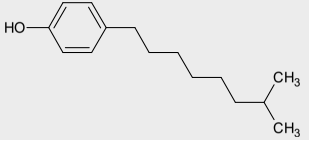
Table 5.1: Properties of used epoxy resins

Epoxy resin Epikote	Type	Epoxy Equivalent Weight in g/eq	Epoxy Group Content in mmol/kg	Viscosity at 25 °C in Pas	Physical State	Remarks
162	DGEBA	170 - 174	5744 - 5883	4.0 - 5.0	Liquid	Distilled, high purity grade
827	DGEBA	179 - 184	5430 - 5590	8.0 - 10.0	Liquid	Low viscosity
828LVEL	DGEBA	182 - 187	5340 - 5500	10.0 - 12.0	Liquid	Low hydrolyzable chlorine, low viscosity
828	DGEBA	184 - 190	5260 - 5420	12.0 - 14.0	Liquid	Standard unmodified bisphenol A resin
834	DGEBA	235 - 263	3800 - 4250	2.1 - 2.4*	Semi-solid	*Viscosity of 40 % solution in MEK
862⋆	DGEBF	165 - 173	5780 - 6060	2.5 - 4.5	Liquid	Standard unmodified bisphenol F resin

⋆ Only used for demonstration of up-scaling of dispersion process

A mixture of Epikure RIMH137 and RIMH134 (80/20 by weight) was used as curing agent. These are commonly used curing agents in the wind-craft energy industry. According to its data sheet [364], RIMH137 consists of poly(oxypropylene)diamine (50 -75 wt.%) and 3-aminomethyl-3,5,5-trimethylcyclohexylamine (35 -50 wt.%). The ingredients of RIMH134 are according to its datasheet [365] 2-piperazin-1-ylethylamine (35 -50 wt.%), 3-aminomethyl-3,5,5-trimethylcyclohexylamine (25 -35 wt.%), poly (oxypropylene) diamine (20 -25 wt.%), benzyl alcohol (3 - 7 wt.%), phenol(4,4'-(1-methylethylidene)bis-polymer with 5-amino-1,3,3-trimethylcyclohexanemethan amine and (chloromethyl)oxirane (1 -2.5 wt.%) and branched 4-nonylphenol (0.25 -0.5 wt.%). RIMH134 enables an accelerated cure kinetic. Table 5.2 lists the molecular formulas as well as the properties of the components of the curing agents. Furthermore, a blend of bisphenol-A-diglycidyl-ether Epikote 828LVEL (85 wt.%) and bisphenol F-diglycidyl-ether Epikote 862 (15 wt.%) epoxy resin was used for demonstration of the scalability of the three roll milling dispersion process. This blend is a standard mixture for industrial application. Addition of bisphenol-F-diglycidyl-ether into bisphenol A-diglycidyl-ether lowers the viscosity and improves crystallization resistance. Epikote 862 offers a viscosity of 2.5 to 4.5 Pas. This blend was cured with RIMH137. Hexion supplied all resins and curing agents.

Table 5.2: Components of used epoxy resins and curing agents

Agent name	Chemical structure	Synonyms	Formula	Description
Diaminopolypropylene glycol		Poly(oxypropylene)diamine	(C3-H6-O)mult-C6-H16-N2-O	Standard epoxy curing agent offering low viscosity, vapor pressure and miscibility with a wide variety of solvents resulting in tough, clear, impact resistant coatings, castings and adhesives[366][367]
Isophorone diamine		3-aminomethyl-3,5,5-trimethylcyclohexylamine, 5-amino-1,3,3-trimethylcyclohexanemethan amine	C10-H22-N2	Ingredient for epoxy curing agents to improve hydrophobicity, corrosion protection and heat distortion temperature [368][43]
Aminoethylpiperazine		2-piperazin-1-ylethylamine	C6-H15-N3	Additive to increase of the reactivity of curing agent [369]
Benzyl alcohol		Benzenemethanol	C7-H8-O	Lowers viscosity, solvent for amines and catalyst for epoxy resin curing [47].
Bisphenol A		phenol(4,4'-(1-methylethylidene)bis-polymer	C15-H16-O2	Used with epichlorohydrin to produce epoxy resins[52]
Epichlorohydrin		(chloromethyl)oxirane	C3-H5-Cl-O	Used primarily in the manufacture of epoxy and phenoxy resins precursor to monomers[50]
Isononylphenol (branched)		4-nonylphenol	C15-H24-O	Acts as catalyst for epoxy resin curing[370], nonreactive epoxy resin diluent[53]

5.1.1 Characterization of Uncured Epoxy Resins

In a first step the molecular weight distributions of the used epoxy resins are evaluated and discussed. By FTIR analysis the chemical bonds within the polymer are excited and the absorbed energies can be correlated with the molecular structure [371, 372]. Figure 5.1 (a) gives the absorbance spectra in dependency of the wave number. The spectra of the different epoxy resins do not differ much. The hydroxy (OH) bond at around 3500 cm^{-1} [373] can be correlated with the number of repetitions n within the DGEBA. Figure 5.1 (b) gives a detailed view at the region around 3500 cm^{-1}.

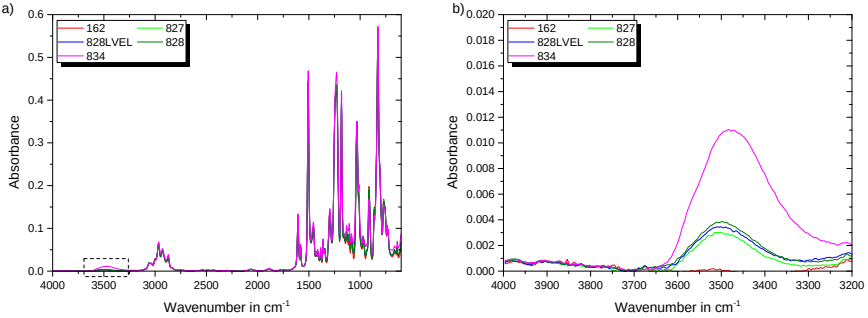


Figure 5.1: FTIR spectra of Epikote 162, 827, 828LVEL and 834 (**a**) full spectra and (**b**) detailed spectra from wavenumber 4000 to 3200 cm^{-1} (excitation range for hydroxy bond)

Epikote 162 exhibits no absorbance for hydroxy bond excitation. This indicates the purity of the distilled epoxy resin. Epikote 827, 828LVEL and 828 show nearly the same degree of absorbance. It is lowest for Epikote 827 and highest for Epikote 828. In contrast, Epikote 834 shows the highest absorbance and therefore, inhibit the highest amount of repeating groups. With increasing repeating number n the amount of hydroxy groups increases, too. This is for Epikote 162 $n = 0$ and will be highest for Epikote 834.
A common method to evaluate the precise composition of the polymer's molecular weight is the size exclusion chromatography [374–378]. Figure 5.2 (a) gives the resulting chromatogram for the SEC of the different epoxy resins used in this work. Five molecular weight peaks can be identified. These peaks

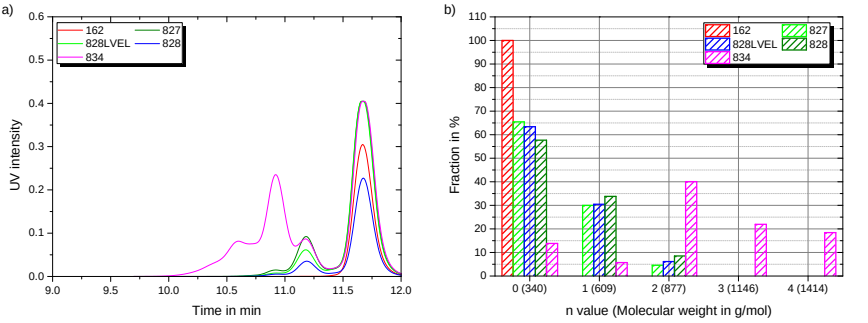


Figure 5.2: SEC results for Epikote 162, 827, 828LVEL and 834 (**a**) chromatogram and (**b**) percentaged molecular weight distribution

were evaluated and the molecular weight distribution in percentage is given by Figure 5.2 (b). As already

demonstrated by FTIR, Epikote 162 consists only of molecules with $n = 0$. Epikote 827, 828LVEL and 828 show only little differences in their composition. They mainly consist of molecules with a repeating number $n = 0$. The amount of higher molecular weight fractions increases for 828LVEL and 828 in comparison to 827. Epiktote 834 mainly consists of molecules with a repeating number $n = 2$. From these results following conclusion can be derived. Epikote 162 should have the lowest viscosity and 834 the highest. The cross-linking density should be highest for Epikote 162 and lowest for 834. This higher cross-linking density should lead to a higher Young's modulus and glass transition temperature for Epikote 162 and should decrease with increasing molecular weight. Epikote 834 should have the highest fracture toughness and 162 the lowest.

Figure 5.3 (a) displays the frequency-sweeps of the five epoxy resins at 30 °C. Small amplitude oscillation (SAOS) of the linear viscoelasticity of complex fluids allows the differentiation of formed networks (gels, glass forming materials, etc.) within the polymer [379]. The loss modulus G'' is for all materials larger

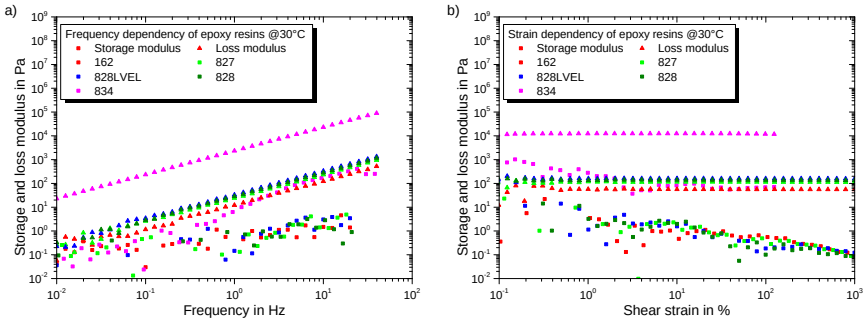


Figure 5.3: Rheological characterization of Epikote 162, 827, 828LVEL and 834 (**a**) frequency-sweeps and (**b**) strain-sweeps

compared to their storage modulus G'. Both, G' and G'' rise with increasing frequency. No cross-over occurs. Therefore, all resins can be considered as Newtonian-like fluids. Figure 5.3 (b) gives the results for the performed strain-sweeps of all resins. Again, the storage and loss modulus are displayed. The loss modulus is higher than the storage modulus. For the evaluated strain range, the loss modulus stays constant, but the storage modulus decreases for all resins. This contributes to chain alignment at high strains. The test of Epikote 834 stopped at 100 %, because the force limit of the rheometer was reached.

Figure 5.4 (a) gives the frequency dependency of all epoxy resins' complex viscosity in a frequency range from 0.01 Hz to 80 Hz. Epikote 162 provides the lowest viscosity. The complex viscosity values of Epikote 827, 828LVEL and 828 are very close to each other. Whereby, 827 shows the lowest and 828 the highest. The complex viscosity of Epikote 834 is, in comparison, two magnitudes higher. This results are in good agreement with the observed molecular weight distributions. All resins show Newtonian-like behavior, their complex viscosity stays constant over the evaluated frequency range. Also, their complex viscosity is strain independent. This is revealed by Figure 5.4 (b). The complex viscosity values are the same for strain- and frequency-sweeps. Figure 5.4 (c) shows the dependency of the complex viscosity on the temperature. For increasing temperature, the complex viscosity decreases significantly for all resins. At 80 °C all resins provide a viscosity below 1 Pas. As mentioned, pristine BADGE tends to crystallize. This behavior was investigated by time-sweeps. The results are shown in Figure 5.4 (d). Only the pristine Epikote 162 with a number of repeating groups $n = 0$ crystallizes. At 25 °C crystallization occurs after 6 h. This can be extended to 48 h by increasing the temperature to 30 °C. Due to the affinity of Epikote 162 to crystallize, a dispersion temperature of 30 °C was chosen.

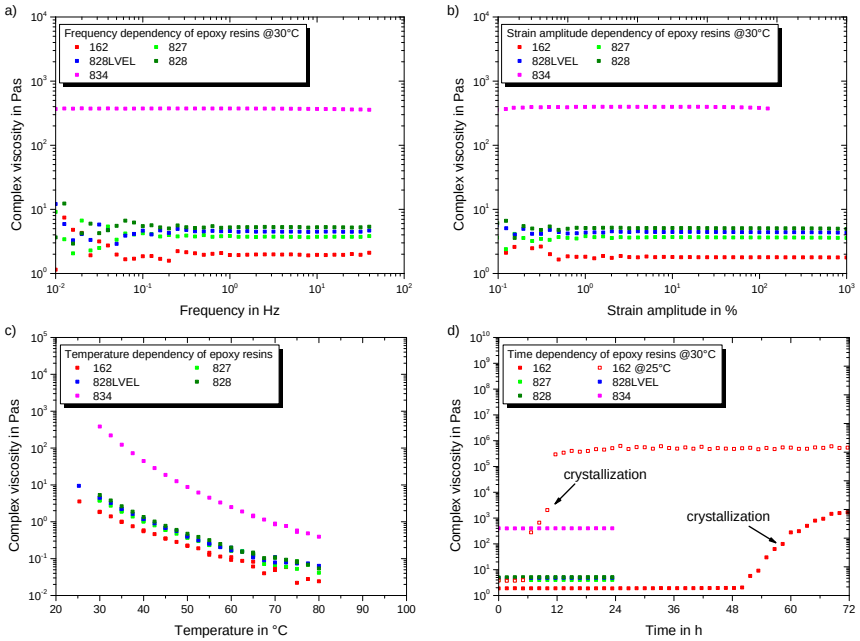


Figure 5.4: Rheological behavior in terms of complex viscosity for Epikote 162, 827, 828LVEL, 828 and 834 in (**a**) frequency-sweeps, (**b**) strain-sweeps, (**c**) temperature-sweeps and (**d**) time-sweeps

Figure 5.6 shows the curing behavior of the different resins used in this study. The tests were performed at 30 °C, because otherwise the Epikote 162 would have been crystallized. Initially, all resins have been cured for 9 h at 30 °C and post cured for 15 h at 80 °C. The parameters for post curing were taken from the data sheet [352]. Curing near T_G reduces curing induced thermal stresses, because relaxation is enabled

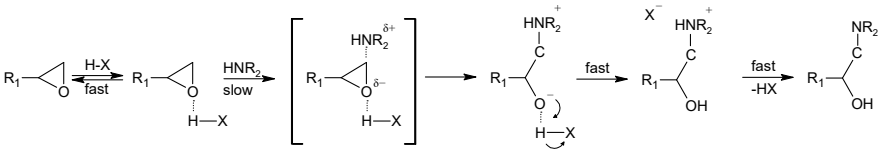


Figure 5.5: Accelerated reaction mechanism of epoxies with primary amines in presence of hydroxyl groups adapted from [380, 381]

[382, 383]. A curing for 9 h at 30 °C does not lead to a sufficient degree of curing and in the heating step to the elevated temperature the viscosity of the epoxy drops to the liquid state. Therefore, the curing step at 30 °C was extended to 13 h. For increasing molecular weight, the pot-life of the resins decreases and is lowest for Epikote 834. Epikote 827, 828LVEL and 828 exhibit a similar curing behavior. Curing is longest for Epikote 162. This has two chemical reasons. At first, the higher the molecular weight the lower the epoxy group content per weight. Therefore, a lower amount of groups has to react for a fully cross-linked polymer network. At second, the amount of hydroxy groups increases with increasing epoxy

molecular weight. This increases the presence of proton donators. The presence of proton donators (e.g. alcohols) significantly lowers the activation energy for epoxy ring opening. This accelarates the reaction compared to pristine epoxy [384–387]. Hydroxy groups show the strongest catalytic effect [388]. The reaction mechanism is shown in Figure 5.5. The curing mechanism of epoxies with amines results in the formation of new hydroxy groups, which further accelerates the cross-linking kinetics. The viscosity increase due to filler addition in combination with the extreme short shelf life makes the material not processible in vacuum assisted resin infusion into the closed mold in case of Epikote 834. Only plates with neat resin will be manufactured from this high molecular weight resin type.

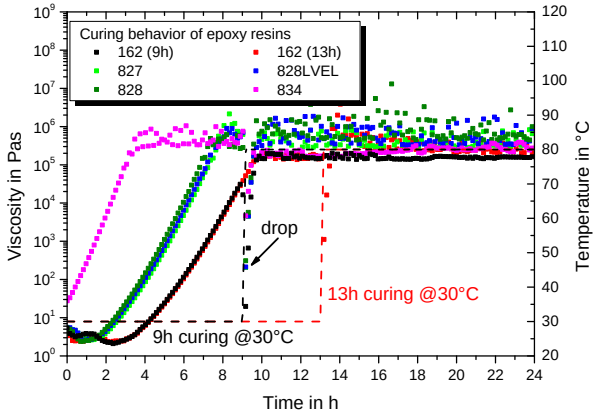


Figure 5.6: Curing behavior of the neat resins evaluated by rheological measurements

5.1.2 Properties of Cured Epoxy Resins

The physical properties of the resins after curing will be discussed in this section. Differential scanning calorimetry allows the evaluation of curing degree of the samples as well as the determination of glass transition temperatures [389]. Figure 5.7 (a) gives the differential heat flow of the epoxy resins after curing.

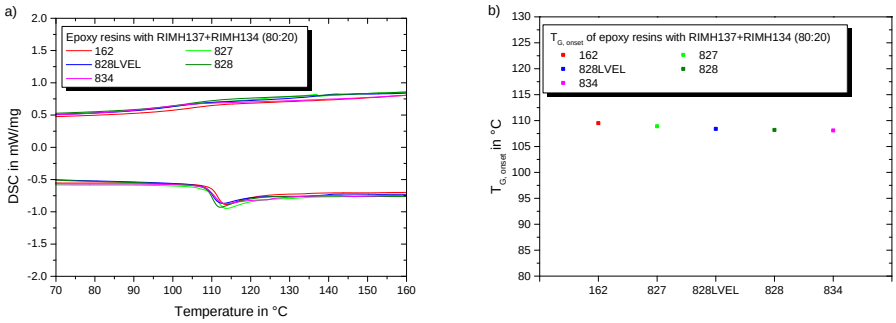


Figure 5.7: Thermal properties of the cured epoxy resins (**a**) DSC curves and (**b**) evaluation of the onset of glass transition temperature

No exothermal peak can be identified and the entropic relaxation of the samples is small. The material is fully cured and has a low degree of internal stresses. Figure 5.7 (b) gives the onset glass transition temperatures of the materials, evaluated by tangent method. Epikote 162 has the highest T_G and it decreases with increasing molecular weight of the neat resins. This result is consistent with the observations in literature [390]. Figure 5.8 displays the resulting curves of the complex modulus E^*, determined by DMTA, in dependency of the temperature.

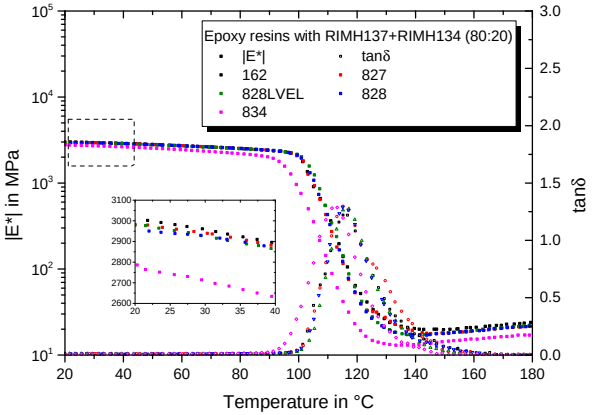


Figure 5.8: Resulting DMTA curves with detailed view for the used epoxy resins

Three characteristic regions occur for linear cross-linked amorphous polymers of the elasto-viscous behavior: The glassy region at low temperatures below T_G and the rubbery region at high temperatures exceeding T_G. Within the transition region around T_G a pronounced time dependency of the material is given [391].

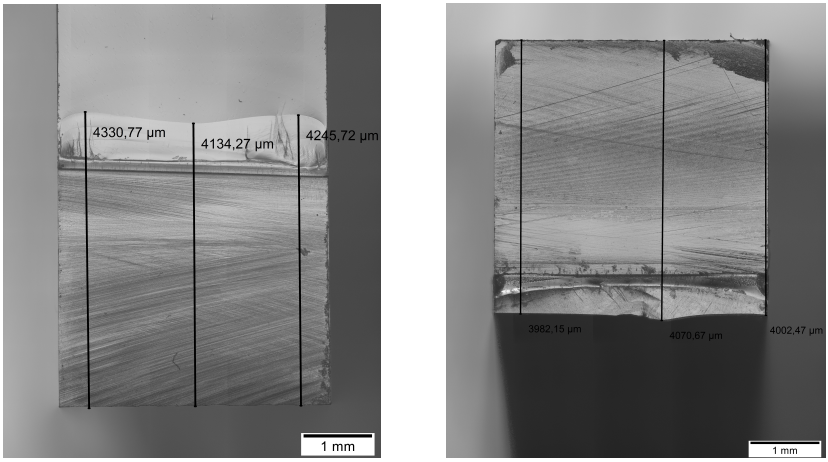


Figure 5.9: Representative machined notch and pre-crack for (**left**) mode I and (**right**) mode II

Epikote 834 inhibits the lowest modulus in the low and high temperature region. Whereby, Epikote 162 offers the highest modulus in both temperature regions. The T_G is highest for the low molecular weight resin 162. By utilization of Equation (2.6) the cross-link densities will be derived. The cross-link density for the epoxies are listed in Table 5.3. The calculated cross-link densities decrease with increasing molecular weight. Achieved cross-link densities are comparable to the values reported in literature [392]. Figure 5.9 shows a representative machined notch with the inserted pre-crack of the mode I (left) and mode II (right). The crack length is homogeneous and the crack tip very sharp, due to the introduced notching technique. Figure 5.10 gives the stress intensity factors K_{IC} and K_{IIC} for the different molecular weight epoxy resins. The K_{IC} value is lowest for Epikote 162, which offers the lowest molecular weight. The

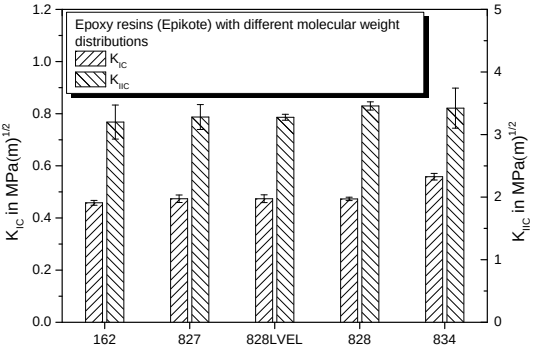


Figure 5.10: Evaluated fracture toughness in mode I and II for the used epoxy resins

failure mechanism consists, according to Chevalier et al., of crack nucleation near a defect, a crack arrest step and a re-initiation process including crack tip blunting [393]. Highly cross-linked epoxies offer in tension mode a yield stress that is larger compared to the fracture stress. This leads to brittle failure before macroscopic yielding occurs [394].

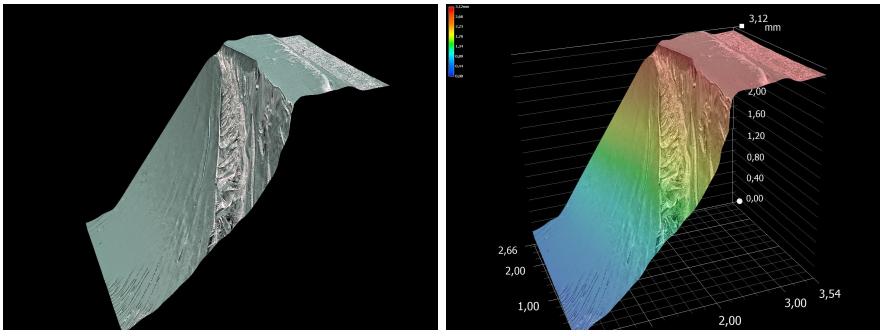


Figure 5.11: Representative digital light microscopic image of a fracture surface of a mode II specimen (**left**) fracture surface and (**right**) height profile

Highest K_{IIC} values are achieved with Epikote 834, which offers the highest molecular weight und lowest cross-link density. The values are in a similar range as reported by Liu et al. [331]. Furthermore, the fracture surface of a mode II specimen is shown in Figure 5.11. It is well known that cracks in mode II try

to initiate from the crack tip in the direction of the inserted pre-crack and take onwards a curved path converging the direction of mode I loading, under an angle of 70 ° from the initial direction [395]. Ramsteiner states in his publication that the crack often initiates in mode I direction, even for mode II loading due to a non-ideal crack-tip. Therefore, K_{IIC} is often reported to be in the range of K_{IC}, due to inaccurate notch preparation [395]. The introduced sharp pre-crack prevents crack initiation in mode I in shear loading. Initially, the formation of voids occurs at the beginning of shear fracture. With increasing load, the voids rotate and form crazes, oriented in load direction [396]. The process zone in mode II is three times larger compared to mode I, as already shown in Figure 2.16. Hence, more energy can be stored in the plastic zone in mode II, leading to higher fracture toughness for shear loading of neat polymers. Table 5.3 summarizes the physical properties of the cured epoxy resins.

Table 5.3: Physical properties of the cured epoxy resins

Resin	$T_{G,DSC}$ in °C	$T_{G,DMTA}$ in °C	Complex modulus below T_G in GPa	Complex modulus above T_G in MPa	Cross-link density in 10^{21} cm^{-3}	K_{IC} in MPa(m)$^{0.5}$	K_{IIC} in MPa(m)$^{0.5}$
162	109.5	106	2.96	19.83	9.35	0.46 ± 0.01	3.2 ± 0.27
827	108.9	103	2.93	17.80	9.28	0.47 ± 0.01	3.28 ± 0.20
828LVEL	108.4	102	2.92	17.20	9.26	0.47 ± 0.01	3.28 ± 0.05
828	108.2	101	2.91	17.01	9.25	0.47 ± 0.01	3.46 ± 0.07
834	108.1	96	2.76	12.99	9.09	0.56 ± 0.01	3.42 ± 0.32

5.2 Carbon Nanoparticles

An extensive set of particle types was chosen to evaluate the effect of different carbon nanoparticle morphologies on the dispersion behavior as well as on the final physical properties. Table 5.4 summarizes the determined properties of the used nanoparticles. Appendix B.1 gives the detailed results of the performed experiments. Commercially available carbon black Printex L, purchased from Orion Engineered Carbons, offers a spherical shape. It is a carbon black pigment recommended for conductive coating applications. Its structure makes it easy to disperse, because it can not entangle and the size distribution is narrow. It offers an amorphous structure and the highest decomposition temperature of the used particles. MWCNT NC7000, supplied by Nanocyl, are cylindrical and rigid tubes. Additionally, research grade MWCNT, supplied by Future Carbon, were used. CNTB are the reference type of the neat MWCNT. CNTA and CNTP are argon and atmospheric plasma treated CNTB, respectively. All the MWCNT offer similar properties. A specific surface area of about 300 m^2/g, an aspect ratio of 150 and a decomposition temperature of 565 °C. The anorganic impurity content is lower for CNTA due to the argon plasma treatment. The oxygen content is increased for atmospheric plasma treated CNTP and the impurity content is lower. CNTN are CNTB type MWCNT equipped with elastomer side chains, which are amino functionalized and therefore able to cross-link with the epoxy resins [397]. The two decomposition temperatures result from the elastomeric component, which decomposes at 427.3 °C and the carbon based part, which decomposes at 525.0 °C. Nitrogen content, revealed by EDX, proofs the amino functionalization. SWCNT Tuball 75, supplied by OCSiAl, are cylindrical and, due to their small diameter, flexible nanotubes. They possess a highly entangled and bundled structure. They offer a high aspect ratio as well as an outstanding specific surface area. Their degree of graphitization is very high, but they contain a high amount of anorganic impurities. Their market price at industrial scale is 50 times lower compared to other SWCNT suppliers [398].

Table 5.4: Properties of used carbon nanoparticles

Nanoparticle	BET surface area in m^2/g	Layers, walls or bundle size	Aspect ratio	Shape	Diameter or thickness in nm	Decomposition temperature in °C	Fit peaks	I_D/I_G	Graphitization in %	Crystalline width in nm	Impurities in wt.%	EDX composition in wt.%
Printex L	125	Amorphous	1	spherical	31 ± 8	635.0	2	1.25	44.50	3.5	0.25	C (96.51), O (2.69), S (0.80)
NC7000	321	10 ± 2	150	Cylindrical	12 ± 3	562.4	2	1.44	40.99	3.1	9.17	C (92.15), O (5.96), Al (1.81), Si (0.08)
CNTB	319	10 ± 3	150	Cylindrical	11 ± 3	565.8	2	1.63	37.99	2.7	10.35	C (85.34), O (8.78), Al (5.07), Fe (0.36), Co (0.22), Si (0.15), S (0.08)
CNTA	296	9 ± 2	150	Cylindrical	10 ± 1	565.0	2	1.77	36.11	2.5	10.64	C (88.77), O (7.97), Al (2.73), Fe (0.24), Si (0.14), S (0.07)
CNTP	312	10 ± 2	150	Cylindrical	11 ± 3	564.4	2	1.62	38.08	2.7	7.84	C (85.39), O (11.89), Al (1.79), Si (0.44), S (0.25), Na (0.25)
CNTN*	N/A	N/A	N/A	Cylindrical	N/A	427.3 525.0	4	1.61	38.24	2.7	4.39	C (90.53), N (4.78), O (4.21), Al (0.37), Cl (0.11)
Tuball 75	605	11 ± 3	3570	Cylindrical	1.4 ± 0.4	561.9	3	0.01	95.94	104	17.98	C (81.96), Fe (15.01), O (2.26), Si (0.44), S (0.32)
Tuball purified	598	13 ± 3	3570	Cylindrical	1.5 ± 0.1	528.8 627.7	3	0.04	98.93	406.3	2.09	C (90.61), O (6.36), Si (1.74), Cl (1.03), Fe (0.26)
FLG	128	10 ± 2	6250	Planar	4 ± 1	542.5	3	1.34	42.71	3.3	5.81	C (88.33), O (9.15), Mn (0.65), Si (0.62), S (0.35), Al (0.32), Fe (0.24), Na (0.22), Cl (0.08), Ca (0.06)
ExG**	18	47 ± 11	525	Planar	19 ± 5	608.9	2	1.47	40.52	3.0	10.90	C (88.08), O (11.02), S (0.45), Cu (0.25), Si (0.12), Na (0.08)
fExG**	6	52 ± 19	475	Planar	21 ± 9	542.0	3	1.43	41.17	3.1	11.73	C (82.60), O (15.89), S (1.28), Cu (0.23)

* This particle bases on CNTB and features amino-functionalized elastomer side chains and 20 to 25 wt.% CNT content

** This particle type was delivered solved in ethanol and was dried before measurements

OCSiAl provided a purified variant of their SWCNT, too. The purification is achieved by an acid treatment utilizing HCl for removal of metallic impurities. A further heat treatment led to an even higher degree of graphitization, but the chemical treatment lowers the decomposition temperature. Few-layered graphene Avan2, supplied by Avanzare Innovación Tecnológica, offers a planar structure. It offers around 10 layers and a low impurity content. A second evaluated planar particle type was electro-chemically expanded graphite (ExG). Additionally, a functionalized variant of it was used. The manufacturing was performed according to the process described by Parvez et al. [124] at Technische Universität Dresden, which produces the ExG under a license from Sixonia Tech. Two graphite foils are inserted into an aqueous electrolyte solution. They act as anode and cathode. Applying a DC voltage of 10 V the exfoliation starts. The functionalized variant of electro-chemically expanded graphite (fExG) was prepared via in-situ functionalization during electro-chemical exfoliation in water. For compounding, the ExG was first separated from the electrolyte and washed with deionized water [112, 125, 399]. Instead of a subsequent dispersion step, which is typically employed to destroy the graphene agglomerates and liberate pristine exfoliated graphene sheets, the expanded, but still agglomerated product, was transferred into ethanol, to prepare highly concentrated slurries. They offer about 50 layers. The functionalization decreases the decomposition temperature.

6 Dispersion of Carbon Nanoparticles in Epoxy Resins via Three Roll Mills

6.1 Rheo-Electrical Characterization of Carbon Nanoparticle/Epoxy Composites - Revealing the Driving Force for Dispersion

This section focuses on the superior efficiency of dispersion processes by TRM and will reveal that it not only bases on the applied shear rate. Furthermore, it will explain the agglomeration of particles while processing and material handling, by assessing the changes in network morphology by characterizing the materials' electrical properties under shear. The novelty of this approach is the aim to differentiate shear rate-induced structural changes either by increasing frequency or amplitude.
For the performed tests a model composite consisting of rigid MWCNT Nanocyl NC7000 and Epikote 828LVEL, which provides a medium viscosity, was used. MWCNT NC7000 are of commercial relevance and in industrial scale available nanotubes. Epikote 828LVEL is widely used as standard epoxy resin by the industry. The stated properties, like the viscosity, and the nanotube's dimensions make them suitable as components for a model nanocomposite. The investigation of particle network changes require the formation of a distinct particle network, hence, for this section a filler loading above the percolation threshold was chosen. Figure 2.8 reveals an electrical percolation threshold of 0.3 wt.% for NC7000 dispersed in epoxy resin. At this point, the utilization of the point of inflection was applied to determine the percolation threshold. A filler loading of 0.5 wt.% provides a formed particle network, leading to a solid-like behavior of the MWCNT epoxy resin nanocomposite.

6.1.1 Strain and Frequency Dependent Behavior of Nanocomposites

As reported, the strain and frequency dependent complex viscosity of 0.5 wt.% NC7000/EP composite shows a shear-thinning behavior. Figure 6.1 (a) shows the behavior of the material resulting from strain-sweeps for measurements at different frequencies.

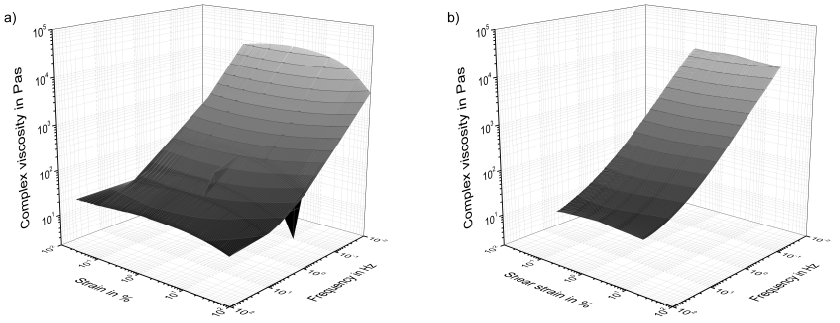


Figure 6.1: 3D visualization of complex viscosity development for 0.5 wt.% NC7000 dispersed in Epikote 828LVEL gathered from (**a**) strain-sweeps at different frequencies and (**b**) frequency-sweeps at different strain levels

Figure 6.1 (b) shows the behavior of the material from frequency-sweeps at different strain levels. Both experiments result in an identical plot. Each rheological state is defined by a frequency and a shear strain amplitude. The complex viscosity of the material is more sensitive to applied frequency than to applied

shear strain. It decreases, with an initial plateau, for increasing frequencies and reaches a lower plateau. For strain-sweeps, the complex viscosity shows a pronounced initial plateau and starts to decrease at a yield point. The explanation of this material behavior is given in the following sections.

6.1.2 Rheological Properties of Neat Resins

Firstly, strain- and frequency-sweeps were performed at room temperature for the neat epoxy resin to verify the Newtonian behavior even for temperatures below 30 °C. The complex viscosity of the system is independent of the applied strain amplitude and frequency, referring to Figure 6.2 (a) and (b), respectively. Storage and loss modulus show an independence of applied strain in strain-sweeps, as well (see Figure 6.2 (c)). However, they increase with increasing frequency (see Figure 6.2 (d)). In both tests, G'' is two magnitudes higher than G', revealing a fluid-like behavior of the resin. Therefore, taking Equation (2.37) into account following dependency is valid for the complex modulus:

$$G^* = G'' \text{ with } G'' >> G' \tag{6.1}$$

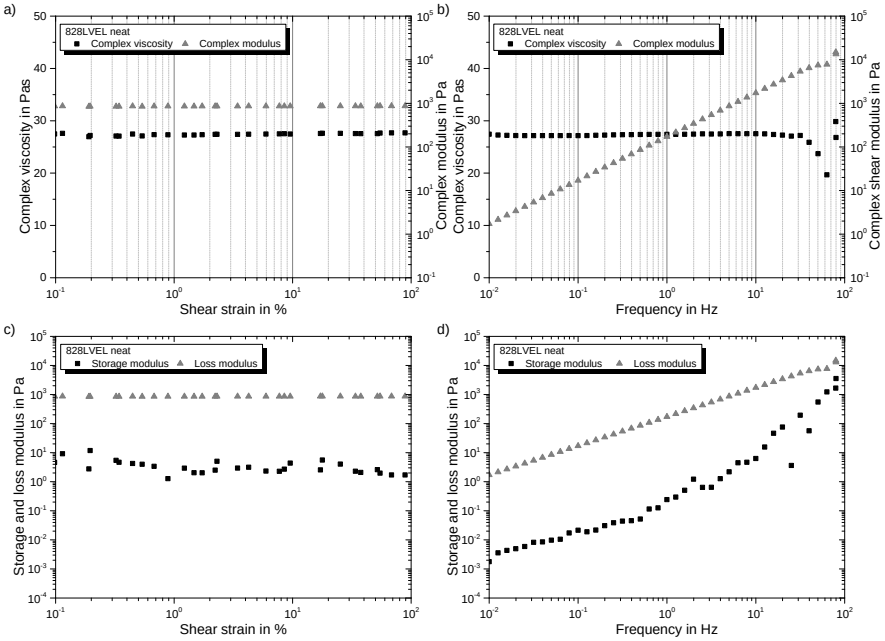


Figure 6.2: Oscillatory rheology results of 0.5 wt.% NC7000 in Epikote 828LVEL: (**a**) dependency of complex viscosity and complex modulus on shear strain ($f = 5$ Hz) and (**b**) dependency of complex viscosity and complex modulus with increasing frequency ($\gamma_0 = 10\,\%$); (**c**) dependency of storage and loss modulus on shear strain ($f = 5$ Hz); (**d**) dependency of storage and loss modulus on frequency ($\gamma_0 = 10\,\%$)

6.1.3 Time Dependent Behavior of Nanocomposites

To verify the time dependent behavior of the material, an oscillatory measurement with parallel DC measurement was performed; see Figure 6.3 (a). Besides that, the change of AC electrical behavior was measured in a cylinder with two aluminum electrodes with a spacing of 10 mm to reveal the structural changes

after the dispersion process; compare Figure 6.3 (b). Structural changes were highest in the first 10 h after dispersion, which was reported by Alig et al., too [400, 401]. Therefore, the material was stored for 72 h before testing to achieve the steady state. The development of G^* was fitted by a molecular growth model with the following formula [402] utilizing the Levenberg-Marquardt algorithm:

$$y = A_1 - A_2 e^{-kx} \tag{6.2}$$

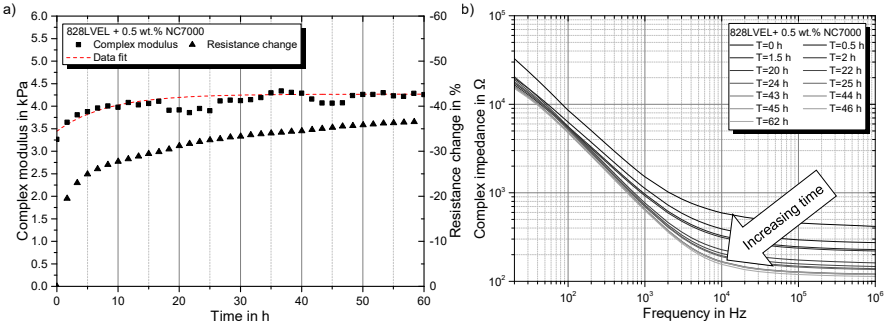


Figure 6.3: Change of (**a**) complex modulus and electrical resistance in oscillation and (**b**) development of complex impedance over time

6.1.4 Strain Dependency of Nanocomposites

Going into detail for the strain dependent rheological properties of the material, an initial plateau in the complex viscosity for all evaluated test frequencies occurs until a critical strain is reached. After that, distinct shear-thinning occurs; compare Figure 6.4. All curves of $tan\delta$, except for 80 Hz, show a solid-liquid transition (indicated by the red line at $tan\delta = 1$).

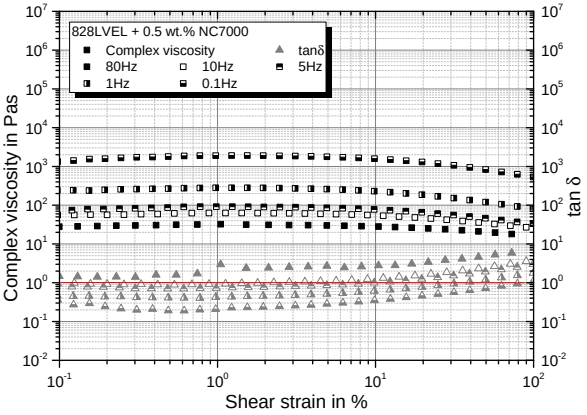


Figure 6.4: Shear strain dependency of complex viscosity and $tan\delta$

In Figure 6.5 (a), the storage modulus G' and loss modulus G'' are plotted vs. the applied shear strain. The cross-over, indicated by red circles, occurs for higher test frequencies at lower strains. This is considered

as the yield point of the material, allowing the explanation of shear rate dependency. With Equation (2.31), the previous plot can be transferred into a shear rate $\dot{\gamma}$-dependent plot of storage and loss modulus; compare Figure 6.5 (b). The cross-over occurs for higher frequencies at higher shear rate. Therefore, the structural change of the material seems to be shear rate independent. To reveal the structural changes in the material during the strain-sweeps, the electrical resistance was measured simultaneously.

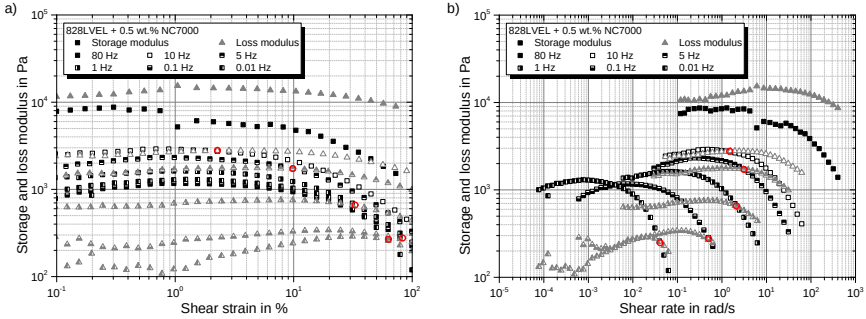


Figure 6.5: Dependency of storage and loss modulus on (**a**) shear strain and (**b**) shear rate

For comparability, the measured resistance was normalized to the initial resistance. The resistance change can be calculated as follows:

$$\Delta R = \frac{R_{el} - R_{el,0}}{R_{el,0}} \tag{6.3}$$

A negative value indicates an improved conductivity of the network structure, in comparison to its initial state. In Figure 6.6 (a) the complex modulus and the resistance change are plotted versus the applied strain. For low strains, the complex modulus increases and the resistance decreases. This indicates a more solidified particle structure. The minimum of the resistance change occurs in the same regime as the maximum in the complex modulus (indicated by the gray box in Figure 6.6 (a)). With beginning of the decrease of the complex modulus, an enormous increase in resistance change can be observed. This reveals the break-down of the conductive particle network. By utilizing Equation (2.38), the shear rate corresponding shear stress can be calculated. The log-log plot of shear stress vs. shear rate in Figure 6.6 (b) shows the same slope as for the neat resin (red dotted curve) for all tested frequencies, but they are shifted. At a certain shear rate, just for low frequencies, the shear stress is limited and does not increase further by increasing shear rate. By reaching $\tau_{max,CNT}$, the destruction of the particle network begins, and consequently, shear-thinning occurs. For high frequencies, the material's response becomes more and more like the response of the neat resin, and the yield point vanishes. Finally, for very high test frequencies, the material fully responses like the neat resin, and the particles do not influence the rheological behavior despite the over percolated network structure.

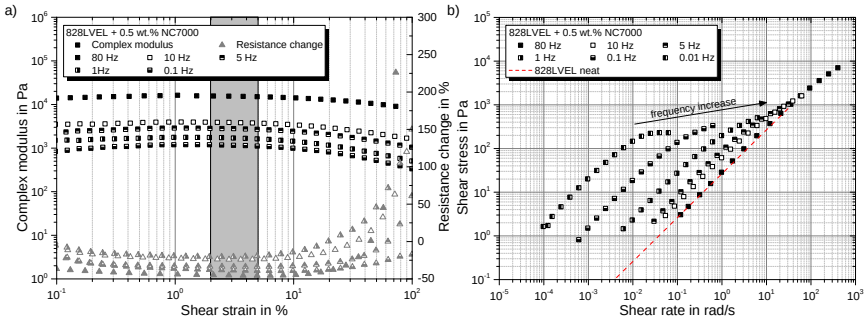


Figure 6.6: (**a**) Rheo-electrical material behavior in strain-sweeps at different frequencies and (**b**) shear stress in dependency of shear rate

6.1.5 Frequency Dependency of Nanocomposites

The behavior of the complex viscosity in frequency-sweeps for different strain levels γ_0 is shown in Figure 6.7 (a). Additionally, the development of $tan\delta$ is given. For each frequency, an initial plateau in the complex viscosity is observed. This plateau disappears for a second performed frequency-sweep of the same sample (red symbols). All tested amplitude levels show a solid-liquid transition in the $tan\delta$ curves. This occurs for amplitudes over 5 % at lower frequencies. Figure 6.7 (b) gives solid-like behavior for frequencies below 11 Hz. The loss and storage modulus for 20 % strain amplitude are plotted in Figure 6.7 (b).

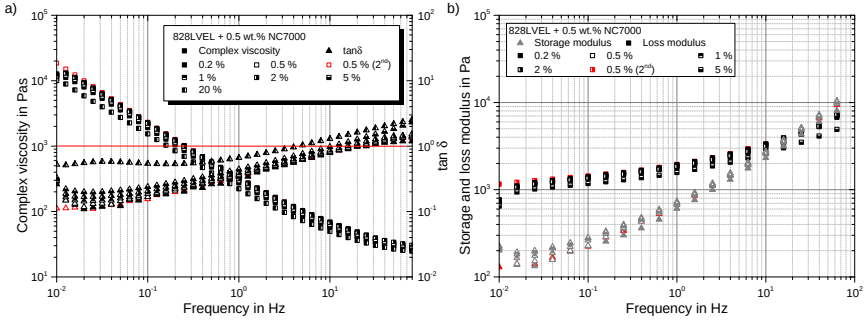


Figure 6.7: Frequency dependency of (**a**) complex viscosity and $tan\delta$ and (**b**) storage and loss modulus

Table 6.1 summarizes the relaxation times for the strain amplitudes. Higher amplitudes lead to higher relaxation times. This indicates a stronger network interaction.

Table 6.1: Relaxation times λ for strain amplitudes γ_0

chanγ_0 in %	ω_c in rad/s	f_c in Hz	λ in s
0.2	150.80	24.00	0.041
0.5	131.27	20.89	0.048
0.5*	131.27	20.89	0.048
1	114.35	18.20	0.055
2	95.13	15.14	0.066
5	68.86	10.96	0.091
20	27.39	4.36	0.229

* Second frequency-sweep on the same sample.

The electrical resistance change and complex modulus in dependency of the frequency are plotted in Figure 6.8 (a). For all curves, the resistance decreases and ends up in a plateau after 1 Hz. Measuring the same sample a second time leads to no further change in resistance. This is shown exemplary for a 0.5 wt.% filler concentration. The fact that with increasing frequency, no further changes in resistance occur, leads to the assumption that the changes in the filler network structure are less dependent on applied frequencies. For a strain amplitude of 20 %, the resistance change is constant at low frequencies. It increases up to frequencies of 1 Hz and begins, exceeding this frequency, to decrease continuously; compare Figure 6.8 (b).

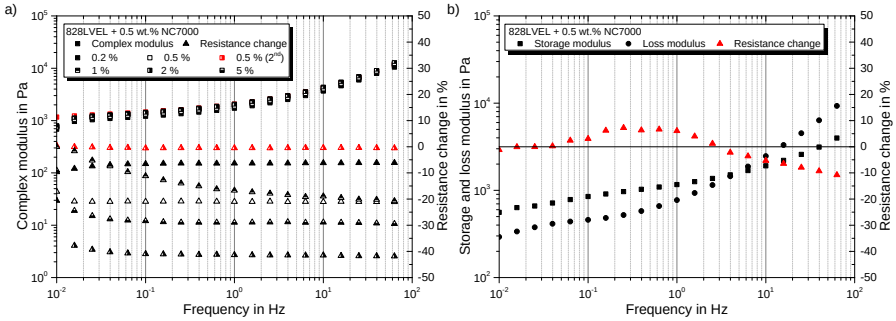


Figure 6.8: Frequency dependency of (**a**) complex modulus and resistance change and (**b**) storage, loss modulus and resistance change for a 20 % strain amplitude

The influence of a second measurement of the same sample in a frequency-sweep is given in Figure 6.9 (a). The initial plateau disappears, indicating no further changes in the network structure. Plotting shear stress vs. shear rate in Figure 6.9 (b), shows an asymptotic convergence to the material behavior of the neat resin for high frequencies. Here again, the structural changes occur for low frequencies and therefore in the first oscillation cycles. At high frequencies, the resin seems to be only excited. A reasonable assumption is that the rigid particles are too inert to follow the movement of the oscillation. At this point it needs to be highlighted that high frequency tests allow the measurement of the matrix viscosity without affecting the network structure.

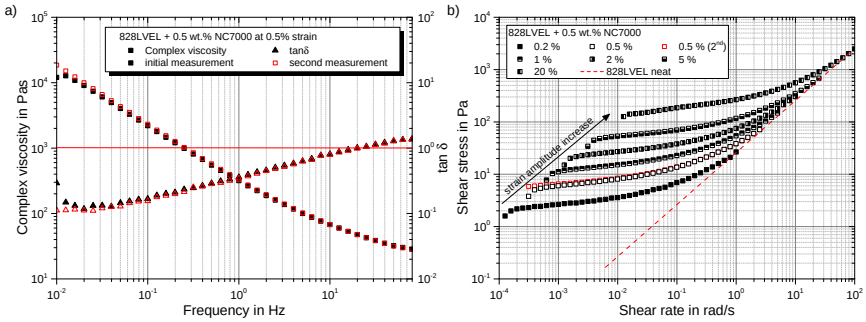


Figure 6.9: Dependency of (**a**) complex viscosity on frequency and (**b**) shear stress on shear rate

Summarizing, the following observations were made:

1) Low strain amplitudes in the strain-sweeps lead to a build-up of the filler network (decreased resistance)

2) High strain amplitudes in the strain-sweeps destruct the filler network (exponential increase of resistance)

3) Material responses are similar for high frequencies in strain-sweeps

4) Shear rate independent solid-liquid transition for the tested frequencies in strain-sweeps

5) After initial resistance decrease, there is no further resistance change in frequency-sweeps

6) Asymptotic convergence to the material behavior of the neat resin at high frequencies in frequency-sweeps

Combining Figure 6.6 (b) and Figure 6.9 (b) leads to the master curve for the rheological material behavior of the nanocomposite, shown in Figure 6.10. The black circles indicate data gathered from strain-sweeps at different freqency levels and red dashed lines give the data from frequency-sweeps with different strain amplitudes. The gray line indicates the measured material behavior of the neat resin. Increasing shear amplitudes in a strain-sweep (black circles) lead to higher shear stresses resulting from a more pronounced solid behavior (high G^*) due to build-up of the particle network. The build-up is limited to a maximum shear stress. A further increase of the strain amplitude does not result in increasing shear stresses, although the shear rate further increases. The break-down of the particle network starts. The increase of the shear rate by an increase of frequency does not lead to a structural change within the composite. Therefore, no frequency dependent increase of shear stress can be observed in the lower frequency range. With high frequencies, the material behavior is dominated by the neat resin. A schematic model is given in Figure 6.11 (a). The nanocomposite consists of a CNT and a polymer network. The CNT network is elastic and the polymer network viscous. Hence, the CNT network can be described by a spring with the modulus G_{CNT} and the polymer by a classical Kelvin-Voigt element, consisting of a spring with the modulus $G_{polymer}$ and a dash pot with the viscosity $\eta_{polymer}$. A parallel circuit of both as shown in Figure 6.11 (b) can be described with the equations given below.

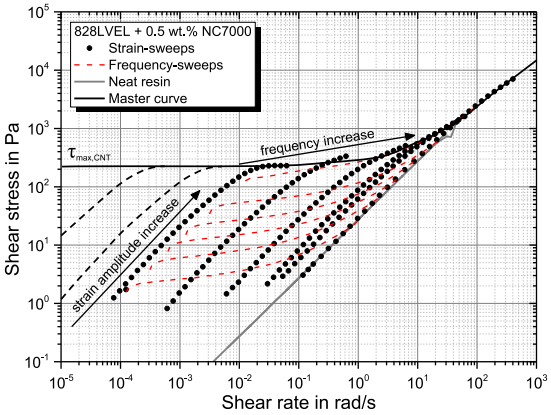


Figure 6.10: Master curve of the rheological properties of 0.5 wt.% NC7000 dispersed in Epikote 828LVEL

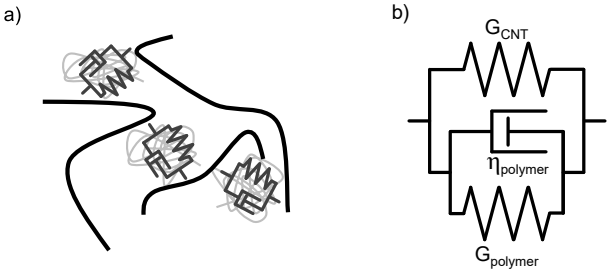


Figure 6.11: Schematical sketch of the (**a**) CNT-polymer-composite adapted from [279] and (**b**) the applied material model using mechanical elements

The shear strain in all elements is equivalent:

$$\gamma = \gamma_{CNT} = \gamma_{polymer} \tag{6.4}$$

The shear stress of the CNT-network with dependency on the applied shear strain γ is given by:

$$\tau_{CNT} = G_{CNT} \cdot \gamma \tag{6.5}$$

and the dependency of stresses within the polymer on the applied shear strain ε and shear rate $\dot{\varepsilon}$ is given by:

$$\begin{aligned} \tau_{polymer,elastic} &= G_{polymer} \cdot \gamma \\ \tau_{polymer,viscous} &= \eta_{polymer} \cdot \dot{\gamma} \end{aligned} \tag{6.6}$$

The total shear stress of the system results in the following equation:

$$\begin{aligned} \tau_{tot} &= \tau_{CNT} + \tau_{polymer,elastic} + \tau_{polymer,viscous} \\ &= G_{CNT} \cdot \gamma + G_{polymer} \cdot \gamma + \dot{\gamma} \cdot \gamma_{polymer} \end{aligned} \tag{6.7}$$

The stiffness of the CNT network G_{CNT} is much higher compared to the polymer's stiffness $G_{polymer}$. This simplifies the equation as follows:

$$\tau_{tot} = G_{CNT} \cdot \gamma + \dot{\gamma} \cdot \eta_{polymer} \tag{6.8}$$

A material response, as shown in Figure 6.10, results from following facts. The elastic stress within the particle network increases with the applied shear strain γ until it exceeds a specific yield shear stress $\tau_{max,CNT}$:

$$\tau_{CNT} = G_{CNT} \cdot \gamma = \tau_{max,CNT} \tag{6.9}$$

The viscous contribution, which depends only on the shear rate, is given by following limitations:

$$\begin{aligned} \lim_{\dot{\gamma} \to \infty} \dot{\gamma} \cdot \eta_{polymer} &= \infty \\ \lim_{\dot{\gamma} \to 0} \dot{\gamma} \cdot \eta_{polymer} &= 0 \end{aligned} \tag{6.10}$$

By utilization of this model nanocomposite, consisting of MWCNT and epoxy resin, the following conclusions, universally valid for nanoparticle filled liquid resins, can be stated. At low frequencies the elastic response of CNT network dominates the material behavior. The stress scales with applied shear strain. For higher frequencies, the strain rate increases at constant strain, and therefore, the polymeric viscous behavior becomes more dominant. For $\tau_{CNT} > \tau_{max,CNT}$, shear-thinning occurs, resulting in no further increase of ealstic stress at low frequencies. By this observation, the superior efficiency of continuous dispersion processes like three roll milling over oscillatory methods, like ultrasonication, can be justified. The shear rate for ultrasonication is far higher, but the total amplitudes are lower compared to TRM. These investigations prove that high shear amplitudes are mandatory to separate agglomerates. Ultrasonication leads, despite the high energy level, not to the separation, but to the fracture of single rigid particles. The shear rate has a minor influence. The pretended shear-thinning in frequency-sweeps is not due to changes in the network structure, but rather corresponds to the rheological behavior of the polymer matrix. For steady shear flows, the absolute amplitude should be considered stronger than the shear rate.

Concluding, shear amplitudes are mandatory for changes in the CNT thermoset network structure. The shear rate has minor influence on changing the CNT particle network, but is essentially influenced by the absolute applied shear deformation. High frequencies do not change the network structure for low strain amplitudes in oscillatory rheology measurements. High test frequencies allow the determination of the rheological properties of the neat polymer matrix within the nanocomposite material, without structural changes.

6.2 Online Monitoring of Carbon Nanoparticle Dispersion Processes via Three Roll Mills

To overcome the bottle neck in the value chain of carbon nanoparticle/epoxy composite production, a development of online monitoring methods and their implementation into the dispersion process is mandatory. For this purpose, optical coherence tomography, impedance spectroscopy and the evaluation of process data out of the three roll mill will be analyzed in this section.

6.2.1 Particle Size Evaluation by Optical Coherence Tomography

A blend of Epikote 828LVEL and 862 (ratio: 85 wt.% to 15 wt.%) was modified with SWCNT Tuball 75. Chosen epoxy resin combination is a commonly used blend for industrial applications. The utilized filler particles are available in industrial scale and offer ultra low filler loadings to achieve an electrical percolation within the composite material. Filler loadings of 0.01 wt.% and 0.05 wt.% relating to the cured composite were processed on a three roll mill 120E-250 with the introduced 7 step dispersion process at 30 °C. These comparable low filler concentrations, near the percolation threshold, were evaluated to validate the analysis approaches for dispersion states of technical relevant filler concentrations. For industrial application, like ESD protection, these filler contents are of importance to ensure the required conductivities. The acquired OCT images were evaluated by the programmed Matlab script. The particle size was

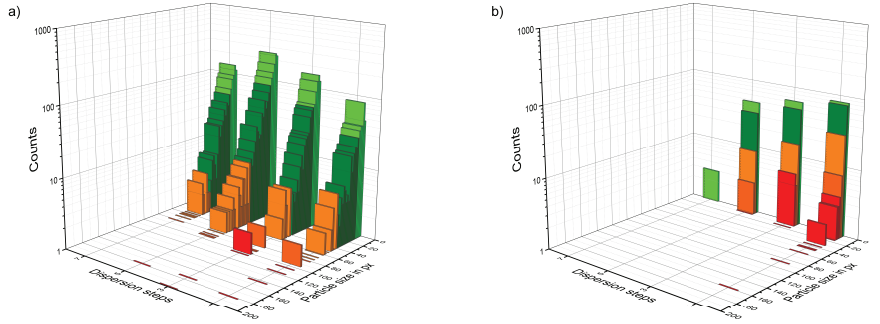


Figure 6.12: Evaluation of particle size distribution with OCT for SWCNT concentrations of (**a**) 0.01 wt.% and (**b**) 0.05 wt.%

evaluated in pixel size (px), because the scattering behavior and refraction index of the composite change over the dispersion process. For both filler concentrations the particle size distributions of dispersion step 1, 3, 5 and 7 are plotted in Figure 6.12.

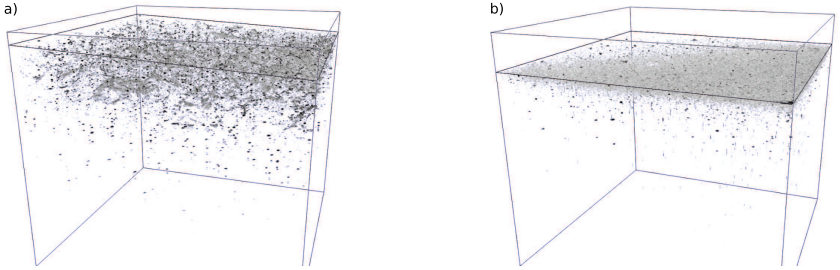


Figure 6.13: Three dimensional OCT image for 0.05 wt.% (**a**) after dispersion step 1 and (**b**) after dispersion step 7

The resulting histograms are given for the stated dispersion steps. For both filler loadings, precisely 0.01 wt.% and 0.05 wt.%, the results are comparable. Initially, the particle size distribution is very inhomogeneous. With an increasing amount of dispersion steps the maximum particle size as well as their amount decrease. The reduction of counted particles contributes to the chosen threshold of the grey value.

For this threshold the material is considered as homogeneous. It was evaluated during development of the matlab script. A lower threshold leads to an identification of the homogeneous part of the dispersion (well distributed and small particles) as single big phase. Figure 6.13 (a) and (b) show three dimensional images for 0.05 wt.% filler concentration after dispersion step 1 and the final one, respectively. It is obvious that agglomerate size decreases. The material becomes much more homogeneous and the penetration depth decreases.

Concluding, OCT offers the possibility of a qualitative determination of the particle size distribution in dispersions. Also an online acquisition of OCT images is possible and they can be directly evaluated by the used Matlab script. Therefore, OCT is a favorable approach for in-line dispersion evaluation.

6.2.2 Impedance Spectroscopy

The applicability of impedance spectroscopy as in-line monitoring method will be discussed within this section. The gathered data for both concentrations were evaluated in Nyquist and Bode plots, consisting of the frequency dependency of the absolute value of the impedance $|Z^*|$ and the phase shift. Additionally, the imaginary part of the impedance Z'' is evaluated over the frequency. Firstly, the results gathered from the 0.01 wt.% filler content modification will be discussed. Figure 6.14 (a) (symbols) shows the frequency dependency of the absolute value of the impedance $|Z^*|$. After dispersion step 1 a percolated network has still not formed. Therefore, the real part of the impedance is extremly high ($Z' \approx \infty$). This forms a semicircle with infinite radius in the Nyquist plot. For all further processing steps an initial plateau until a cut-off frequency f_c can be observed. This plateau contributes to formation of a percolated network. The lowest resistance at low frequencies is achieved after dispersion step 4. With ongoing dispersion steps, the resistance rises again. This result is in good accordance to literature. Faiella et al. observed that longer ultrasonication leads to higher percolation thresholds [190]. This contributes to more separation of the particles with increasing amounts of dispersion steps [211]. Highest resistance is observed after dispersion step 7. Figure 6.14 (b) gives the dependency of the phase shift on frequency. For dispersion step 1 the phase shift is 90 ° contributing to a capacitive behavior without any conductivity. Beginning with dispersion step 2, the phase shift begins at 0 ° for a conductive behavior and is then rising at cut-off frequency f_c to 90 °. Nyquist plots (or Cole-Cole plots) reveal the frequency dependency of real and imaginary parts of the impedance [403]. Figure 6.14 (c) gives the Nyquist plot for this system. For dispersion step 7 the highest Z'' occurs. High values of Z'' correlate with high capacitor properties of the material, induced by well separated particles. The behavior of the system can be described by superposition of two semicircles. Whereby the formation of the second semicircle (micro capacitors) is most pronounced for dispersion step 7. Gomez et al. observed the appearance of a second semi circle in the Nyquist plot for reduced graphene oxides incorporated in thermoplastic polyurethane (TPU) at elevated temperatures. They attributed this phenomenon to the softening of TPU, which allows the deformation and displacement of the rGO particles [404]. In their, as well as in the presented case, the separation leads to a higher capacity on micro scale. Charge carriers can explore clusters on different scales within one alternating period below the critical frequency f_c [405]. Figure 6.14 (d) shows the frequency dependency of Z''. Here the highest Z'' can be correlated with the lowest cut-off frequency f_c occurring for dispersion step 7, too. The highest Z'' value after dispersion step 7 results from the good particle separation even at micro scale. For better physical understanding of the network formation throughout the dispersion process, an equivalent circuit model was derived. Literature suggests for gathered Nyquist plots a series of two parallel circuits consisting of a resistor and non ideal capacitors, represented through constant phase elements [358, 406, 407].

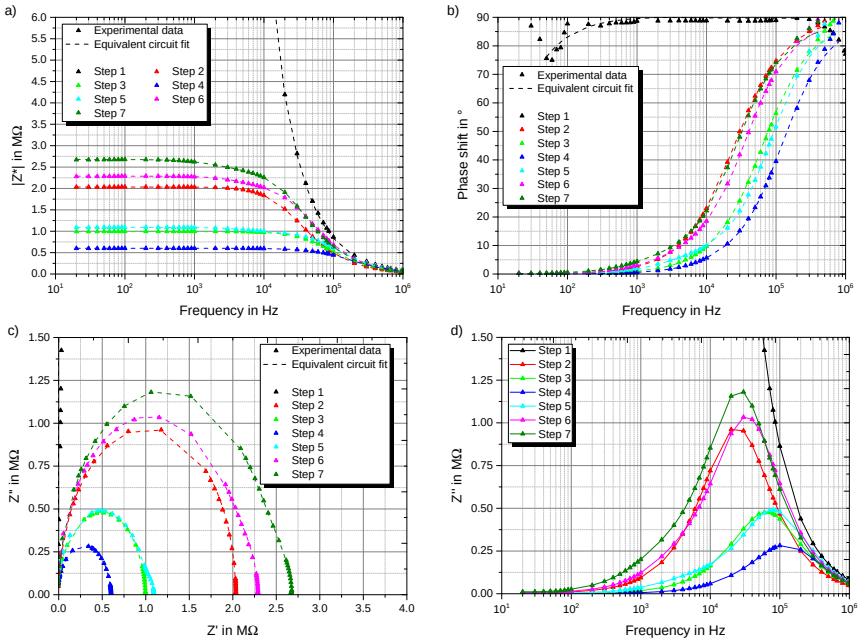


Figure 6.14: Impedance spectroscopy data evaluated for 0.01 wt.% filler concentration (**a**) dependency of absolute impedance of frequency, (**b**) dependency of phase shift on frequency, (**c**) Nyquist plot and (**d**) dependency of imaginary part Z'' on frequency

Figure 6.15 (a) shows the derived equivalent circuit and the schematic dependency of $|Z^*|$ on frequency and Figure 6.15 (b) the Nyquist plot. A perfect capacitor leads to a semicircle in the Nyquist plot. Hereby, the first element represents the behavior of the bulk material and second element corresponds to the behavior of the formation of micro capacitors. A superposition of both is possible. Following equation describes the frequency dependent behavior of the equivalent circuit:

$$|Z^*| = \frac{1}{R_{el,Bulk} \cdot Q_{Bulk} \cdot (j\omega)^{m_{Bulk}}} + \frac{1}{R_{el,Agg} \cdot Q_{Agg} \cdot (j\omega)^{m_{Agg}}} \tag{6.11}$$

The sum of $R_{el,Bulk}$ and $R_{el,Agg}$ can be considered as the DC resistance $R_{el,0}$ of the material. After the second cut-off circular frequency $R_{el,\infty}$ is almost negligible. Dotted lines in Figure 6.14 represent the results of the fitted model. The results are in good accordance with the measured values, verifying that chosen equivalent circuits are accurate.

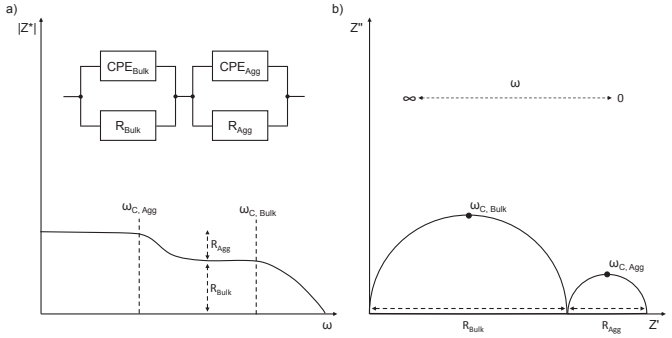


Figure 6.15: Derived equivalent circuit model and (**a**) schematic dependency of $|Z^*|$ on circular frequency and (**b**) complete theoretical Nyquist plot inspired by Han et al. [408]

Table 6.2 sums up the used fitting parameters. With increasing amount of dispersion steps after homogenization, the resistance, contributed to the formation of micro capacitors, rises. Exponent m shows a resistive behavior on macro scale ($m_{Bulk} \approx 0$) and capacitive behavior on micro scale ($m_{Agg} \approx 1$), showing a well percolated a macro network and a good distribution on micro scale (refer Equation 6.11 and 2.25).

Table 6.2: Equivalent circuit parameters for 0.01 wt.% filler concentration in the cured state

Step	$R_{el,Bulk}$ in Ω	Q_{Bulk} in pF	m_{Bulk}	$R_{el,Agg}$ in Ω	Q_{Agg} in pF	m_{Agg}
1	$7 \cdot 10^9$	0.0018	1.00	NA	NA	NA
2	$1 \cdot 10^6$	0.0071	1.00	$8 \cdot 10^5$	0.0056	1.00
3	$5 \cdot 10^5$	0.0039	1.00	$5 \cdot 10^5$	0.0084	0.98
4	$6 \cdot 10^5$	0.0023	1.00	$3 \cdot 10^5$	0.3656	0.99
5	$1 \cdot 10^6$	0.0018	1.00	$1 \cdot 10^5$	0.2616	0.97
6	$2 \cdot 10^6$	0.0022	1.00	$3 \cdot 10^5$	0.1286	1.00
7	$2 \cdot 10^6$	0.0030	0.99	$3 \cdot 10^5$	0.4658	0.92

For deeper understanding of electrical network formation, in the next step a higher filler concentration, close above the percolation threshold, is evaluated. Figure 6.16 (a) (symbols: measurement data and dotted lines: fitted data) gives the frequency dependency of the absolute value of the impedance $|Z^*|$ for the 0.05 wt.% filler concentration. The impedance behavior of the material after step 1 is similar to the ones resulting for 0.01 wt.% filler concentration. After dispersion step 3 the lowest resistance is achieved. After that, the resistance rises again. Figure 6.16 (b) gives the dependence of phase shift on frequency. For dispersion step 1 the phase shift development is similar to the one resulting from a filler loading of 0.01 wt.%. The Nyquist plot of this system is given in Figure 6.16 (c). For dispersion step 1, a semicircle occurs. The interpretation of following dispersion steps is difficult, because the distinct semicircle vanishes

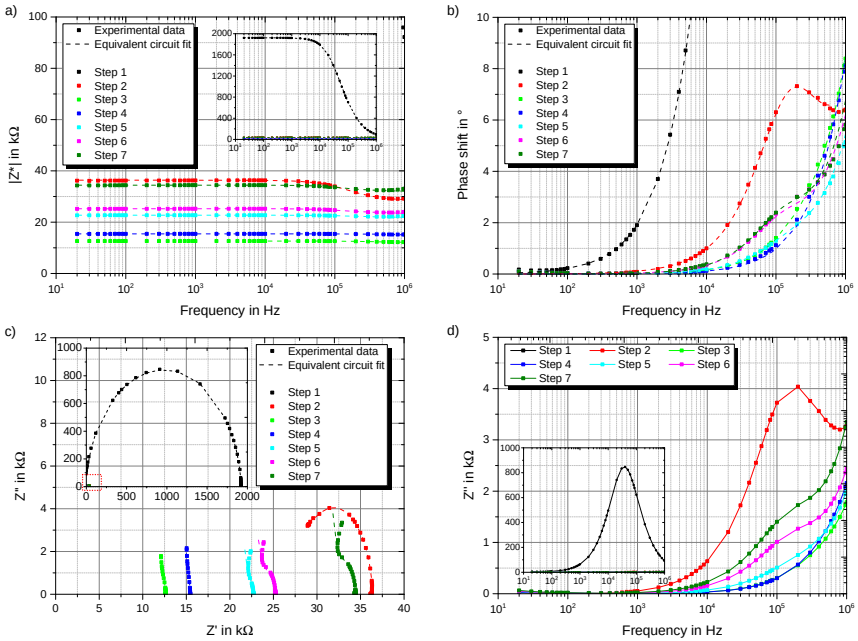


Figure 6.16: Impedance spectroscopy data evaluated for 0.05 wt.% filler concentration (**a**) dependency of absolute impedance of frequency and (**b**) dependency of phase shift on frequency (**c**) Nyquist plot (**d**) dependency of imaginary part Z'' on frequency

in the evaluated frequency range with increasing dispersion steps and only a part of it remains. Here, a broader frequency range has to be evaluated in future studies.

Nevertheless, the formation of the second semicircle (micro capacitor) is most pronounced for dispersion step 7. By evaluation of the slopes of Figure 6.16 (d) the highest Z'' value occurs again after dispersion step 7. Table 6.3 sums up the used fitting parameters for 0.05 wt.%. Here the results are similar to the ones before, but due to the evaluated range (just parts of semicircles) the accuracy of the fitting parameters is weak. The material shows a capacitive behavior on macro and micro scale with this filler loading. The real part of the impedance Z', evaluated at frequencies below 1 kHz, can be considered as DC resistance of the material [197]. Therefore, it was evaluated at a low frequency of 100 Hz. Figure 6.17 (a) gives the development of the DC resistance with the amount of dispersion steps. A minimum occurs for each filler concentration after dispersion step 3 or 4. With regard to electrical properties the chosen three roll milling process can be optimized. After the occurring lowest resistance a break-down of particle network seems to happen. Figure 6.17 (b) gives the maximum in the imaginary part of the complex impedance Z''_{max} and the corresponding frequency. The lowest Z''_{max} and the corresponding frequency underpin the break-down of the particle network. For increased amount of dispersion steps Z'' rises and the frequency reduces. A reduced cut-off frequency corresponds to a less stable particle network and a high Z'' corresponds to high a capacative ratio, therefore, a well separated particle network.

Table 6.3: Equivalent circuit parameters for 0.05 wt.% filler concentration in the cured state

Step	$R_{el,Bulk}$ in Ω	Q_{Bulk} in pF	m_{Bulk}	$R_{el,Agg}$ in Ω	Q_{Agg} in pF	m_{Agg}
1	$1 \cdot 10^6$	0.0069	0.95	$5 \cdot 10^5$	0.0047	1.00
2	$3 \cdot 10^4$	0.0005	1.00	$8 \cdot 10^3$	0.2749	0.95
3	$1 \cdot 10^4$	0.0018	1.00	449	2.4809	0.95
4	$2 \cdot 10^4$	0.0040	0.94	240	0.0012	0.23
5	$2 \cdot 10^4$	0.0018	0.94	650	2.4743	0.96
6	$2 \cdot 10^4$	0.0042	0.89	1300	1.0295	1.00
7	$3 \cdot 10^4$	0.0008	0.98	2136	0.6618	0.99

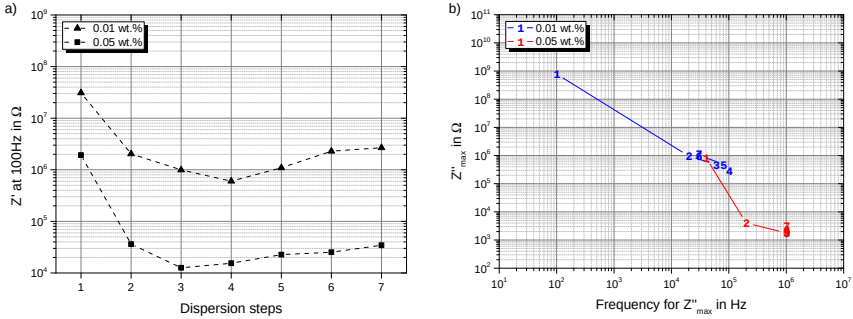


Figure 6.17: (**a**) development of the real part Z' of the impedance at 100 Hz and (**b**) development of the maximum imaginary part Z''_{max} of the impedance and corresponding frequency

Taking these results as basis, a model for the network formation within CNP/EP composites can be derived, leading to a more fundamental understanding of the physical processes in the material (see Figure 6.18). Starting with a non percolated network, where the agglomerates do not touch each other, a high Z' occurs in the Nyquist plot (compare Figure 6.18 (a)). This results in capacitive behavior of the material, revealed by a semicircle with infinite radius. For example, this dispersion state results after dispersion step 1 at a filler concentration of 0.01 wt.% (refer Figure 6.14 (c)). Near the percolation threshold it is unlikely that the agglomerates, which exist in a dense micro structure, touch each other without dispersion. With further dispersion a percolated macro network is formed, resulting in a finite semicircle in the Nyquist plot. This state is gathered for the further dispersion steps of 0.01 wt.% (compare Figure 6.18 (b)). A further dispersion for higher filler concentrations results in the separation of particles on micro scale. This leads to a formation of a second semicircle in the Nyquist plot (compare Figure 6.18 (c)). Ongoing dispersion leads to a further break-down of agglomerates, resulting in further separation of the semicircles in the Nyquist plot, see Figure 6.18 (d). The frequency dependency reveals the resistive and capacitive nature of the composites and in combination with the developed model the direct interpretation of the dispersion state on macro and micro level is enabled.

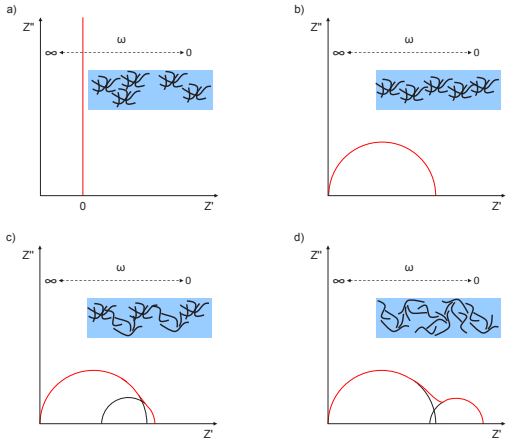


Figure 6.18: Network formation over the dispersion process: (**a**) badly distributed agglomerates ⇒ no el. network ⇒ capacitive behavior, (**b**) well distributed agglomerates ⇒ el. network ⇒ semi circle, (**c**) separation of CNT within agglomerates ⇒ micro capacitors ⇒ formation of 2nd semi circle and (**d**) further separation of CNT ⇒ more distinct micro capacitors ⇒ separation of semi circles

Concluding, impedance spectroscopy was verified as easily applicable indirect solution for in-line monitoring of CNT/EP composite dispersion process on TRM. With these results a model for better understanding of the mechanisms behind the electrical network formation on micro and macro scale was obtained. The dispersion state of the network can be evaluated by impedance spectroscopy.

6.2.3 Evaluation of Process Data from Three Roll Milling Processes

A third evaluated method, suitable for online monitoring of the three roll milling process, is the acquisition and interpretation of occurring process data. New generation of three roll mills are enabled to measure the occurring line loads between the rollers and to monitor the temperature within the rollers during the dispersion process. Figure 6.19 (a) gives the process data of a standard seven-step dispersion process of

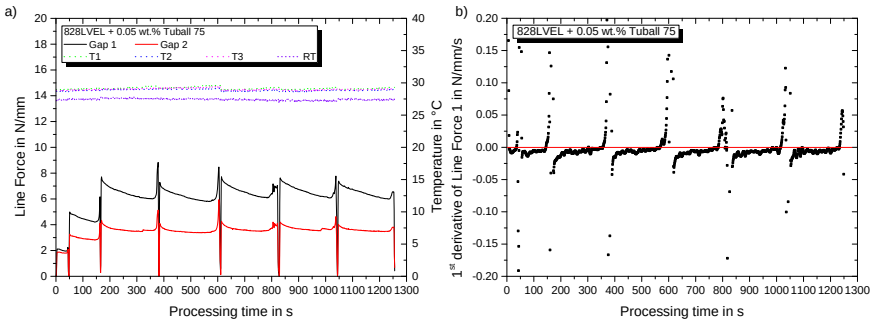


Figure 6.19: Filler loading of 0.05 wt.% Tuball 75 dispersed in 828LVEL: (**a**) line load and temperature development and (**b**) first derivative of line load in the feeding gap

0.05 wt.% SWCNT Tuball 75 in Epikote 828LVEL (normalized on the final composition with curing agent). The black line represents the occurring line load in the feeding gap (gap 1) and the red line gives the line load in the dispersion gap (gap 2). Dotted lines indicate the ambient temperature and the development of the temperature within the rollers. Each dispersion step is indicated by a rise of line load in the beginning and ends with the drop of the line load to 0 N/mm. After each dispersion step, the total amount of material is collected and, after accompanying measurements, re-fed into the feeding gap. The first two production steps homogenize the material with gap spacing of 120 µm/40 µm and 40 µm/13 µm, respectively. The gap spacing ratio for the last five dispersion steps is 13 µm/5 µm. With decreasing gap spacing the average line load increases in both gaps. In each dispersion step, the line load decreases over the dispersion step and at the end, when the material runs empty, the line load rises. This is due to material separation. It is clearly visible, during the processing that the material is more dry and offers a higher particle concentration at the end of the processing. This separation peak at the end of the steps becomes less distinct with increasing amount of dispersion steps, concluding an improved dispersion of the particles. To find a criterion to quantify the quality of the dispersion the origin of the separation peak needs to be investigated. In order to monitor the occurrence of material separation, a line load increase at the end of the dispersion step must be identified. A applicable criterion is given by the time derivative of the line load in the feeding gap. The course of the curve is similar for the feeding and dispersion gap, with higher values in the feeding gap. Therefore, the derivative of the line load in the feeding gap was chosen. This first process time derivative of the line load can be easily accessed and visualized. If the derivative curve is negative, no separation peak occurs. A positive derivative indicates a separation peak, which gives an adequate criterion to evaluate the dispersion quality. The value must be negative or at least zero at the end of the dispersion step to consider the material as homogeneous. Figure 6.19 (b) visualizes the first process time derivative of the occurring line load in the feeding gap. For this particle type the separation does not vanish. In the previous section, the optimum dispersion, regarding the electrical properties, was achieved after three or four dispersion steps. For further investigations, a combination of impedance spectroscopy and evaluation of the three roll mill data will be utilized for evaluation of the dispersion quality. Further optical coherence tomography will only be performed for the demonstration of the scalability of the three roll mill process (Chapter 8).

Summarizing, a negative or equal to zero first time derivative of the line load indicates a homogeneous dispersion and is a applicable criterion for process optimization.

6.3 Monitoring of Three Roll Milling Processes - Variation of Machine, Particle Type and Epoxy Resin

Within this section the results from the dispersion processes of different particle types in different epoxy resins with variation of the filler content will be presented. Furthermore, the impact of the processing machine and the dependency on matrix viscosity will be revealed. In case of particle dispersion, after each dispersion step an impedance spectroscopy and a rheological characterization was performed.

6.3.1 Three Roll Milling - Viscosity Dependency

To reveal the dependency of the line load on matrix viscosity, different viscosity standards were processed on the three roll mill. Figure 6.20 (a) gives the strain dependent complex viscosity of the four used viscosity standards at 30 °C.

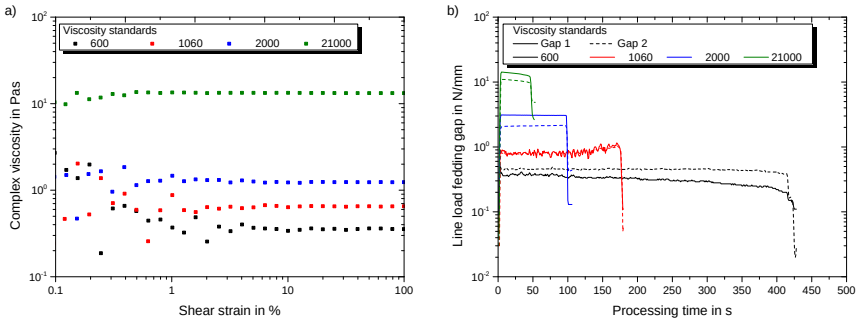


Figure 6.20: Dependency of (**a**) complex viscosity on applied shear strain and (**b**) occuring line load in the feeding gap

They can be considered as Newtonian-like fluids, due to their strain amplitude independency. Their complex viscosity varies from 360 mPas to 13 Pas. Figure 6.20 (b) gives the line loads in both gaps at a processing temperature of 30 °C with a gap ratio of 13 µm/5 µm. The used TRM was the 80E-Plus$^+$. Higher viscosity results in higher line loads. This contributes to the higher modulus for higher viscosity and pronounced cohesion. Therefore, the material flow is more constrained at the entrance of the gap and it is less squeezable. The processing time reduces with increasing viscosity. Higher viscosity results by longer molecule chains. This leads to higher cohesive forces and the material flow rate is improved. The behavior of the different molecular weight epoxy resins was investigated with the standard parameters of the seven-step three roll milling process. The resulting line loads in the feeding gap are given by Figure 6.21. With increasing viscosity, the average line load increases, too. For very high molecular weight Epikote 834 a distinct continuous decrease of the line load can be observed. This may result from temperature increase, resulting from inner friction. This material behavior becomes more distinct with increasing molecular weight of the resin.

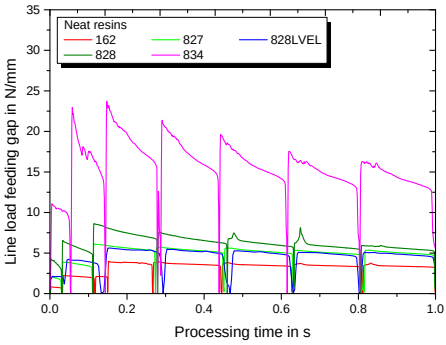


Figure 6.21: Resulting line loads for processing the different epoxy resins in a seven-step dispersion process on TRM 80E-Plus$^+$

6.3.2 Influence of Processing Machine

To identify the influence of the processing machine, neat Epikote 828LVEL was processed on the larger diameter 120E-250 three roll mill at 30 °C. Figure 6.22 gives the resulting line loads for the standard seven-step process.

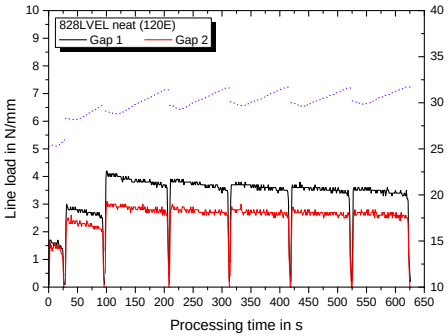


Figure 6.22: Line force and temperature development of a seven-step dispersion process of neat Epikote 828LVEL on TRM 120E-250

With decreasing gap spacing the line loads increase again. Furthermore, the line loads are smaller compared to the smaller 80E-Plus$^+$. This results from the larger diameter, which reduces the drag-in angle and applies a smoother compression to the material. For this process the decrease in line load over dispersion time can be observed, too. Taking the temperature development of the material within the feeding gap into account (dotted line), a clear increase of its temperature can be observed. This temperature increase must result from the inner friction of the material. For determination of influences resulting from the size of the processing machine on the dispersion behavior of carbon nanoparticle filled epoxy resin 0.3 wt.% MWCNT NC7000 were dispersed on both TRM and the process data were compared to each other. The line force as well as the temperatures were monitored. Figure 6.23 gives the results from the dispersion processes. Monitored data from the 120E-250 (Figure 6.23 (a)) show a constant value of the line loads in the first homogenization step. Both occurring line loads are at comparable level. In the second homoge-

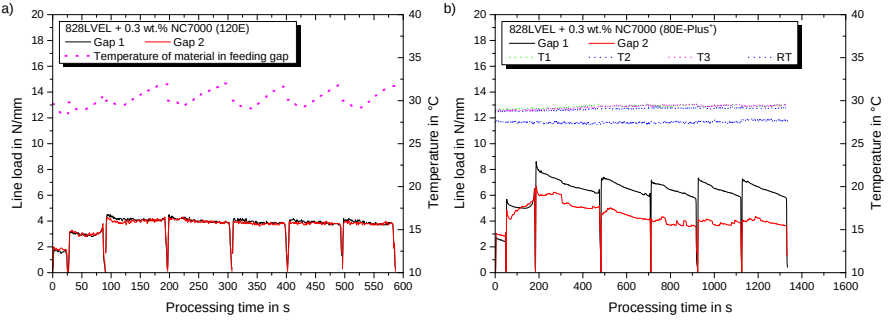


Figure 6.23: Line force data for dispersion process on (**a**) 120E-250 and (**b**) 80E-Plus$^+$

nization step at smaller gap spacing, the line force signal exhibits a line force increase of both signals at

its end. This contributes to a separation of the material, which is clearly visible from the flow behavior at the apron blade. The material is less wetted at the end of this step. All following dispersion steps result in identical curves, which are at a constant level. For the 120E-250 equipped with the measuring box the signal to noise ratio is very high. In every step, the temperature drops towards 30 °C at the beginning and rises during the dispersion step. Figure 6.23 (b) shows the results gained by dispersing the same material on the 80E-Plus$^+$. In the first homogenization step the line force drops for both gaps during processing. At the end of this step the line force rises. In the second step the line loads decrease in the beginning and then increase due to separation. This material separation has a high impact on the line force of the dispersion gap. For the next two steps the line force drops during the whole dispersion time. At the end of this step the line force slightly increases. The last three steps show a continuous decrease of the line force with processing time. In general, the line force starts at a higher value compared to the last value of the previous step and decreases. Temperatures inside the rollers do not increase. A comparison of processing times, by taking into account the variation of friction width l, leads to a 20 % increase of production capacity by using the 120E-250 model. Due to the larger diameter, the drag-in angle of the material is less steep for the 120E-250 TRM compared to the 80E-Plus$^+$. This allows the material to be dragged in uniformly. Furthermore, it offers a higher surface area, to which the material can adhere. All further dispersions within this section were processed on the 80E-Plus$^+$. Gathered impedance spectroscopy results of the dispersions, displayed in Figure 6.24, show that the dispersion quality is TRM independent. Resulting impedance spectra of two dispersion processes on 80E-Plus$^+$ verify the high repeatability of this processing technique.

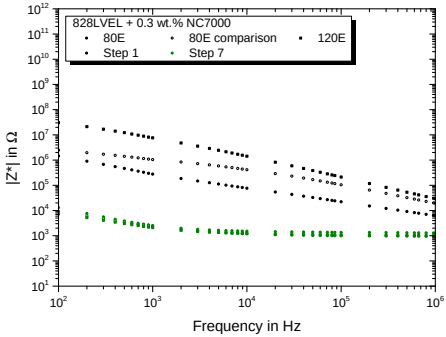


Figure 6.24: Absolute impedance $|Z^*|$ for 0.3 wt.% NC7000 dispersed in Epikote 828LVEL on 120E-250 and 80E-Plus$^+$

Futhermore, the dispersions were investigated in terms of their rheo-electrical properties. Figure 6.25 (a) gives the development of the strain dependency of storage and loss modulus over the dispersion steps for 0.3 wt.% NC7000 dispersed in Epikote 828LVEL with a TRM 120E-250. Initially, the storage modulus is lower compared to the loss modulus. With increasing dispersion steps, the storage modulus increases. With increasing amount of dispersion steps, the shear-thinning effect, revealed by a decrease of storage modulus with increasing applied shear strain, develops. This results from a percolated particle network.

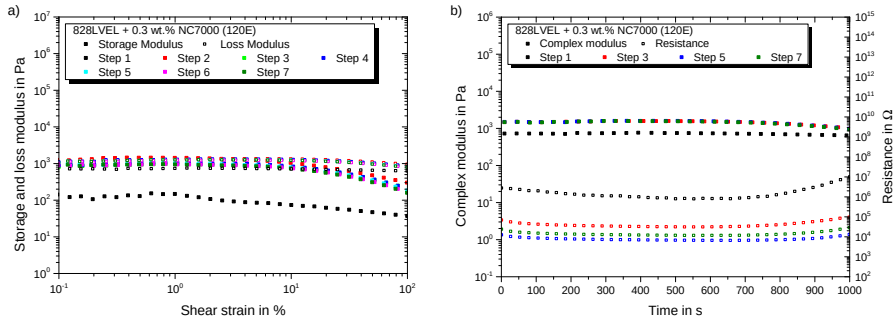


Figure 6.25: Evaluation of rheological behavior of 0.3 wt.% MWCNT NC7000 dispersed in 828LVEL over the whole process: (**a**) dependency of storage and loss modulus on applied shear strain and (**b**) complex modulus and electrical resistance over testing time

Going into detail of the network state, by utilizing the introduced method from the previous section, the resistance decreases with increasing dispersion steps, see Figure 6.25 (b). The complex modulus increases with increasing amount of dispersion steps. The particle network, in terms of electrical and rheological properties, becomes more developed. Increased shear strain in strain-sweeps results in shear-thinning and increase in electrical resistance. The particle network is broken down, but becomes more stable with increased dispersion steps. For improved understanding and correct interpretation of the resulting TRM-data, the influence of matrix viscosity, filler loading and particle type are evaluated.

6.3.3 Influence of Resins' Viscosity

For evaluation of the impact of matrix viscosity on the dispersion process, 0.5 wt.% NC7000 were dispersed in Epikote 162, 827 and 828. Figure 6.26 (a) gives the line load development of the dispersion processes with interim performed impedance spectroscopy and rheology measurements. All curves show similar

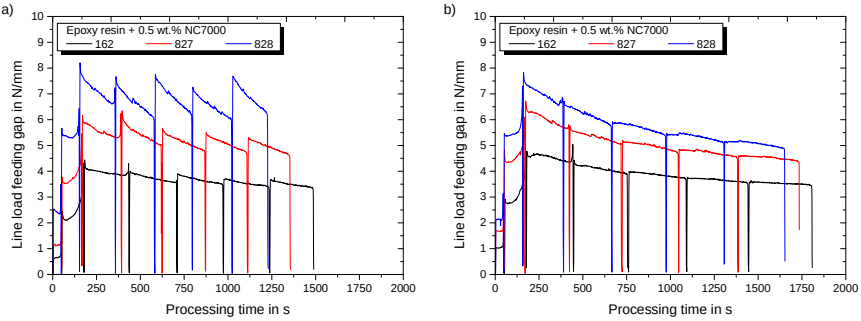


Figure 6.26: Influence of resin viscosity on line force for dispersion of 0.5 wt.% in epoxy resins with different molecular weight distributions. (**a**) dispersion with a break of 15 minutes for impedance spectroscopy measurements after each step and (**b**) continuous dispersion process

curve characteristics. In the first step the line load is constant over the processing time and at the end it drastically increases due to separation. In the second step the line load drops in the beginning and afterwards rises with increasing slope until the end of this step. Until the third step the initial line load

rises. This originates from decreasing gap spacing, which results in higher compression of the material, dragged into the gap. The third step shows a decrease of the line load during dispersion. In the end it rises again. All following steps exhibit a continuous decrease of line load and possess the same initial line load value. With increasing resin molecular weights, the line loads rise. Additionally, the processing time decreases by 15 %. This results from the higher cohesive nature of the higher molecular weight resins. Comparing these results to a continuous dispersion process, where the material is directly re-fed into the feeding gap after each step without additional time consuming characterizations, the curve characteristics change. Figure 6.26 (b) shows the line load curves for a continuous process.

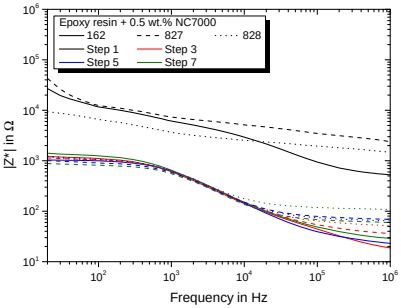


Figure 6.27: Resulting impedance spectra in dependency of resin viscosity for NC7000 dispersions

The first two steps are similar to the non-continuous process. Beginning with the third cycle the line load constantly decreases. An increase of the measured line load at the end of the step is only observable for the third step. The initial line load is similar to the last value of the previous step. The decrease over processing time seems to be the temperature related effect, again. This will be addressed in the next section. Figure 6.27 gives the impedance spectroscopy curves after step 1, 3, 5 and 7. In the low frequency range, which can be considered as bulk behavior, $|Z^*|$ shows nearly the same value for all configurations after step 3 and remains nearly constant. On macro scale the material behavior does not change anymore. This correlates with the extinction of material separation after dispersion step 3 in the line load curves. In the high frequency range $|Z^*|$ increases with further dispersion. Here, the material with Epikote 828 results in highest complex impedance after final dispersion step. With decreasing molecular weight of the resin,

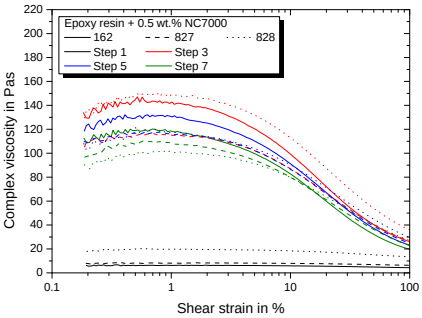


Figure 6.28: Complex viscosity resulting from strain-sweeps in dependency of resin viscosity for NC7000 dispersions

the complex impedance decreases as well. This indicates an improved dispersion on micro scale due to the higher molecular weight, inducing improved shear stress transfer to separate the agglomerates. This result is supported by the rheological results, given in Figure 6.28. As expected, the complex viscosity is lowest after dispersion step 1 for the low molecular weight resin Epikote 162 and increases with molecular weight increase. After the final dispersion step, the high molecular weight Epikote 828 offers lowest viscosity. Low complex viscosity results from less particle interaction within the material. The correlation of this with the previous shown impedance spectra confirms the conclusion that the particles' dispersion is superior for high molecular weight epoxy resins.

6.3.4 Temperature Dependency of Dispersion Process

A dispersion of a masterbatch consisting of 1 wt.% NC7000 in Epikote 828LVEL on the 80E-Plus^{+} with steel rollers was monitored by infrared thermography to analyze the temperature development over the dis-

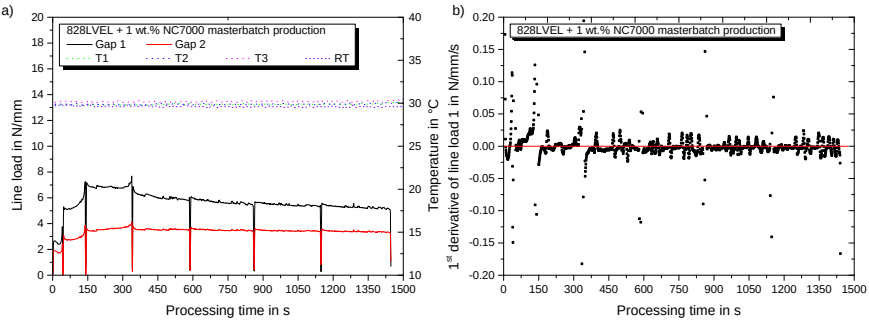


Figure 6.29: Dispersion process of 1 wt.% NC7000 in Epikote 828LVEL: (**a**) line load and temperature development within the rollers and (**b**) first derivative of line load in the feeding gap

persion process and its effect on the line load. Figure 6.29 (a) shows the line load development and temperature development over the processing time. Temperature inside the rollers increases slightly. The characteristics of the curve are similar to the already shown results. After step 3 no more separation occurs.

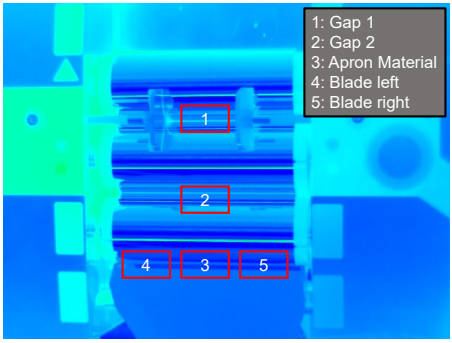


Figure 6.30: Areas of interest of the 1 wt.% NC7000 masterbatch dispersion

Figure 6.29 (b) gives the process time derivative of the line load in the feeding gap. After step 3 the criterion of vanishing separation is fulfilled. For correlation with line load data several areas of interests were chosen, which are given in Figure 6.30. The temperature was monitored in the feeding gap (1), dispersion gap (2), material on the apron blade (3) and for the apron blade itself (4,5). The temperature development of the material is given for both gaps in Figure 6.31 (a). Figure 6.32 (a) gives the temperature distribution at the initial state of the machine. The rollers are on the set temperature of 30 °C and in steady state. After the first dispersion step (Figure 6.32 (b)) a temperature increase of the material becomes visible. At the parts of the apron blade, where the metal blade runs without material, the temperature increase is most pronounced. For the remaining steps (Figure 6.32 (c) to (h)) the heat generation is more and more pronounced. Finally, a temperature increase over 10 K can be observed for the dispersed material. Curve characteristics of temperature development in the dispersion gap correlates with the line load curve. The temperature and line load approach a threshold. A temperature increase results in lower viscosities of the matrix material, which lowers the occurring line loads. Figure 6.31 (b) verifies that the highest heat input results from the steel apron blade, which runs on the steel roller without a resin film acting as lubricant in between. A full utilization of the friction width would lead to a fully lubricated apron blade and will maximize the material output.

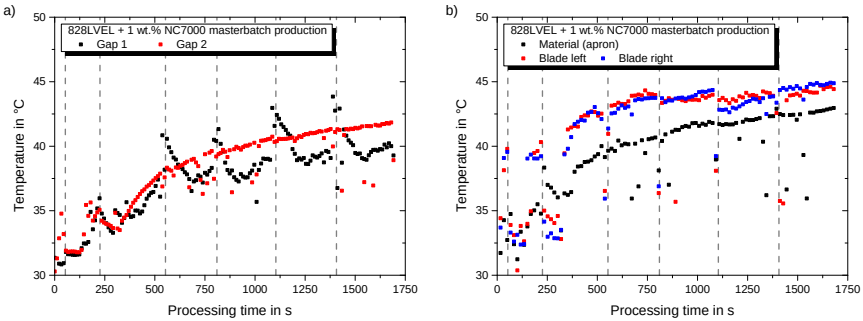


Figure 6.31: Temperature development of dispersion process with 1 wt.% NC7000 in Epikote 828LVEL: (**a**) material in feeding and dispersion gap and (**b**) material at apron blade and the blade itself

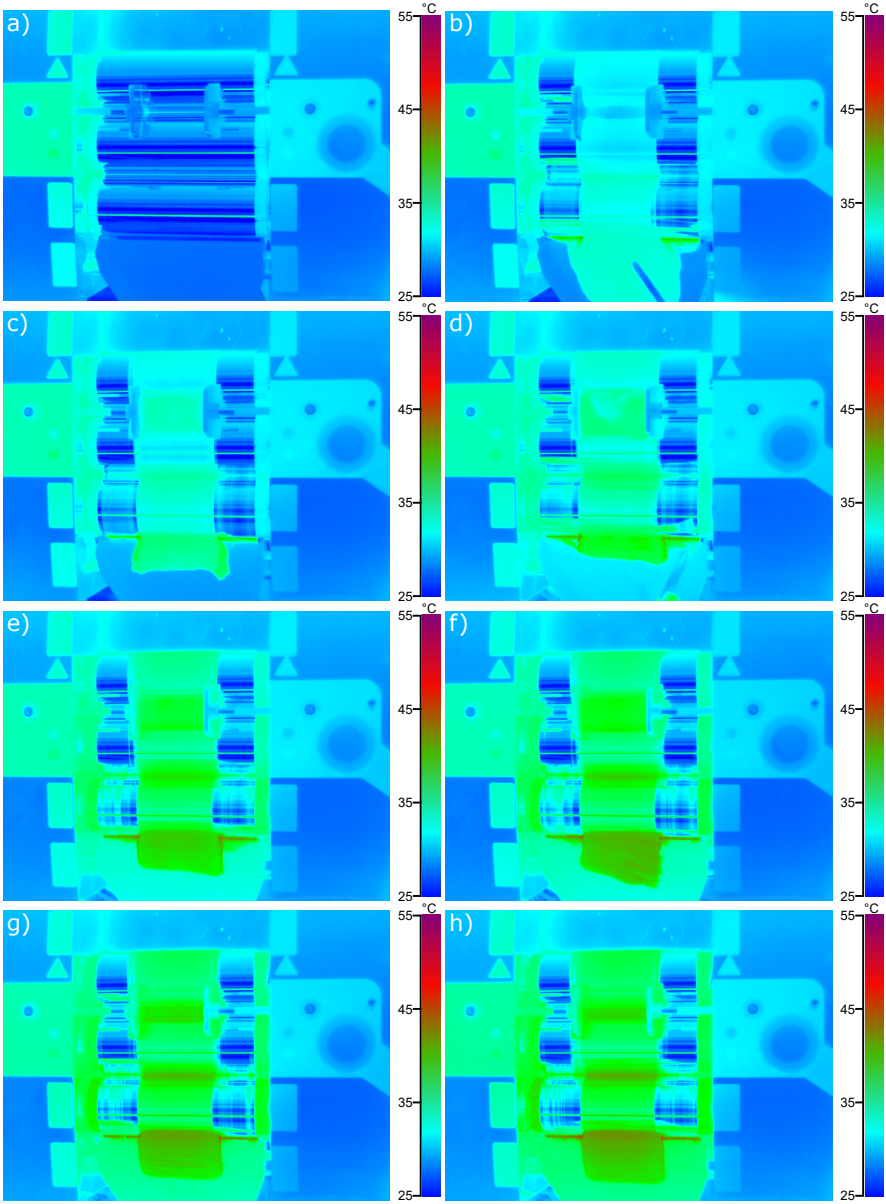


Figure 6.32: Temperature development during dispersion visualized by infrared thermography for (**a**) initial state, (**b**) after step 1, (**c**) after step 2, (**d**) after step 3, (**e**) after step 4, (**f**) after step 5, (**g**) after step 6 and (**h**) after step 7

6.3.5 Dispersion of Carbon Black - Orion Engineered Carbons Printex L

For evaluation of the influence of spherical particles on dispersion behavior as well as the influence of filler content, carbon black Printex L was dispersed in Epikote 828LVEL with concentrations of 1 wt.%, 4 wt.%, 8 wt.% and 12 wt.%. Figure 6.33 shows the resulting line load and temperature development over the process time. The line load curves decrease within each step. The initial value increases again for the first three steps and remains constant in the following steps. No increase in temperature can be observed inside the rollers.

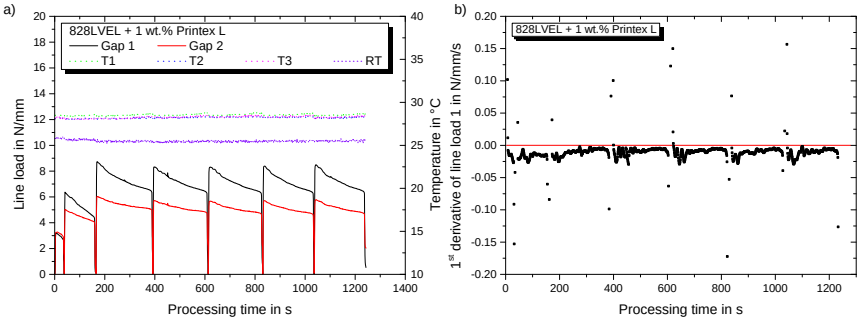


Figure 6.33: Carbon black Printex L dispersed in 828LVEL: (**a**) line load and temperature development for 1 wt.% and (**b**) first derivative of line load in the feeding gap

Figure 6.33 (b) gives the first derivative of the line load in the feeding gap. In none of the dispersion steps separation occurs, judging from the fact that the values are always negative at the end of each dispersion step. Increasing filler contents result in higher line loads and an increase in processing time (Figure 6.34 (a)). This contributes to the pronounced filler network for highly filled polymers, changing the visco-elastic behavior of the material more to a solid-like nature. Displayed impedance spectra in Figure 6.34 (b) reveal different dispersion mechanisms with varying filler content. For 1 wt.% at low frequencies a conductive network, formed by the aggregated structure of the CB, exists after the first dispersion step.

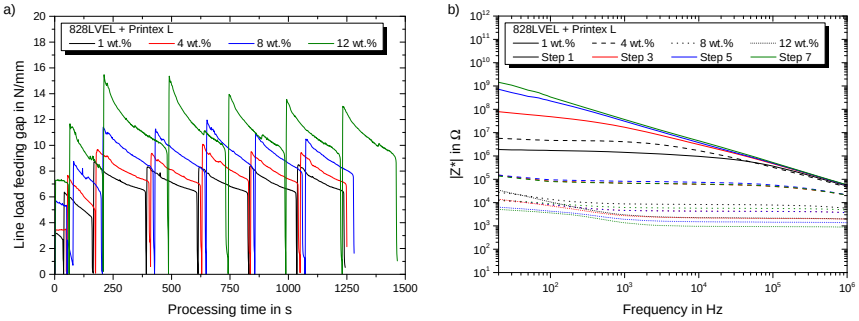


Figure 6.34: Carbon black Printex L dispersed in 828LVEL: (**a**) influence of filler content on the line load and (**b**) comparison of impedance spectra for 1 wt.%, 4 wt.%, 8 wt.% and 12 wt.%

By further dispersion, the capacitive nature of the material becomes more dominant. After seven dispersion steps the composite offers a pure insulating nature. For 4 wt.% the complex impedance decreases with further dispersion and reaches a steady value after step 3. This behavior is also observed for 8 wt.% and 12 wt.% filler loading, respectively. After step 3 the impedance does not change significantly by further processing.
In addition to the impedance measurements the material was analyzed by the introduced rheo-electrical method. The DC resistance was measured during strain-sweeps. Figure 6.36 (a), (c), (e) and (f) give the storage and loss modulus development in dependency of the applied shear strain for the evaluated filler concentrations after each dispersion step. Taking the criterion $G' > G''$ for the definition of the rheological percolation into account, the rheological percolation threshold is reached with a filler concentration of 8 wt.%. For 1 wt.% and 4 wt.% the loss modulus is not affected by filler addition. The storage modulus rises in contrast. Dispersion does not change the rheological behavior of the material for these two filler concentrations. For 1 wt.% the typical initial plateau with following decrease of storage modulus is barely visible, due to the resolution of the rheometer. For 4 wt.% the plateau and decrease is more distinct for the measured storage modulus. In case of loss modulus a slight decrease of the plateau can be identified. Reaching the rheological percolation threshold, both, storage and loss modulus, exhibit a decrease. With increasing filler content the decrease of loss modulus becomes more distinct.

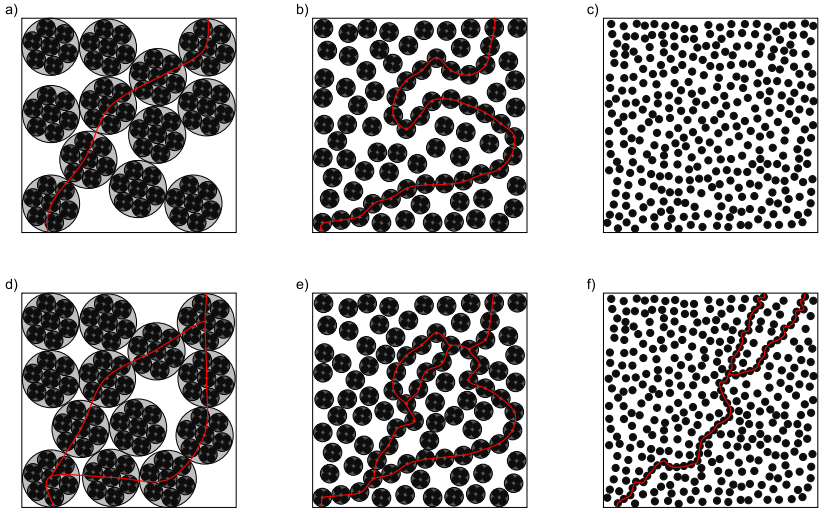


Figure 6.35: Schematical visualization of the separation mechanism and agglomerate size change throughout the dispersion process and its effect on conductive paths in the material: (**a**) to (**c**) low filler content and (**d**) to (**f**) high filler content

Figure 6.36 (b), (d), (f) and (h) give the development of the complex modulus and the resistance of the material tested in the strain-sweep for each filler content after each dispersion step. For the lowest filler concentration of 1 wt.% neither the complex modulus nor the electrical resistance changes due to dispersion. No particle interaction influences the material behavior for this filler content. With increasing filler

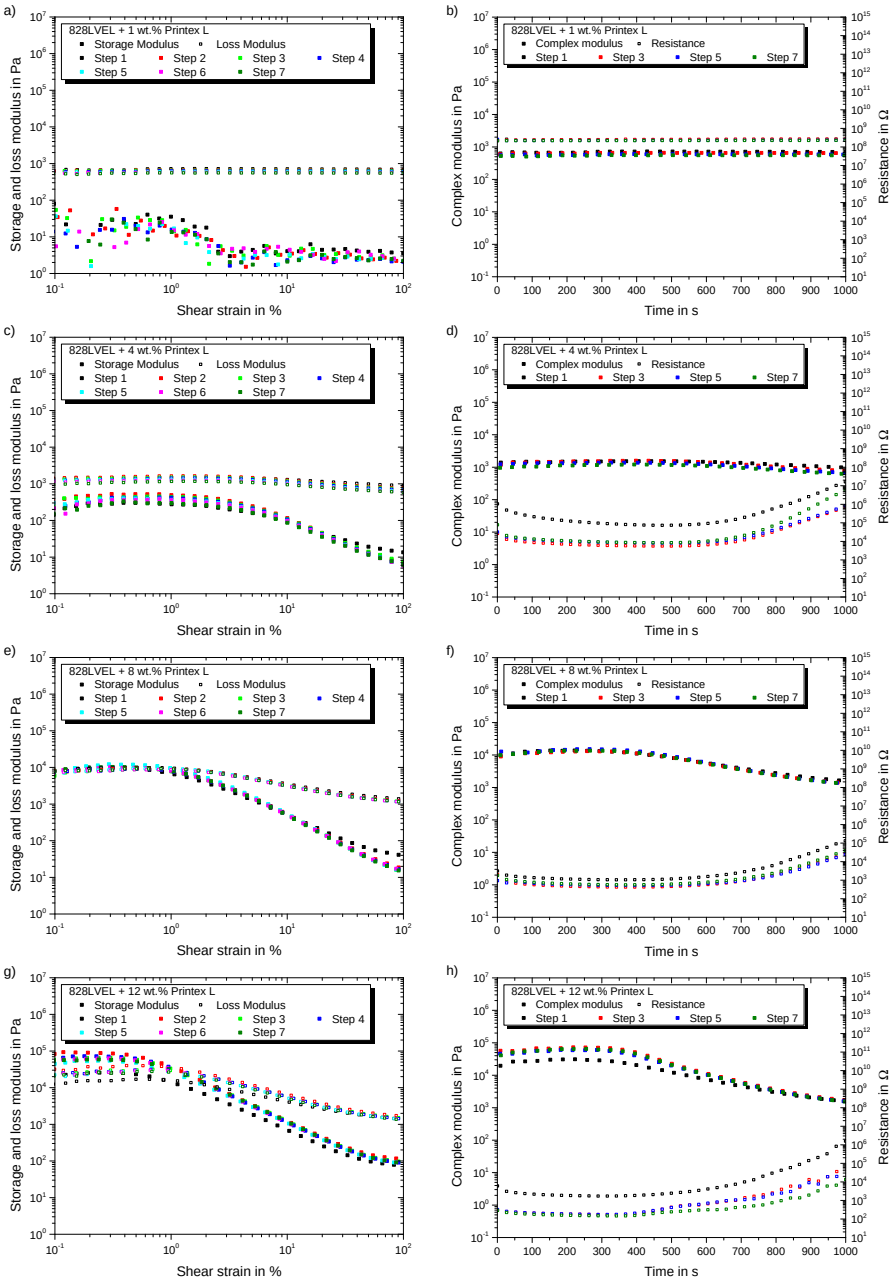


Figure 6.36: CB Printex L dispersed in 828LVEL: storage and loss modulus for (**a**) 1 wt.%, (**c**) 4 wt.%, (**e**) 8 wt.% and (**g**) 12 wt.% filler loading; complex viscosity and resistance over testing time for (**b**) 1 wt.%, (**d**) 4 wt.%, (**f**) 8 wt.% and (**h**) 12 wt.% filler loading

content, the complex modulus rises and the electrical resistance decreases. Beginning with 4 wt.%, the resistance drops after the first dispersion step. Furthermore, a plateau occurs in the complex modulus as well as a break-down of the particle network at elevated strains, revealed by an increase in resistance. The decrease in complex modulus results from the decrease in storage modulus (Figure 6.36 (b)). In comparison, the elevated shear strain does not affect the loss modulus. This material behavior changes with increasing filler content. The plateau becomes more distinct because the loss modulus is more affected by the applied shear strain. Furthermore, the material does not change further after dispersion step 1. The rheo-electrical characterization confirms the results gathered by impedance spectroscopy and line force evaluation. Seven dispersion steps are not necessary to achieve the best electrical conductivity for CB dispersion in EP.

Figure 6.35 visualizes the governing mechanism for this material behavior. The particles are present in their agglomerated state. Mixing them into the resin and homogenization during the first dispersion step leads to a conductive network (red line in Figure 6.35 (a)). The size of the spherical agglomerates is of such a size that they touch each other. By further dispersion, the size of the agglomerates is reduced and they finally fill the polymer without touching each other (compare Figure 6.35 (b) and (c)). Increasing the filler content changes the mechanism. This is visualized by Figure 6.35 (d) to (f).

After the first homogenization step, the agglomerates touch each other and by further dispersion steps a higher redundancy of the particle network builds up by forming more conductive paths. This improves the final conductivity.

6.3.6 Dispersion of Multi-Walled Carbon Nanotubes

6.3.6.1 Nanocyl NC7000

The impact of rigid cylindrical particles on the process data is analyzed by dispersing 0.1 wt.%, 0.3 wt.%, 0.5 wt.% and 0.7 wt.% of NC7000 MWCNT in Epikote 828LVEL, respectively. The results of the 0.3 wt.% were already discussed in section 6.3.2. Figure 6.37 (a) and (b) show no significant differences between line load and processing time with increasing filler content. Just the line load in gap 2 slightly decreases. Impedance spectroscopy data reveal a change in mechanisms for this material, too (compare Figure 6.38).

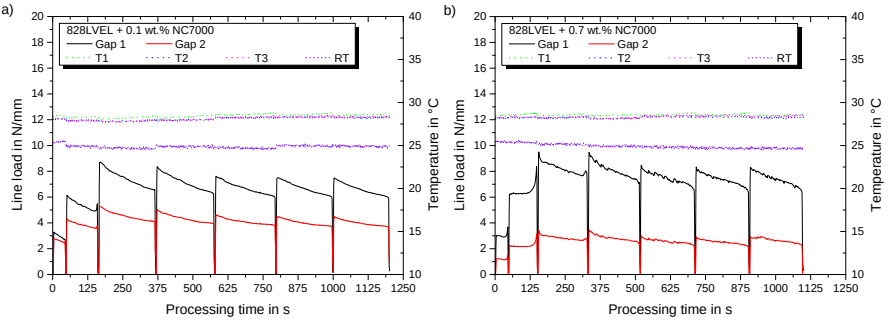


Figure 6.37: MWCNT NC7000 dispersed in 828LVEL: (**a**) line load and temperature development for 0.1 wt.% and (**b**) line load and temperature development for 0.7 wt.%

For 0.1 wt.% the absolute value of the complex impedance drops for low frequencies from first to third dispersion step and increases again with further dispersion. Beginning with 0.3 wt.% the material shows the same behavior as carbon black. After the third dispersion step no further decrease in impedance is achieved. This correlates with the extinction of the separation peak. Summarizing, rigid particles like

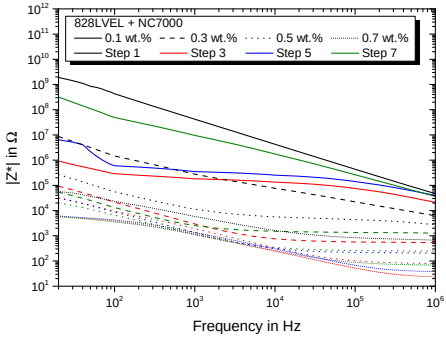


Figure 6.38: Comparison of impedance spectra for 0.1 wt.%, 0.3 wt.%, 0.5 wt.% and 0.7 wt.% NC7000 in 828LVEL

CB or MWCNT need only few dispersion steps to be homogeneously dispersed. Higher filler content increases processing time for CB but shows no significant increase for MWCNT. Figure 6.39 (a), (c), (e) and (g) display the development of storage and loss modulus during the strain-sweep test.

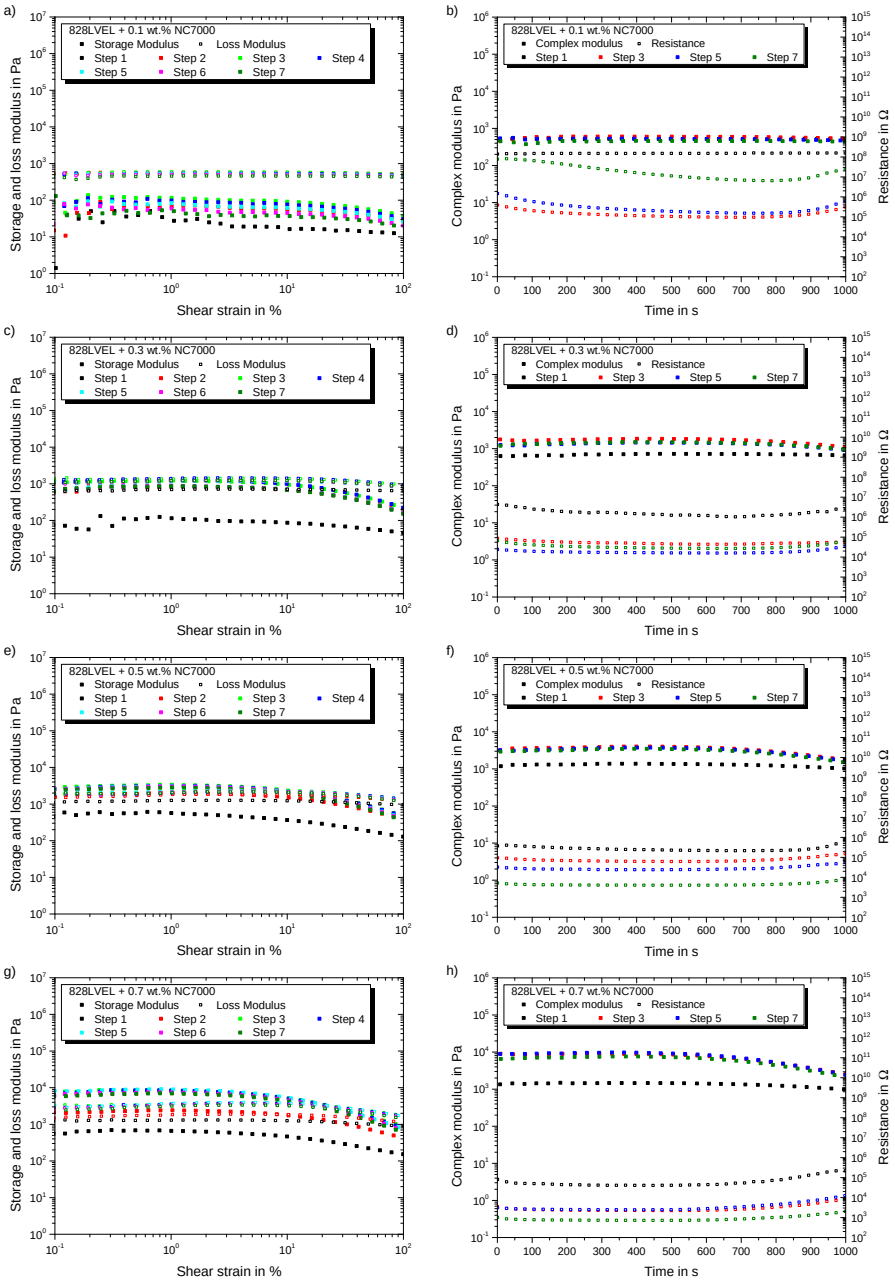


Figure 6.39: MWCNT NC7000 dispersed in 828LVEL: storage and loss modulus for (**a**) 0.1 wt.%, (**c**) 0.3 wt.%, (**e**) 0.5 wt.% and (**g**) 0.7 wt.% filler loading; complex viscosity and resistance over testing time for (**b**) 0.1 wt.%, (**d**) 0.3 wt.%, (**f**) 0.5 wt.% and (**h**) 0.7 wt.% filler loading

The rheological percolation of this filler type is reached by 0.3 wt.% filler addition. A similar behavior of the material can be observed compared to carbon black. Below the rheological percolation the loss modulus is not affected by increasing shear strain. With increasing filler loading, the decrease, which follows the plateau in storage and loss modulus, becomes more distinct. This nanocomposite does not further change its rheological behavior after the first step of dispersion with a gap spacing of 13 µm/5 µm. Figure 6.39 (b), (d), (f) and (h) give the development of the complex modulus and the electrical resistance for NC7000 modified Epikote 828LVEL during the strain-sweep test for each dispersion step of each filler content. For 0.1 wt.%, the complex modulus does not change with the amount of dispersion steps, but the electrical resistance is minimal for dispersion step 3 and 5. These results are in good accordance with the impedance measurements and the derived model for carbon black. The electrical resistance measurement is much more sensitive to particle network changes than the rheological measurement. For 0.5 and 0.7 wt.% the minimum in resistance occurs after dispersion step 7.

6.3.6.2 Future Carbon CNTB

The impact of plasma treatment of rigid cylindrical particles on the process data is analyzed by dispersing 0.1 wt.%, 0.3 wt.% and 0.5 wt.% of MWCNT CNTB as a reference material and plasma treated variants (Section 6.3.6.3 and 6.3.6.4) of it in Epikote 828LVEL, respectively. Figure 6.40 (a) gives the line load and temperature development of the 7 step dispersion process. The same characteristic curve as described before occurs.

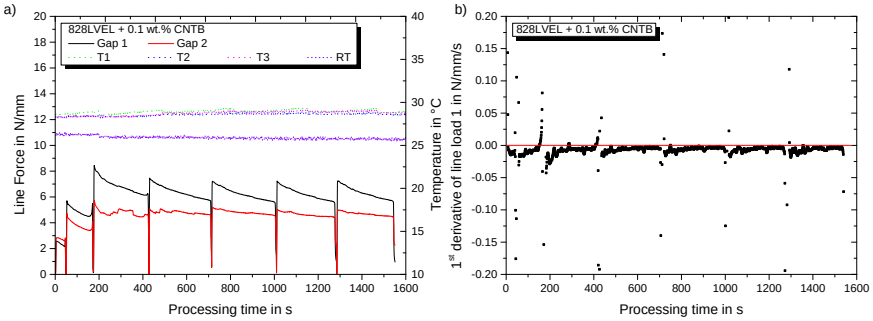


Figure 6.40: CNTB dispersed in 828LVEL: (**a**) line load and temperature development for 0.1 wt.% and (**b**) first derivative of line load in the feeding gap

Figure 6.40 (b) gives the first processing time derivative of the line load of the feeding gap. The criteria for homogeneous dispersion is fulfilled after dispersion step 3. Figure 6.41 (a) gives the line load of the feeding gap for the evaluated filler contents during the dispersion process. For this particle type, the processing time reduces with increasing filler content, too. A filler loading of 0.5 wt.% requires four dispersion steps to match the criteria for the homogeneous dispersion, by extinction of the separation peak. This was not the case for NC7000. The line loads have an identical value, independent of the filler content. Figure 6.41 (b) gives the impedance spectra for the investigated filler contents in dependency of the dispersion step. For 0.1 wt.% filler loading the lowest resistance is achieved after dispersion step 3. By further dispersion, the resistance rises again. For higher filler loadings, the complex impedance in the low frequency plateau does not significantly change anymore by further dispersion after the third dispersion step. This is not the case for the high frequency region. Here, further dispersion leads to higher complex impedance values, revealing improved dispersion on micro level.

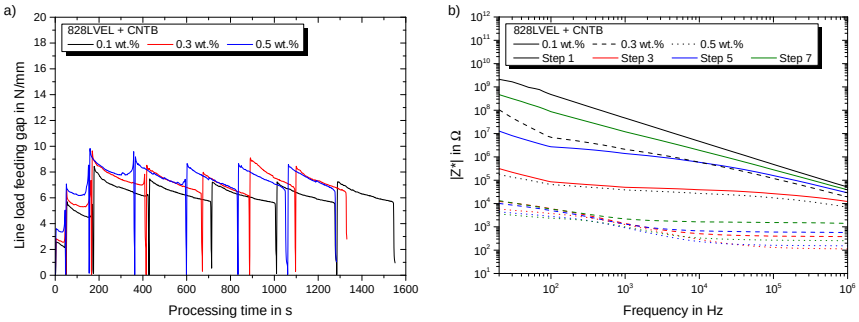


Figure 6.41: CNTB dispersed in 828LVEL: (**a**) line load for 0.1 , 0.3 and 0.5 wt.% and (**b**) impedance spectra for different filler contents and dispersion steps

Figure 6.42 (a), (c) and (e) display the storage and loss modulus dependency on the applied strain for the different filler loadings after each dispersion step. The material shows a similar behavior as NC7000. Rheological percolation occurs with addition of 0.3 wt.% of CNTB. Figure 6.42 (b), (d) and (f) give the resulting curves from the rheo-electrical measurements. Lowest resistance for the lowest filler content is achieved after dispersion step 3 and 5. For higher filler concentrations the resistance does not significantly change anymore by further dispersion after dispersion step 3.

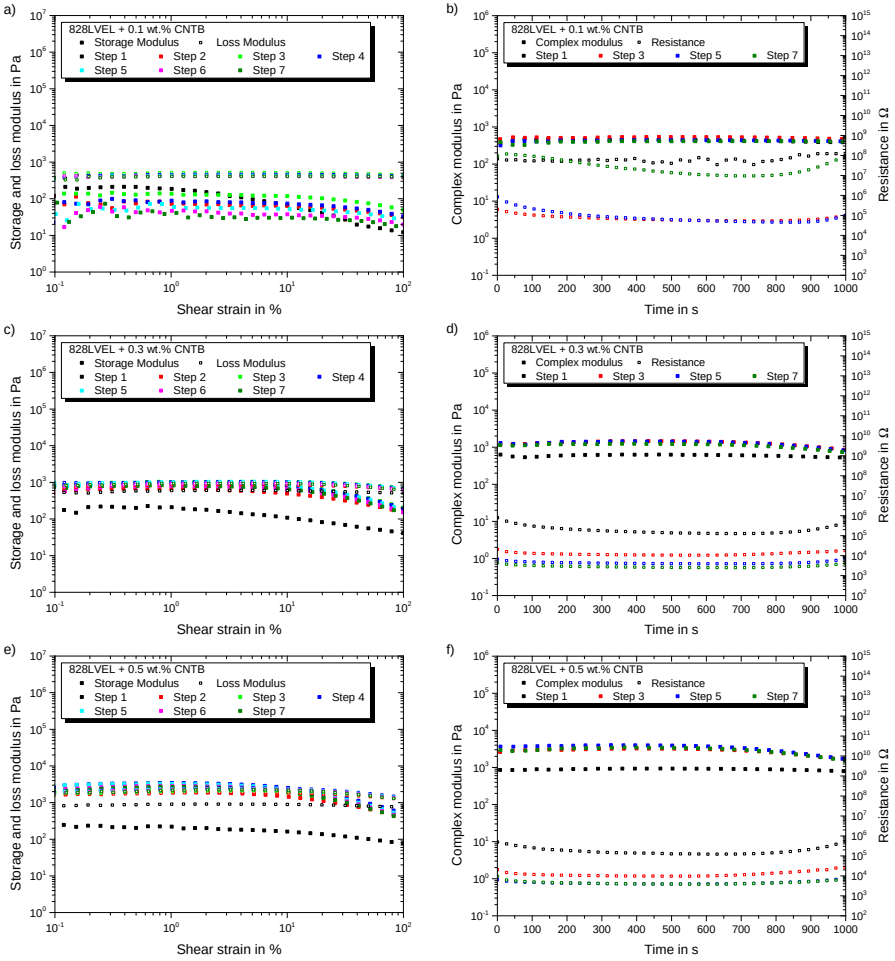


Figure 6.42: MWCNT CNTB dispersed in 828LVEL: storage and loss modulus for (**a**) 0.1 wt.%, (**c**) 0.3 wt.% and (**e**) 0.5 wt.% filler loading; complex viscosity and resistance over testing time for (**b**) 0.1 wt.%, (**d**) 0.3 wt.% and (**f**) 0.5 wt.% filler loading

6.3.6.3 Future Carbon CNTA

The impact of argon plasma treatment of MWCNT on the dispersion behavior is evaluated by dispersing 0.1 wt.%, 0.3 wt.% and 0.5 wt.% of CNTA MWCNT in Epikote 828LVEL. Figure 6.43 (a) gives the process data of a dispersion process of 0.1 wt.% filler loading. The separation peak disappears after the fourth dispersion step. The time derivative of the line load in the feeding gap is given in Figure 6.43 (b).

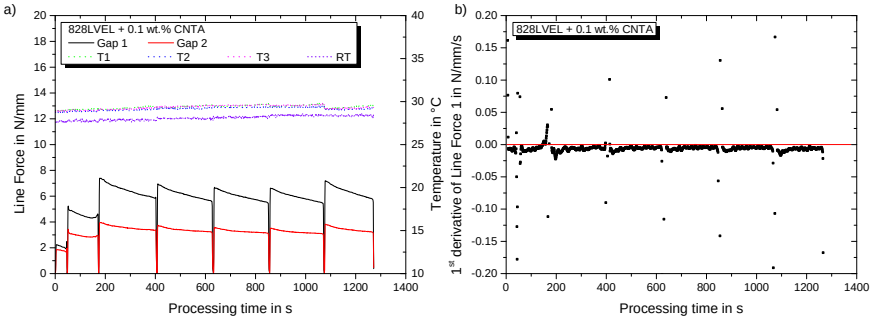


Figure 6.43: CNTA dispersed in 828LVEL: (**a**) line load and temperature development for 0.1 wt.% and (**b**) first derivative of line load in the feeding gap

For this particle type, the minimum processing time occurs for 0.3 wt.% particle loading, refer Figure 6.44 (a). The line loads have an identical value, independent of the filler content. The difference in processing time between 0.3 wt.% and 0.5 wt.% is not high. Figure 6.44 (b) displays the resulting curves acquired by the impedance measurements. They offer comparable characteristics to the ones gathered from the NC7000 and CNTB addition. Lowest resistance occurs in case for 0.1 wt.% filler loading after dispersion step 3. For higher filler loadings the complex impedance does not significantly change further after dispersion step 3 in the low frequency region. At higher frequencies, the complex impedance increases with further dispersion due to more particle separation on micro level. Figure 6.45 (a), (c) and (e) show

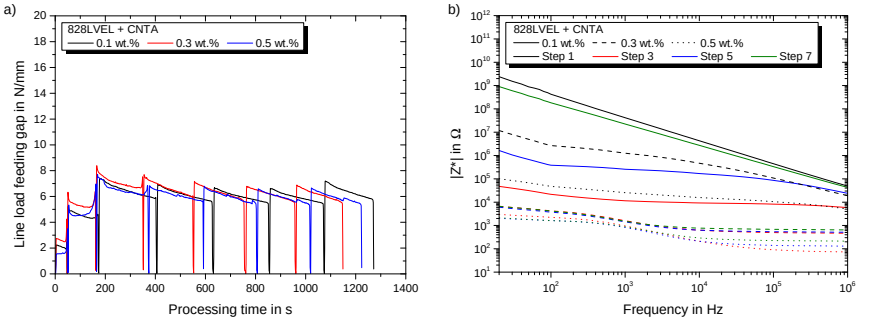


Figure 6.44: CNTA dispersed in 828LVEL: (**a**) line load for 0.1 wt.%, 0.3 wt.% and 0.5 wt.% and (**b**) impedance spectra for different filler contents and dispersion steps

the storage and loss modulus development in strain-sweeps for the investigated filler contents over the dispersion process. The compostite rheologically percolates at a filler loading of 0.3 wt.%. The material behaves like the MWCNT eoxy composites investigated before. Also, the presented rheo-electrical curves

in Figure 6.45 (b), (d) and (g) show no difference to the prior investigated CNTB. A minimum resistance for 0.1 wt.% is achieved after three dispersion steps and for higher filler loadings the resistance does not significantly change by further dispersion after dispersion step 3. Argon plasma funtionalization has no influence on the rheological and electrical properties.

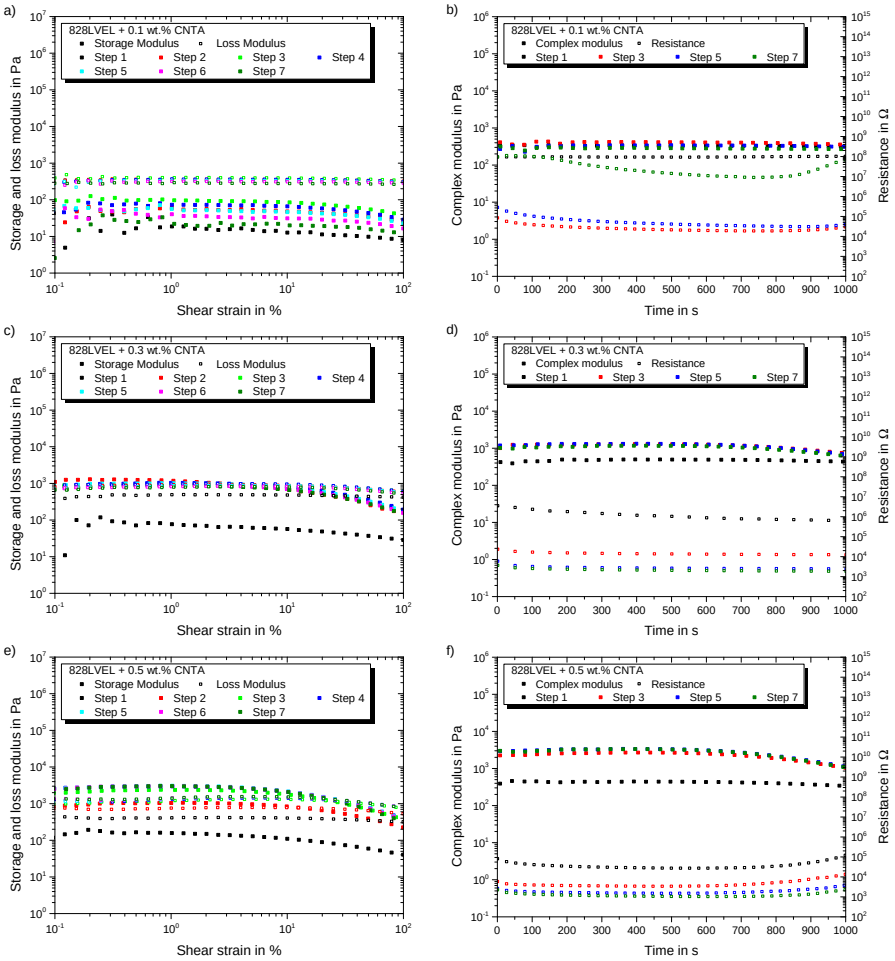


Figure 6.45: MWCNT CNTA dispersed in 828LVEL: storage and loss modulus for (**a**) 0.1 wt.%, (**c**) 0.3 wt.% and (**e**) 0.5 wt.% filler loading; complex viscosity and resistance over testing time for (**b**) 0.1 wt.%, (**d**) 0.3 wt.% and (**f**) 0.5 wt.% filler loading

6.3.6.4 Future Carbon CNTP

The impact of atmospheric plasma treatment of MWCNT on the dispersion behavior is evaluated by dispersing 0.1 wt.%, 0.3 wt.% and 0.5 wt.% of CNTP MWCNT in Epikote 828LVEL. Figure 6.46 (a) gives the process data of a dispersion process of 0.1 wt.% filler loading. The separation peak disappears after the fourth dispersion step. The time derivative of the line load in the feeding gap is given in Figure 6.46 (b).

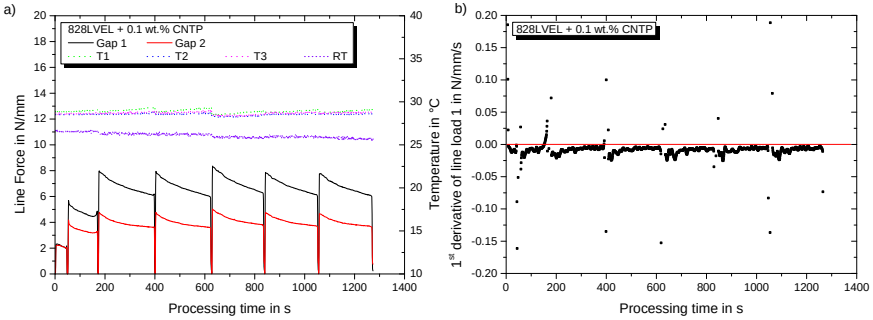


Figure 6.46: CNTP dispersed in 828LVEL: (**a**) line load and temperature development for 0.1 wt.% and (**b**) first derivative of line load in the feeding gap

For this particle type, the minimum processing time occurs for 0.5 wt.% particle loading, refer Figure 6.47 (a). In the first dispersion steps, the highest line load occurs for the highest filler content. In the last dispersion steps, the line loads have an identical value, independent of the filler content. Figure 6.47 (b) displays the resulting curves from the impedance measurements. They offer comparable characteristics as the ones gathered from the other MWCNT modifications. Lowest resistance occurs in case for 0.1 wt.% filler loading after dispersion step 3. For higher filler loadings the complex impedance does not significantly change further after dispersion step 3 in the low frequency region. At higher frequencies, the complex impedance increases with further dispersion due to more particle separation on micro level. Figure 6.48 (a), (c) and (e) show the storage and loss modulus development in strain-sweeps for

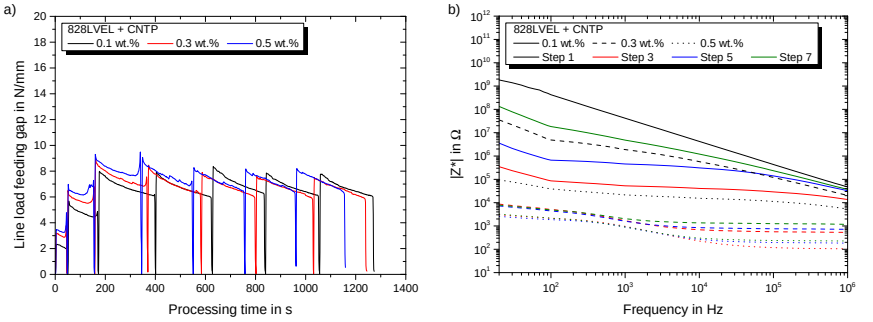


Figure 6.47: CNTP dispersed in 828LVEL: (**a**) line load for 0.1 , 0.3 and 0.5 wt.% and (**b**) impedance spectra for different filler contents and dispersion steps

the investigated filler contents over the dispersion process. The composite rheologically percolates at a

filler loading of 0.3 wt.%, too. The material behaves like the before investigated MWCNT epoxy composites. Also, the presented rheo-electrical curves in Figure 6.45 (b), (d) and (f) show no difference to the prior investigated CNTB and CNTA. A minimum resistance for 0.1 wt.% is achieved after three dispersion steps and for higher filler loadings the resistance does not significantly change by further dispersion after dispersion step 3. Atmospheric plasma funtionalization has no influence on the rheological and electri-

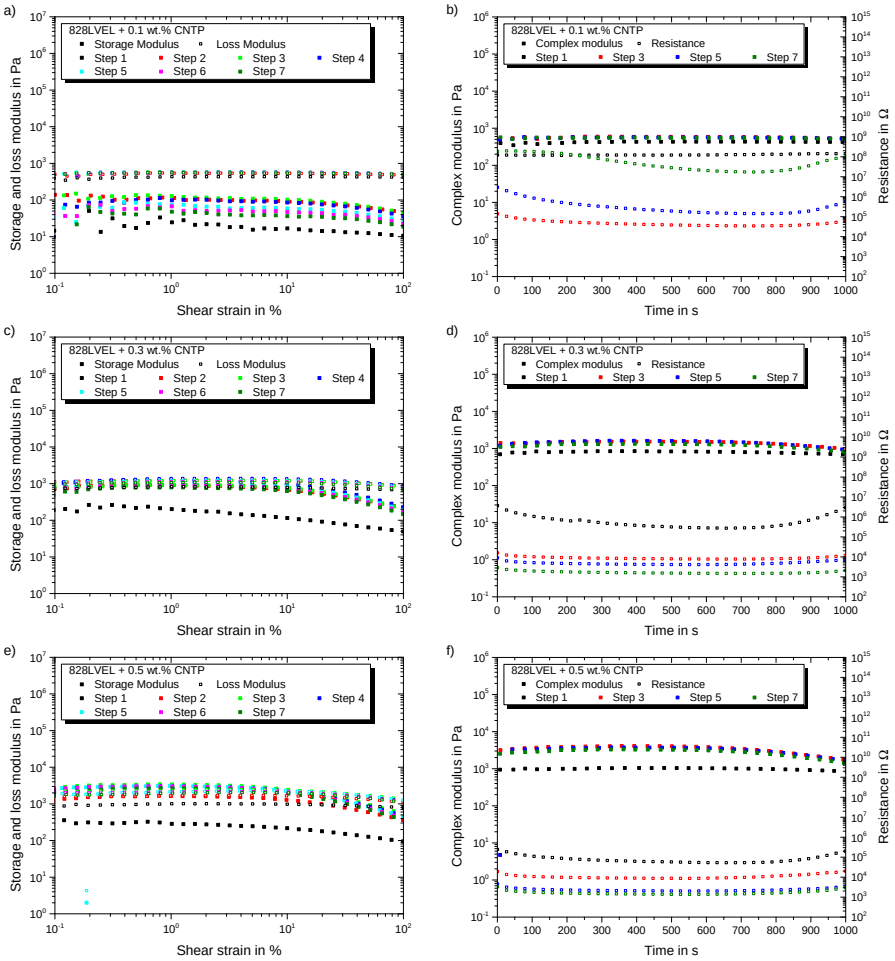


Figure 6.48: MWCNT CNTP dispersed in 828LVEL: storage and loss modulus for (**a**) 0.1 wt.%, (**c**) 0.3 wt.% and (**e**) 0.5 wt.% filler loading; complex viscosity and resistance over testing time for (**b**) 0.1 wt.%, (**d**) 0.3 wt.% and (**f**) 0.5 wt.% filler loading

cal properties. Gojny et al. concluded in their work that the build-up of an electrical conductive carbon nanoparticle network depends on the aspect ratio of the filler, its dispersibility and the ability to agglomerate [152]. Multi-walled carbon nanotubes CNTB, CNTA and CNTP offer the same specific surface area and decomposition behavior in the TGA, compare Figure B.4 in the Appendix B.1.3. Therefore, it can

be concluded that the plasma treatments did not degrade the MWCNT and hence the aspect ratio stays the same. Therefore, the electrical properties, dominated by the tunnel mechanism, remain after plasma treatment. The particle geometry is mainly responsible for rheological percolation, too. Therefore, the rheological properties of the nanocomposites are the same for the CNTB, CNTA and CNTP.

6.3.6.5 Future Carbon CNTN

The impact of elastomeric side chain equipped MWCNT CNTB with amino functionalization on the process data is analyzed by dispersing 0.1 wt.%, 0.5 wt.% and 1 wt.% of CNTN in Epikote 828LVEL, respectively. Figure 6.49 (a) gives the resulting process data from the dispersion of 0.1 wt.%. In contrast to the previous discussed dispersions, this material shows a high variation in the line load signal. This results from the compression of the big elastomeric domains of the functionalized MWCNT during dispersion. The domain size is revealed clearly by the SEM images (refer Figure B.21 Appendix B.1.4). With higher

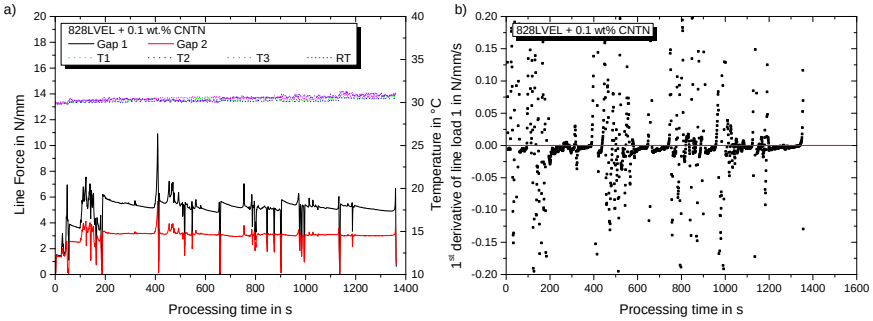


Figure 6.49: CNTN dispersed in 828LVEL: (**a**) line load and temperature development for 0.1 wt.% and (**b**) first derivative of line load in the feeding gap

amount of dispersion steps, the signal becomes more smooth, due to improved homogenization through break-down and improved distribution of the elastomeric domains. The interpretation of the first processing time derivative, given by Figure 6.49 (b), is difficult, caused by the high variations in the line load signal. Figure 6.50 (a) compares the line load responses for the different filler loadings. With increased filler loading, the processing time doubles. Additionally, the variation in the line load signal reaches a level, which makes an interpretation impossible. Resulting impedance spectra, given in Figure 6.50 (b), only show an electrical conductivity after the first dispersion step of 0.5 wt.% and 1 wt.%. With further dispersion, the electrical network does not percolate any more. Figure 6.51 (a), (c) and (e) give the development of storage and loss modulus for the different evaluated filler loadings analyzed in strain-sweeps over the dispersion process. Figure 6.51 (b), (d) and (f) gives the resulting curves from the rheo-electrical characterization. For 0.1 wt.% filler loading the storage modulus is highest after dispersion step 3. The loss modulus does not change over the dispersion process and stays constant in each strain-sweep. The complex modulus and resistance do not change with dispersion, either. For 0.5 wt.% the material is rheologically percolated after dispersion step 1. This is the only state for this filler content, which shows a distinct plateau in storage modulus at low strains and then a decrease of it occurs at higher strains. This indicates the formation of a particle network. The rheo-electrical test confirms this interpretation. At a certain level of strain, the resistance increases, resulting from the break-down of the particle network. Surprisingly, for 1 wt.% no rheological percolation can be observed. Further more, none of the dispersion states offer a particle network to break-down. The elastomeric side chains prevent particles from agglomerating and

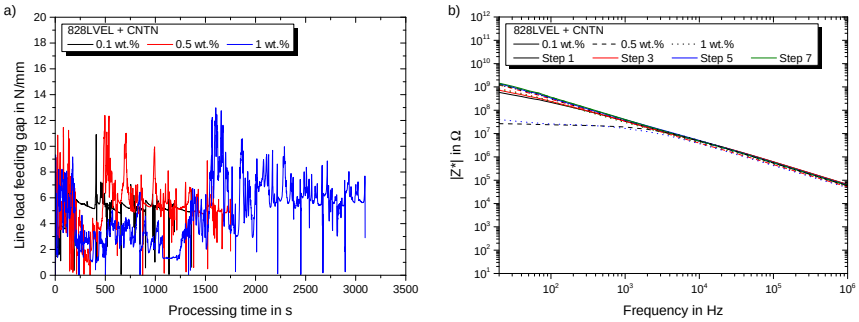


Figure 6.50: CNTN dispersed in 828LVEL: (**a**) line load for 0.1 wt.%, 0.5 wt.% and 1 wt.% and (**b**) impedance spectra for different filler contents and dispersion steps

building up a network. Summarizing, the dispersion of this particle type via three roll mill seems to be not the best technique. The elastomeric domain size is too large and thus, they are rather compressed than sheared during dispersion. The broken down elastomeric domains still cover the CNT due to their covalent bond and prevent the reduction of tunnel resistance.

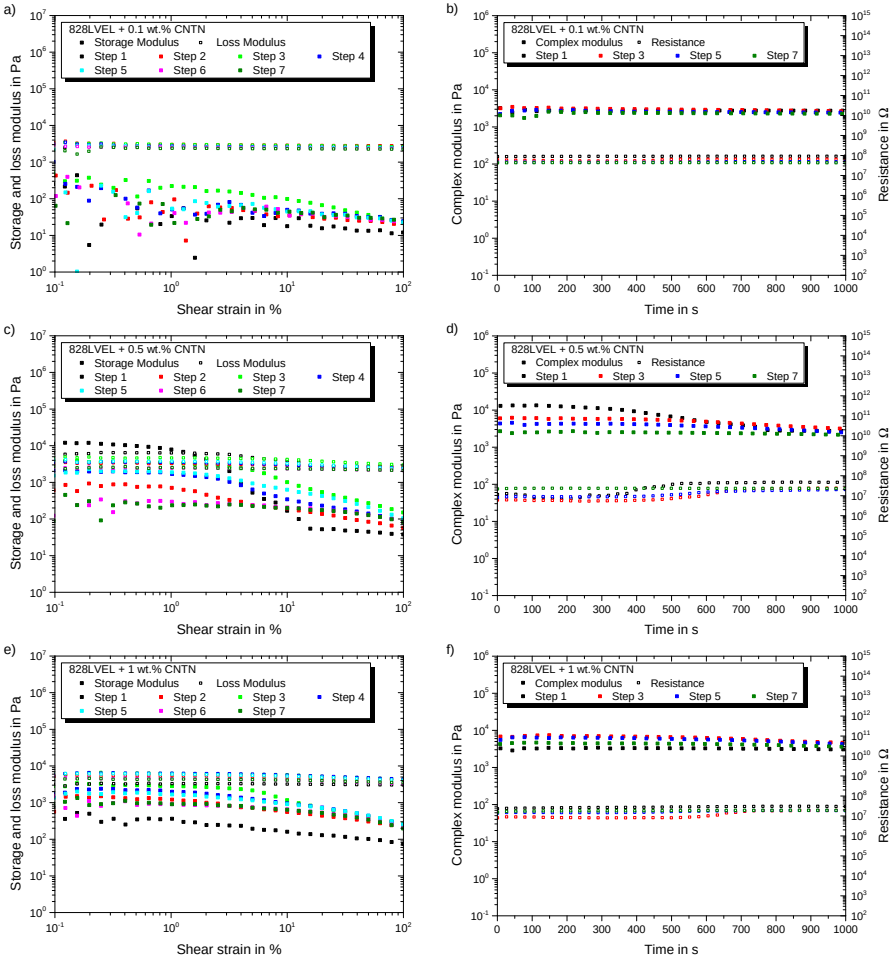


Figure 6.51: MWCNT CNTP dispersed in 828LVEL: storage and loss modulus for (**a**) 0.1 wt.%, (**c**) 0.5 wt.% and (**e**) 1 wt.% filler loading; complex viscosity and resistance over testing time for (**b**) 0.1 wt.%, (**d**) 0.5 wt.% and (**f**) 1 wt.% filler loading

6.3.7 Dispersion of Planar Particles

6.3.7.1 Few-Layered Graphene - Avanzare Innovación Tecnológica Avan2

The impact of planar particles on the process is analyzed by dispersing 0.5 wt.%, 1 wt.% and 2 wt.% of FLG in Epikote 828LVEL. A filler content beyond 2 wt.% could not be processed, because the resin did not wet the particles any more and the became much too dry. Figure 6.52 (a) shows the line load data for the lowest concentration of FLG. After the seventh step of the dispersion process the separation peak still exists. This is also revealed by the first derivative of the line load, compare Figure 6.52 (b).

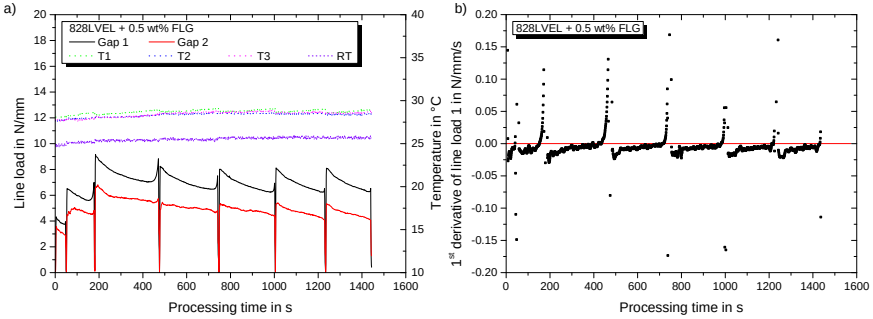


Figure 6.52: Few-layered Graphene dispersed in 828LVEL: (**a**) line load and temperature development for 0.5 wt.% and (**b**) first derivative of line load in the feeding gap

Figure 6.53 (a) compares the line load data for increasing filler loadings. The separation peak vanishes for 2 wt.% after dispersion step 7. With increasing filler content the processing time shortens. The impedance spectra given in Figure 6.53 (b) reveal a completely different mechanism for this particle type. For all filler concentrations, the capacitive contribution becomes more pronounced by further dispersion. A filler content of 0.5 wt.% does not lead to a conductive network at any point. Increasing the filler content to 1 wt.% the composite starts to exhibit a low conductive network, which becomes purely capacitive after dispersion. A plateau in the low frequency as well as high frequency region exists for 2 wt.% of FLG in epoxy in the initial state. As already mentioned, the lower plateau stands for a conductive micro network and vanishes by dispersion. The low frequency plateau shifts to much higher impedance values over the processing time. This observation leads to the conclusion that a mechanical exfoliation of the graphene sheets takes place. Mechanical exfoliation of graphene via TRM is well described in publications of Li et al., Chen et al. and Kernin et al. [231, 409–411]. Even the laminar flows within the TRM are sufficient to achieve exfoliation [412].

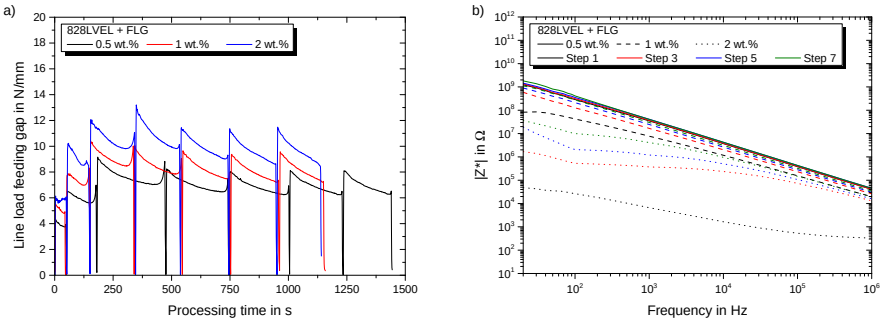


Figure 6.53: Few-layered Graphene dispersed in 828LVEL: (**a**) line load for 0.5 wt.%, 1 wt.% and 2 wt.%, (**b**) impedance spectra for different filler contents and dispersion steps

Li et al. give in their publication a fomular to estimate the number of cycles required for optimal exfoliation of graphite [413]. They assumed that one dispersion cycle cuts the graphite stacks in half. The required amount of cycles o can be calculated as follows:

$$s_\infty = k \cdot \frac{1}{2}^{2o} \cdot s_0 \tag{6.12}$$

s_0 denotes the initial graphite stack thickness, s_∞ denotes the final thickness and k is a factor between 5 and 10. The 2 in the exponent results from the two gaps of the three roll mill. In this study, the first gap is utilized as film forming gap, therefore the 2 in the exponent decreases to 1 dispersion gap.

$$s_\infty = k \cdot \frac{1}{2}^{o} \cdot s_0 \tag{6.13}$$

In the equation, the thicknesses can be substituted by the number of layers. This would result in six dispersion steps in case of FLG, offering 10 layers in the initial state. This is in good accordance to the presented results, whereby, the first two cycles, offering a large gap spacing, are only for purpose of homogenization. Figure 6.54 (a), (c) and (e) give the strain dependency of storage and loss modulus after each dispersion step for all evaluated filler loadings, respectively. Rheo-electrical characterization, shown in Figure 6.54 (b), (d) and (f), reveal the condition of the particle network. With further dispersion the storage modulus of the material decreases. Increased filler content leads to the formation of the characteristic plateau with shear-thinning. Also, the complex modulus decreases with increased amount of dispersion steps for all filler contents. The electrical resistance is not affected by dispersion for 0.5 wt.% and 1 wt.%. Even with 2 wt.% filler loading a rheological percolation is not achieved. The resistance of the material increases for this filler loading with the amount of dispersion steps. The rheo-electrical characterization reveals a break-down of the network with increasing strain amplitude. The shear-thinning runs into a plateau and the electrical resistance shows a plateau at high strains. High strains lead to a rebuild-up of the particle network.

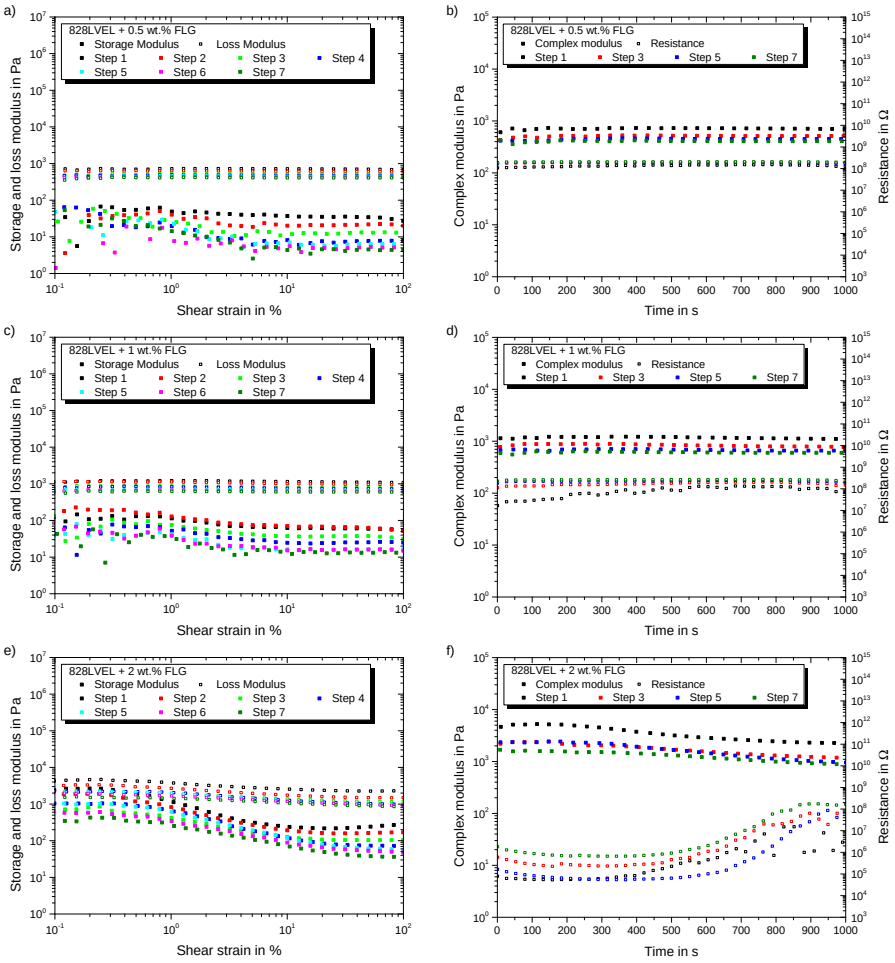


Figure 6.54: Few-layered Graphene dispersed in 828LVEL: storage and loss modulus for (**a**) 0.5 wt.%, (**c**) 1 wt.% and (**e**) 2 wt.% filler loading; complex viscosity and resistance over testing time for (**b**) 0.5 wt.%, (**d**) 1 wt.% and (**f**) 2 wt.% filler loading

6.3.7.2 Electro-Chemically Expanded Graphite

The influence of electro-chemically expanded graphite stabilized in ethanol in comparison to FLG is analyzed by dispersion of 1 wt.%, 2 wt.% and 3 wt.% of it in Epikote 828LVEL. First of all, it has to be stated that high filler contents as 3 wt.% were dispersible without complications due to the pre-wetting with ethanol. The ethanol lowers the viscosity of the composite significantly. Figure 6.55 (a) shows the line load data over process time for 1 wt.% filler content. The material was processed until no more separation occurred, compare Figure 6.55 (b). This took two homogenization and 8 dispersion steps. The calculation according to Equation 6.13 gives these 8 required cycles. Additional steps were performed at a

gap spacings of 13 µm and 5 µm, respectively. The line load rises from nearly 0 N/mm to 8 N/mm from step to step. This is due to the evaporation of the ethanol on the enormous surface area of the tempered rollers and improved dispersion. The presented DSC curves in the next section show the complete evaporation of the ethanol over the dispersion process, refer Figure 6.60 (b).

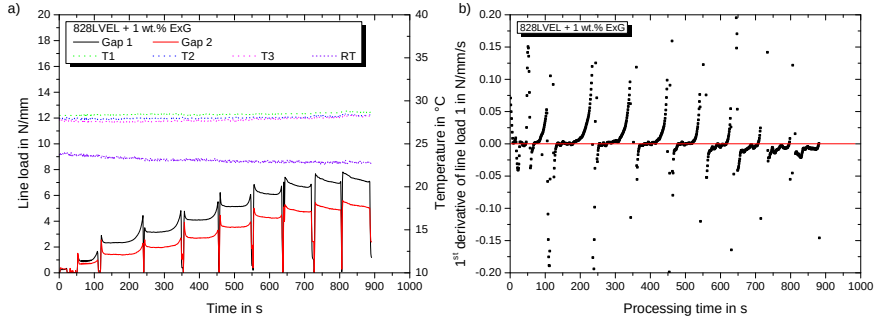


Figure 6.55: Exfoliated Graphene dispersed in 828LVEL: (**a**) line load and temperature development for 1 wt.% and (**b**) first derivative of line load in the feeding gap

The influence of filler content on line load is shown in Figure 6.56 (a). An increase of filler content accompanies with longer processing times. This is visible in the first two dispersion steps. For the 1 wt.% many separation peaks occur during processing. This attributes to non-continuous material feeding.

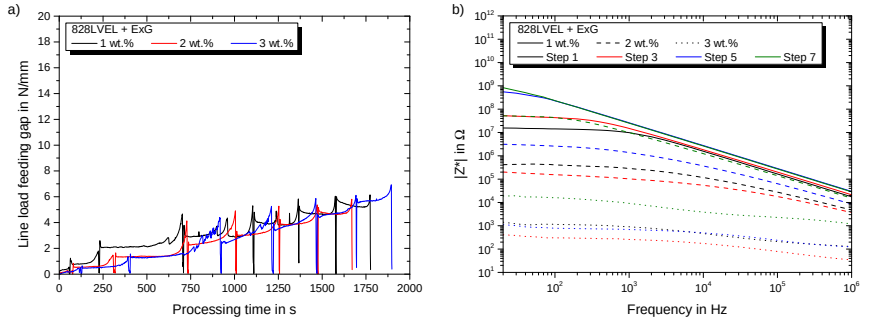


Figure 6.56: Exfoliated Graphene dispersed in 828LVEL: (**a**) line load for 1 wt.%, 2 wt.% and 3 wt.% and (**b**) impedance spectra for different filler contents and dispersion steps

Figure 6.56 (b) gives the impedance spectra for the dispersed filler contents. The composite with 1 wt.% starts with a low conductive filler network, which vanishes over the dispersion process. This correlates with the results from FLG, allowing the conclusion that mechanical exfoliation leads to this behavior. For 2 wt.% and 3 wt.% the impedance in the low frequency regime decreases from step 1 to step 2. This results from the volume loss due to evaporating ethanol. After step 3 the low frequency impedance increases, but the plateau does not vanish. A slightly formed conductive particle network still exists. Dispersion processes of the same material configuration result in the same filler network structure for this material, too. Impedance spectra for 1 wt.% processes, shown in Figure 6.57, demonstrate the high reproducibility of the process.

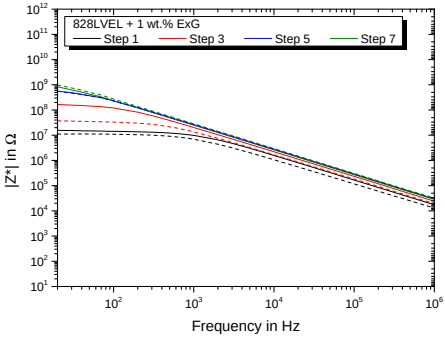


Figure 6.57: Comparison of two dispersion processes with 1 wt.% ExG in Epikote 828LVEL

Figure 6.58 (a), (c), (e) and (g) give the strain dependency of storage and loss modulus after each dispersion step for all evaluated filler loadings, respectively. Rheo-electrical characterizations, shown in Figure 6.58 (b), (d), (f) and (h), reveal the condition of the particle network. Figure 6.58 (a) and (c) give the resulting strain-sweeps for two 1 wt.% filler loading dispersion processes. Both show the same characteristics. Storage and loss modulus increase with increasing amount of dispersion steps. This results by the evaporation of the ethanol. The difference between the last two steps is marginal, revealing a full evaporation of the ethanol. Figure 6.58 (b) and (d) reveal that the complex modulus increases with increased amount of dispersion steps. The resistance increases as well with increasing amount of dispersion steps. Increase in complex modulus results from evaporating ethanol and increase in resistance from the ongoing exfoliation of the electro-chemically expanded graphite. The three roll milling process offers a high reproducibility even in the rheological and DC properties. For increasing filler content results in a more pronounced development of the plateau with following shear-thinning. A rheological percolation is achieved by 3 wt.% filler addition. The complex modulus does not further increase after dispersion step 3. A distinct break-down of the particle network can be only observed after the seventh dispersion step with 3 wt.% filler content. For this particle type the resistance as well as the complex modulus reach a plateau at high strain amplitudes. This reveals an additional build-up of the particle network.

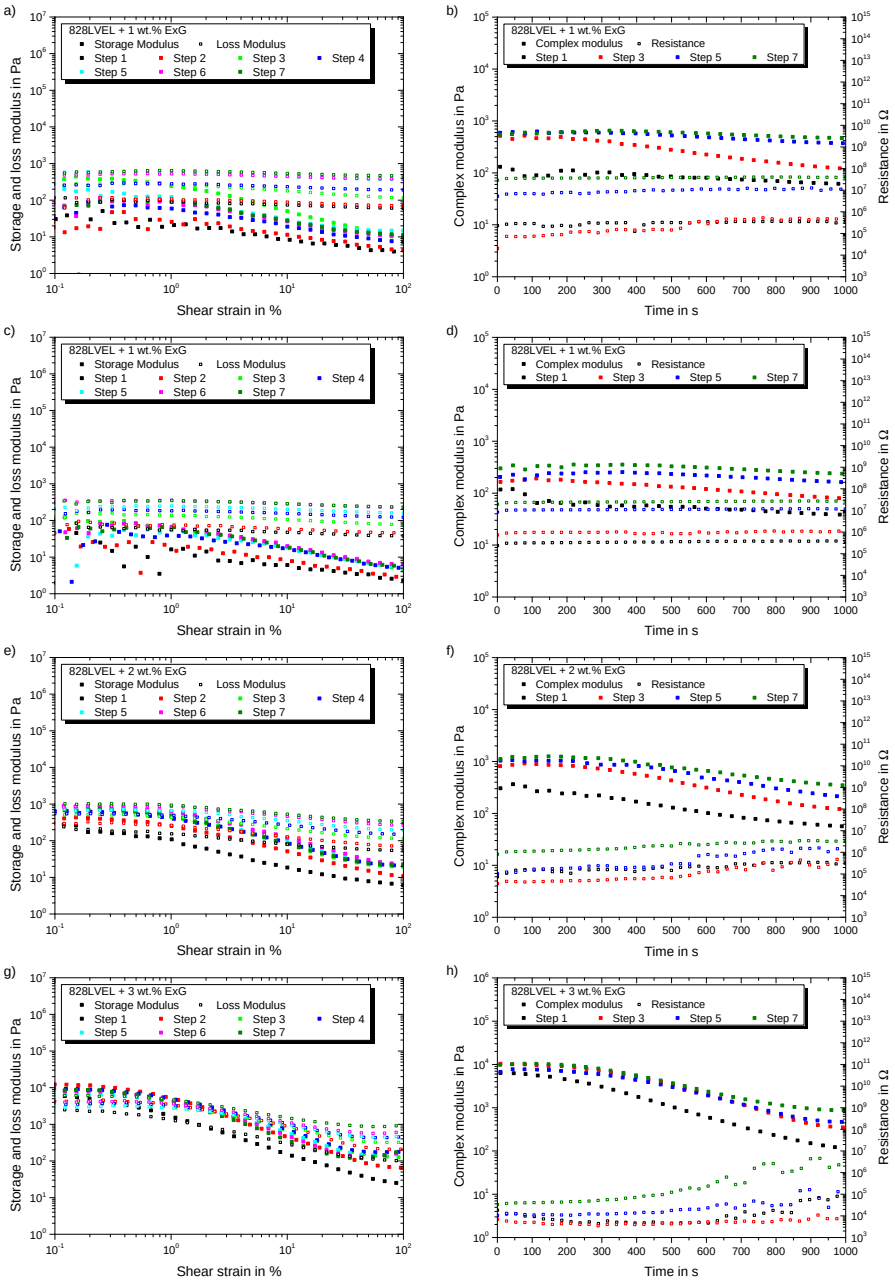


Figure 6.58: ExG dispersed in 828LVEL: storage and loss modulus for (**a**), (**c**) 1 wt.%, (**e**) 2 wt.% and (**g**) 3 wt.% filler loading; complex viscosity and resistance over testing time for (**b**) and (**d**) 1 wt.%, (**f**) 2 wt.% and (**h**) 3 wt.% filler loading

6.3.7.3 Functionalized Electro-Chemically Expanded Graphite

The impact of functionalization of electro-chemically expanded graphite stabilized in ethanol in comparison to conventional ExG on the dispersion process is analyzed by dispersing 1 wt.%, 2 wt.% and 3 wt.% of it in Epikote 828LVEL. Figure 6.59 (a) gives the line load data for an 11 step dispersion process of 1 wt.% filler loading. The dispersion curves show the same characteristics as the dispersion of ExG. Ethanol evaporates and increases the viscosity. For this material two homogenization and 8 dispersion steps are necessary for best homogenization. Calculations according to Equation 6.13 result in 8 required dispersion steps, too. Although the amount of layers is higher for fExG compared to ExG, the amount of dispersion steps practically is even the same. This may attribute to the functionalization and therefore eased separation behavior. The corresponding derivative of the line load is shown in Figure 6.59 (b). Impedance spectra, displayed in Figure 6.60 (a), show a continuous increase of low frequency impedance for all filler concentrations. For 1 wt.% the conductive network vanishes. It remains for higher filler concentrations after dispersion. This material results in higher capacitive nature compared to ExG. This indicates improved dispersion and wetting behavior. Summarizing, all investigated planar particles (FLG, ExG and fExG) show predominating mechanical exfoliation.

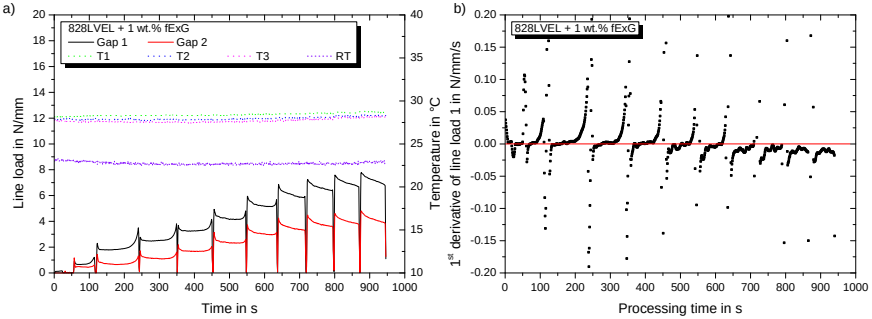


Figure 6.59: Functionalized Exfoliated Graphene dispersed in 828LVEL: (**a**) line load and temperature development for 1 wt.% and (**b**) first derivative of line load in the feeding gap

Figure 6.60 (b) gives the DSC curves for liquid modified resins. All resins show no endothermic evapora-

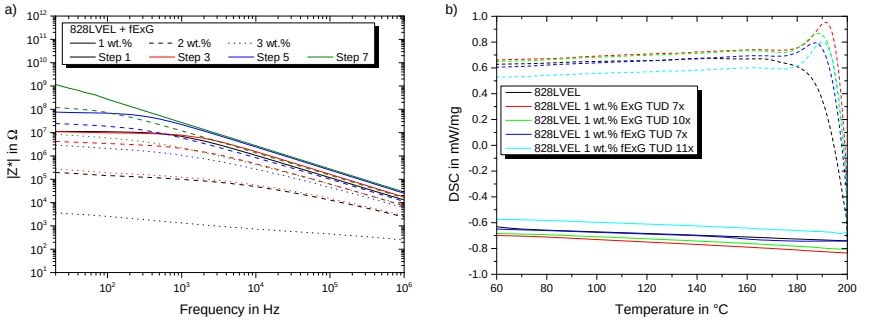


Figure 6.60: Functionalized Exfoliated Graphene dispersed in 828LVEL: (a) impedance spectra and (**b**) DSC curves for cured Epikote 828LVEL with 1 wt.% ExG and fExG modification after curing

tion peak. This should be at 78 °C, which is the boiling point of ethanol. Three roll milling leads to full evaporation of the ethanol. A special post treatment for this particle type is not necessary. Figure 6.61 (a), (c) and (e) give the strain dependency of storage and loss modulus after each dispersion step for all evaluated filler loadings, respectively. Rheo-electrical characterization, shown in Figure 6.61 (b), (d) and (f), reveals the condition of the particle network. For 1 wt.% the loss modulus increases with increasing amounts of dispersion steps. This again contributes to the evaporation of the ethanol. The complex modulus and the electrical resistance increase with increasing amount of dispersion steps, resulting from ongoing exfoliation of the graphene sheets. This material rheologically percolates at a filler loading of 2 wt.%. Increased filler loadings show a distinct plateau in the rheological properties with following shear-thinning. Even for the highest filler loading the resistance does not change due to increased applied strain.

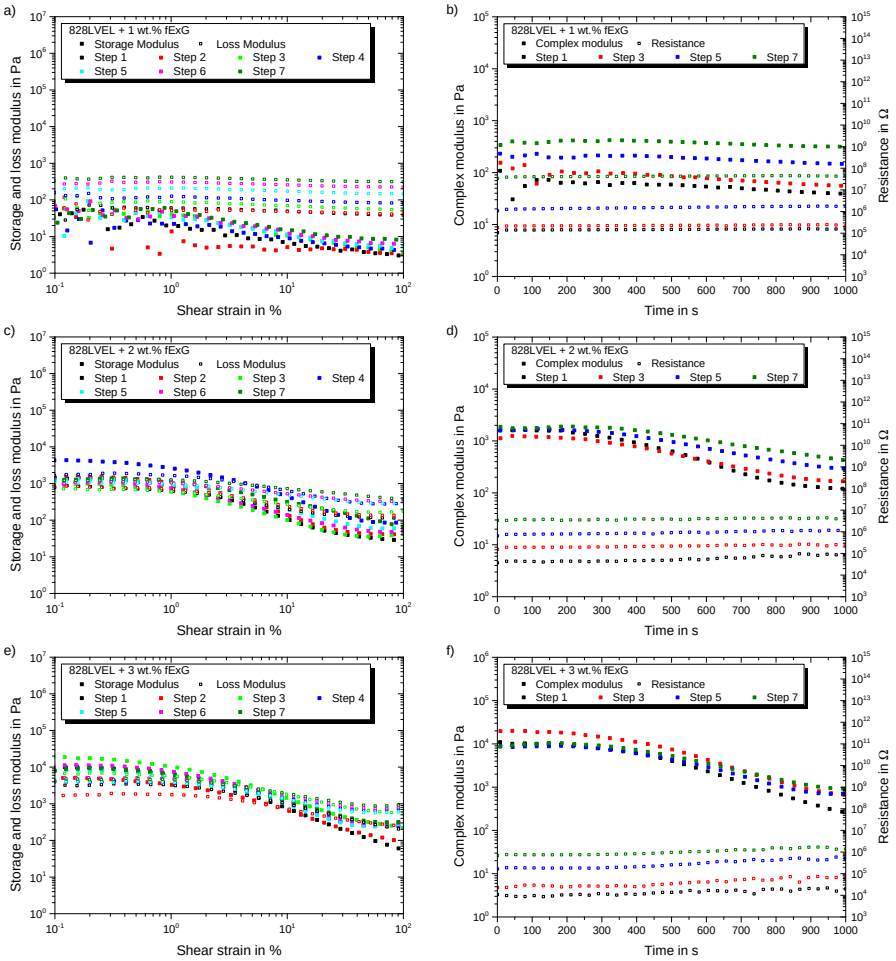


Figure 6.61: fExG dispersed in 828LVEL: storage and loss modulus for (**a**) 1 wt.%, (**c**) 2 wt.% and (**e**) 3 wt.% filler loading; complex viscosity and resistance over testing time for (**b**) 1 wt.%, (**d**) 2 wt.% and (**f**) 3 wt.% filler loading

6.3.8 Dispersion of Single-Walled Carbon Nanotubes

6.3.8.1 OCSiAl Tuball 75

The impact of flexible cylindrical particles is analyzed by dispersing 0.01 wt.%, 0.05 wt.%, 0.1 wt.% and 0.5 wt.% of Tuball 75 SWCNT in Epikote 828LVEL. For 0.01 wt.% filler concentration the separation peak vanishes after dispersion step 6, compare Figure 6.62 (a). This can be clearly seen by the first processing time derivative of the line load in the feeding gap, given by Figure 6.62 (b). For 0.05 wt.% the separation

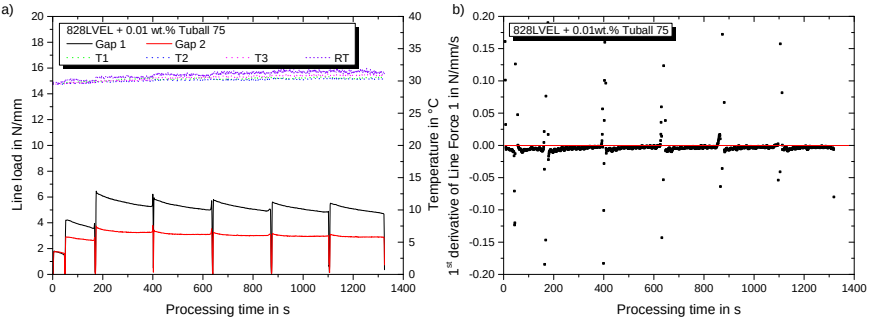


Figure 6.62: Tuball 75 dispersed in 828LVEL: (**a**) line load and temperature development for 0.01 wt.% and (**b**) first derivative of line load in the feeding gap

peak is more pronounced and does not vanish (compare Figure 6.63 (a)). It remains even after seven dispersion steps. A further increase of filler loading by one order of magnitude to 0.5 wt.% results in even more pronounced separation in the first dispersion steps. The line loads of the last dispersion steps look similar in the last steps for filler contents above 0.05 wt.%. A filler content increase does not affect the processing time, although it leads to an increase in line load. Figure 6.63 (b) gives an overview of the resulting impedance spectra. For all filler loadings, the complex impedance at low frequencies decreases by further dispersion. For filler contents above 0.05 wt.% the low frequency complex impedance does not change significantly for more than three dispersion steps. Only at comparable high filler loading of 0.5 wt.% a change of the micro network can be observed at high frequencies. The difference of this particle

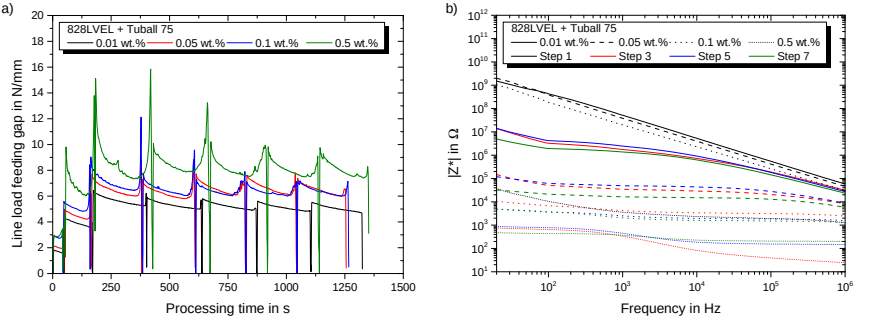


Figure 6.63: Tuball 75 dispersed in 828LVEL: (**a**) line load for 0.01 wt.%, 0.05 wt.%, 0.1 wt.% and 0.5 wt.% and (**b**) impedance spectra for different filler contents and dispersion steps

type compared to the others lays in their microstructure. SEM image, shown in Figure 6.64, reveals a highly

entangled and bundled structure of the flexible SWCNT. This explains the high tendency for separation of matrix and filler, because the material is difficult to homogenize. This benefits the build-up of an electrical conductive network and explains their low percolation threshold. This phenomenon was also observed by Yoon et al. [174] and Leopold et al. [414]. An optimization of the dispersion process for this particle type is only possible by utilizing additional impedance spectroscopy measurements. With regard to electrical properties, no significant change is given after maximum five dispersion steps. Figure 6.65 (a), (c), (e), and (g) give the strain dependency of storage and loss modulus after each dispersion step for all evaluated filler loadings, respectively. Rheo-electrical characterization, shown in Figure 6.65 (b), (d), (f) and (h), reveals the condition of the particle network. Beginning with 0.01wt.%, the storage modulus increases after each dispersion step, revealing a more rigid network by pronounced particle separation, leading to more particle-particle interaction. The loss modulus is not affected by dispersion. Furthermore, the storage modulus is not affected by the increasing shear strain. For all dispersion states, the complex modulus stays constant with increasing strain, too. The material's electrical resistance after dispersion step 1 is constant independent of applied strain and with increasing dispersion an initial decrease can be observed. The particle network tightens due to the applied strain and the particles come closer. A break-down at high shear strains does not occur. Lowest resistance correlates with highest storage modulus and results from maximum amount of dispersion steps. With increasing filler concentration the characteristic plateau with

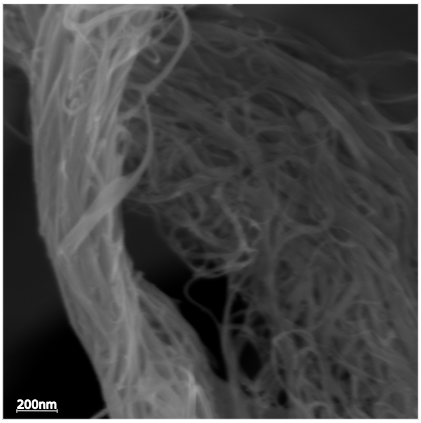


Figure 6.64: Scanning electron microscopy of Tuball 75 SWCNT

following decrease of storage modulus develops. The storage modulus increases and electrical resistance decreases for all filler loadings with increasing amount of dispersion steps. Rheological percolation results from 0.5 wt.% filler loading. Surprisingly, a break-down of the particle network, induced by applied strain amplitude, does not occur, although the material shows a distinct shear-thinning behavior. The flexible SWCNT bundles spread through the material and build a highly entangled and uniform network, which does not consist of single agglomerates.

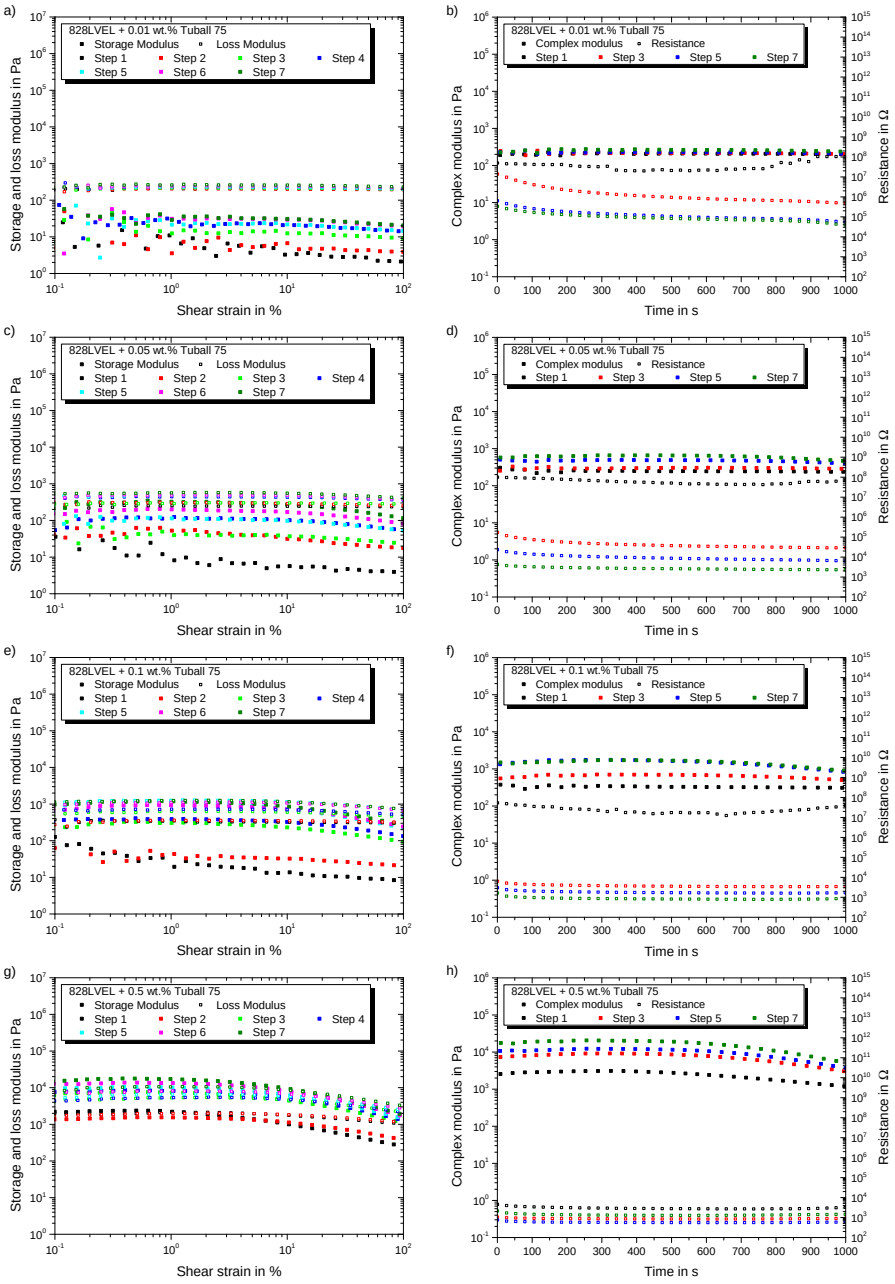


Figure 6.65: Tuball 75 dispersed in 828LVEL: storage and loss modulus for (**a**) 0.01 wt.%, (**c**) 0.05 wt.%, (**e**) 0.1 wt.% and (**g**) 0.5 wt.% filler loading; complex viscosity and resistance over testing time for (**b**) 0.01 wt.%, (**d**) 0.05 wt.%, (**f**) 0.1 wt.% and (**h**) 0.5 wt.% filler loading

6.3.8.2 OCSiAl Tuball purified

Dispersion of the purified Tuball SWCNT in Epikote 828LVEL gives the impact of higher SWCNT content (less impurities at the same weight) carbon nanoparticles on the dispersion behavior. Filler loadings of 0.01 wt.%, 0.05 wt.% and 0.1 wt.% were dispersed. In contrast to Tuball 75, this SWCNT type offers lower metallic impurity content, realized by acid treatment, and higher graphitization, resulting from an annealing process at elevated temperatures in inert atmosphere. Figure 6.66 (a) gives the process data from the dispersion process of 0.01 wt.%. The separation peak vanishes after the third step of the process. This is clearly revealed by the first processing time derivative of the line load in the feeding gap. The purification reduces the processing time.

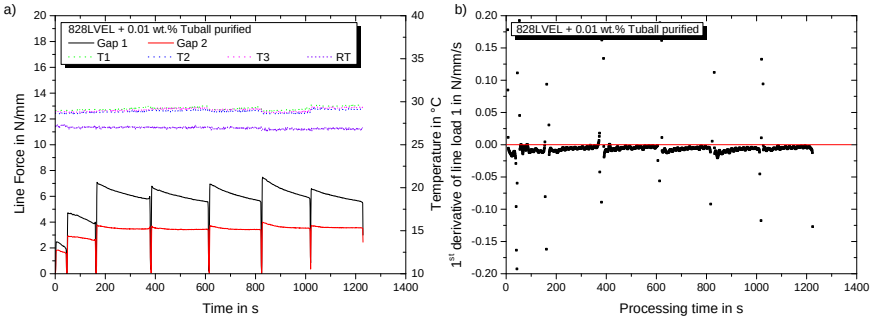


Figure 6.66: Tuball purified dispersed in 828LVEL: (**a**) line load and temperature development for 0.01 wt.% and (**b**) first derivative of line load in the feeding gap

Figure 6.67 (a) gives the comparison of the line loads during dispersion for all evaluated filler contents. Surprisingly, the filler content does not affect the processing time and the height of the line load. With increasing filler content the separation peak remains even after seven dispersion steps. Figure 6.67 (b) gives the impedance spectra for the different dispersion states. For 0.01 wt.% the lowest resistance occurs after dispersion step 5. For higher filler loadings the dispersion state does not change anymore after dispersion step 5 on macro scale. The micro dispersion improves by further dispersion. Figure 6.68 (a), (c) and (e)

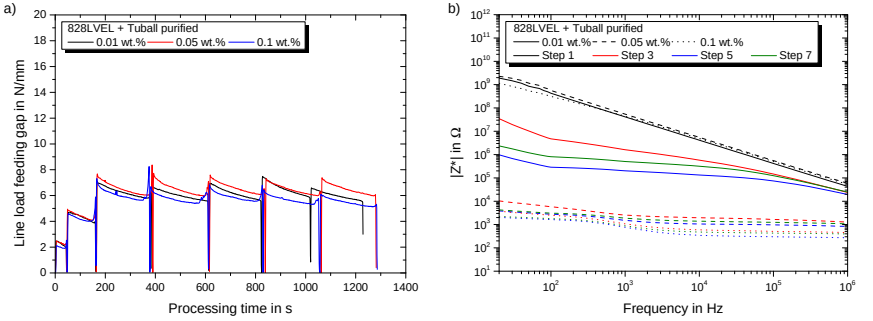


Figure 6.67: Tuball purified dispersed in 828LVEL: (**a**) line load for 0.01 wt.%, 0.05 wt.% and 0.1 wt.% and (**b**) impedance spectra for different filler contents and dispersion steps

give the strain dependency of storage and loss modulus after each dispersion step for all evaluated filler

loadings, respectively. Rheo-electrical characterization, shown in Figure 6.68 (b), (d) and (f), reveals the condition of the particle network. The curves are similar to the ones gathered for the as produced SWCNT. For 0.01 wt.% the storage modulus increases with amount of dispersion steps. The loss modulus is not affected by dispersion. Highest storage modulus corresponds to the lowest resistance. This contributes to the distinct formed particle network. With increasing filler loading highest storage modulus results from maximum dispersion steps, which leads to lowest resistance. Shear-thinning is more pronounced for higher filler loadings, but a break-down of particle network, which results in increased resistance, cannot be observed. In comparison, the purification leads to an easier dispersion of the particles.

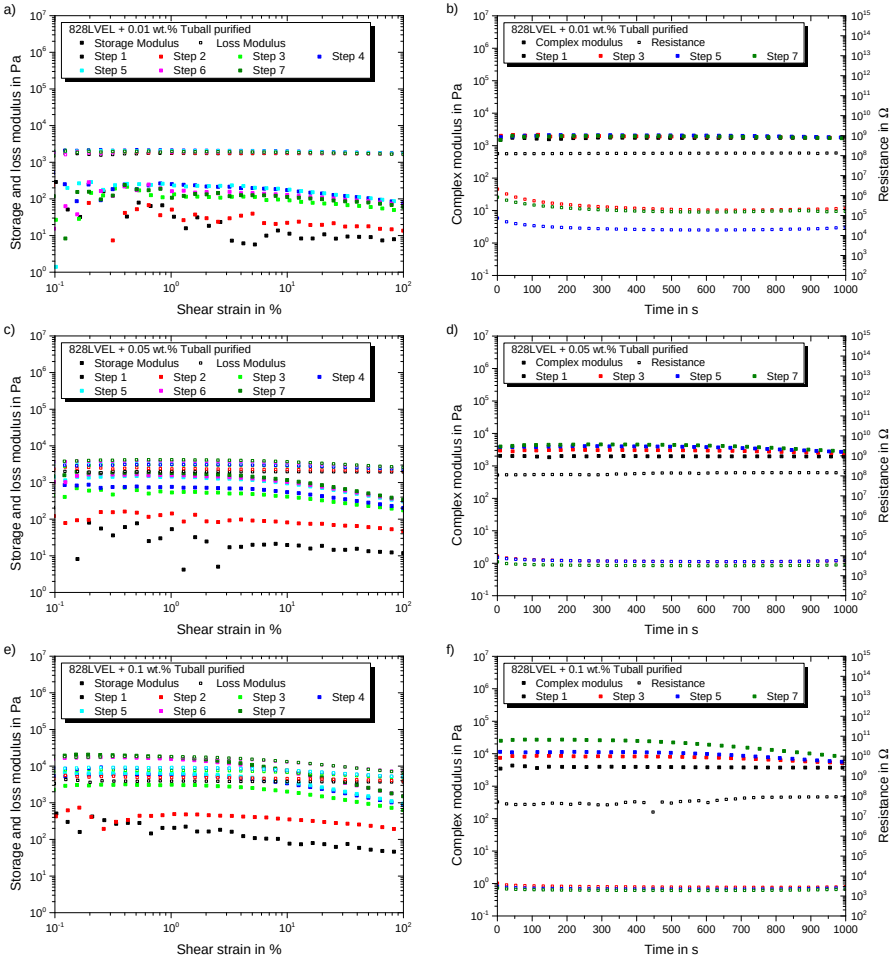


Figure 6.68: Tuball purified dispersed in 828LVEL: storage and loss modulus for (**a**) 0.01 wt.%, (**c**) 0.05 wt.% and (**e**) 0.1 wt.% filler loading; complex viscosity and resistance over testing time for (**b**) 0.01 wt.%, (**d**) 0.05 wt.% and (**f**) 0.1 wt.% filler loading

6.4 Optimization of Heat Dissipation

The original material of the rollers, namely steel, offers a thermal conductivity of 10 $W\,m^{-1}\,K^{-1}$ to 73 $W\,m^{-1}\,K^{-1}$ [415]. For all shown dispersion processes the thermo fluid within the rollers kept its temperature constant although the material was heated over 10 °C. This contributes to a bad heat transfer between the material and the rollers. The heat is not transferred into the thermo fluid. To address this issue, a set of silicon carbide (SiC) rollers was installed on the three roll mill 80E-Plus^{+} and 1 wt.% MWCNT NC7000

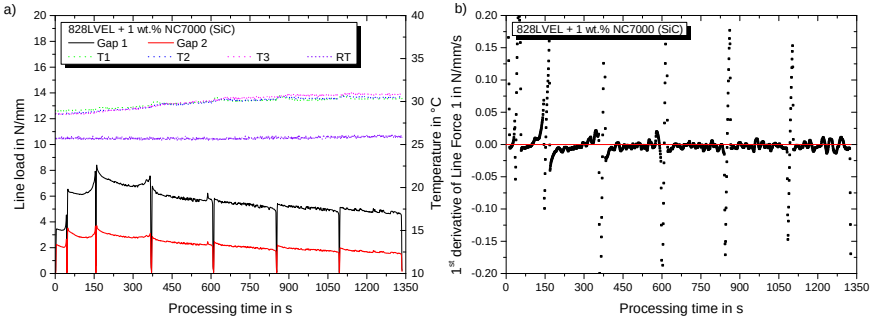


Figure 6.69: NC7000 dispersed in 828LVEL with SiC rollers: (**a**) line load and temperature development for 1 wt.% and (**b**) first derivative of line load in the feeding gap

were dispersed in Epikot 828LVEL. Figure 6.69 (a) gives the recorded data for this dispersion process. The process time is 50 s shorter compared to the same process performed on the same machine with steel rollers. Furthermore, a clear increase of the temperature of the thermo fluid occurs. SiC offers a thermal

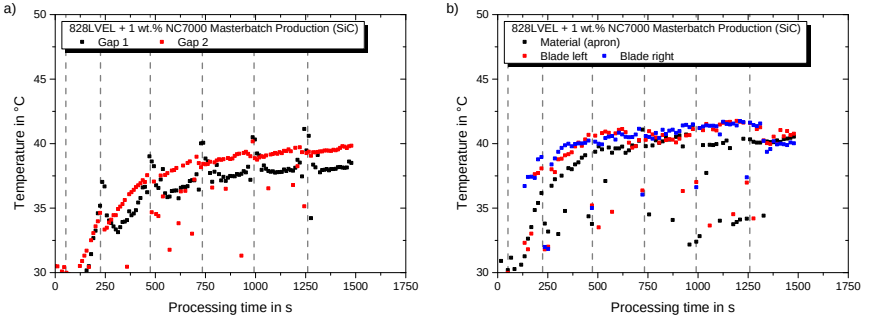


Figure 6.70: Temperature development of dispersion process with 1 wt.% NC7000 in Epikote 828LVEL with SiC rollers: (**a**) material in feeding and dispersion gap and (**b**) material at apron blade and the blade itself

conductivity of 120 $W\,m^{-1}\,K^{-1}$ [416]. This enables the dissipation of generated heat through the rollers into the thermo-fluid. Figure 6.69 (b) gives the first process time derivative of the line load in the feeding gap. The separation peak vanishes after four dispersion steps. Figure 6.70 (a) gives the temperature development of the material in the feeding and dispersion gap over the whole dispersion process. The temperature does not increase as much as for the same process conducted with steel rollers, compare Figure 6.31. Also, the heat generation at the apron blade is lower, compare Figure 6.70 (b). Improved heat dissipation by SiC rollers leads to lower temperatures within the material, resulting in a lower viscosity of the neat resin. This

enhances the cohesion of the resin and the material drag-in is promoted. Therefore, the processing time is reduced.

Summarizing, higher viscous matrices are favorable to reduce processing time. Surprisingly, a viscosity increase, due to increase of particle loading, does not significantly affect processing time. This offers high potential for the design of efficient dispersion processes. The TRM dispersion process is highly reproducible independent of the used machine size. Reproducible dispersion qualities can be obtained with all used particle types. Continuous negative first processing time derivative of the line load indicates the homogeneity of the dispersion. Combination of line load evaluation with impedance spectroscopy leads to very precise knowledge of dispersion state. Mild energy input through three roll mills is sufficient to spread tightly entangled SWCNT bundles to a highly conductive electrical network. Evaluated SWCNT show no changes in electrical network with applied strain. This is a noteworthy advantage with regard to processibility. This behavior remains even at high filler loading although accompanying shear-thinning occurs. It was also confirmed that graphene-like materials and precursors can be efficiently dispersed and further exfoliated during the dispersion process. Especially the use of electro-chemically expanded graphite, stabilized in ethanol, showed promising results towards the cost-effective production of graphene/epoxy composites with extreme high filler loadings, which is a key factor for masterbatch production. Furthermore, an improved heat dissipation by changing the roller material to SiC leads to less material heat-up, which results in lower viscosity drop of the matrix resin with preservation of its cohesion and hence, improved heat dissipation shortens the processing time.

7 Carbon Nanoparticle/Epoxy Composites - Resulting Physical Properties

This section presents the results of the material characterization after dispersion of the CNP/EP composites beginning with the dependency of composite viscosity on particle type and filler loading. In a next step the electrical properties of the fully cured materials are discussed, followed by a presentation of the thermo-mechanical and fracture toughness properties.

7.1 Characterization Subsequent to Curing Agent Addition

7.1.1 Rheology

The rheological behavior, primarily determined by the viscosity, is one of the main properties to consider for the manufacturing of parts out of polymers and their composites. Besides the knowledge of the material's viscosity, the knowledge of the rheological behavior in dependency of applied shear strain is important, as reported in the previous sections. Figure 7.1 gives the shear strain dependent complex viscosity for CB modified epoxy resin after addition of the curing agent. Until a specific shear strain, the complex viscosity exhibits a plateau. Reaching a critical shear strain, the material shows a shear-thinning behavior. A substantial increase in viscosity is observed for CB at high concentrations (12 wt.%), whereas the impact is low up to a loading of 8 wt.%. The critical shear strain for beginning of shear-thinning is strongly decreased for a filler loading of 12 wt.%. Figure 7.2 (a) to (d) give the rheological behavior of

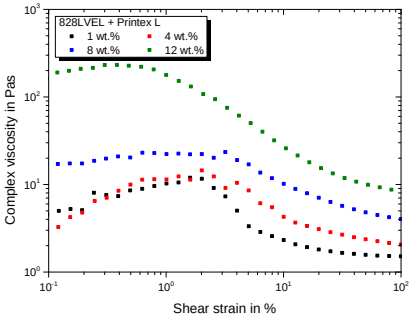


Figure 7.1: Rheological behavior of CB modified 828LVEL and RIMH137/134

investigated MWCNT composites, except CNTN. All MWCNT modified epoxy systems show a similar increase of viscosity with increasing filler content. Furthermore, the critical shear strain for beginning of shear-thinning is not affected by the filler loading. All used MWCNT offer a specific surface area of about 300 m^2/g (compare Table 5.4) leading to identical rheological behavior.

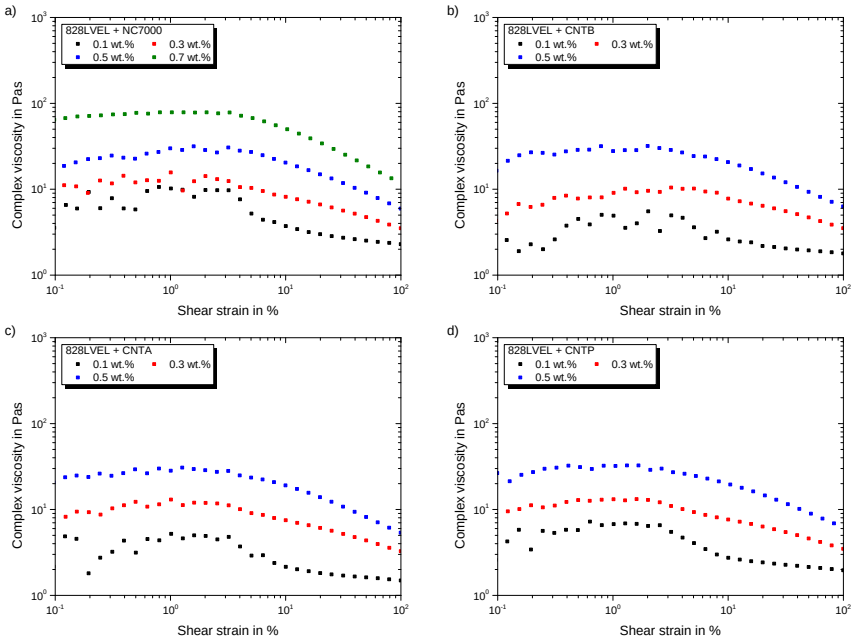


Figure 7.2: Rheological behavior: MWCNT in 828LVEL/RIMH137/134 **(a)** NC7000, **(b)** CNTB, **(c)** CNTA and **(d)** CNTP

Figure 7.3 gives the rheological behavior for the CNTN modification. Due to the elastomeric and amino-functionalized side chains, the viscosity rises distinctively with increasing filler loading of CNTN. It is important to note that the filler loading of CNTN relates to the pure CNT content without elastomer.

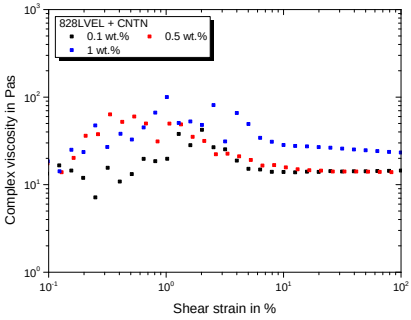


Figure 7.3: Rheological behavior of CNTN modified 828LVEL and RIMH137/134

After shear-thinning, the complex viscosity reaches a plateau, which is much higher compared to pristine MWCNT's viscosity. Figure 7.4 (a), (b) and (c) give the development of complex viscosity with increasing shear strain for FLG, ExG and fExG modified epoxy resin, respectively. For planar FLG, ExG and fExG the increase in complex viscosity in the low shear strain region is one magnitude lower compared to MWCNT,

even up to a filler loading of 3 wt.%. As already stated, a strong exfoliation for this particle type leads to a very good wetting of the layers, which simplifies sliding of them and eases the dispersion process. The good wettability results in low viscosities of the composite. All curves for FLG differ only in the high shear strain range. Higher filler loadings lead to increased plateau viscosities after shear-thinning. ExG increases the viscosity in the low shear rate region with a filler loading of 3 wt.%. Below this filler loading the viscosity is not increased in the low shear rate region. After shear-thinning the viscosity is higher for increased filler loading. An increased filler loading of fExG increases the complex viscosity in the low shear strain region. The particle network initially builds up and results in a maximum in the complex viscosity curve, followed by shear-thinning. An increase of filler content leads to an increase of complex viscosity in the high shear strain region. This results from an accelerated cure kinetic caused by the particles. The high impact on cure kinetics by nanoparticles and functionalized derivatives was observed by Choi et al. [417]. They concluded that the addition of carbon nanoparticles highly influences the initiation of reaction and cure kinetics, which can be more pronounced for functionalized carbon naoparticles. In this case, for fExG, the cross-linking happens rapidly.

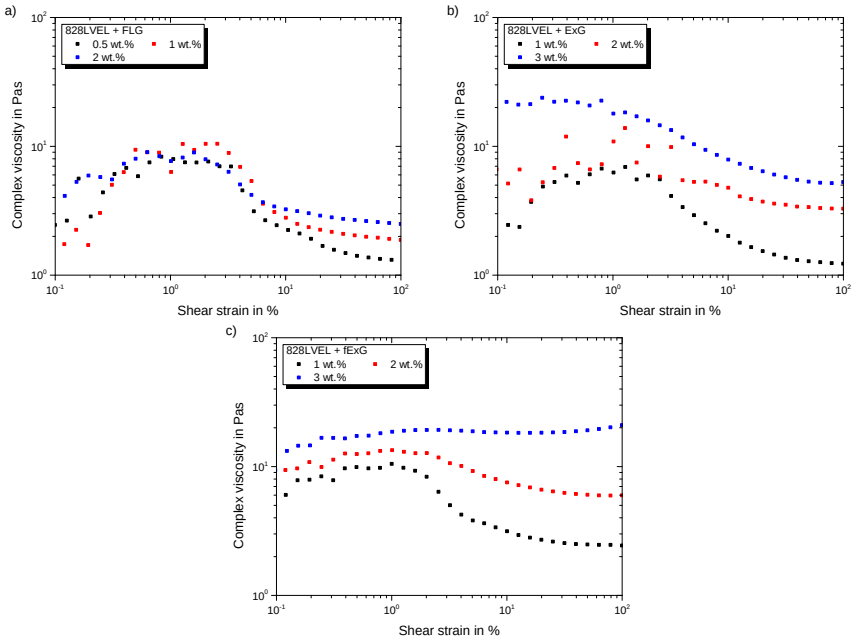


Figure 7.4: Rheological behavior of Graphene modified 828LVEL and RIMH137/134 **(a)** FLG, **(b)** ExG and **(c)** fExG

Figure 7.5 (a) gives the rheological behavior of Tuball 75 and (b) the purified SWCNT, respectively. An addition of 0.01 wt.% of Tuball 75 does not affect the rheological behavior. Starting with a filler loading of 0.05 wt.% the typical plateau arises and the viscosity increases. The purified Tuball SWCNT exhibit the highest impact on the viscosity. An addition of 0.01 wt.% of purified SWCNT results in the same rheologial behavior as for an addition of 0.1 wt.% Tuball 75. This relates to their extensive specific surface area and high purity. Therefore, they possess a higher carbon content per weight, compared to Tuball 75.

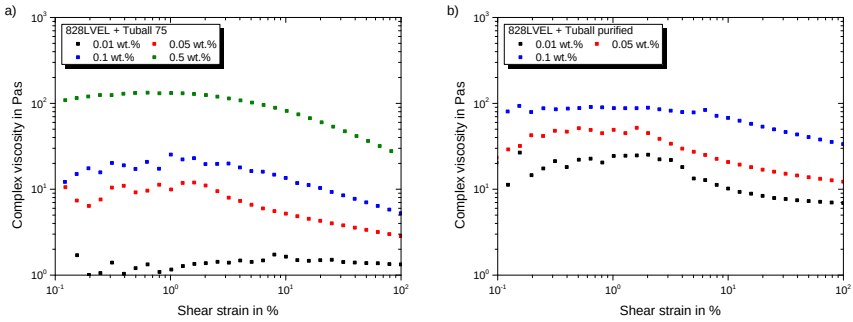


Figure 7.5: Rheological behavior of SWCNT modified 828LVEL and RIMH137/134 **(a)** Tuball 75 and **(b)** Tuball purified

Figure 7.6 (a) sums up the change of viscosity in dependency of the filler loading of used SWCNT and MWCNT as well as the effect of different molecular weight epoxy resins. Only the resin's molecular weight influences the viscosity of the composite for same particle type and filler loading. Even the way of plasma treatment and particle supplier have no significant effect on the composites' viscosity. This is lower for lower molecular weight resins and is particularly pronounced for Epikote 162. The increase in viscosity is mainly dependent on the offered specific surface area. Figure 7.6 (b) shows the impact of CB, CNTN and all planar particles on the viscosity. In conclusion, particles with lower specific surface area allow good composite processing.

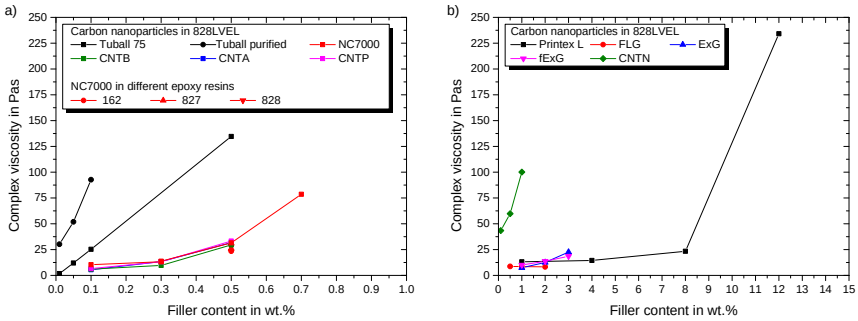


Figure 7.6: Impact of particle modification on the rheological properties for **(a)** evaluated MWCNT and SWCNT in epoxy resin with curing agent and **(b)** evaluated planar particles, CB and CNTN in epoxy resin after addition of curing agent

7.1.2 Impedance Analysis

Addition of a curing agent into the particle/epoxy dispersion leads to an increase of free ions in the system. This is due to the inductive effect of the alkyl group of the amine. The carbon bonded nitrogen offers more electrons compared to hydrogen, leading to improved compensation of positive charges. Figure 7.7 (a) gives the impedance spectrum for neat epoxy resin Epikote 828LVEL, the neat curing agent blend and the freshly mixed resin with addition of curing agent. The neat resin shows no conductivity and behaves like a dielectric fluid. For the neat curing agent a finite resistance can be measured in the low frequency region. The free ions contribute to this conductivity. A mixture of epoxy resin and the amine based curing agent offers a higher resistance in the low frequency region, due to lower ionic content. Furthermore, the curing agent offers a lower viscosity in comparison to the mixture with epoxy. This results in a higher cut-off frequency in the impedance spectra, caused by higher ion mobility. The imaginary part of the complex impedance Z'' becomes dominant if the orientation of the dipoles is not possible anymore. This occurs at lower frequencies for higher viscous fluids [418]. Figure 7.7 (b) gives the impedance spectra for Epikote 828LVEL with Printex L modification. The green curves represent the material without curing agent after the final dispersion step and the red curves subsequent to addition of curing agent. Addition of curing agent leads to the three following changes of the system. Due to the alkaline character of the curing agent, the content of free ions increases, which adds a conductivity into the system. Also, these ions disturb the double layer, which stabilized the carbon nanoparticle/epoxy dispersion. Mixing ratio of curing agent and epoxy resin is about 30 parts per weight, which adds additional volume into the system and lowers therefore the particle concentration. For 1 wt.% the colloidal dispersion in the neat epoxy offers no conductive network.

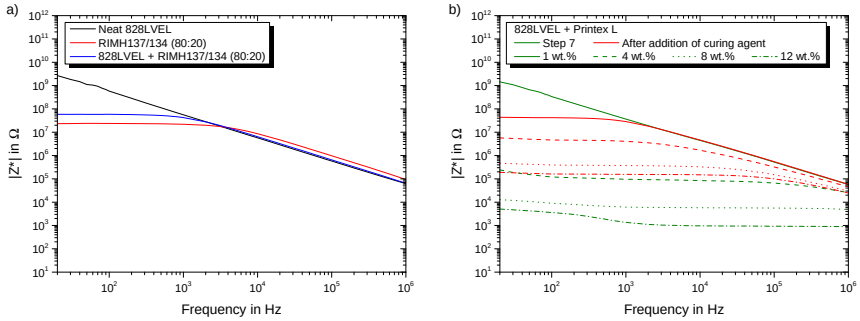


Figure 7.7: Impact of curing agent addition (RIMH137/134) on the impedance spectra for **(a)** neat Epikote 828LVEL and **(b)** Printex L modification of Epikote 828LVEL

After addition of curing agent, a finite resistance can be measured. This is the base resistance of the epoxy/curing agent mixture. For a filler loading of 4 wt.% the resistance of the material increases, because the volume of the dispersion increases, but the amount of particles stays the same. The two higher filler concentrations show a formed micro network, revealed by two plateaus. With addition of curing agent, the second plateau vanishes. This is explainable by the disturbance of the stabilizing Stern-layer, which leads to agglomeration [419] and a break-down of the micro network. Figure 7.8 (a) to (d) give the impedance spectra for NC7000, CNTB, CNTA and CNTP in Epikote 828LVEL and after addition of curing agent. In case of NC7000 modification with a filler loading of 0.1 wt.%, the neat epoxy with MWCNT addition offers no conductivity. After addition of the curing agent the resistance of the material drops by three orders of magnitude, which is far lower compared to the resistance of epoxy/curing agent blend. This results from a

pronounced agglomeration of the particle network. Schwarz and Martin et al. observed similar behavior for MWCNT/epoxy composites after addition of amine based curing agents [105, 160]. A filler loading of 0.3 wt.% leads to similar results. For higher filler concentrations, the resistance increases after addition of curing agent, due to the increased matrix volume within the composite. This material behavior occurs in

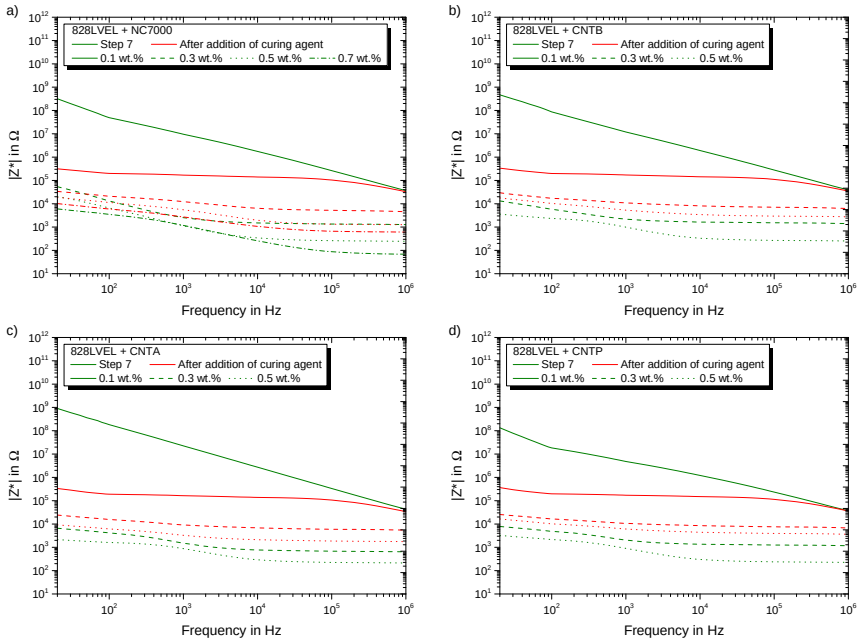


Figure 7.8: Impact of curing agent addition (RIMH137/134) on the impedance spectra for MWCNT modification of Epikote 828LVEL **(a)** NC7000, **(b)** CNTB, **(c)** CNTA and **(d)** CNTP

the same way for CNTB modification. An atmospheric or argon plasma treatment of the MWCNT does not affect the material behavior and results in similar curves. Figure 7.9 gives the impedance spectra for

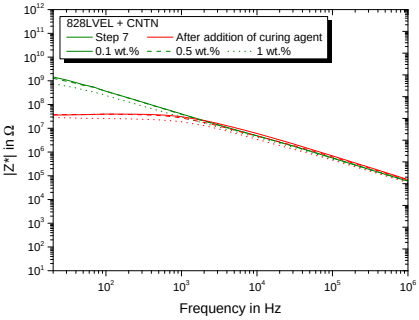


Figure 7.9: Impact of curing agent addition (RIMH137/134) on the impedance spectra for CNTN modification of Epikote 828LVEL

CNTN, which of the elastomeric side chain functionalization. Independent of the filler content, the material shows the same material behavior. Before addition of curing agent the material shows a full capacitive behavior and after addition of curing agent, the resistance equals the one gathered for the pristine epoxy resin/curing agent blend. Figure 7.10 (a), (b) and (c) give the impedance spectra for few-layered graphene, electro-chemically expanded graphite and the functionalized electro-chemically expanded graphite, respectively. Filler loadings of 0.5 wt.% and 1 wt.% FLG do not lead to a conductive particle network in the neat epoxy composite. The materials behave purely capacitive. After addition of curing agent, the materials' impedance spectra equal the ones of the epoxy/curing agent blend. For a filler loading of 2 wt.% FLG in the neat epoxy a conductive network is formed. Due to increased matrix volume after curing agent addition, the resistance increases. An addition of 1 wt.% ExG does not lead to a conductivity in the neat resin. Addition of curing agent leads again to a impedance spectra, which is similar to the one of the epoxy/curing agent blend. An addition of 2 wt.% ExG into the epoxy leads to a conductive network. Addition of curing agent slightly decreases the complex impedance in the low frequency region. For 3 wt.% filler addition a conductive network is formed. The addition of curing agent increases again the volume and hence the resistance increases. The results of fExG are comparable to the ones gathered with FLG. Increasing filler loading decreases the resistance in case of modification of neat epoxy. Addition of curing agent leads to an increase in resistance, due to the increased volume.

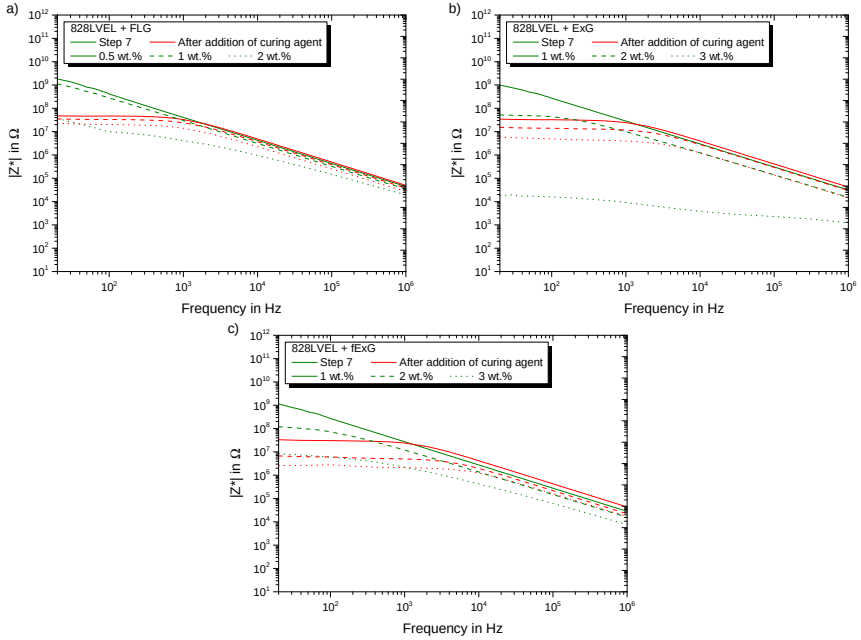


Figure 7.10: Impact of curing agent addition (RIMH137/134) on the impedance spectra for modification with planar particles of Epikote 828LVEL **(a)** FLG, **(b)** ExG and **(c)** fExG

Figure 7.11 (a) and (b) give the impedance spectra for Tuball 75 and the purified SWCNT variant.

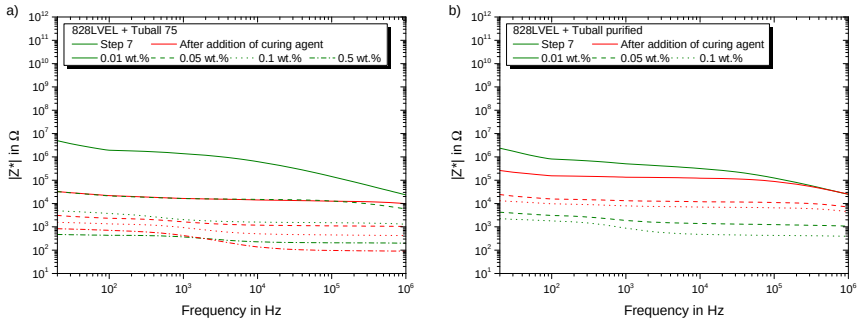


Figure 7.11: Impact of curing agent addition (RIMH137/134) on the impedance spectra for SWCNT modification of Epikote 828LVEL **(a)** Tuball 75 and **(b)** Tuball purified

Even at a low filler loading of 0.01 wt.% Tuball 75, the material offers a conductivity. This decreases with addition off the curing agent. The second cut-off frequency disappears. The micro-network agglomerates and the capacitive behavior of the material vanishes. It is purely resistive in the high frequency region. This behavior remains for the higher filler loadings up to 0.1 wt.%. For 0.5 wt.% filler addition, the resistance in the low frequency region increases again, due to increased matrix volume. The resistance in the high frequency region decreases due to agglomeration of micro-scale. Surprisingly, the material behavior of the purified SWCNT is different. For 0.01 wt.% filler loading, the SWCNT/epoxy composite shows the same impedance spectrum as the Tuball 75. The addition of curing agent leads to a decreased resistance, which is not as pronounced as for Tuball 75. The particle network must be more stable. For higher filler loadings, the resistance increases after addition of curing agent and the second cut-off frequency vanishes. Figure 7.12 gives the influence of different molecular weight epoxy resins on the resulting impedance spectra of 0.5 wt.% NC7000 modification. As already stated, the higher molecular weight leads to an improved particle separation. This results from the higher viscosity and is revealed by the increased complex impedance at high frequencies for increased molecular weight. For low frequencies the conductivities are comparable. Addition of curing agent leads to an increase in volume and hence, results in a higher resistance.

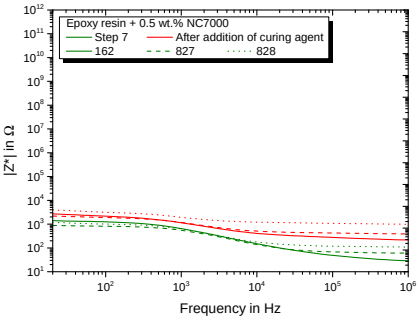


Figure 7.12: Impact of curing agent addition (RIMH137/134) on the impedance spectra for MWCNT modification of epoxy resins with different molecular weight distributions

7.2 Characterization in Cured State

7.2.1 Impedance Analyses

To reveal the changes in the particle network, caused by the curing process, the cured and cut into the final rectangular test geometry nanocomposites were measured by impedance spectroscopy. The fully cured epoxy resins show a purely capacitive behavior in the impedance spectra. Figure 7.13 gives the impedance spectra for the carbon black modified Epikote 828LVEL in the cured state. A particle loading of 1 wt.% and 4 wt.% does not lead to a conductive network. During curing, the previously formed network is destroyed by the higher ionic content. Higher filler contents result in lower resistance and a higher cut-off frequency.

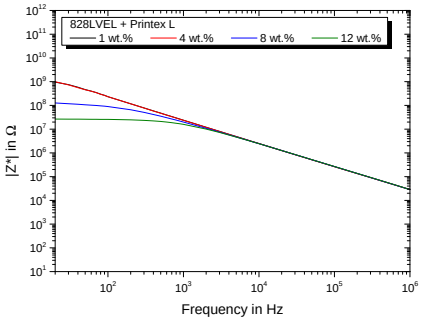


Figure 7.13: Impact of particle modification on the impedance spectra of CB in cured epoxy

Figure 7.14 (a) to (d) give the impedance spectra for all MWCNT modifications of Epikote 828LVEL after curing. A modification with 0.1 wt.% NC7000 leads to a finite resistance, which was not the case before the addition of the curing agent. Hence, the higher ionic content and the curing process lead to the formation of conductive paths within the nanocomposite. The second plateau vanishes for all filler loadings of NC7000, resulting from re-agglomeration on micro scale. Faiella et al. utilized the network changes resulting from the curing process to tailor the electrical conductivity [420]. These network changes lead to a dynamic percolation, which is highly dependent on the curing agent, introduced shear forces [421], initial dispersion state and curing temperature [422]. This may also lead to lower percolation thresholds than predicted by classical statistical percolation theory [423]. A higher filler content leads to a lower complex impedance. Beginning with 0.3 wt.% filler addition, only one plateau occurs. This means that the micro dispersion does not exist any more. Furthermore, no cut-off frequency can be identified. The material behaves fully resistive. In contrast, CNTB modification shows a cut-off frequency for 0.1 wt.% and 0.3wt.%. For 0.5 wt.% the material behaves purely resistive again. The atmospheric plasma treated MWCNT show a similar behavior as the non-treated variant. Modification with argon plasma treated MWCNT leads for all filler loadings to a cut-off frequency in the impedance spectra. This shifts to higher frequencies for higher filler contents, revealing a more redundant particle network. Argon plasma treatment seems to stabilize the dispersion.

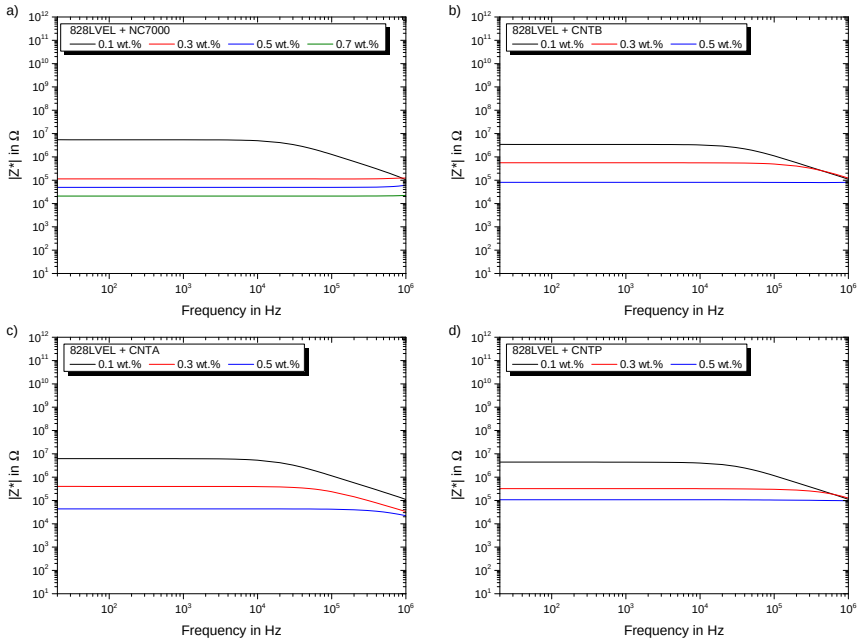


Figure 7.14: Impact of particle modification on the impedance spectra of MWCNT in cured epoxy (**a**) NC7000, (**b**) CNTB, (**c**) CNTA and (**d**) CNTP

Figure 7.15 gives the impedance spectra for the CNTN modifications after curing. All filler loadings result in a purely capacitive behavior. No conductive network has formed.

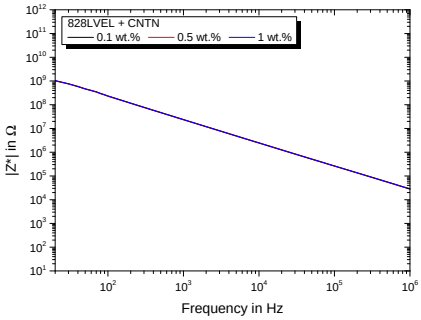


Figure 7.15: Impact of particle modification on the impedance spectra of CNTN in cured epoxy

Figure 7.16 (a) to (c) give the resulting impedance spectra for the cured modifications with FLG, ExG and fExG, respectively.

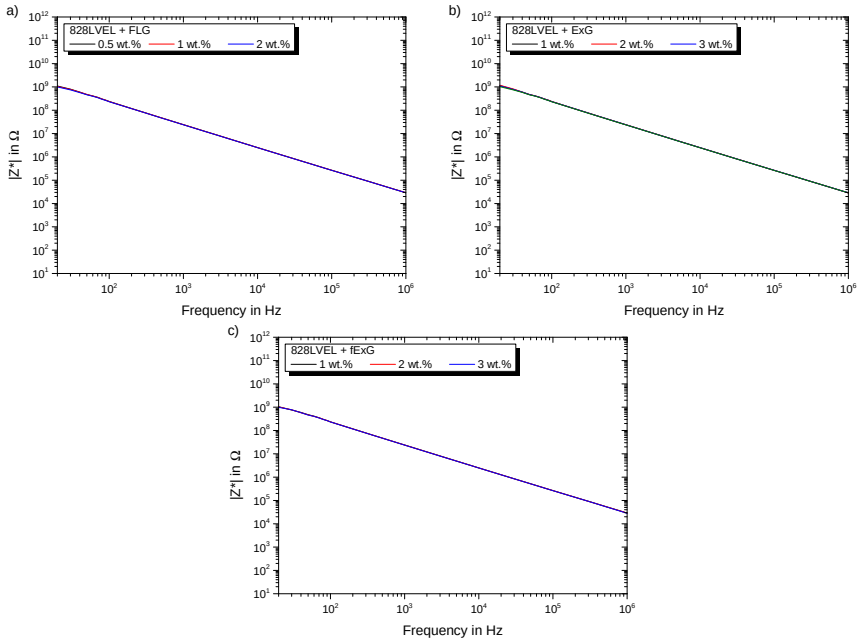


Figure 7.16: Impact of particle modification on the impedance spectra of planar particles in cured epoxy (**a**) FLG, (**b**) ExG and (**c**) fExG

All modifications with planar particles do not lead to a conductive network and show a purely capacitive behavior independent of the filler content. The addition of curing agent and following curing process lead

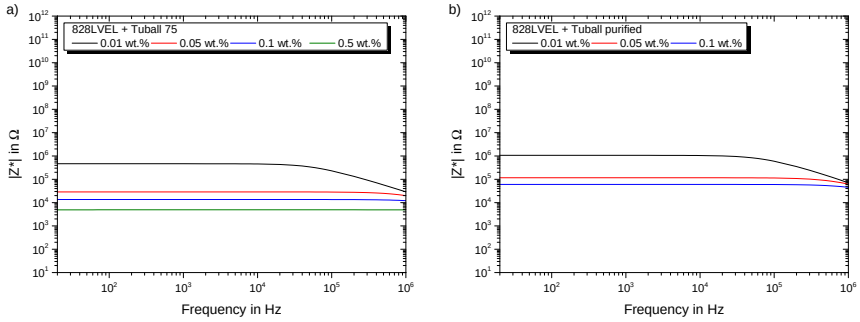


Figure 7.17: Impact of particle modification on the impedance spectra of SWCNT in cured epoxy (**a**) Tuball 75 and (**b**) Tuball purified

to a break-down of the conductive network after dispersion. Figure 7.17 (a) and (b) give the impedance spectra for Tuball 75 and the purified Tuball SWCNT, respectively. Both modifications with 0.01 wt.% show one plateau with a cut-off frequency. The complex impedance of Tuball 75 modification is slightly

lower, compared to the purified variant. The higher filler loadings of Tuball 75 and purified SWCNT modification lead to a purely resistive material response in the impedance spectra. The modification with higher filler loadings of purified SWCNT results in higher resistances compared to the non-treated SWCNT. This indicates a more stable particle network during curing, which is in good accordance to the results presented in the previous section. Figure 7.18 gives the impedance spectra for 0.5 wt.% NC7000 modification in the different molecular weight epoxy resins. After addition the nanocomposites showed a similar impedance spectra in the low frequency region. The curing process leads to a purely resistive behavior for all modified epoxies. Furthermore, the highest molecular weight epoxy resin offers the highest complex impedance. With decreasing molecular weight, the complex impedance decreases as well. This contributes to the lower viscosity of the material, which enables a pronounced agglomeration and formation of conductive pathways. This is a similar temperature induced behavior, observed by Martin et al. [160]. They showed that an increased curing temperature results in higher conductive nanoparticle clusters, resulting from the lower viscosity, which destabilizes the dispersion.

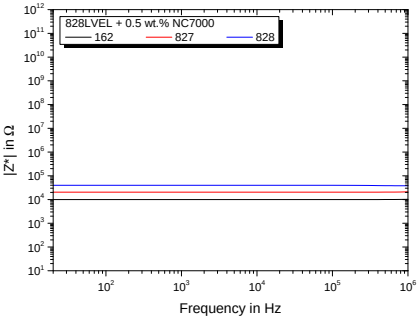


Figure 7.18: Impact of particle modification on the impedance spectra of MWCNT NC7000 in cured epoxy with different molecular weight distributions

7.2.2 DC Conductivity

Figure 7.19 (a) gives the electrical percolation behavior in dependency of SWCNT and MWCNT filler content. The SWCNT show an electrical conductivity of 10^{-3} S/m, even at low filler loading of 0.01 wt.%. Results for Tuball 75 are in good accordance with reported values in [349]. The purified SWCNT modification results in lower final conductivities compared to Tuball 75. A ternary network is formed for the non-purified variant, due to the metallic impurities, leading to improved network formation. This effect is reported by Sumfleth et al. [424], as well. All MWCNT composites show a similar percolation behavior, independent of their treatment. Due to lower resin viscosity the agglomeration during curing is more pronounced for Epikote 162 resulting in higher conductivities. Martin et al. reported this correlation as well [160]. The electrical conductivity of carbon nanoparticle-polymer composites is dominated by electron hopping and formation of conductive networks, while network formation is the governing mechansim after percolation [425]. Seidel et al. revealed that electron hopping is much more pronounced for SWCNT compared to MWCNT, leading to much lower percolation thresholds [426]. Figure 7.19 (b) gives the percolation behavior of CNTN, CB and planar particles. Despite the high filler loading of CNTN the conductivity is much lower in comparison to other MWCNT. This can be explained by the elastomeric side chains covering the CNTs and thus hindering the build-up of a conductive particle network. CB percolates between 4 wt.% and 8 wt.%, which is also reported in a prior study for a comparable CB type [14]. Both

investigated planar particles have a low impact on the electrical conductivity even up to filler loadings of 3 wt.%. The significant increase in electrical conductivity (electrical percolation) arises for all particles at lower filler loadings compared to the corresponding filler loading, which results in viscosity increase (rheological percolation). The explanation is given by the different network formation mechanisms. The tunnel distance mainly influences the electrical conductivity, whereas for an increase in viscosity a strong physical interaction of filler particles network is required to ensure a stiff network [20].

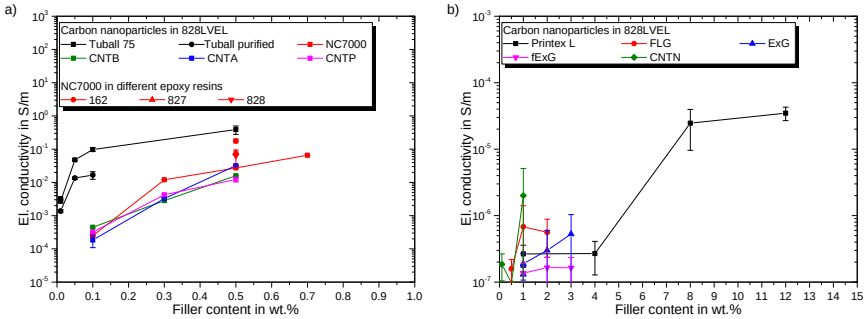


Figure 7.19: Electrical percolation behavior of **(a)** evaluated MWCNT and SWCNT in epoxy resin and **(b)** evaluated planar particles, CB and CNTN in epoxy resin

7.2.3 Dynamic Mechanical Thermal Analysis

The influence of particle type and filler loading as well as molecular weight of resin on dynamic-thermo-mechanical properties are discussed in this section. Below the glass transition temperature T_G a high modulus is desirable. For temperatures exceeding T_G the complex modulus reveals the strength of the particle network interconnection. Figure 7.20 (a) gives the resulting DMTA curves for all investigated epoxy resins and their modification with 0.5 wt.% NC7000 MWCNT. At low temperatures the complex modulus is not affected by the particles and only a slightly, as already stated, by the molecular weight of the resins. Also, a shift of the glass transition temperature T_G, evaluated at the maximum of the damping factor $tan\delta$, is not observed. In the high temperature regime (exceeding T_G) the complex modulus increases with decreasing molecular weight of the resins due to increased cross-link density of the thermoset. A modification with NC7000 increases the complex modulus at high temperatures, too. This indicates the formation of a percolated particle network and correlates with the previously observed increase in viscosity. For further investigations, the complex modulus is evaluated for all composites at 30 °C and 170 °C. The shift in T_G is analyzed by the peak temperature of the damping factor $T(tan\delta_{peak})$.

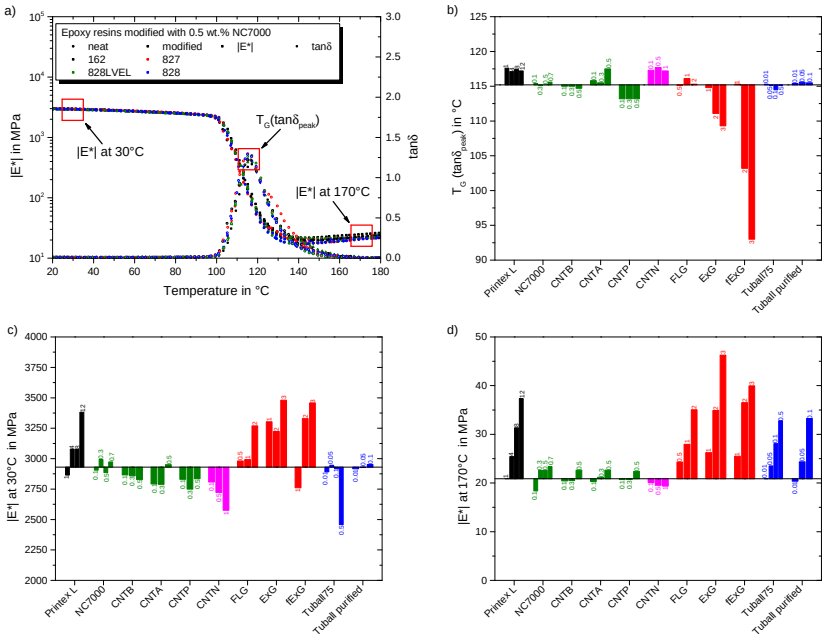


Figure 7.20: Resulting DMTA properties: **(a)** impact of 0.5 wt.% NC7000 in epoxy resins Epikote 162, 827, 828LVEL and 828, **(b)** effect of evaluated particles on the glass transition temperature, **(c)** effect of evaluated particles on the complex modulus at 30 °C and **(d)** effect of evaluated particles on the complex modulus at 170 °C

Figure 7.20 (b) gives the influence of particle type and filler loading on the T_G. The black solid line indicates the value for the neat Epikote 828LVEL. CB increases the T_G independently of the filler loading. NC7000 and CNTB do not influence the T_G. Beginning with rheological percolation, the T_G rises for CNTA. The T_G is lower compared to the neat resin for a modification with CNTP. Argon plasma treatment does not only improve the electrical percolation but also leads to a slight improvement of the

T_G, whilst atmospheric plasma treatment lowers electrical conductivity and T_G of the composite. The amino functionalized elastomeric side chains of CNTN increase the T_G prospectively due to an increased cross-linking and incorporation of the particles into the polymeric network. The influence of amino funtionalization of carbon nanoparticles on the cure kinetics of thermosets was investigated by Seyhan et al., too. They concluded that an amino surface modification of CNP alters the cure kinetics and final properties of the composite [427]. FLG has no influence on the resulting T_G. ExG and fExG decrease the T_G for filler loadings over 1 wt.% and this is even more pronounced for the functionalized variant. This is in correspondence to the observed viscosity increase. Prolongo et al. reported that graphene sheets hinder the curing and lower cross-linking density [428]. This results in a higher mobility of the polymer chains and thus lower T_G. Contradictory results were presented by Yu et al. [429]. They observed an increase in T_G as well as complex modulus. The accelerated reaction, revealed by the rheological investigations, disturb the formation of the cross-linked polymer network. This leads to the low T_G. Figure 7.20 (c) gives an overview on the development of the complex modulus in the enthalpy elastic state for the manufactured composites. The black solid line indicates the value for the neat Epikote 828LVEL. For CB the complex modulus increases with increasing filler loading. This correlation is as well reported in literature [430]. A filler loading of 12 wt.% leads to the highest increase. NC7000 shows no effect on complex modulus at this temperature. For CNTB the modulus decreases with increasing filler loading. For plasma treated CNT the complex modulus decreases until 0.3 wt.% and then increases for a filler loading of 0.5 wt.%. This increase correlates with the rheological percolation. For CNTN the complex modulus drops with increasing filler loading, resulting from the high elastomeric content. For planar FLG, ExG and fExG the complex modulus increases with increasing filler loading. SWCNT do not effect complex modulus below a filler loading of 0.5 wt.%. A significant decrease is observed for 0.5 wt.% filler loading of Tuball 75. This attributes to the dominating network of flexible SWCNT within the composite. Figure 7.20 (d) shows the dependency of complex modulus in the entropy elastic state on particle type and filler loading. The black solid line indicates the value for the neat Epikote 828LVEL. With increasing filler loading of CB the complex modulus rises. For all MWCNT types the complex modulus increases with beginning of rheological percolation. Due to the elastomeric chains the complex modulus drops with increasing filler loading of CNTN. Increased filler loading of FLG, ExG, fExG and both SWCNT types significantly increases the complex modulus above T_G.

Summarizing, only carbon black enhances the T_G and the complex modulus at low temperature. The planar particles offer the opportunity to enhance the complex modulus at low temperature. For FLG the T_G is not affected, but ExG und fExG significantly lower the T_G. All MWCNT modifications lead to a lower complex modulus at at low temperature, but do not detrimentally affect the T_G with exception of atmospheric plasma treated MWCNT. Low filler addition of SWCNT do neither affect the T_G nor the complex modulus at low temperature.

7.2.4 Fracture Toughness Mode I and II

7.2.4.1 Mode I

For mode I fracture the reinforcement mechanisms are crack separation, bifurcation, pinning, deflection and separation of particles [320, 321, 431, 432]. The results of the influence of nanoparticle type and filler loading on the mode I fracture toughness are summarized by Figure 7.21.

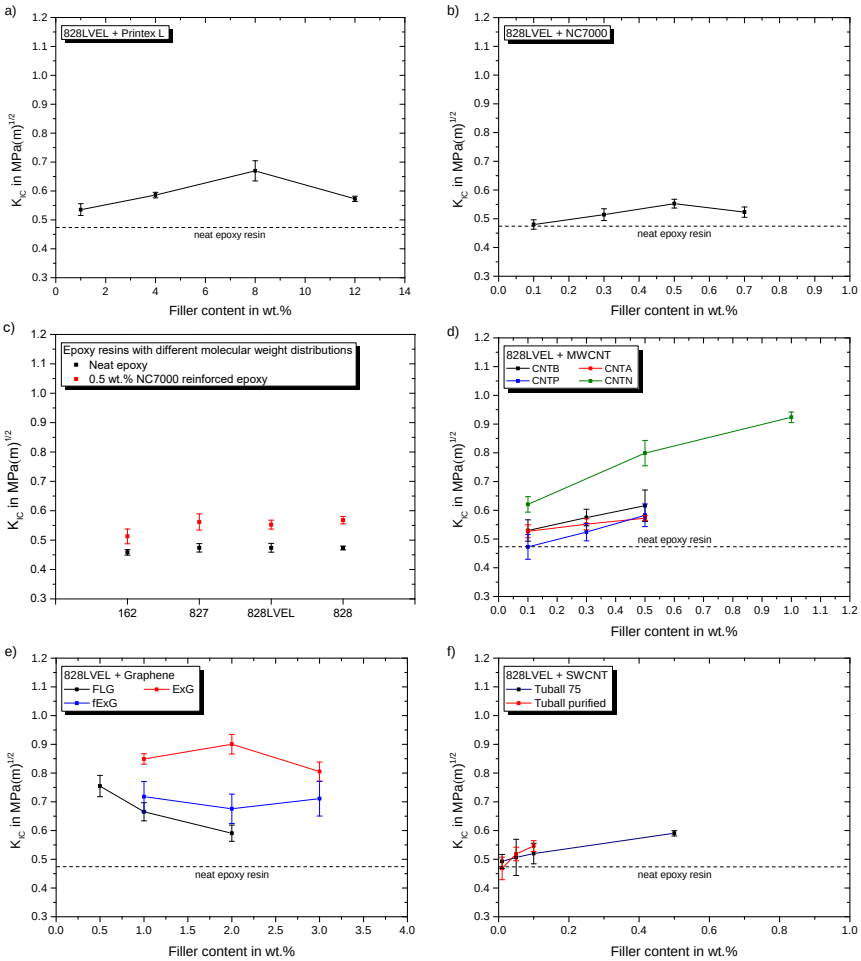


Figure 7.21: Particles impact on fracture toughness in mode I for **(a)** CB in Epikote 828LVEL, **(b)** NC7000 in Epikote 828LVEL, **(c)** 0.5 wt.% NC7000 in different MW epoxy resins, **(d)** CNTB, CNTA, CNTP and CNTN in Epikote 828LVEL, **(e)** FLG, ExG and fExG in Epikote 828LVEL and **(f)** Tuball 75 and Tuball purified in Epikote 828LVEL

CB shows a maximum at 8 wt.% filler loading (Figure 7.21 (a)). NC7000 exhibit a maximum of the K_{IC}, too (Figure 7.21 (b)). Both maxima lay in the range of the rheological percolation, which is also reported by Nadiv et al. [316, 317]. Figure 7.21 (c) shows the impact of 0.5 wt.% NC7000 on the K_{IC} of the different molecular weight resins. The increase in fracture toughness in mode I is lowest for Epikote 162. Figure 7.21 (d) gives the impact of atmospheric and argon plasma treatment on the fracture toughness in mode I in dependency of their filler loading. Furthermore, the influence of CNTN is shown. CNTN show the highest potential for fracture toughness improvement with nanotubes, whereby the plasma treatments have minor influence on the mode I fracture toughness. Figure 7.21 (e) shows the influence of the used planar particles on the fracture toughness. The ExG modification results in a maximum at 2 wt.% filler loading, similarly high as CNTN at 1 wt.%. The functionalized variant of ExG results in a constant improvement of the K_{IC} value. For FLG the maximum in mode I fracture toughness supposedly lays below 0.5 wt.%. A maximum for this particle type is reported at 0.05 wt.% [433]. A pilot survey, utilizing same FLG, but another similar epoxy resin, investigated the K_{IC} value as well. Figure 7.22 gives the merged curves. The maximum in K_{IC} occurs at 0.5 wt.%, which is the starting concentration in this study.

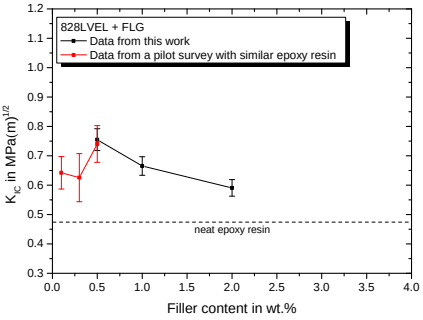


Figure 7.22: Particles impact on fracture toughness in mode I for FLG combined with data from a pilot survey

A correlation with the rheological or electrical percolation for planar particles is not possible. Figure 7.21 (f) gives similar improvement in fracture toughness for both SWCNT types. They result in lower enhancement due to their flexible nature. For pristine carbon nanotubes the best improvement is achieved with 0.5 wt.% of CNTB.

7.2.4.2 Mode II

Figure 7.23 (a) and (b) show the impact of CB and NC7000 filler content on the fracture toughness in mode II, respectively. For both particle types the K_{IIC} value drops with increasing filler loading. The influence of 0.5 wt.% NC7000 on the evaluated epoxy resins is given in Figure 7.23 (c). For all resins K_{IIC} decreases with this particle modification. This is less pronounced for the highest molecular weight resin Epikote 828. CNTB and CNTA do not weaken the fracture toughness in mode II, as shown in Figure 7.23 (d). Atmospheric plasma treated CNTP, offering a higher oxygen content, decrease the fracture toughness in mode II with increasing filler content. The K_{IIC} value drops for a CNTN modification to a constant lower value, seemingly independent of the filler concentration. Figure 7.23 (e) gives the influence of used planar particles on the fracture toughness. The fracture toughness is reduced with increasing filler loading. This is most pronounced for 3 wt.% fExG, which also showed the highest decrease in T_G. The influence of filler loading of SWCNT on K_{IIC} is shown in Figure 7.23 (f). With increasing filler content of

Tuball 75, K_{IIC} decreases. This reduction is less pronounced for the purified SWCNT at the investigated range of filler contents.

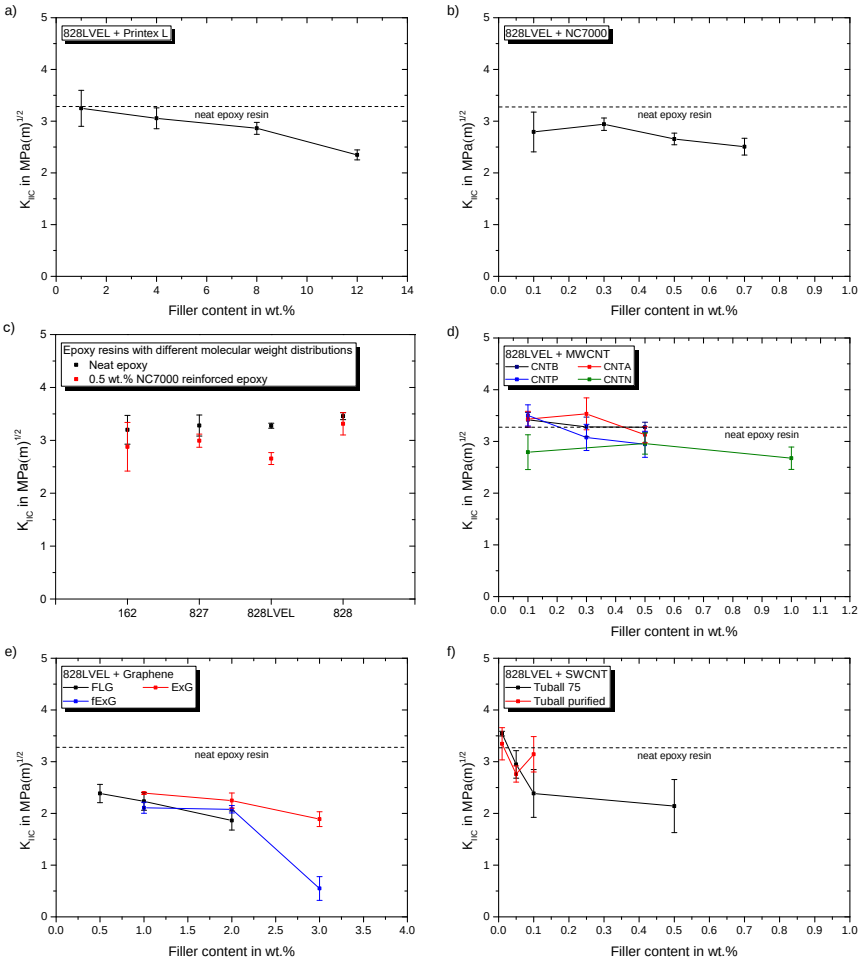


Figure 7.23: Particles impact on fracture toughness in mode II for **(a)** CB in Epikote 828LVEL, **(b)** NC7000 in Epikote 828LVEL, **(c)** 0.5 wt.% NC7000 different MW epoxy resins, **(d)** CNTB, CNTA, CNTP and CNTN in Epikote 828LVEL, **(e)** Avan2, ExG and fExG in Epikote 828LVEL and **(f)** Tuball 75 and Tuball purified in Epikote 828LVEL

Surprisingly, only for low filler contents of CNTB, CNTA and CNTP a slight increase of K_{IIC} is observed, whereas CNTA modification shows the highest potential. The measurement of K_{IIC} is discussed controversially in literature, because it is highly dependent on notch shape and loading condition [434, 435]. Many studies report an improvement of fracture toughness in mode II due to nanoparticle modification e.g. [307, 322, 328], but the mechanisms are not elaborated comprehensively. Figure 7.24 schematically shows the loading conditions for mode I and mode II at the crack tip before and after crack propagation.

In mode I the crack propagation initiates in the direction of the pre-crack and propagates further in this direction due to crack opening in tension mode.

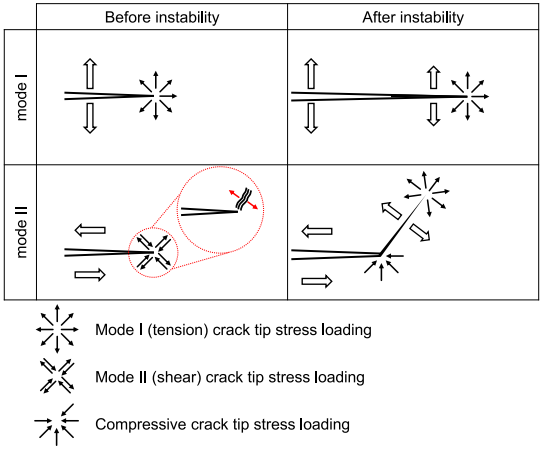


Figure 7.24: Illustration of crack propagation before and after instability in **(top)** mode I and **(bottom)** mode II with craze initiation at particle - adapted from [305]

Figure 7.25 (a) and (b) show the SEM images of the with 0.1 wt.% Tuball purified and Tuball 75 modified composite in mode I, respectively.

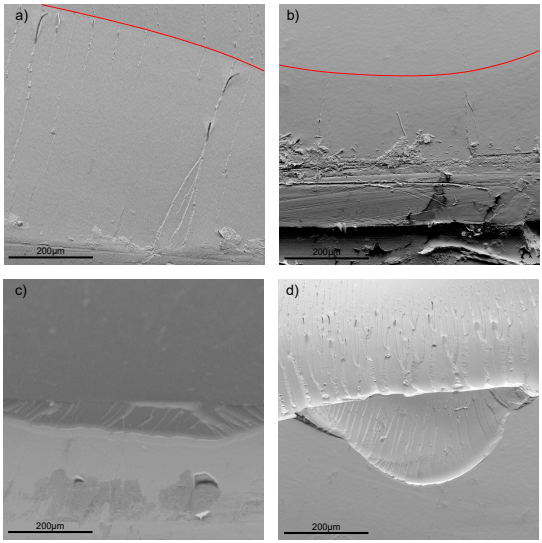


Figure 7.25: SEM images of the fracture surfaces of 0.1 wt.% SWCNT in Epikote 828LVEL (**a**) Tuball purified mode I (**b**) Tuball 75 mode II (**c**) Tuball purified mode II (**d**) Tuball 75 mode II

The red line indicates the pre-notch. For both modifications, the crack propagates in the direction of the pre-notch. For mode II the crack tries to initiate, as already stated, as well in the direction of the pre-crack. However, the propagation is in mode I under an angle of 70 °, due to the lower fracture toughness in mode I [436]. For particle filled polymers the crack may initiate in shear loading in mode I, caused by initiation of craze formation at particles near the crack tip. Crazing in polymers is initiated at defects or impurities [437, 438]. The formation of crazes is enabled by the tendency of usually brittle epoxy to show high possible plastic deformations under pure shear loading [439, 440]. A high deformation of 20 % occurs at the notch prior to failure [441] or are even higher in small volumes [442]. Zhang et al. made this observation for nanocomposites, too [443]. Craze formation is more pronounced for lager particles and more likely for higher filler loading. The weakly bonded layered structure of the planar graphitic particles further promotes crack initiation in shear loading condition [444]. This means for fiber composite applications that cracks will divert straight from the tough interlaminar matrix region into the fiber-bed [445]. Figure 7.25 (c) and (d) show the SEM images of the 0.1 wt.% Tuball purified and Tuball 75 modified composite in mode II, respectively. For Tuball 75 modified samples the disruption at crack initiation point is much deeper and has a larger excess compared to the purified variant. This contributes to the impurities in the Tuball 75 SWCNT variant, which promote crack initiation. Particularly at the edges of the disruption, the formation of crazes is visible. This is not the case for the purified variant, supporting the mechanisms given in Figure 7.24.

7.3 Conflict of Objective - Enhancement of Physical Properties and Loss of Processibility?

The previously presented results reveal an optimum particle loading for enhancement of K_{IC} of the composites. All particles enhance the fracture toughness in mode I and highest values are achieved with the planar particles and CNTN. The highest decrease in K_{IIC} results from FLG, ExG and the non-purified Tuball 75 modification. So, the decrease is more pronounced for SWCNT with metal impurities. CNTN

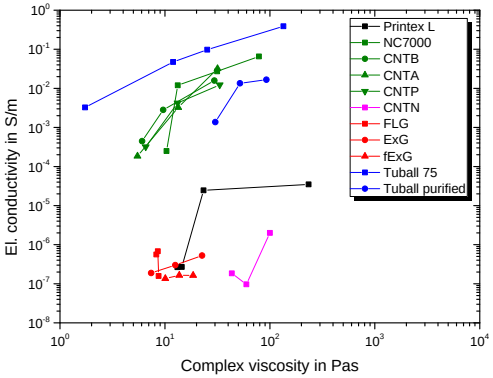


Figure 7.26: Summary of the electrical conductivity (cured state) in correspondence to the complex viscosity for all evaluated particle types in Epikote 828LVEL/RIMH137/134 (liquid state)

feature the same elastomer domain size independent of the filler loading and therefore have the same decrease. Application demands a compromise between the enhancement of physical properties, in this case electrical conductivity and fracture toughness, and processibility represented by the resulting composite's viscosity. Figure 7.26 shows the electrical conductivity and the corresponding viscosities for the modified Epikote 828LVEL. Tuball 75 modification results in highest electrical conductivity at any given viscosity.

Also all types of MWCNT show good results. Figure 7.27 gives K_{IIC} and the corresponding K_{IC} values for the composites. Only Tuball 75 at 0.01 wt.% filler loading and CNTA up to 0.3 wt.% increase both fracture toughness values. CNTN modification results in a low decrease in K_{IIC} accompanying a high increase in K_{IC}, but offer a very low electrical conductivity and a comparably high viscosity increase. Therefore, Tuball 75 show highest application potential with regard to requirement of electrical conductivity and ExG for improvement of mode I fracture toughness.

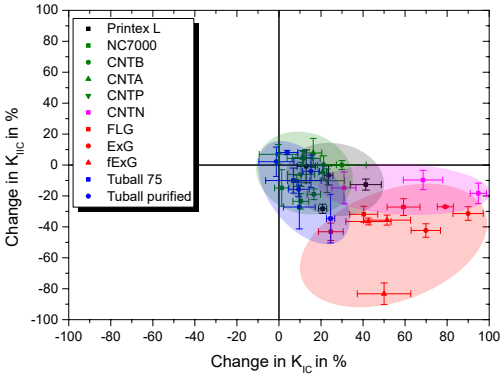


Figure 7.27: Summary of resulting K_{IIC} and K_{IC} values for all investigated particle types in Epikote 828LVEL

In conclusion, the novel three-step pre-cracking method allowed an exact introduction of the pre-crack and led to low variation in fracture toughness values. Especially, the measured mode II fracture toughness values were as high as reported in literature, due to prevention of crack initiation in tension mode. The plastic zone in front of the crack-tip in mode II stores much more energy compared to mode I, due to its dimension. For mode II loading of a pre-crack in a nanocomposite, the particles act as crack initiator in tension mode, lowering the fracture toughness in mode II. SWCNT Tuball 75 offer the highest conductivities at any given viscosity and the lowest percolation threshold. This makes them favorable for applications where high conductivities are demanded. MWCNT and CB show a good compromise of processibility and physical property enhancement. Addition of planar and globular carbon nanoparticles leads to comparably low electrical conductivities, but ExG can achieve a very high mode I fracture toughness at only slightly increased viscosities. All fillers lead to a decrease of K_{IIC} above a certain loading threshold, due to promotion of crack initiation.

8 Demonstration of Industrial Scale Masterbatch Production (10 kg)

In this section, the previous introduced in-line monitoring methods will be applied to monitor the TRM processing of a 10 kg SWCNT epoxy masterbatch containing 1 wt.% Tuball 75. Utilized monitoring methods are the evaluation of line loads and temperature by the three roll mill, impedance spectroscopy and OCT. From OCT the particle size distribution is derived and the results are correlated with direct particle size analysis by grindometry. The 10 kg masterbatch production was conducted by processing of eight batches, containing 1 wt.% SWCNT Tuball 75 in the resin blend of Epikote 828 and 862. The batches were processed in the standard seven step process on a TRM 120E-250. As already shown, the dispersion quality is independent of the size of the used machine. This 10 kg masterbatch production was performed to demonstrate the scalability of the TRM process and its reproducibility as well as the efficiency of the derived online monitoring methods. For the 10 kg masterbatch process, OCT and impedance spectroscopy were performed after every dispersion step of each batch.
Figure 8.1 gives the gathered data from the TRM for the processing of the 10 kg masterbatch containing a filler loading of 1 wt.% SWCNT.

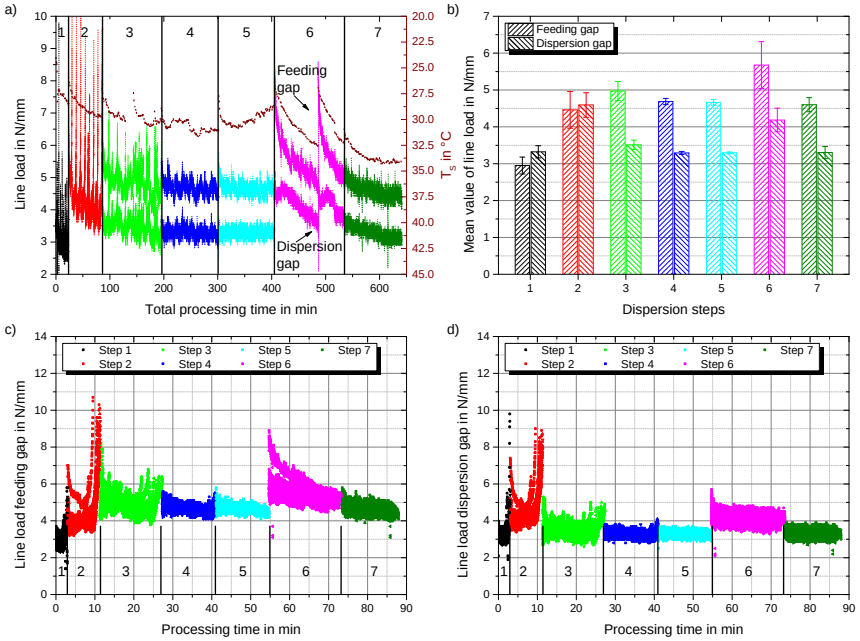


Figure 8.1: Line loads of TRM process for (**a**) whole process, (**b**) step-wise mean values of occurring line forces, (**c**) batch-wise variation of line force in feeding gap and (**d**) batch-wise variation of line force in dispersion gap

Figure 8.1 (a) shows the line loads in the feeding gap and dispersion gap as well as the sample temperature development T_S over the processing time. The temperature axis is plotted in inverse direction. Each color

stands for one dispersion step and consists of the 8 batches. The total processing time is 10 h and 41 min. In dispersion step 1 (black) and 2 (red) a significant rise of the line force occurs at the end of processed batch. This contributes to the aforementioned separation of SWCNT and resin caused by insufficient initial dispersion. This becomes less pronounced with further dispersion. For the two homogenization steps the line loads do not differ much between the two processing gaps. Figure 8.1 (b) compares the average occurring line loads of feeding gap and dispersion gap for each processing step. Line force increases from step 1 to 3. This contributes to better homogenization and reduction of gap spacing. From step 3 to step 5 the line load decreases. This results from the heat input into the material. Going into detail for step 6, unexpectedly, it starts with higher line loads. This is due to a discontinuity of the dispersion process. After step 5 the material rested and cooled down (see T_S in Figure 8.1 (a)). This accompanies with an increase of viscosity leading to higher loads within the gaps. The development of T_S correlates in a good manner with occurring line loads. Taking the processing time into account, this process is very time consuming and must be optimized.

In Figure 8.1 (c) and d the line loads of feeding gap and dispersion gap are compared batch-wise for each dispersion step. It is obvious that the processing time is batch independent in between each step. With decreasing gap spacing processing time increases. Noticeable is the higher line load in the feeding gap compared to dispersion gap although the gap size of the dispersion is one third and the material flow is adjusted. In terms of quality the scattering of the line loads lowers over the dispersion process. This indicates a homogeneous and repeatable quality of the process and the final product. As mentioned in the previous sections, utilizing only the line load evaluation is not sufficient to access the quality of the dispersion. Therefore, the direct and indirect evaluation of particle size and dispersion state by optical coherence tomography and impedance spectroscopy was utilized. Firstly, the particle size is measured by grindometry to gather the size of the largest agglomerate. The evaluation by grindometry of the 1 wt.% masterbatch shows a significant decrease of particles sizes, see Figure 8.2 (a).

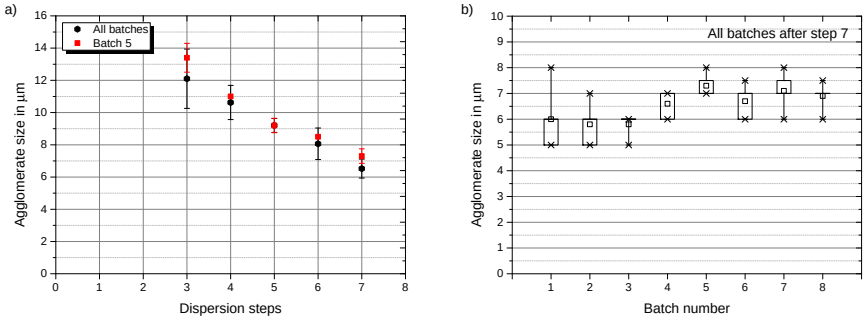


Figure 8.2: Particle size evaluated with grindometry (**a**) step-wise evaluation and (**b**) inter-batch variation after step 7

Plotted is the particle size development of a single batch (red) in comparison to all batches (black). With increasing amount of dispersion steps the particle size decreases significantly. Furthermore, after the last dispersion step the variation is smallest. This underpins the high quality and homogeneity of the material. Figure 8.2 (b) compares the final particle sizes of all processed batches. The particle sizes show a narrow variation within each batch and between the batches. This as well confirms the reproducibility and high quality of the TRM process. Figure 8.3 gives the size evaluation by optical coherence tomography over the dispersion process. The particle size is given for every second step, beginning with the first dispersion step. The size of the large particles decreases significantly, which is in good accordance to the evaluation

by grindometry. Particle size is reduced by one order of magnitude. Optical coherence tomography is a robust method, which allows an in-line evaluation of the particle size in industrial environment and is applicable for large-scale production, as already stated in one of the previous sections. Both evaluation methods reveal a decrease of particle size with increasing amount of dispersion steps, but an optimization towards electrical conductivity of the final product is not possible by utilizing these methods.

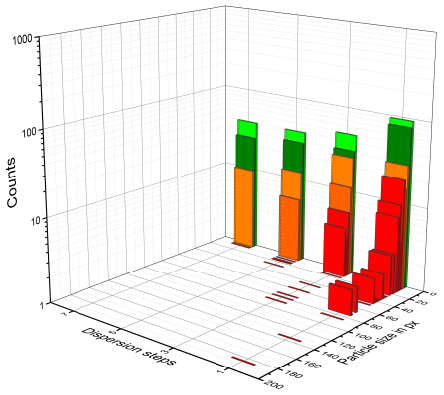


Figure 8.3: Evaluation of particle size distribution with OCT for SWCNT concentrations of 1 wt.%

Therefore, the masterbatch dispersion process was additionally monitored by impedance spectroscopy, too. Figure 8.4 gives the resulting measurement data. Figure 8.4 (a) gives the complex impedance in dependency of the applied measurement frequency for the nanocomposite after each dispersion step. The complex impedance has a plateau in the low frequency region up to a frequency of around 1 kHz. Reaching f_c, the value of $|Z^*|$ starts to decrease until the second plateau occurs. Beginning with dispersion step 1 the system is electrically percolated due to the high filler concentration of 1 wt.% SWCNT, which is a much higher concentration as needed for the low percolation threshold. After dispersion step 2 the homogenization is complete. The initial plateau decreases from 250 Ω to about 160 Ω. Dispersion step 3

Table 8.1: Equivalent circuit parameters for 1wt.% filler concentration in the liquid state

Step	$R_{el,Bulk}$ in Ω	Q_{Bulk} in pF	m_{Bulk}	$R_{el,Agg}$ in Ω	Q_{Agg} in pF	m_{Agg}
1	172	20	0.69	73	2315	0.82
2	70	71405	0.25	98	973	0.90
3	24	136040	0.26	56	1102	0.93
4	47	17669	0.33	43	1607	0.91
5	47	801	0.49	46	1798	0.88
6	84	3711	0.40	88	2202	0.87
7	112	495	0.49	111	1267	0.91

results in the lowest value of the first plateau. With further dispersion the initial height of the plateau in $|Z^*|$ rises for all further dispersion steps. Table 8.1 gives the fitted values for the equivalent circuit model.

The values show that the resistance on macro scale $R_{el,Bulk}$ is lowest after dispersion step 3. The network is well penetrated by electrical path ways, revealed by the high non-ideal character of the CPE element. Figure 8.4 (b) shows the phase shift in dependency of the frequency.

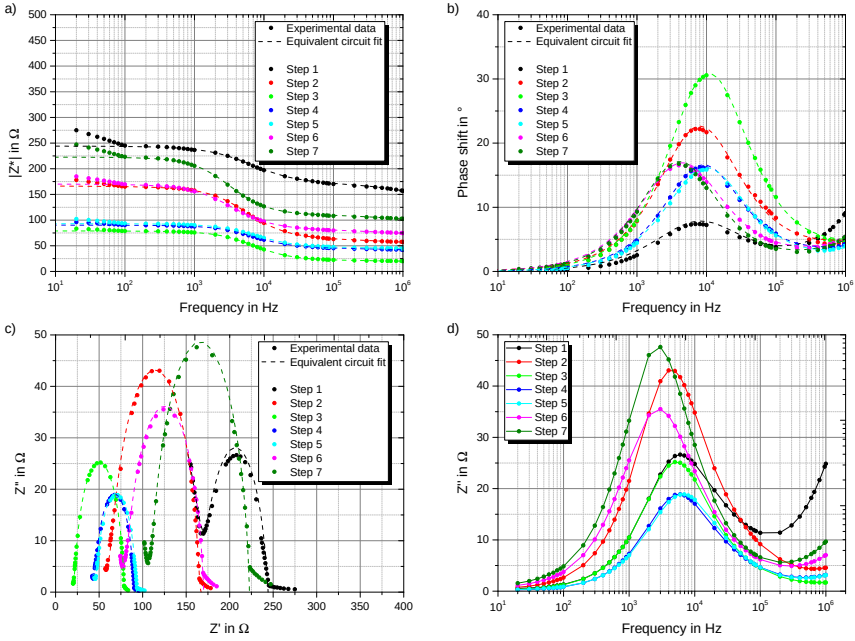


Figure 8.4: Impedance spectroscopy data evaluated for 1 wt.% filler concentration of SWCNT (**a**) dependency of absolute impedance of frequency, (**b**) dependency of phase shift on frequency, (**c**) Nyquist plot and (**d**) dependency of imaginary part Z'' on frequency

For dispersion step 3 the highest phase shift occurs and furthermore, the maximum occurs at highest frequency. A high value of phase shift corresponds to a high ratio of imaginary part and real part of the complex impedance. In this case, the maximum represents the highest capacitive behavior of the material. The higher the frequency of the maximum the more stable is the conductive particle network. Figure 8.4 (c) gives the Nyquist plot for the processing of this 1 wt.% masterbatch. With regard to the electrical properties, a small radius of the circle is desired. Figure 8.4 (d) gives the corresponding imaginary part of the complex impedance in dependency of the applied frequency. Lowest values of the occurring maximum result by application of four and five dispersion steps. A good approach to optimize the dispersion process with regard to the design target of highest conductivity at low amount of dispersion steps is the evaluation of the complex impedance in the low frequency region at 100 Hz. In case of an initial plateau the value corresponds to the initial real part Z' of the nanocomposite. Figure 8.5 (a) gives the development of Z' over the amount of dispersion steps. Lowest resistance is achieved after dispersion step 3. It is notable that the resistance rises after dispersion step 5. This may result from a damage of the particle network. Figure 8.5 (b) displays the development of the maximum imaginary part of the complex impedance Z'' and the corresponding frequency in dependency of the amount of dispersion steps.

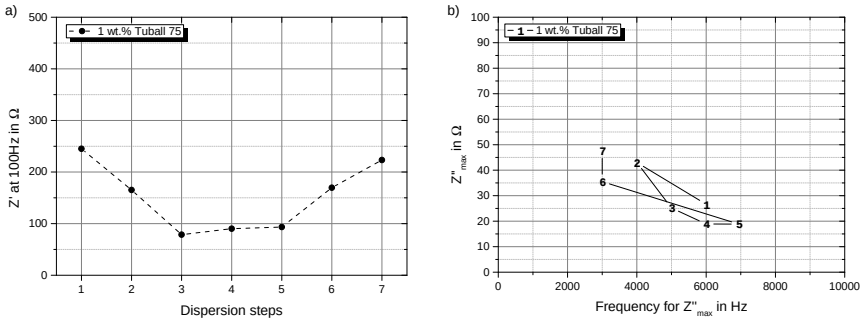


Figure 8.5: Particle size evaluated with grindometry (**a**) step-wise evaluation and (**b**) inter-batch variation after step 7

Lowest Z'' occurs for dispersion step 5, which offers as well the highest corresponding frequency. This stands for a stable particle network. For dispersion optimization the lowest Z' should be considered, because it is the target value. In this case, the masterbatch dispersion process can be reduced by 7 h and 26 min (70 %). The development of the maximum imaginary part Z''_{max} and the corresponding frequency gives a good relation with the particle dispersion. Hence, impedance spectroscopy is a mighty in-line method to evaluate the dispersion state in an easy way.

9 Application of SWCNT in a Colored GFRP with Antistatic Properties

The potential of adjustable electrical properties combined with the outstanding mechanical properties normalized on fiber-reinforced carbon nanofiller modified polymers' density, leads to promising novel industrial applications and opens further markets. Furthermore, possibility of coloring fulfills the customers' demands for individualized products. In the past carbon black was mostly utilized to achieve conductivity in polymers. In the past, multi-walled carbon nanotubes offered a huge cost advanatage compared to SWCNT, which were only available in small amounts [446]. If color was a requirement, then the addition of carbon-based fillers could not be applied. With the development of next generation carbon nanotubes, especially SWCNT, ultra-low filler addition leads to a sufficient conductivity of the polymer, as demonstrated in the previous sections. This section will give the demonstration of a signal colored and at the same time ESD protective glass fiber reinforced plastic (GFRP) flooring by utilization of ultra-low filler addition of previously used SWCNT and color pigments.
Unsaturated polyester (UP) resin AROPOL FS7993M-25, in combination with a cobalt accelerator and the peroxide catalyst ME50LY (Romar Voss) was used as polymer matrix. UP resins are mixed condensates of saturated and unsaturaded dicarbon acids with divalent alcohol groups [447] and offer several advantages. They are low cost materials, which offer adequate resistance against environmental and chemical influences. Furthermore, they withstand temperatures up to 80 °C, which is sufficient for most applications, offer low viscosity, resulting in good wetting properties of fibers and a low shrinkage [49, 448–450]. The utilized UP resin provides a low volatile organic content (VOC). Dicyclopentadiene (DCPD) serves as replacement for styrene for environmental safety purpose, flame-retardation and improved fiber wetting [451]. A low viscosity of 100 to 150 mPas makes it suitable for vacuum infusion processing [452]. Incorporation of SWCNT Tuball 75 enables the required electrical conductivity for ESD protection of the material. Addition of coloring paste PU5011 lemon yellow provided by Altropol leads to signal color of the composite. It contains organic pigments yellow PY74, a hydrocarbon based binder and a dispersing agent based on alkylammonium salt and pyrogenic silica (also known as fumed silica) to stabilize the dispersion [453]. It is reported that the resulting color is not affected by the grinding degree of the yellow pigment [454]. For manufacturing of GFRP by infusion processing unidirectional non-crimp glass fiber fabric (91 % warp, 9 % weft, 600 g/m^2) in $[0]_6$ configuration was used. In a first step, the percolation behavior of the SWCNT in neat polyester resin composite (without coloring and glass fiber) was investigated. Incorporation of SWCNT into the polymer was realized by the standard seven-step three roll milling process on TRM 120E-250. The dispersion of carbon nanoparticles in UP resin was reported before [430] and comes along with the issue of evaporation of volatile components [455]. This is addressed by utilization of the low VOC resin. After dispersion process, 1 wt.% catalyst and 0.5 wt.% accelerator were added and subsequently the dispersion was stirred under vacuum. Infusion took place with vacuum assistance into a closed aluminum mold (170 mm x 81 mm x 4 mm). Curing took place after the suggestion in the data sheet for 25 h at 30 °C [452]. The cured plate was cut into rectangular specimens (80 mm x 10 mm x 4 mm) and electrical silver paint contacts were applied on the edges. The DC resistance was determined according to the procedure reported before. Accompanying analysis of the dispersion quality via light microscopy as well as determining the influence of particle modification on glass transition temperature via differential scanning calorimetry were conducted.
With the gathered results the most adequate filler content out of the percolation curve was picked for vacuum assisted infusion process of the SWCNT modified GFRP plate as well as the colored SWCNT modified

GFRP plate. Six areas were cut from the manufactured plates and the volume and surface resistance were determined according to ASTM D257-07 [354].
The SWCNT/resin composite shows an expected decrease of the resistance with increasing filler content (see Figure 9.1 (a)). Beginning with a filler content of 0.007 wt.% the material fulfills the requirements for

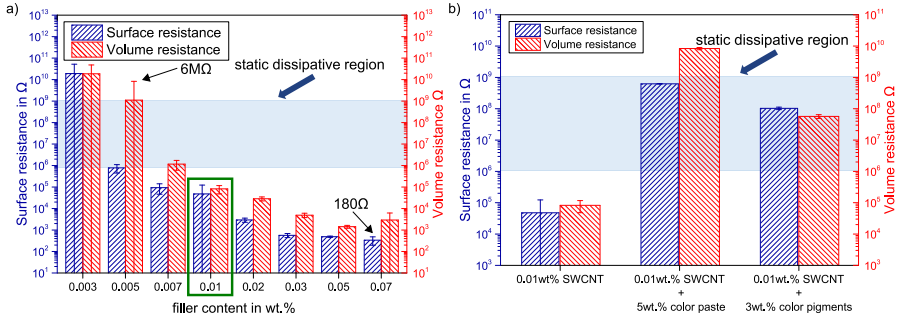


Figure 9.1: **(a)** Dependency of the surface and volume resistance on filler content and **(b)** influence of color additives on the nanocomposites' resistances

ESD protection. For the further material development a filler content of 0.01 wt.% was chosen, because an increase of resistance was assumed, resulting from addition of coloring paste and color pigments. This low filler content preserves a more resin dominated character of the final composite in comparison to highly filled modification with CB. For instance, this benefits higher chemical resistance of the material.
Multi-filler systems offer either a double percolated network (parallel existence of two percolated networks), a cooperative percolation (percolated network is formed by both particles), an aggregation of both particles or a local network anisotropy [456]. Two effects in multi-filler systems consisting of CNT and another type of filler are reported. Sumfleth [291, 424, 457] as well as Ma et al. [458] investigated the electrical properties of multi-filler systems consisting of MWCNT and CB dispersed in epoxy resin.

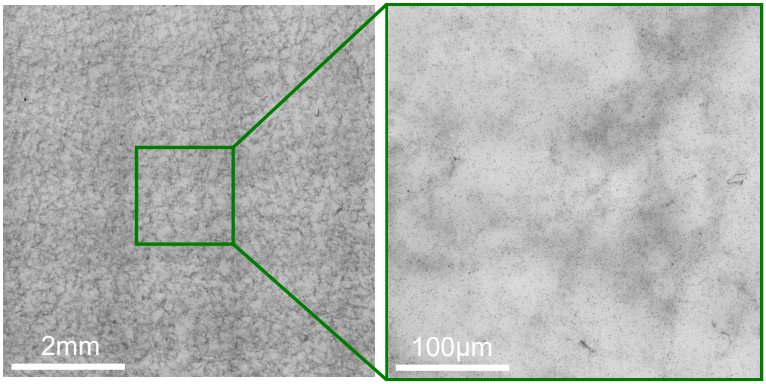


Figure 9.2: Light microscopy of unsaturated polyester resin modified with 0.01 wt.% SWCNT and 5 wt.% PU5011 lemon yellow coloring paste

Highly conductive, spherical carbon black shows a synergetic effect in combination with CNT regarding the electrical properties. The spherical particles settle at the free ends of the CNT. There they function

as bridges between the CNT and benefit the formation of the percolating electrical network by reducing tunneling distances. Non-conductive particles like titania (TiO_2) [459–461] or silica [462] combined with MWCNT have a synergetic effect, too. At optimum ratio, the conductive carbon nanoparticles cover the larger non-conductive filler particles, which promotes the formation of conductive pathways. Figure 9.1 (b) visualizes the influence of either 5 wt.% coloring paste or 3 wt.% color pigment addition on the electrical resistance. As expected, the resistance increases by addition of both coloring additives. Only pigment addition fulfills the required demands. In case of coloring paste addition, the increase in resistance exceeds the resistance range required for ESD application. Conducted DSC measurements show that color paste lowers the glass transition temperature slightly. Transfer of the aforementioned mechanisms in ternary systems to this study, the globular color pigments settle at the free ends of the SWCNT as well. These intrinsic electrically insulating pigments disturb the tunnel mechanism and therefore the electrical resistance increases. Acquired light microscopy images of the UP/SWCNT/coloring paste composite show a homogeneous distribution of particles and fine structure, compare Figure 9.2. The magnification reveals well distributed pigment particles within the SWCNT. Alkylammonium salt and pyrogenic silica act as dispersing agents [463, 464], which stabilize the dispersion and disturb the formation of the percolating network. Figure 9.3 displays a light microscopy image of the UP/SWCNT/coloring pigment composite.

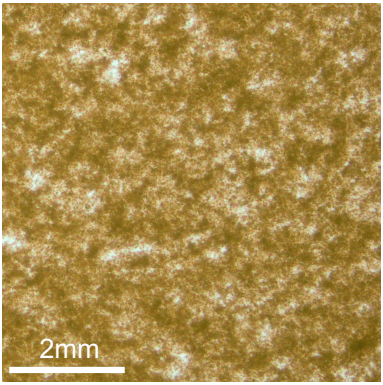


Figure 9.3: Light microscopy of unsaturated polyester resin modified with 0.01 wt.% SWCNT and 3 wt.% color pigment yellow PY74

At same magnification, this system offers a more coarse morphology. This results in more pathways and lower resistances. The composition of the coloring paste results in significant higher resistances in comparison to the addition of pristine pigments. Thus, the SWCNT modified resin with the pristine pigment features ESD protection. This composition of SWCNT and pigments is transferred into the GFRP. Figure 9.4 shows the results for the only SWCNT modified GFRP. This composite fulfills the requirements for ESD protection, all resistance values are in the demanded range.

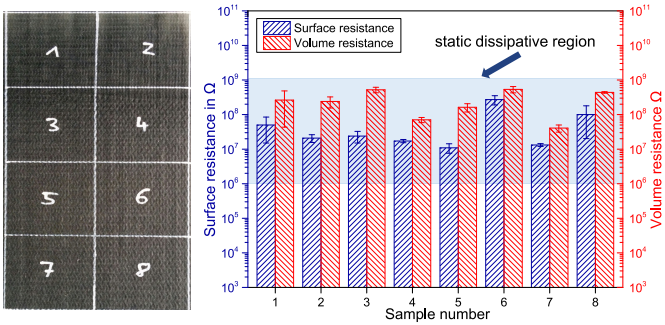


Figure 9.4: Surface and volume resistances for 0.01 wt.% SWCNT modified UP/GFRP

Figure 9.5 shows the colored GFRP with SWCNT modification and the resulting surface and volume resistances. In comparison, the surface and volume resistance values are slightly lower for the colored GFRP, but the developed colored GFRP still fulfills the requirements for ESD protection. The deviation of the measurements is much lower compared to the non-colored GFRP. Ma et al. [458] and Yue et al. [465] concluded that additional particles stabilize dispersions. Different particle geometries may lead to a concentrated re-agglomeration [466, 467] and accelerate dynamic percolation [468].

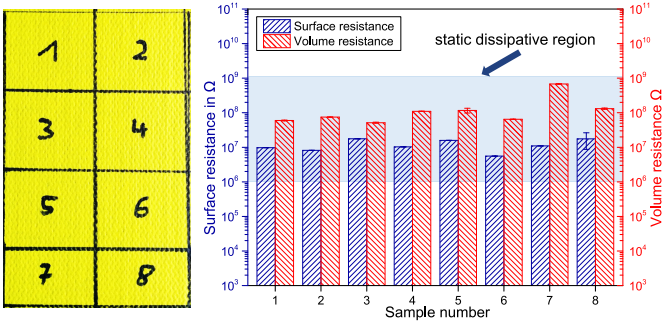


Figure 9.5: Surface and volume resistances for 0.01 wt.% SWCNT and 3 wt.% color pigment yellow PY74 modified UP/GFRP

Summarizing, the usage of new generation of SWCNT leads to an electrical percolating network even at ultra-low filler loadings of 0.01 wt.%. Within the development process, ESD protection in the nanocomposite was achieved. Transferring the used modification parameters into the fiber composite leads to the desired antistatic properties. Even with coloring, the GFRP does not lose the ESD protective properties. Ultra-low filler addition of novel SWCNT allows customizing with respect to the color and even adjustment of signal colors. Another noteworthy advantage is the ultra low required filler addition, which results on the one side in a cost advantage and on the other side the nature of the resin remains. This leads for instance in a fiber composite application to higher chemical resistance and the possibility of adjustment of other material properties by the addition of a second particle type like silica for wear resistance improvement [469].

10 Conclusion and Future Prospects

The results of this study demonstrate the high potential for application of new generation SWCNT in commercial products. An ultra low filler loading of just 0.01 wt.% leads to demanded electrical conductivity, sufficient for electrostatic discharge protection, making them superior to other available carbon based nanoparticles. This filler loading saves product costs at the material site. Rheo-electrical measurements revealed that applied shear amplitude is of major importance. The applied shear rate has minor influence. This explains the outstanding efficiency of the three roll milling process in comparison to ultrasonication. Furthermore, a technique for determination of the neat polymer's complex viscosity within a uncured nanocomposite was introduced. This could be measured by a high frequency oscillation test at low strains, without disturbing the particle network structure.

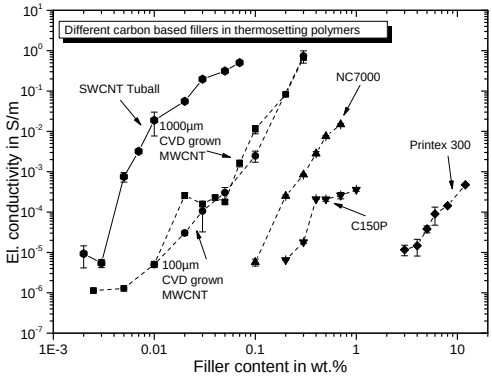


Figure 10.1: Percolation curves for carbon based nanoparticles in epoxy resin, combination of published results from [349] and [14]

Evaluation of line loads during dispersion, taking into account developed criteria for sufficient dispersion, revealed potential for process time reduction in case of carbon black, multi-walled carbon nanotubes and planar carbon nanoparticles. The highly entangled morphology of the single-walled carbon nanotubes made the utilization of a second evaluation method necessary. Successfully applied optical coherence tomography shows a decreasing particle size with increasing dispersion steps as well as the resulting particle size distribution. Impedance spectroscopy revealed the formation of the particle networks and led to the direct correlation of the target value, the electrical conductivity. A derived electrical equivalent circuit model, fitted to impedance spectra, supported the deeper understanding of particle network morphology on macro and micro level during processing. Furthermore, rheo-electrical measurements demonstrated that the particle network in case of SWCNT is not broken down by applied shear strain. This is a noteworthy advantage in case of the processibility of the material. During dispersion the highly entangled SWCNT agglomerates are spread firstly, leading to an superior increase in electrical conductivity and with ongoing dispersion steps the network structure is broken down, resulting in decrease of conductivity. The scale-up of the three roll milling process to a production of 10 kg SWCNT/epoxy masterbatch was monitored by line load evaluation and impedance spectroscopy. The total processing time was reduced by 70 %, which

makes three roll milling a compatible dispersion technique for carbon nanoparticle/epoxy composite industrial processing. Furthermore, it was proofed that dispersion by three roll milling is a highly reproducible process for a wide range of nanoparticles. The process parameters can be easily transferred from a lab scale TRM to a production TRM without affecting the dispersion quality. Figure 10.1, which adds the percolation curve of SWCNT Tuball 75 to Figure 2.8, demonstrates the high potential of the industrially available SWCNT for applications, requiring ESD properties. The required filler loading for electrical percolation lays one decade lower compared to CVD grown MWCNT offering highest quality and length. This investigated SWCNT type showed best processing properties in terms of maintaining the low viscosity of the matrix resin after dispersion. Additionally, the fracture properties, especially in mode II, were not weakened by this particle type. Their unique entangled network morphology leads to the successful application in a bright colored glass fiber reinforced plastic with antistatic properties.

The outcome of this work significantly contributed to the successful application of the project "Multifunktionale Komposite - Gedruckte Elektronik zur strukturintegrierten Zustandsüberwachung von Faser-Kunststoff-Verbunden" funded by the German Research Foundation (DFG) with the grant number 393868053.

Furthermore, the subject of this work will be continued in the consecutive applied and granted project "SCALE-Nano2Industry - SWCNT- und Graphen-Konzentrate: Vom Labormaß zum erforderlichen industriellen Produktionsmaßstab", funded by the Federal Ministry of Education and Research (BMBF) with the grant number 03XP0209C. Together with the TRM manufacturer and a resin supplier, the industrialization of the three roll milling process by demonstration of a SWCNT/unsaturated polyester masterbatch of 500 kg will be conducted. The introduced online monitoring methods will be utilized and the limitations of measuring constraints of this work will be overcome by new analytical devices. Figure 10.2 gives a impedance spectrum of 1 wt.% Printex L dispersed in EP 828LVEL, measured with the HP 4284A precision LCR meter used in this work and a Metrohm PGSTAT 204. With this device a higher electrical resistance range and a broader frequency domain can be measured. Mechanisms which could not be revealed in this work can be addressed in future studies.

Additional research, performed aside the topic of this thesis, in the field of a novel 3D-printing technology of thermosetting polymers and composites resulted in the registration of a patent as well as the successful application for the BMBF funded research project "HM3D - Reaktiver multifunktionaler Duromerwerkstoff mit thermoplastischen Eigenschaften für Filament-basierte 3D-Druckprozesse" (grant number 03XP0292C).

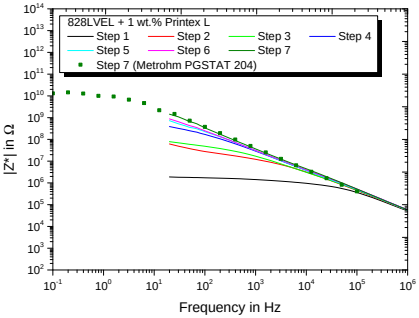


Figure 10.2: Comparison of impedance spectra measured with HP 4284A precision LCR meter and Metrohm PGSTAT 204

Bibliography

[1] Fan, Z. and Advani, S. G.: Rheology of multiwall carbon nanotube suspensions. In: *Journal of Rheology* 51 (2007),4, 585–604

[2] Rahatekar, S. S.; Koziol, K. K. K.; Butler, S. A.; Elliott, J. A.; Shaffer, M. S. P.; Mackley, M. R. and Windle, A. H.: Optical microstructure and viscosity enhancement for an epoxy resin matrix containing multiwall carbon nanotubes. In: *Journal of Rheology* 50 (2006),5, 599–610

[3] Tibbetts, G.; Lake, M.; Strong, K. and Rice, B.: A review of the fabrication and properties of vapor-grown carbon nanofiber/polymer composites. In: *Composites Science and Technology* 67 (2007),7-8, 1709–1718

[4] Atchudan, R.; Pandurangan, A. and Joo, J.: Effects of Nanofillers on the Thermo-Mechanical Properties and Chemical Resistivity of Epoxy Nanocomposites. In: *Journal of Nanoscience and Nanotechnology* 15 (2015),6, 4255–4267

[5] Khalil, H. P. S. A.; Noriman, N. Z.; Ahmad, M. N.; Ratnam, M. M. and Fuaad, N. A. N.: Polyester Composites Filled Carbon Black and Activated Carbon from Bamboo (Gigantochloa scortechinii): Physical and Mechanical Properties. In: *Journal of Reinforced Plastics and Composites* 26 (2007),3, 305–320

[6] Coleman, J. N.; Khan, U.; Blau, W. J. and Gun'ko, Y. K.: Small but strong: A review of the mechanical properties of carbon nanotube–polymer composites. In: *Carbon* 44 (2006),9, 1624–1652

[7] Stat Peel: *CNT & Graphene*. `https://www.statpeel.com/materials/cnt-carbon/`, Last checked: 05.10.2019

[8] Punetha, V. D.; Rana, S.; Yoo, H. J.; Chaurasia, A.; McLeskey, J. T.; Ramasamy, M. S.; Sahoo, N. G. and Cho, J. W.: Functionalization of carbon nanomaterials for advanced polymer nanocomposites: A comparison study between CNT and graphene. In: *Progress in Polymer Science* 67 (2017), 1–47

[9] Baughman, R. H.; Zakhidov, A. A. and Heer, W. A.: Carbon nanotubes–the route toward applications. In: *Science* 297 (2002),5582, 787–792

[10] Schüler, R.: *Entwicklung polymerer Verbundwerkstoffe mit elektrischer Leitfähigkeit: Ph.D. Thesis*. Hamburg, 1994

[11] Sandler, J.; Shaffer, M.; Prasse, T.; Bauhofer, W.; Schulte, K. and Windle, A.: Development of a dispersion process for carbon nanotubes in an epoxy matrix and the resulting electrical properties. In: *Polymer* 40 (1999),21, 5967–5971

[12] Tang, L.-C.; Wan, Y.-J.; Yan, D.; Pei, Y.-B.; Zhao, L.; Li, Y.-B.; Wu, L.-B.; Jiang, J.-X. and Lai, G.-Q.: The effect of graphene dispersion on the mechanical properties of graphene/epoxy composites. In: *Carbon* 60 (2013), 16–27

[13] Xie, X.; Mai, Y. and Zhou, X.: Dispersion and alignment of carbon nanotubes in polymer matrix: A review. In: *Materials Science and Engineering: R: Reports* 49 (2005),4, 89–112

[14] Meeuw, H.; Viets, C.; Liebig, W. V.; Schulte, K. and Fiedler, B.: Morphological influence of carbon nanofillers on the piezoresistive response of carbon nanoparticle/epoxy composites under mechanical load. In: *European Polymer Journal* 85 (2016), 198–210

[15] Novoselov, K. S.; Fal'ko, V. I.; Colombo, L.; Gellert, P. R.; Schwab, M. G. and Kim, K.: A roadmap for graphene. In: *Nature* 490 (2012),7419, 192–200

[16] Schumacher, T. and Thostenson, E. T.: Development of structural carbon nanotube–based sensing composites for concrete structures. In: *Journal of Intelligent Material Systems and Structures* 25 (2014),11, 1331–1339

[17] Stolten, D. (Hrsg.); Grube, T. (Hrsg.); M. Grundler (Hrsg.); T. Derieth (Hrsg.); P. Beckhaus (Hrsg.) and A. Heinzel (Hrsg.): *Schriften des Forschungszentrums Jülich Reihe Energie & Umwelt*. Bd. Bd. 78,1: *18th World Hydrogen Energy Conference 2010 - WHEC 2010: Proceedings*. Jülich: Forschungszentrum IEF-3, 2010

[18] Volder, M. F. L.; Tawfick, S. H.; Baughman, R. H. and Hart, A. J.: Carbon nanotubes: Present and future commercial applications. In: *Science* 339 (2013),6119, 535–539

[19] Beigbeder, A.; Degee, P.; Conlan, S. L.; Mutton, R. J.; Clare, A. S.; Pettitt, M. E.; Callow, M. E.; Callow, J. A. and Dubois, P.: Preparation and characterisation of silicone-based coatings filled with carbon nanotubes and natural sepiolite and their application as marine fouling-release coatings. In: *Biofouling* 24 (2008),4, 291–302

[20] Bauhofer, W. and Kovacs, J. Z.: A review and analysis of electrical percolation in carbon nanotube polymer composites. In: *Composites Science and Technology* 69 (2009),10, 1486–1498

[21] Bryning, M. B.; Islam, M. F.; Kikkawa, J. M. and Yodh, A. G.: Very Low Conductivity Threshold in Bulk Isotropic Single-Walled Carbon Nanotube-Epoxy Composites. In: *Advanced Materials* 17 (2005),9, 1186–1191

[22] Seoul, C.; Kim, Y.-T. and Baek, C.-K.: Electrospinning of poly(vinylidene fluoride)/dimethylformamide solutions with carbon nanotubes. In: *Journal of Polymer Science Part B: Polymer Physics* 41 (2003),13, 1572–1577

[23] Kymakis, E.; Alexandou, I. and Amaratunga, G.: Single-walled carbon nanotube–polymer composites: Electrical, optical and structural investigation. In: *Synthetic Metals* 127 (2002),1-3, 59–62

[24] M. Predtechensky and Y. Koropachinsky: *Low-cost scalable production and applications of single-walled carbon nanotubes*. Santa Clara, 2014-05-20 (Oral presentation). `http://sites.ieee.org/sfbanano/2014/04/24/low-cost-scalable-production-and-applications-of-single-walled-carbon-nanotubes/`

[25] Ren, W. and Cheng, H.-M.: The global growth of graphene. In: *Nature nanotechnology* 9 (2014),10, 726–730

[26] Eldridge, T.: *Graphene: Challenges and Opportunities*. Koblenz: Deutsche Keramische Gesellschaft, 2017-04-20 (Oral presentation given at Sitzung des Fachausschusses: Neue Kohlenstoffformen - Arbeitskreis Kohlenstoff)

[27] Zhang, Q.; Huang, J.-Q.; Qian, W.-Z.; Zhang, Y.-Y. and Wei, F.: The road for nanomaterials industry: A review of carbon nanotube production, post-treatment, and bulk applications for composites and energy storage. In: *Small* 9 (2013),8, 1237–1265

[28] Inkwood Research: *GLOBAL CARBON NANOTUBES MARKET FORECAST 2018-2026*. https://www.giiresearch.com/report/ink519825-global-carbon-nanotube-market-forecast.html. Version: 2018, Last checked: 23.09.2018

[29] *Graphene Market Size, Share , Analysis and Forecast to 2020*. https://www.marketwatch.com/press-release/graphene-market-size-share-analysis-and-forecast-to-2020-2018-04-30, Last checked: 25.09.2018

[30] *Graphene Market to Expand With Strong CAGR of 33.5% by 2023; Companies Indulging in Collaborations to Sustain Market Position*. https://www.prnewswire.com/news-releases/graphene-market-to-expand-with-strong-cagr-of-335-by-2023-companies-indulging-in-collaborations-to-sustain-market-position-680258713.html, Last checked: 25.09.2018

[31] OCSiAl: *Partnership Program*. https://ocsial.com/assets/documents/OCSiAl_Partnership_Program.pdf. Version: 2014, Last checked: 04.10.2017

[32] The Sixth Element: *About Us - The Sixth Element (Changzhou) Materials Technology Co.,Ltd*. http://www.c6th.com/about-us, Last checked: 24.04.2019

[33] Nanocyl: *Our core commitments - Nanocyl*. https://www.nanocyl.com/about-us/our-core-commitments/, Last checked: 24.04.2019

[34] Grobert, N.: Carbon nanotubes – becoming clean. In: *Materials Today* 10 (2007),1-2, 28–35

[35] OCSiAl: *Certification and H&S*. https://ocsial.com/en/certification/, Last checked: 22.09.2018

[36] OCSiAl: *The First Time Ever, Single Wall Carbon Nanotubes Complete REACH Registration*. https://ocsial.com/en/news/217/, Last checked: 04.11.2017

[37] *Sixth Element Achieves REACH Registration For Graphene And Graphene Oxide - Company news - News - The Sixth Element (Changzhou) Materials Technology Co.,Ltd*. http://www.c6th.com/news/sixth-element-achieves-reach-registration-for-15828913.html, Last checked: 25.09.2018

[38] Ma, P.-C.; Siddiqui, N. A.; Marom, G. and Kim, J.-K.: Dispersion and functionalization of carbon nanotubes for polymer-based nanocomposites: A review. In: *Composites Part A: Applied Science and Manufacturing* 41 (2010),10, 1345–1367

[39] Zhou, L.; Forman, H. J.; Ge, Y. and Lunec, J.: Multi-walled carbon nanotubes: A cytotoxicity study in relation to functionalization, dose and dispersion. In: *Toxicology in vitro : an international journal published in association with BIBRA* 42 (2017), 292–298

[40] Google LLC: *Google Scholar Profile - Hauke Voormann*. `https://scholar.google.com/citations?user=PNi5wGUAAAAJ&hl=de`, Last checked: 17.03.2021

[41] Jin, F.-L.; Li, X. and Park, S.-J.: Synthesis and application of epoxy resins: A review. In: *Journal of Industrial and Engineering Chemistry* 29 (2015), 1–11

[42] Oil and Colour Chemists' Association: *Surface coatings*. Bd. v. 1: *Raw materials and their usage: Raw Materials and Their Usage*. Dordrecht: Springer-Science+Business Media, 1993

[43] Petrie, E. M.: *Epoxy adhesive formulations*. New York: McGraw-Hill, 2006

[44] Guo, Q.: *Thermosets: Structure, properties and applications*. Cambridge UK and Philadelphia PA: Woodhead Publishing, 2012 (Woodhead Publishing in Materials)

[45] Petersen, H.: *Bisphenol A-Diglycidylether: Vorkommen, Ersatzstoffe und Reaktionen mit Lebensmittelbestandteilen: Ph.D. Thesis*. Hamburg, 2003

[46] Dümichen, E.: *Einsatz neuer thermoanalytischer Verfahren zur Untersuchung thermischer und thermo-oxidativer Degradationsmechanismen sowie dem Netzwerkaufbau von Polymeren: Ph. D. Thesis*. Berlin, 2015

[47] Le Craz, S. and Pethrick, R. A.: Solvent Effects on Cure 1-Benzyl Alcohol on Epoxy Cure. In: *International Journal of Polymeric Materials* 60 (2011),7, 441–455

[48] Osumi, Y.: One-Part Epoxy Resin. In: *Three Bond Technical News* (1987),19

[49] Ehrenstein, G. W.; Bittmann, E. and Hoffmann, L.: *Duroplaste: Aushärtung - Prüfung - Eigenschaften*. München: Hanser, op. 1997

[50] Pham, H. Q. and Marks, M. J.: Epoxy Resins. Version: 2010. In: *Ullmann's encyclopedia of industrial chemistry* Bd. 45. Weinheim: Wiley-VCH Verlag GmbH & Co. KGaA, 2010, 1

[51] Durig, J. D.: Comparisons of Epoxy Technology for Protective Coatings and Linings in Wastewater Facilities. In: Technology Publishing Company (Hrsg.): *The Industrial Protective Coatings Conference and Exhibit*, 2000 (SSPC), 31–37

[52] Jolanki, R.; Kanerva, L. and Estlander, T.: Epoxy Resins. In: Kanerva, L. (Hrsg.); Elsner, P. (Hrsg.); Wahlberg, J. E. (Hrsg.) and Maibach, H. I. (Hrsg.): *Condensed handbook of occupational dermatology*. New York: Springer, 2004, 347–363

[53] Ash, I. and Ash, M.: *Handbook of fillers, extenders, and diluents*. 2nd ed. Endicott, NY: Synapse Information Resources, 2007

[54] Ellis, B.: *Chemistry and technology of epoxy resins*. 1st edition. Dordrecht: Springer-Science+Business Media, 2015

[55] Flick, E. W.: *Epoxy resins, curing agents, compounds, and modifiers: An industrial guide*. 2nd ed. Park Ridge, N.J.: Noyes Publications, 1993

[56] Montserrat, S.: Vitrification and further structural relaxation in the isothermal curing of an epoxy resin. In: *Journal of Applied Polymer Science* 44 (1992),3, 545–554

[57] Gilbert, M. D.: *Mechanism and kinetics of the dicyandiamide cure of epoxy resins: Ph.D. Thesis*. Massachusetts, 1988

[58] Pascault, J.-P. and Williams, R. J. J.: *Epoxy polymers: New materials and innovations*. Weinheim: Wiley-VCH, 2010

[59] Mijovic, J. and Wijaya, J.: Reaction Kinetics of Epoxy/Amine Model Systems. The Effect of Electrophilicity of Amine Molecule. In: *Macromolecules* 27 (1994),26, 7589–7600

[60] Erdmann, M.; Trappe, V.; Sturm, H.; Braun, U. and Duemichen, E.: Cure conversion of structural epoxies by cure state analysis and in situ cure kinetics using nondestructive NIR spectroscopy. In: *Thermochimica Acta* 650 (2017), 8–17

[61] Guadagno, L.; Naddeo, C.; Raimondo, M.; Barra, G.; Vertuccio, L.; Russo, S.; Lafdi, K.; Tucci, V.; Spinelli, G. and Lamberti, P.: Influence of carbon nanoparticles/epoxy matrix interaction on mechanical, electrical and transport properties of structural advanced materials. In: *Nanotechnology* 28 (2017),9, 094001

[62] Fox, T. G. and Flory, P. J.: Second–Order Transition Temperatures and Related Properties of Polystyrene. I. Influence of Molecular Weight. In: *Journal of Applied Physics* 21 (1950),6, 581–591

[63] Flory, P. J.: Molecular Theory of Rubber Elasticity. In: *Polymer Journal* 17 (1985),1, 1–12

[64] Flory, P. J.: Introduction to branched molecules. In: *Annals of the New York Academy of Sciences* 57 (1953),4, 327–331

[65] Shen, M. C. and Tobolsky, A. V.: Rubber elasticity of preswollen polymer networks: Lightly crosslinked vinyl-divinyl systems. In: *Journal of Polymer Science Part A: General Papers* 2 (1964),6, 2513–2521

[66] Tobolsky, A. V.: *Properties and Structure of Polymers*. London: John Wiley and Sons Inc., 1960

[67] Tobolsky, A. V.; Carlson, D. W. and Indictor, N.: Rubber elasticity and chain configuration. In: *Journal of Polymer Science* 54 (1961),159, 175–192

[68] Tobolsky, A. V.; Katz, D.; Takahashi, M. and Schaffhauser, R.: Rubber elasticity in highly crosslinked systems: Crosslinked styrene, methyl methacrylate, ethyl acrylate, and octyl acrylate. In: *Journal of Polymer Science Part A: General Papers* 2 (1964),6, 2749–2758

[69] Elias, H.-G.: *Macromolecules: Volume 1 · Structure and Properties*. Boston, MA: Springer, 1977

[70] Ogata, M.; Kinjo, N. and Kawata, T.: Effects of crosslinking on physical properties of phenol–formaldehyde novolac cured epoxy resins. In: *Journal of Applied Polymer Science* 48 (1993),4, 583–601

[71] Barszczewska-Rybarek, I. M.; Korytkowska-Wałach, A.; Kurcok, M.; Chladek, G. and Kasperski, J.: DMA analysis of the structure of crosslinked poly(methyl methacrylate)s. In: *Acta of bioengineering and biomechanics* 19 (2017),1, 47–53

[72] Madsen, P. A. and Foister, R. T.: Network structure and properties of imidazole-cured epoxy novolac adhesives. In: *Journal of Applied Polymer Science* 37 (1989),7, 1931–1959

[73] Xu, J.; Yang, J.; Liu, X.; Wang, H.; Zhang, J. and Fu, S.: Preparation and characterization of fast-curing powder epoxy adhesive at middle temperature. In: *Royal Society open science* 5 (2018),8, 180566

[74] Levita, G.; Petris, S.de; Marchetti, A. and Lazzeri, A.: Crosslink density and fracture toughness of epoxy resins. In: *Journal of Materials Science* 26 (1991),9, 2348–2352

[75] Gupta, V. B.; Drzal, L. T.; Lee, C. Y.-C. and Rich, M. J.: The effects of stoichiometry and structure on the dynamic torsional properties of a cured epoxy resin system. In: *Journal of Macromolecular Science, Part B* 23 (1984),4-6, 435–466

[76] Nielsen, L. E.: Cross-Linking–Effect on Physical Properties of Polymers. In: *Journal of Macromolecular Science, Part C* 3 (1969),1, 69–103

[77] Allen, M. J.; Tung, V. C. and Kaner, R. B.: Honeycomb carbon: a review of graphene. In: *Chemical reviews* 110 (2010),1, 132–145

[78] Kroto, H. W.; Heath, J. R.; O'Brien, S. C.; Curl, R. F. and Smalley, R. E.: C60: Buckminsterfullerene. In: *Nature* 318 (1985),6042, 162–163

[79] Hirsch, A. and Brettreich, M.: *Fullerenes: Chemistry and reactions*. Weinheim: Wiley-VCH, 2004

[80] Iijima, S.: Helical microtubules of graphitic carbon. In: *Nature* 354 (1991),6348, 56–58

[81] Novoselov, K. S.; Geim, A. K.; Morozov, S. V.; Jiang, D.; Zhang, Y.; Dubonos, S. V.; Grigorieva, I. V. and Firsov, A. A.: Electric field effect in atomically thin carbon films. In: *Science* 306 (2004),5696, 666–669

[82] Nair, R. R.; Ren, W.; Jalil, R.; Riaz, I.; Kravets, V. G.; Britnell, L.; Blake, P.; Schedin, F.; Mayorov, A. S.; Yuan, S.; Katsnelson, M. I.; Cheng, H.-M.; Strupinski, W.; Bulusheva, L. G.; Okotrub, A. V.; Grigorieva, I. V.; Grigorenko, A. N.; Novoselov, K. S. and Geim, A. K.: It's still all about graphene. In: *Nature materials* 10 (2011),1, 1

[83] Geim, A. K. and Novoselov, K. S.: The rise of graphene. In: *Nature materials* 6 (2007),3, 183–191

[84] Taghioskoui, M.: Trends in graphene research. In: *Materials Today* 12 (2009),10, 34–37

[85] Hirsch, A.: The era of carbon allotropes. In: *Nature materials* 9 (2010),11, 868–871

[86] Mecklenburg, M.: *Ultra-hoch gefüllte orientierte CNT- und 3D-vernetzte Aerographit/Epoxid Komposite: Synthese, Herstellung und Eigenschaften: Ph.D. Thesis*. Hamburg, 2017

[87] Singh, V.; Joung, D.; Zhai, L.; Das, S.; Khondaker, S. I. and Seal, S.: Graphene based materials: Past, present and future. In: *Progress in Materials Science* 56 (2011),8, 1178–1271

[88] Li, H.; Xu, C.; Srivastava, N. and Banerjee, K.: Carbon Nanomaterials for Next-Generation Interconnects and Passives: Physics, Status, and Prospects. In: *IEEE Transactions on Electron Devices* 56 (2009),9, 1799–1821

[89] Terrones, M.; Botello-Méndez, A. R.; Campos-Delgado, J.; López-Urías, F.; Vega-Cantú, Y. I.; Rodríguez-Macías, F. J.; Elías, A. L.; Muñoz-Sandoval, E.; Cano-Márquez, A. G. and Charlier, J.-C.: Graphene and graphite nanoribbons: Morphology, properties, synthesis, defects and applications. In: *Nano Today* 5 (2010),4, 351–372

[90] Rock, P. A.: *Chemical thermodynamics*. University Science Books, 2013

[91] Bundy, F. P.; Bassett, W. A.; Weathers, M. S.; Hemley, R. J.; Mao, H. U. and Goncharov, A. F.: The pressure-temperature phase and transformation diagram for carbon; updated through 1994. In: *Carbon* 34 (1996),2, 141–153

[92] Gulbransen, E. A.; Andrew, K. F. and Brassart, F. A.: The Oxidation of Graphite at Temperatures of 600° to 1500°C and at Pressures of 2 to 76 Torr of Oxygen. In: *Journal of the Electrochemical Society* 110 (1963),6, 476

[93] Fitzer, E.; Kochling, K.-H.; Boehm, H. P. and Marsh, H.: Recommended terminology for the description of carbon as a solid (IUPAC Recommendations 1995). In: *Pure and Applied Chemistry* 67 (1995),3

[94] Klose, W.: *Fachausschussbericht / Deutsche Keramische Gesellschaft ... Bericht des Arbeitskreises "Kohlenstoff"*. Bd. 3: *Terminologie zur Beschreibung von Kohlenstoff als Feststoff*. Kassel: Kassel Univ. Press, 2009

[95] Mecklenburg, M.; Schuchardt, A.; Mishra, Y. K.; Kaps, S.; Adelung, R.; Lotnyk, A.; Kienle, L. and Schulte, K.: Aerographite: ultra lightweight, flexible nanowall, carbon microtube material with outstanding mechanical performance. In: *Advanced materials* 24 (2012),26, 3486–3490

[96] onlineidc: *Classification of carbon materials*. `http://www.idc-online.com/technical_references/pdfs/chemical_engineering/Classification_of_carbon_materials.pdf`, Last checked: 11.11.2018

[97] Harold Scholz & Co GmbH: *Carbon Black*. `https://www.harold-scholz.de/produkte-hs/carbon-black`, Last checked: 11.11.2018

[98] Pentacarbon: *Unser Wiki: Alles rund um Carbon Black - PentaCarbon GmbH*. `https://pentacarbon.de/wiki/`, Last checked: 11.11.2018

[99] Ronco, C. (Hrsg.); Bellomo, R. (Hrsg.); Kellum, J. A. (Hrsg.) and Ricci, Z. (Hrsg.): *Critical care nephrology*. Third edition. Philadelphia, PA: Elsevier, 2019

[100] Baur, E.: *Saechtling Kunststoff Taschenbuch*. 31. Ausg. München: Carl Hanser Verlag GmbH & Co. KG, 2013

[101] ICBA: *Carbon Black User's Guide: Safety, Health, & Environmental Information*. `http://www.carbon-black.org/images/docs/2016-ICBA-Carbon-Black-User-Guide.pdf`, Last checked: 03.03.2019

[102] Suarez-Martinez, I.; Grobert, N. and Ewels, C. P.: Nomenclature of sp2 carbon nanoforms. In: *Carbon* 50 (2012),3, 741–747

[103] Odom, T. W.; Huang, J.-L.; Kim, P. and Lieber, C. M.: Atomic structure and electronic properties of single-walled carbon nanotubes. In: *Nature* 391 (1998),6662, 62–64

[104] Thostenson, E. T.; Ren, Z. and Chou, T.-W.: Advances in the science and technology of carbon nanotubes and their composites: A review. In: *Composites Science and Technology* 61 (2001),13, 1899–1912

[105] Schwarz, M.-K.: *Elektrisch leitfähige Füllstoffnetzwerke in Duroplasten auf der Basis von Kohlenstoff-Nanopartikeln, -Nanofasern und -Nanotubes*. 1. Aufl. Göttingen: Cuvillier, 2006

[106] Balasubramanian, K. and Burghard, M.: Chemically functionalized carbon nanotubes. In: *Small (Weinheim an der Bergstrasse, Germany)* 1 (2005),2, 180–192

[107] Spasenovic, M.: *McKinsey estimates a $70 billion market for graphene semiconductors in 2030*. `https://www.graphenea.com/blogs/graphene-news/mckinsey-estimates-a-70-billion-market-for-graphene-semiconductors-in-2030`, Last checked: 02.03.2019

[108] Chandrasekaran, S.: *Development of nano-particle modified polymer matrices for improved fibre reinforced composites: Ph.D. Thesis*. Hamburg, 2014

[109] Hummers, W. S. and Offeman, R. E.: Preparation of Graphitic Oxide. In: *Journal of the American Chemical Society* 80 (1958),6, 1339

[110] Ramanathan, T.; Abdala, A. A.; Stankovich, S.; Dikin, D. A.; Herrera-Alonso, M.; Piner, R. D.; Adamson, D. H.; Schniepp, H. C.; Chen, X.; Ruoff, R. S.; Nguyen, S. T.; Aksay, I. A.; Prud'Homme, R. K. and Brinson, L. C.: Functionalized graphene sheets for polymer nanocomposites. In: *Nature nanotechnology* 3 (2008),6, 327–331

[111] Steurer, P.; Wissert, R.; Thomann, R. and Mülhaupt, R.: Functionalized Graphenes and Thermoplastic Nanocomposites Based upon Expanded Graphite Oxide. In: *Macromolecular rapid communications* 30 (2009),4-5, 316–327

[112] Yang, S.; Ricciardulli, A. G.; Liu, S.; Dong, R.; Lohe, M. R.; Becker, A.; Squillaci, M. A.; Samorì, P.; Müllen, K. and Feng, X.: Ultrafast Delamination of Graphite into High-Quality Graphene Using Alternating Currents. In: *Angewandte Chemie (International ed. in English)* 56 (2017),23, 6669–6675

[113] Yang, S.; Ricciardulli, A. G.; Liu, S.; Dong, R.; Lohe, M. R.; Becker, A.; Squillaci, M. A.; Samorì, P.; Müllen, K. and Feng, X.: Ultraschnelle Schichtablösung von Graphit zu qualitativ hochwertigem Graphen durch Nutzung von Wechselstrom. In: *Angewandte Chemie* 129 (2017),23, 6770–6776

[114] Wick, P.; Louw-Gaume, A. E.; Kucki, M.; Krug, H. F.; Kostarelos, K.; Fadeel, B.; Dawson, K. A.; Salvati, A.; Vázquez, E.; Ballerini, L.; Tretiach, M.; Benfenati, F.; Flahaut, E.; Gauthier, L.; Prato, M. and Bianco, A.: Classification framework for graphene-based materials. In: *Angewandte Chemie (International ed. in English)* 53 (2014),30, 7714–7718

[115] Bianco, A.; Cheng, H.-M.; Enoki, T.; Gogotsi, Y.; Hurt, R. H.; Koratkar, N.; Kyotani, T.; Monthioux, M.; Park, C. R.; Tascon, J. M. and Zhang, J.: All in the graphene family – A recommended nomenclature for two-dimensional carbon materials. In: *Carbon* 65 (2013), 1–6

[116] Feynman, R. P.: *There's plenty of room at the bottom, lecture at the American Physical Society, Caltech, The Pleasure of Finding Things Out and the Meaning of It All*. 1959 (Annual meeting of American Physical Society)

[117] Castro Neto, A. H.; Guinea, F.; Peres, N. M. R.; Novoselov, K. S. and Geim, A. K.: The electronic properties of graphene. In: *Reviews of Modern Physics* 81 (2009),1, 109–162

[118] Stankovich, S.; Dikin, D. A.; Piner, R. D.; Kohlhaas, K. A.; Kleinhammes, A.; Jia, Y.; Wu, Y.; Nguyen, S. T. and Ruoff, R. S.: Synthesis of graphene-based nanosheets via chemical reduction of exfoliated graphite oxide. In: *Carbon* 45 (2007),7, 1558–1565

[119] Hernandez, Y.; Nicolosi, V.; Lotya, M.; Blighe, F. M.; Sun, Z.; De, S.; McGovern, I. T.; Holland, B.; Byrne, M.; Gun'Ko, Y. K.; Boland, J. J.; Niraj, P.; Duesberg, G.; Krishnamurthy, S.; Goodhue, R.; Hutchison, J.; Scardaci, V.; Ferrari, A. C. and Coleman, J. N.: High-yield production of graphene by liquid-phase exfoliation of graphite. In: *Nature nanotechnology* 3 (2008),9, 563–568

[120] Emtsev, K. V.; Bostwick, A.; Horn, K.; Jobst, J.; Kellogg, G. L.; Ley, L.; McChesney, J. L.; Ohta, T.; Reshanov, S. A.; Röhrl, J.; Rotenberg, E.; Schmid, A. K.; Waldmann, D.; Weber, H. B. and Seyller, T.: Towards wafer-size graphene layers by atmospheric pressure graphitization of silicon carbide. In: *Nature materials* 8 (2009),3, 203–207

[121] Sutter, P. W.; Flege, J.-I. and Sutter, E. A.: Epitaxial graphene on ruthenium. In: *Nature materials* 7 (2008),5, 406–411

[122] Kim, K. S.; Zhao, Y.; Jang, H.; Lee, S. Y.; Kim, J. M.; Kim, K. S.; Ahn, J.-H.; Kim, P.; Choi, J.-Y. and Hong, B. H.: Large-scale pattern growth of graphene films for stretchable transparent electrodes. In: *Nature* 457 (2009),7230, 706–710

[123] Choucair, M.; Thordarson, P. and Stride, J. A.: Gram-scale production of graphene based on solvothermal synthesis and sonication. In: *Nature nanotechnology* 4 (2009),1, 30–33

[124] Parvez, K.; Wu, Z.-S.; Li, R.; Liu, X.; Graf, R.; Feng, X. and Müllen, K.: Exfoliation of graphite into graphene in aqueous solutions of inorganic salts. In: *Journal of the American Chemical Society* 136 (2014),16, 6083–6091

[125] Li, J.; Sollami Delekta, S.; Zhang, P.; Yang, S.; Lohe, M. R.; Zhuang, X.; Feng, X. and Östling, M.: Scalable Fabrication and Integration of Graphene Microsupercapacitors through Full Inkjet Printing. In: *ACS nano* 11 (2017),8, 8249–8256

[126] Bae, J. H.; Shanmugharaj, A. M.; Noh, W. H.; Choi, W. S. and Ryu, S. H.: Surface chemical functionalized single-walled carbon nanotube with anchored phenol structures: Physical and chemical characterization. In: *Applied Surface Science* 253 (2007),9, 4150–4155

[127] Mittal, G.; Dhand, V.; Rhee, K. Y.; Park, S.-J. and Lee, W. R.: A review on carbon nanotubes and graphene as fillers in reinforced polymer nanocomposites. In: *Journal of Industrial and Engineering Chemistry* 21 (2015), 11–25

[128] Gojny, F. H.; Nastalczyk, J.; Roslaniec, Z. and Schulte, K.: Surface modified multi-walled carbon nanotubes in CNT/epoxy-composites. In: *Chemical Physics Letters* 370 (2003),5-6, 820–824

[129] Avilés, F.; Cauich-Rodríguez, J. V.; Moo-Tah, L.; May-Pat, A. and Vargas-Coronado, R.: Evaluation of mild acid oxidation treatments for MWCNT functionalization. In: *Carbon* 47 (2009),13, 2970–2975

[130] Gojny, F. H.; Wichmann, M. H.; Fiedler, B.; Bauhofer, W. and Schulte, K.: Influence of nano-modification on the mechanical and electrical properties of conventional fibre-reinforced composites. In: *Composites Part A: Applied Science and Manufacturing* 36 (2005),11, 1525–1535

[131] Geng, Y.; Liu, M. Y.; Li, J.; Shi, X. M. and Kim, J. K.: Effects of surfactant treatment on mechanical and electrical properties of CNT/epoxy nanocomposites. In: *Composites Part A: Applied Science and Manufacturing* 39 (2008),12, 1876–1883

[132] Leon, V.; Parret, R.; Almairac, R.; Alvarez, L.; Babaa, M.-R.; Doyle, B. P.; Ienny, P.; Parent, P.; Zahab, A. and Bantignies, J.-L.: Spectroscopic study of double-walled carbon nanotube functionalization for preparation of carbon nanotube / epoxy composites. In: *Carbon* 50 (2012),14, 4987–4994

[133] Pourfayaz, F.; Khodadadi, A. A.; Mortazavi, Y. and Jafari, S.-H.: Plasma Functionalization of MWCNTs in He Followed by NH3 Treatment and its Application in PMMA Based Nanocomposites. In: *Plasma Processes and Polymers* 7 (2010),12, 1001–1009

[134] Pourfayaz, F.; Khodadadi, A. A.; Jafari, S.-H.; Mortazavi, Y. and Khonakdar, H. A.: Ultra-low Electrical and Rheological Percolation Thresholds in PMMA/Plasma-Functionalized CNTs Nanocomposites. In: *Polymer-Plastics Technology and Engineering* 53 (2014),14, 1450–1455

[135] Pidoll, U.von: Helmut Krämer memorial lecture: Electrostatic assessment of products and processes – A view backwards and forwards. In: *Journal of Electrostatics* 71 (2013),3, 586–590

[136] Perrin, L.; Laurent, A.; Falk, V.; Dufaud, O. and Traoré, M.: Dust and electrostatic hazards, could we improve the current standards? In: *Journal of Loss Prevention in the Process Industries* 20 (2007),3, 207–217

[137] Drake, N.: *Polymeric materials for electrostatic applications: A report from Rapra's Industry Analysis and Publishing Group*. Shrewsbury: Rapra Technology Ltd, 1996

[138] Britton, L. G.: *Avoiding static ignition hazards in chemical operations*. New York, NY: Center for Chemical Process Safety of the American Institute of Chemical Engineers, 1999 (A CCPS concept book)

[139] American National Standards Institute (ANSI), American National Standards Institute: *ESDA/-JEDEC Joint Standard for Electrostatic Discharge Sensitivity Testing - Human Body Model (HBM) - Component Level*. 2017

[140] Wypych, G. (Hrsg.) and Pionteck, J. (Hrsg.): *Handbook of antistatics*. Second edition. Toronto: ChemTec Publishing, 2016

[141] ASTM F150 - F06: *Test Method for Electrical Resistance of Conductive and Static Dissipative Resilient Flooring*. West Conshohocken: ASTM International, 2006

[142] proHPL Fachgruppe Dekorative Schichtstoffplatten: *Elektrostatische Ableitfähigkeit von Dekorativen Schichtstoffen (HPL): HPL nach EN 438*. Frankfurt am Main, 2008

[143] Bao, W. S.; Meguid, S. A.; Zhu, Z. H. and Weng, G. J.: Tunneling resistance and its effect on the electrical conductivity of carbon nanotube nanocomposites. In: *Journal of Applied Physics* 111 (2012),9, 093726

[144] Paschen, S.; Bussac, M. N.; Zuppiroli, L.; Minder, E. and Hilti, B.: Tunnel junctions in a polymer composite. In: *Journal of Applied Physics* 78 (1995),5, 3230–3237

[145] Wei, C.; Akinwolemiwa, B.; Yu, L.; Hu, D. and Chen, G. Z.: Polymer Composites with Functionalized Carbon Nanotube and Graphene. Version: 2019. In: Pielichowski, K. (Hrsg.) and Majka, T. M. (Hrsg.): *Polymer composites with functionalized nanoparticles*. Amsterdam, Netherlands and Cambridge, MA: Elsevier, 2019 (Micro and nano technologies), 211–248

[146] Sherman, R. D.; Middleman, L. M. and Jacobs, S. M.: Electron transport processes in conductor-filled polymers. In: *Polymer Engineering and Science* 23 (1983),1, 36–46

[147] Li, C.; Thostenson, E. T. and Chou, T.-W.: Sensors and actuators based on carbon nanotubes and their composites: A review. In: *Composites Science and Technology* 68 (2008),6, 1227–1249

[148] Alamusi; Hu, N.; Fukunaga, H.; Atobe, S.; Liu, Y. and Li, J.: Piezoresistive strain sensors made from carbon nanotubes based polymer nanocomposites. In: *Sensors (Basel, Switzerland)* 11 (2011),11, 10691–10723

[149] Simmons, J. G.: Generalized Formula for the Electric Tunnel Effect between Similar Electrodes Separated by a Thin Insulating Film. In: *Journal of Applied Physics* 34 (1963),6, 1793–1803

[150] Dirac, P. A. M.: Quantum Mechanics and a Preliminary Investigation of the Hydrogen Atom. In: *Proceedings of the Royal Society A: Mathematical, Physical and Engineering Sciences* 110 (1926),755, 561–579

[151] Schrödinger, E.: An Undulatory Theory of the Mechanics of Atoms and Molecules. In: *Physical Review* 28 (1926),6, 1049–1070

[152] Gojny, F. H.; Wichmann, M. H.; Fiedler, B.; Kinloch, I. A.; Bauhofer, W.; Windle, A. H. and Schulte, K.: Evaluation and identification of electrical and thermal conduction mechanisms in carbon nanotube/epoxy composites. In: *Polymer* 47 (2006),6, 2036–2045

[153] Mathew, M.; Schilling, T. and Oettel, M.: Connectivity percolation in suspensions of hard platelets. In: *Physical review. E, Statistical, nonlinear, and soft matter physics* 85 (2012),6, 061407

[154] Manta, A.; Gresil, M. and Soutis, C.: Predictive Model of Graphene Based Polymer Nanocomposites: Electrical Performance. In: *Applied Composite Materials* 24 (2017),2, 281–300

[155] Zallen, R.: *The physics of amorphous solids*. Weinheim: Wiley, 2004

[156] Schueler, R.; Petermann, J.; Schulte, K. and Wentzel, H.-P.: Agglomeration and electrical percolation behavior of carbon black dispersed in epoxy resin. In: *Journal of Applied Polymer Science* 63 (1997),13, 1741–1746

[157] Kirkpatrick, S.: Percolation and Conduction. In: *Reviews of Modern Physics* 45 (1973),4, 574–588

[158] Celzard, A.; McRae, E.; Deleuze, C.; Dufort, M.; Furdin, G. and Marêché, J. F.: Critical concentration in percolating systems containing a high-aspect-ratio filler. In: *Physical Review B* 53 (1996),10, 6209–6214

[159] Balberg, I.; Anderson, C. H.; Alexander, S. and Wagner, N.: Excluded volume and its relation to the onset of percolation. In: *Physical Review B* 30 (1984),7, 3933–3943

[160] Martin, C. A.; Sandler, J.; Shaffer, M.; Schwarz, M.-K.; Bauhofer, W.; Schulte, K. and Windle, A. H.: Formation of percolating networks in multi-wall carbon-nanotube–epoxy composites. In: *Composites Science and Technology* 64 (2004),15, 2309–2316

[161] Fiedler, B. and Schulte, K.: 6.8 Carbon Nanotube-Based Composites. Version: 2018. In: Zweben, C. H. (Hrsg.) and Beaumont, P. W. R. (Hrsg.): *Comprehensive composite materials II*. Amsterdam, Netherlands: Elsevier, 2018, 201–229

[162] Novotny, V. J.: Physics of Nonaqueous Colloids. In: Hair, M. L. (Hrsg.): *Colloids and surfaces in reprographic technology* Bd. 200. Washington, DC: American Chemical Society, 1982, 281–306

[163] Gast, A. P. and Zukoski, C. F.: Electrorheological fluids as colloidal suspensions. In: *Advances in colloid and interface science* 30 (1989), 153–202

[164] Brezesinski, G. and Mögel, H.-J.: *Grenzflächen und Kolloide: Physikalisch-chemische Grundlagen ; mit 3 Tabellen*. 1993

[165] Hunter, R. J.: *Introduction to modern colloid science*. Reprinted with corr. Oxford u.a.: Oxford Univ. Press, 1996

[166] Ruffmann, B. and Zimehl, R.: Der Einfluss von adsorbiertem Lösungsmittel (Lyosphären)auf die Kolloidstabilität. In: *Chemie Ingenieur Technik* 72 (2000),3, 256–259

[167] Boehm, H.: Surface oxides on carbon and their analysis: a critical assessment. In: *Carbon* 40 (2002),2, 145–149

[168] Fowkes, F. M.; Jinnai, H.; Mostafa, M. A.; Anderson, F. W. and Moore, R. J.: Mechanism of Electric Charging of Particles in Nonaqueous Liquids. Version: 1982. In: Hair, M. L. (Hrsg.): *Colloids and surfaces in reprographic technology* Bd. 200. Washington, DC: American Chemical Society, 1982, 307–324

[169] Prasse, T.; Schwarz, M.-K.; Schulte, K. and Bauhofer, W.: The interaction of epoxy resin and an additional electrolyte with non-oxidised carbon black in colloidal dispersions. In: *Colloids and Surfaces A: Physicochemical and Engineering Aspects* 189 (2001),1-3, 183–188

[170] Helmholtz, H.: Über einige Gesetze der Vertheilung elektrischer Ströme in körperlichen Leitern mit Anwendung auf die thierisch-elektrischen Versuche. In: *Annalen der Physik und Chemie* 165 (1853),6, 211–233

[171] Korzeniewski, C.: *Proceedings / Electrochemical Society*. Bd. vol. 97-17: *Proceedings of the Symposium on the Electrochemical Double Layer*. Pennington, NJ: Electrochemical Society, 1997

[172] Zeichner, G. R. and Schowalter, W. R.: Effects of hydrodynamic and colloidal forces on the coagulation of dispersions. In: *Journal of Colloid and Interface Science* 71 (1979),2, 237–253

[173] Hunt, R. J. and Johnson, W. P.: Pathogen transport in groundwater systems: contrasts with traditional solute transport. In: *Hydrogeology Journal* 25 (2017),4, 921–930

[174] Yoon, H.; Yamashita, M.; Ata, S.; Futaba, D. N.; Yamada, T. and Hata, K.: Controlling exfoliation in order to minimize damage during dispersion of long SWCNTs for advanced composites. In: *Scientific reports* 4 (2014), 3907

[175] Gojny, F. H.; Wichmann, M.; Köpke, U.; Fiedler, B. and Schulte, K.: Carbon nanotube-reinforced epoxy-composites: Enhanced stiffness and fracture toughness at low nanotube content. In: *Composites Science and Technology* 64 (2004),15, 2363–2371

[176] Ma, A. W. K.; Yearsley, K. M.; Chinesta, F. and Mackley, M. R.: A review of the microstructure and rheology of carbon nanotube suspensions. In: *Proceedings of the Institution of Mechanical Engineers, Part N: Journal of Nanoengineering and Nanosystems* 222 (2009),3, 71–94

[177] Tarlton, T.; Sullivan, E.; Brown, J. and Derosa, P. A.: The role of agglomeration in the conductivity of carbon nanotube composites near percolation. In: *Journal of Applied Physics* 121 (2017),8, 085103

[178] Spitalsky, Z.; Tasis, D.; Papagelis, K. and Galiotis, C.: Carbon nanotube–polymer composites: Chemistry, processing, mechanical and electrical properties. In: *Progress in Polymer Science* 35 (2010),3, 357–401

[179] Li, J.; Ma, P. C.; Chow, W. S.; To, C. K.; Tang, B. Z. and Kim, J.-K.: Correlations between Percolation Threshold, Dispersion State, and Aspect Ratio of Carbon Nanotubes. In: *Advanced Functional Materials* 17 (2007),16, 3207–3215

[180] Majidian, M.; Grimaldi, C.; Forró, L. and Magrez, A.: Role of the particle size polydispersity in the electrical conductivity of carbon nanotube-epoxy composites. In: *Scientific reports* 7 (2017),1, 12553

[181] Fiedler, B.; Gojny, F. H.; Wichmann, M. H.; Nolte, M. C. and Schulte, K.: Fundamental aspects of nano-reinforced composites. In: *Composites Science and Technology* 66 (2006),16, 3115–3125

[182] Moller, B. P.: *Herstellung, Charakterisierung und Weiterverarbeitung von Carbon Nanotube Dispersionen: Ph.D. Thesis*. Stuttgart, 2013

[183] Müller, K.; Bugnicourt, E.; Latorre, M.; Jorda, M.; Echegoyen Sanz, Y.; Lagaron, J. M.; Miesbauer, O.; Bianchin, A.; Hankin, S.; Bölz, U.; Pérez, G.; Jesdinszki, M.; Lindner, M.; Scheuerer, Z.; Castelló, S. and Schmid, M.: Review on the Processing and Properties of Polymer Nanocomposites and Nanocoatings and Their Applications in the Packaging, Automotive and Solar Energy Fields. In: *Nanomaterials* 7 (2017),4

[184] Tung, T. T.; Karunagaran, R.; Tran, D. N. H.; Gao, B.; Nag-Chowdhury, S.; Pillin, I.; Castro, M.; Feller, J.-F. and Losic, D.: Engineering of graphene/epoxy nanocomposites with improved distribution of graphene nanosheets for advanced piezo-resistive mechanical sensing. In: *Journal of Materials Chemistry C* 4 (2016),16, 3422–3430

[185] Al-Hamadani, Y. A.; Chu, K. H.; Son, A.; Heo, J.; Her, N.; Jang, M.; Park, C. M. and Yoon, Y.: Stabilization and dispersion of carbon nanomaterials in aqueous solutions: A review. In: *Separation and Purification Technology* 156 (2015), 861–874

[186] Hielscher, T.: Ultrasonic Production of Nano-Size Dispersions and Emulsions. In: *Dans European Nano Systems Worshop - ENS 2005* (2005)

[187] Texter, J.: Graphene dispersions. In: *Current Opinion in Colloid & Interface Science* 19 (2014),2, 163–174

[188] Frømyr, T. R.; Hansen, F. K. and Olsen, T.: The Optimum Dispersion of Carbon Nanotubes for Epoxy Nanocomposites: Evolution of the Particle Size Distribution by Ultrasonic Treatment. In: *Journal of Nanotechnology* 2012 (2012),6348, 1–14

[189] Gkikas, G.; Barkoula, N.-M. and Paipetis, A. S.: Effect of dispersion conditions on the thermo-mechanical and toughness properties of multi walled carbon nanotubes-reinforced epoxy. In: *Composites Part B: Engineering* 43 (2012),6, 2697–2705

[190] Faiella, G.; Antonucci, V.; Buschhorn, S. T.; Prado, L. A.; Schulte, K. and Giordano, M.: Tailoring the electrical properties of MWCNT/epoxy composites controlling processing conditions. In: *Composites Part A: Applied Science and Manufacturing* 43 (2012),9, 1441–1447

[191] Inam, F.; Reece, M. J. and Peijs, T.: Shortened carbon nanotubes and their influence on the electrical properties of polymer nanocomposites. In: *Journal of Composite Materials* 46 (2011),11, 1313–1322

[192] Huang, Y. Y. and Terentjev, E. M.: Dispersion of Carbon Nanotubes: Mixing, Sonication, Stabilization, and Composite Properties. In: *Polymers* 4 (2012),1, 275–295

[193] Krause, B.; Mende, M.; Pötschke, P. and Petzold, G.: Dispersability and particle size distribution of CNTs in an aqueous surfactant dispersion as a function of ultrasonic treatment time. In: *Carbon* 48 (2010),10, 2746–2754

[194] Pötschke, P.; Mothes, F.; Krause, B. and Voit, B.: Melt-Mixed PP/MWCNT Composites: Influence of CNT Incorporation Strategy and Matrix Viscosity on Filler Dispersion and Electrical Resistivity. In: *Polymers* 11 (2019),2, 189

[195] Müller, M. T.; Krause, B.; Kretzschmar, B. and Pötschke, P.: Influence of a supplemental filler in twin-screw extruded PP/CNT composites using masterbatch dilution. In: *AIP Conference Proceedings*, AIP, 2019 (AIP Conference Proceedings), 090006

[196] Fawad, I. and Ton, P.: Re-agglomeration of Carbon nanotubes in two-part epoxy system; Influence of the concentration. In: *In: 5th International Bhurbhan Conference on Applied Science and Technology (IBCAST 2007)* Islamabad, Pakistan (8-11 January 2007)

[197] Sumfleth, J.; Prehn, K.; Wichmann, M. H.; Wedekind, S. and Schulte, K.: A comparative study of the electrical and mechanical properties of epoxy nanocomposites reinforced by CVD- and arc-grown multi-wall carbon nanotubes. In: *Composites Science and Technology* 70 (2010),1, 173–180

[198] Thostenson, E. T. and Chou, T.-S.: Processing-structure-multi-functional property relationship in carbon nanotube/epoxy composites. In: *Carbon* 44 (2006),14, 3022–3029

[199] Conley, R. F.: *Practical dispersion: A guide to understanding and formulating slurries*. New York: VCH Publishers, 1996

[200] Thostenson, E. T. and Chou, T.-W.: Carbon nanotube-based health monitoring of mechanically fastened composite joints. In: *Composites Science and Technology* 68 (2008),12, 2557–2561

[201] Ancker, F.: *Apparatus for the calendering of polymeric materials*. Patent: US3765817A, 1973 (Google Patents)

[202] OCSiAl: *TUBALL COMP_E EPOXY Production and Quality Control Manual*. 2015

[203] Frydel, J.; Mewes, D.; Luther, S. and Schuster, R. H.: Rubber sheets calendering 1 : Contribution to preventing the occurrence of gas entrapments. In: *KGK Kautschuk Gummi Kunststoffe* 61 (2008),6, 286–293

[204] Magnier, R.; Agassant, J.-F. and Bastin, P.: Experiments and Modelling of Calender Processing for Shear Thinning Thermoplastics between Counter Rotating Rolls with Differential Velocities. In: *International Polymer Processing* 28 (2013),4, 437–446

[205] Luther, S.: *Berücksichtigung der freien Knetoberfläche beim Berechnen von Strömungsfeldern im Kalanderspalt: Ph.D. Thesis*. Hannover, 2003

[206] Gojny, F.; Wichmann, M.; Fiedler, B. and Schulte, K.: Influence of different carbon nanotubes on the mechanical properties of epoxy matrix composites – A comparative study. In: *Composites Science and Technology* 65 (2005),15-16, 2300–2313

[207] Wichmann, M. H. G.; Cascione, M.; Fiedler, B.; Quaresimin, M. and Schulte, K.: Influence of surface treatment on mechanical behaviour of fumed silica/epoxy resin nanocomposites. In: *Composite Interfaces* 13 (2012),8-9, 699–715

[208] Wichmann, M. H. G.; Sumfleth, J.; Fiedler, B.; Gojny, F. H. and Schulte, K.: Multiwall carbon nanotube/epoxy composites produced by a masterbatch process. In: *Mechanics of Composite Materials* 42 (2006),5, 395–406

[209] Aravand, M.; Lomov, S. V.; Verpoest, I. and Gorbatikh, L.: Evolution of carbon nanotube dispersion in preparation of epoxy-based composites: From a masterbatch to a nanocomposite. In: *Express Polymer Letters* 8 (2014),8, 596–608

[210] Caradonna, A.; Badini, C.; Padovano, E. and Pietroluongo, M.: Electrical and Thermal Conductivity of Epoxy-Carbon Filler Composites Processed by Calendaring. In: *Materials* 12 (2019),9

[211] Buschhorn, S. T.; Wichmann, M. H. G.; Sumfleth, J.; Schulte, K.; Pegel, S.; Kasaliwal, G. R.; Villmow, T.; Krause, B.; Göldel, A. and Pötschke, P.: Charakterisierung der Dispersionsgüte von Carbon Nanotubes in Polymer-Nanokompositen. In: *Chemie Ingenieur Technik* 83 (2011),6, 767–781

[212] Kovacs, J. Z.; Andresen, K.; Pauls, J. R.; Garcia, C. P.; Schossig, M.; Schulte, K. and Bauhofer, W.: Analyzing the quality of carbon nanotube dispersions in polymers using scanning electron microscopy. In: *Carbon* 45 (2007),6, 1279–1288

[213] Bugnicourt, E.; Kehoe, T.; Latorre, M.; Serrano, C.; Philippe, S. and Schmid, M.: Recent Prospects in the Inline Monitoring of Nanocomposites and Nanocoatings by Optical Technologies. In: *Nanomaterials* 6 (2016),8

[214] Lee, J.; Kim, M.; Hong, C. K. and Shim, S. E.: Measurement of the dispersion stability of pristine and surface-modified multiwalled carbon nanotubes in various nonpolar and polar solvents. In: *Measurement Science and Technology* 18 (2007),12, 3707–3712

[215] Chauhan, A. P. and Chawla, K.: Comparative studies on Graphite and Carbon Black powders, and their dispersions. In: *Journal of Molecular Liquids* 221 (2016), 292–297

[216] Fujimoto, J. G.; Pitris, C.; Boppart, S. A. and Brezinski, M. E.: Optical Coherence Tomography: An Emerging Technology for Biomedical Imaging and Optical Biopsy. In: *Neoplasia* 2 (2000),1-2, 9–25

[217] Kishi, S.: Impact of swept source optical coherence tomography on ophthalmology. In: *Taiwan journal of ophthalmology* 6 (2016),2, 58–68

[218] Yaqoob, Z.; Wu, J. and Yang, C.: Spectral domain optical coherence tomography: A better OCT imaging strategy. In: *BioTechniques* 39 (2005),6 Suppl, S6–13

[219] Trojanowski, M.; Kraszewski, M.; Strakowski, M. R. and Plucinski, J.: Optical Coherence Tomography for nanoparticles quantitative characterization, SPIE, 2015 (SPIE Proceedings), 95540I

[220] Broughton, W. R.; Koukoulas, T.; Woolliams, P.; Williams, J. and Rahatekar, S. S.: Assessment of nanoparticle loading and dispersion in polymeric materials using optical coherence tomography. In: *Polymer Testing* 32 (2013),7, 1290–1298

[221] Stifter, D.; Wiesauer, K.; Wurm, M.; Schlotthauer, E.; Kastner, J.; Pircher, M.; Götzinger, E. and Hitzenberger, C. K.: Investigation of polymer and polymer/fibre composite materials with optical coherence tomography. In: *Measurement Science and Technology* 19 (2008),7, 074011

[222] Schneider, S.; Eppler, F.; Weber, M.; Olowojoba, G.; Weiss, P.; Hübner, C.; Mikonsaari, I.; Freude, W. and Koos, C.: Multiscale dispersion-state characterization of nanocomposites using optical coherence tomography. In: *Scientific reports* 6 (2016), 31733

[223] Elimat, Z. M.: AC-impedance and dielectric properties of hybrid polymer composites. In: *Journal of Composite Materials* 49 (2013),1, 3–15

[224] Bowen, C. R.; Buschhorn, S. and Adamaki, V.: Manufacture and characterization of conductor-insulator composites based on carbon nanotubes and thermally reduced graphene oxide. In: *Pure and Applied Chemistry* 86 (2014),5

[225] Jonscher, A. K.: The 'universal' dielectric response. In: *Nature* 267 (1977),5613, 673–679

[226] Pfeifer, S.; Park, S.-H. and Bandaru, P. R.: Modeling the Relative Dielectric Permittivity and Impedance of Carbon Nanotube Constituted Polymer Composites in the Sub-GHz Regime. In: *ECS Solid State Letters* 2 (2012),1, M5–M7

[227] Monti, M.; Armentano, I.; Faiella, G.; Antonucci, V.; Kenny, J. M.; Torre, L. and Giordano, M.: Toward the microstructure–properties relationship in MWCNT/epoxy composites: Percolation behavior and dielectric spectroscopy. In: *Composites Science and Technology* 96 (2014), 38–46

[228] Hsu, W.; Kotzeva, V.; Watts, P. and Chen, G.: Circuit elements in carbon nanotube-polymer composites. In: *Carbon* 42 (2004),8-9, 1707–1712

[229] Qiang, Z.; Liang, G.; Gu, A. and Yuan, L.: The dielectric behavior and origin of high-k composites with very low percolation threshold based on unique multi-branched polyaniline/carbon nanotube hybrids and epoxy resin. In: *Composites Part A: Applied Science and Manufacturing* 64 (2014), 1–10

[230] Zhang, X.; Liang, G.; Chang, J.; Gu, A.; Yuan, L. and Zhang, W.: The origin of the electric and dielectric behavior of expanded graphite–carbon nanotube/cyanate ester composites with very high dielectric constant and low dielectric loss. In: *Carbon* 50 (2012),14, 4995–5007

[231] Li, Y.; Zhang, H.; Crespo, M.; Porwal, H.; Picot, O.; Santagiuliana, G.; Huang, Z.; Barbieri, E.; Pugno, N. M.; Peijs, T. and Bilotti, E.: In Situ Exfoliation of Graphene in Epoxy Resins: A Facile Strategy to Efficient and Large Scale Graphene Nanocomposites. In: *ACS Applied Materials & Interfaces* 8 (2016),36, 24112–24122

[232] Huang, Y. Y.; Ahir, S. V. and Terentjev, E. M.: Dispersion rheology of carbon nanotubes in a polymer matrix. In: *Physical Review B* 73 (2006),12

[233] Schulz, S. C.; Faiella, G.; Buschhorn, S. T.; Prado, L.; Giordano, M.; Schulte, K. and Bauhofer, W.: Combined electrical and rheological properties of shear induced multiwall carbon nanotube agglomerates in epoxy suspensions. In: *European Polymer Journal* 47 (2011),11, 2069–2077

[234] Taurozzi, J. S.; Hackley, V. A. and Wiesner, M. R.: *Preparation of Nanoparticle Dispersions from Powdered Material Using Ultrasonic Disruption - Version 1.1*. National Institute of Standards and Technology, 2012

[235] Barnes, H. A.: *A handbook of elementary rheology*. Aberystwyth: Univ. of Wales Institute of Non-Newtonian Fluid Mechanics, 2000

[236] Shenoy, A. V.: *Rheology of Filled Polymer Systems*. Dordrecht and s.l.: Springer Netherlands, 1999

[237] Reiner, M.: *Deformation and Flow. An Elementary Introduction to Rheology*. H.K. Lewis & Company, 1969

[238] Reiner, M.: The Deborah Number. In: *Physics Today* 17 (1964),1, 62

[239] Moreira, L.; Fulchiron, R.; Seytre, G.; Dubois, P. and Cassagnau, P.: Aggregation of Carbon Nanotubes in Semidilute Suspension. In: *Macromolecules* 43 (2010),3, 1467–1472

[240] Winter, H. H.: Can the gel point of a cross-linking polymer be detected by theG? -G? crossover? In: *Polymer Engineering and Science* 27 (1987),22, 1698–1702

[241] Barnes, H. A.; Hutton, J. F. and Walters, K.: *An introduction to rheology*. Elsevier, 1989 (Rheology series)

[242] Tzoganakis, C.: A rheological evaluation of linear and branched controlled-rheology polypropylenes. In: *The Canadian Journal of Chemical Engineering* 72 (1994),4, 749–754

[243] Tanner, R. I.: *Engineering Rheology*. 2. Oxford: Oxford University Press, 2000 (Oxford Engineering Science Series)

[244] Cox, W. P. and Merz, E. H.: Correlation of dynamic and steady flow viscosities. In: *Journal of Polymer Science* 28 (1958),118, 619–622

[245] Gurland, J.: A Study of Contact and Contiguity of Dispersions in Opaque Samples. Version: 1967. In: Elias, H. (Hrsg.): *Stereology*. Berlin: Springer-Verlag, 1967, 250–251

[246] Hassanabadi, H. M.; Wilhelm, M. and Rodrigue, D.: A rheological criterion to determine the percolation threshold in polymer nano-composites. In: *Rheologica Acta* 53 (2014),10-11, 869–882

[247] Penu, C.; Hu, G.-H.; Fernandez, A.; Marchal, P. and Choplin, L.: Rheological and electrical percolation thresholds of carbon nanotube/polymer nanocomposites. In: *Polymer Engineering & Science* 52 (2012),10, 2173–2181

[248] Jiji, A.; Shakira, T.; Soney, C. G. and Sabu, T.: Rheological Percolation in Thermoplastic Polymer Nanocomposites. In: *Rheology: Open Access* 1 (2017),1, 1000102

[249] Song, Y.; Zeng, L.; Guan, A. and Zheng, Q.: Time-concentration superpositioning principle accounting for reinforcement and dissipation of multi-walled carbon nanotubes filled polystyrene melts. In: *Polymer* 121 (2017), 106–110

[250] Du, F.; Scogna, R. C.; Zhou, W.; Brand, S.; Fischer, J. E. and Winey, K. I.: Nanotube Networks in Polymer Nanocomposites: ? Rheology and Electrical Conductivity. In: *Macromolecules* 37 (2004),24, 9048–9055

[251] Kharchenko, S. B.; Douglas, J. F.; Obrzut, J.; Grulke, E. A. and Migler, K. B.: Flow-induced properties of nanotube-filled polymer materials. In: *Nature materials* 3 (2004),8, 564–568

[252] Arrigo, R.; Morici, E.; Cammarata, M. and Dintcheva, N. T.: Rheological Percolation Threshold in High-Viscosity Polymer/CNTs Nanocomposites. In: *Journal of Engineering Mechanics* 143 (2017),5, D4016006

[253] Kinloch, I. A.; Roberts, S. A. and Windle, A. H.: A rheological study of concentrated aqueous nanotube dispersions. In: *Polymer* 43 (2002),26, 7483–7491

[254] Latva-Kokko, M. and Timonen, J.: Rigidity of random networks of stiff fibers in the low-density limit. In: *Physical Review E* 64 (2001),6, 961

[255] Latva-Kokko, M.; Mäkinen, J. and Timonen, J.: Rigidity transition in two-dimensional random fiber networks. In: *Physical Review E* 63 (2001),4, 961

[256] Kota, A. K.; Cipriano, B. H.; Duesterberg, M. K.; Gershon, A. L.; Powell, D.; Raghavan, S. R. and Bruck, H. A.: Electrical and Rheological Percolation in Polystyrene/MWCNT Nanocomposites. In: *Macromolecules* 40 (2007),20, 7400–7406

[257] Liu, Y. and Wilkinson, A.: Rheological percolation behaviour and fracture properties of nanocomposites of MWCNTs and a highly crosslinked aerospace-grade epoxy resin system. In: *Composites Part A: Applied Science and Manufacturing* 105 (2018), 97–107

[258] Dannert, R.; Winter, H. H.; Sanctuary, R. and Baller, J.: Influence of suspension viscosity on Brownian relaxation of filler particles. In: *Rheologica Acta* 56 (2017),7-8, 615–622

[259] Agarwal, S. and Salovey, R.: Model filled polymers. XV: The effects of chemical interactions and matrix molecular weight on rheology. In: *Polymer Engineering and Science* 35 (1995),15, 1241–1251

[260] Krishnamoorti, R. and Giannelis, E. P.: Rheology of End-Tethered Polymer Layered Silicate Nanocomposites. In: *Macromolecules* 30 (1997),14, 4097–4102

[261] Santos, J. P. F. and Bretas, R. E. S.: Effect of polymer matrix on rheological and electrical percolation threshold of MWCNTs. In: *AIP Conference Proceedings*, Author(s), 2016, 040013

[262] Jin, S. H.; Choi, D. K. and Lee, D. S.: Electrical and rheological properties of polycarbonate/-multiwalled carbon nanotube nanocomposites. In: *Colloids and Surfaces A: Physicochemical and Engineering Aspects* 313-314 (2008), 242–245

[263] Abbasi, S.; Carreau, P. J.; Derdouri, A. and Moan, M.: Rheological properties and percolation in suspensions of multiwalled carbon nanotubes in polycarbonate. In: *Rheologica Acta* 48 (2009),9, 943–959

[264] Kulicke, W.-M.: *Fließverhalten von Stoffen und Stoffgemischen*. Basel: Hüthig und Wepf, 1986

[265] Ureña-Benavides, E. E.; Kayatin, M. J. and Davis, V. A.: Dispersion and Rheology of Multiwalled Carbon Nanotubes in Unsaturated Polyester Resin. In: *Macromolecules* 46 (2013),4, 1642–1650

[266] Skipa, T.; Lellinger, D.; Saphiannikova, M. and Alig, I.: Shear-stimulated formation of multi-wall carbon nanotube networks in polymer melts. In: *physica status solidi (b)* 246 (2009),11-12, 2453–2456

[267] Sandler, J. K.; Windle, A. H.; Martin, C. A.; Schwarz, M.-K.; Bauhofer, W.; Schulte, K. and Shaffer, M. S.: Percolation in Multi-Wall Carbon Nanotube-Epoxy Composites Influence of processing parameters, nanotube aspect ratio and electric fields on the bulk conductivity. In: *MRS Proceedings* 788 (2003)

[268] Schulz, S. C. and Bauhofer, W.: Shear influenced network dynamics and electrical conductivity recovery in carbon nanotube/epoxy suspensions. In: *Polymer* 51 (2010),23, 5500–5505

[269] Schulz, S. C.; Schlutter, J.; Buschhorn, S. T.; Schulte, K. and Bauhofer, W.: Rheological properties and irreversible dispersion changes in carbon nanotube/epoxy systems. In: *Polymer Engineering & Science* 52 (2012),4, 849–855

[270] Chapartegui, M.; Markaide, N.; Florez, S.; Elizetxea, C.; Fernandez, M. and Santamar?a, A.: Specific rheological and electrical features of carbon nanotube dispersions in an epoxy matrix. In: *Composites Science and Technology* 70 (2010),5, 879–884

[271] Vahedi, V.; Pasbakhsh, P. and Chai, S.-P.: Toward high performance epoxy/halloysite nanocomposites: New insights based on rheological, curing, and impact properties. In: *Materials & Design* 68 (2015), 42–53

[272] Yokozeki, T.; Carolin Schulz, S.; Buschhorn, S. T. and Schulte, K.: Investigation of shear thinning behavior and microstructures of MWCNT/epoxy and CNF/epoxy suspensions under steady shear conditions. In: *European Polymer Journal* 48 (2012),6, 1042–1049

[273] Song, Y. S. and Youn, J. R.: Influence of dispersion states of carbon nanotubes on physical properties of epoxy nanocomposites. In: *Carbon* 43 (2005),7, 1378–1385

[274] Hilarius, K.; Lellinger, D.; Alig, I.; Villmow, T.; Pegel, S. and Pötschke, P.: Influence of shear deformation on the electrical and rheological properties of combined filler networks in polymer melts: Carbon nanotubes and carbon black in polycarbonate. In: *Polymer* 54 (2013),21, 5865–5874

[275] Skipa, T.; Lellinger, D.; Böhm, W.; Saphiannikova, M. and Alig, I.: Influence of shear deformation on carbon nanotube networks in polycarbonate melts: Interplay between build-up and destruction of agglomerates. In: *Polymer* 51 (2010),1, 201–210

[276] Yearsley, K. M.; Mackley, M. R.; Chinesta, F. and Leygue, A.: The rheology of multiwalled carbon nanotube and carbon black suspensions. In: *Journal of Rheology* 56 (2012),6, 1465–1490

[277] Hilarius, K.: *Elektrische und rheologische Eigenschaften von kohlenstoffbasierten Füllstoffnetzwerken in Polymeren: Ph.D. Thesis*. Darmstadt, 2014

[278] Bauhofer, W.; Schulz, S. C.; Eken, A. E.; Skipa, T.; Lellinger, D.; Alig, I.; Tozzi, E. J. and Klingenberg, D. J.: Shear-controlled electrical conductivity of carbon nanotubes networks suspended in low and high molecular weight liquids. In: *Polymer* 51 (2010),22, 5024–5027

[279] Alig, I.; Pötschke, P.; Lellinger, D.; Skipa, T.; Pegel, S.; Kasaliwal, G. R. and Villmow, T.: Establishment, morphology and properties of carbon nanotube networks in polymer melts. In: *Polymer* 53 (2012),1, 4–28

[280] Schulz, S. C.; Schlutter, J. and Bauhofer, W.: Influence of Initial High Shearing on Electrical and Rheological Properties and Formation of Percolating Agglomerates for MWCNT/Epoxy Suspensions. In: *Macromolecular Materials and Engineering* 295 (2010),7, 613–617

[281] Pötschke, P.; Abdel-Goad, M.; Alig, I.; Dudkin, S. and Lellinger, D.: Rheological and dielectrical characterization of melt mixed polycarbonate-multiwalled carbon nanotube composites. In: *Polymer* 45 (2004),26, 8863–8870

[282] Kim, J. A.; Seong, D. G.; Kang, T. J. and Youn, J. R.: Effects of surface modification on rheological and mechanical properties of CNT/epoxy composites. In: *Carbon* 44 (2006),10, 1898–1905

[283] Martin-Gallego, M.; Bernal, M. M.; Hernandez, M.; Verdejo, R. and Lopez-Manchado, M. A.: Comparison of filler percolation and mechanical properties in graphene and carbon nanotubes filled epoxy nanocomposites. In: *European Polymer Journal* 49 (2013),6, 1347–1353

[284] Elias, L.; Fenouillot, F.; Majeste, J. C. and Cassagnau, P.: Morphology and rheology of immiscible polymer blends filled with silica nanoparticles. In: *Polymer* 48 (2007),20, 6029–6040

[285] Pötschke, P.; Fornes, T. D. and Paul, D. R.: Rheological behavior of multiwalled carbon nanotube/polycarbonate composites. In: *Polymer* 43 (2002),11, 3247–3255

[286] Nobile, M. R.; Valentino, O.; Morcom, M.; Simon, G. P.; Landi, G. and Neitzert, H.-C.: The effect of the nanotube oxidation on the rheological and electrical properties of CNT/HDPE nanocomposites. In: *Polymer Engineering & Science* 57 (2017),7, 665–673

[287] Prashantha, K.; Soulestin, J.; Lacrampe, M. F.; Krawczak, P.; Dupin, G. and Claes, M.: Masterbatch-based multi-walled carbon nanotube filled polypropylene nanocomposites: Assessment of rheological and mechanical properties. In: *Composites Science and Technology* 69 (2009),11-12, 1756–1763

[288] Wu, G.; Asai, S.; Sumita, M.; Hattori, T.; Higuchi, R. and Washiyama, J.: Estimation of flocculation structure in filled polymer composites by dynamic rheological measurements. In: *Colloid & Polymer Science* 278 (2000),3, 220–228

[289] Hobbie, E. K. and Fry, D. J.: Rheology of concentrated carbon nanotube suspensions. In: *The Journal of Chemical Physics* 126 (2007),12, 124907

[290] Handge, U. A. and Pötschke, P.: Deformation and orientation during shear and elongation of a polycarbonate/carbon nanotubes composite in the melt. In: *Rheologica Acta* 46 (2007),6, 889–898

[291] Sumfleth, J.; Buschhorn, S. T. and Schulte, K.: Comparison of rheological and electrical percolation phenomena in carbon black and carbon nanotube filled epoxy polymers. In: *Journal of Materials Science* 46 (2011),3, 659–669

[292] Palza, H.; Kappes, M.; Hennrich, F. and Wilhelm, M.: Morphological changes of carbon nanotubes in polyethylene matrices under oscillatory tests as determined by dielectrical measurements. In: *Composites Science and Technology* 71 (2011),10, 1361–1366

[293] Fogel, M.; Parlevliet, P.; Geistbeck, M.; Olivier, P. and Dantras, É.: Thermal, rheological and electrical analysis of MWCNTs/epoxy matrices. In: *Composites Science and Technology* 110 (2015), 118–125

[294] Cassagnau, P. and Mélis, F.: Non-linear viscoelastic behaviour and modulus recovery in silica filled polymers. In: *Polymer* 44 (2003),21, 6607–6615

[295] Richter, S.; Saphiannikova, M.; Jehnichen, D.; Bierdel, M. and Heinrich, G.: Experimental and theoretical studies of agglomeration effects in multi-walled carbon nanotube-polycarbonate melts. In: *Express Polymer Letters* 3 (2009),12, 753–768

[296] Handge, U. A.; Zeiler, R.; Dijkstra, D. J.; Meyer, H. and Altstädt, V.: On the determination of elastic properties of composites of polycarbonate and multi-wall carbon nanotubes in the melt. In: *Rheologica Acta* 50 (2011),5-6, 503–518

[297] Zeiler, R.; Handge, U. A.; Dijkstra, D. J.; Meyer, H. and Altstädt, V.: Influence of molar mass and temperature on the dynamics of network formation in polycarbonate/carbon nanotubes composites in oscillatory shear flows. In: *Polymer* 52 (2011),2, 430–442

[298] Bai, J.; Goodridge, R. D.; Hague, R. J.; Song, M. and Okamoto, M.: Influence of carbon nanotubes on the rheology and dynamic mechanical properties of polyamide-12 for laser sintering. In: *Polymer Testing* 36 (2014), 95–100

[299] Haward, R. N. and Young, R. J.: *Physics of Glassy Polymers*. Dordrecht: Springer Netherlands, 2012

[300] Deng, F. and Zheng, Q.-S.: An analytical model of effective electrical conductivity of carbon nanotube composites. In: *Applied Physics Letters* 92 (2008),7, 071902

[301] Reddy, C. S.; Zak, A. and Zussman, E.: WS2 nanotubes embedded in PMMA nanofibers as energy absorptive material. In: *Journal of Materials Chemistry* 21 (2011),40, 16086

[302] Vivo, B.de; Lamberti, P.; Tucci, V.; Guadagno, L.; Vertuccio, L.; Vittoria, V. and Sorrentino, A.: Comparison of the physical properties of epoxy-based composites filled with different types of carbon nanotubes for aeronautic applications. In: *Advances in Polymer Technology* 31 (2012),3, 205–218

[303] Fett, T.: Stress intensity factors for edge crack subjected to mixed mode four-point bending. In: *Theoretical and Applied Fracture Mechanics* 15 (1991),1, 99–104

[304] Araki, W.; Nemoto, K.; Adachi, T. and Yamaji, A.: Fracture toughness for mixed mode I/II of epoxy resin. In: *Acta Materialia* 53 (2005),3, 869–875

[305] Kalthoff, J. F.: Failure methodology of mode II loaded crack. In: *Strength, fracture and complexity* 1 (2003),3, 121–138

[306] Bergmannshoff, D.: *Das Instabilitätsverhalten zug-/scherbeanspruchter Risse bei Variation des Belastungspfades: Ph.D. Thesis*. Bochum, 2006

[307] Ayatollahi, M. R.; Shadlou, S. and Shokrieh, M. M.: Fracture toughness of epoxy/multi-walled carbon nanotube nano-composites under bending and shear loading conditions. In: *Materials & Design* 32 (2011),4, 2115–2124

[308] *Test Methods for Plane-Strain Fracture Toughness and Strain Energy Release Rate of Plastic Materials*. West Conshohocken: ASTM International, 2014

[309] Domun, N.; Paton, K. R.; Hadavinia, H.; Sainsbury, T.; Zhang, T. and Mohamud, H.: Enhancement of Fracture Toughness of Epoxy Nanocomposites by Combining Nanotubes and Nanosheets as Fillers. In: *Materials (Basel, Switzerland)* 10 (2017),10

[310] Domun, N.; Hadavinia, H.; Zhang, T.; Sainsbury, T.; Liaghat, G. H. and Vahid, S.: Improving the fracture toughness and the strength of epoxy using nanomaterials–a review of the current status. In: *Nanoscale* 7 (2015),23, 10294–10329

[311] Shtein, M.; Nadiv, R.; Lachman, N.; Daniel Wagner, H. and Regev, O.: Fracture behavior of nanotube–polymer composites: Insights on surface roughness and failure mechanism. In: *Composites Science and Technology* 87 (2013), 157–163

[312] Nadiv, R.; Vasilyev, G.; Shtein, M.; Peled, A.; Zussman, E. and Regev, O.: The multiple roles of a dispersant in nanocomposite systems. In: *Composites Science and Technology* 133 (2016), 192–199

[313] Al Wakeel, S.; Ghanbari, F. and Hubler, M.: Particle arrangement effects on the stress intensity in composite material. In: *Engineering Fracture Mechanics* 202 (2018), 33–46

[314] Kowalewski, T.; Gałęski, A. and Kryszewski, M.: The Structure and Tensile Properties of Cold Drawn Modified Chalk Filled Polypropylene. Version: 1984. In: Kryszewski, M. (Hrsg.); Galeski, A. (Hrsg.) and Martuscelli, E. (Hrsg.): *Polymer blends*. New York: Springer Science+Business Media, 1984, 223–241

[315] Arencón, D. and Velasco, J. I.: Fracture Toughness of Polypropylene-Based Particulate Composites. In: *Materials* 2 (2009),4, 2046–2094

[316] Nadiv, R.; Shachar, G.; Peretz-Damari, S.; Varenik, M.; Levy, I.; Buzaglo, M.; Ruse, E. and Regev, O.: Performance of nano-carbon loaded polymer composites: Dimensionality matters. In: *Carbon* 126 (2018), 410–418

[317] Nadiv, R.; Shtein, M.; Shachar, G.; Varenik, M. and Regev, O.: Optimal nanomaterial concentration: Harnessing percolation theory to enhance polymer nanocomposite performance. In: *Nanotechnology* 28 (2017),30, 305701

[318] Allaoui, A. and Bounia, N.: Rheological and Electrical Transitions in Carbon Nanotube/Epoxy Suspensions. In: *Current Nanoscience* 6 (2010),2, 158–162

[319] Chandrasekaran, S.; Liebig, W. V.; Mecklenburg, M.; Fiedler, B.; Smazna, D.; Adelung, R. and Schulte, K.: Fracture, failure and compression behaviour of a 3D interconnected carbon aerogel (Aerographite) epoxy composite. In: *Composites Science and Technology* 122 (2016), 50–58

[320] Chandrasekaran, S.; Sato, N.; Tölle, F.; Mülhaupt, R.; Fiedler, B. and Schulte, K.: Fracture toughness and failure mechanism of graphene based epoxy composites. In: *Composites Science and Technology* 97 (2014), 90–99

[321] Chandrasekaran, S.; Seidel, C. and Schulte, K.: Preparation and characterization of graphite nanoplatelet (GNP)/epoxy nano-composite: Mechanical, electrical and thermal properties. In: *European Polymer Journal* 49 (2013),12, 3878–3888

[322] Ayatollahi, M. R.; Shadlou, S. and Shokrieh, M. M.: Mixed mode brittle fracture in epoxy/multi-walled carbon nanotube nanocomposites. In: *Engineering Fracture Mechanics* 78 (2011),14, 2620–2632

[323] Zappalorto, M.; Salviato, M. and Quaresimin, M.: Mixed mode (I+II) fracture toughness of polymer nanoclay nanocomposites. In: *Engineering Fracture Mechanics* 111 (2013), 50–64

[324] Fracture toughness and toughening mechanisms of unsaturated polyester-based clay nanocomposites.

[325] Wetzel, B.; Rosso, P.; Haupert, F. and Friedrich, K.: Epoxy nanocomposites – fracture and toughening mechanisms. In: *Engineering Fracture Mechanics* 73 (2006),16, 2375–2398

[326] Behr, S.: *Bulk-Sized Nacre-Inspired Composites by Sedimentation Processes*. Göttingen: Cuvillier Verlag, 2017

[327] Shadlou, S.; Alishahi, E. and Ayatollahi, M. R.: Fracture behavior of epoxy nanocomposites reinforced with different carbon nano-reinforcements. In: *Composite Structures* 95 (2013), 577–581

[328] Quan, D.; Urdániz, J. L. and Ivanković, A.: Enhancing mode-I and mode-II fracture toughness of epoxy and carbon fibre reinforced epoxy composites using multi-walled carbon nanotubes. In: *Materials & Design* 143 (2018), 81–92

[329] Ahmadi Moghadam, B. and Taheri, F.: Fracture and toughening mechanisms of GNP-based nanocomposites in modes I and II fracture. In: *Engineering Fracture Mechanics* 131 (2014), 329–339

[330] Fritsch, D.; Wittich, H. and Fiedler, B.: Graphene Modified CFRP for Enhanced Damage Behavior. In: Materials - European Conference on Composite (Hrsg.): *Proceedings of the 17th European Conference on Composite Materials*. Augsburg: MAI Carbon Cluster Management GmbH, 2016

[331] Liu, C.; Huang, Y. and Stout, M. G.: Enhanced mode-II fracture toughness of an epoxy resin due to shear banding. In: *Acta Materialia* 46 (1998),16, 5647–5661

[332] Ayatollahi, M. R.; Shadlou, S.; Shokrieh, M. M. and Chitsazzadeh, M.: Effect of multi-walled carbon nanotube aspect ratio on mechanical and electrical properties of epoxy-based nanocomposites. In: *Polymer Testing* 30 (2011),5, 548–556

[333] Brunner, A. J.; Necola, A.; Rees, M.; Gasser, P.; Kornmann, X.; Thomann, R. and Barbezat, M.: The influence of silicate-based nano-filler on the fracture toughness of epoxy resin. In: *Engineering Fracture Mechanics* 73 (2006),16, 2336–2345

[334] Ahmadi Moghadam, B.: *Development of a Gighly Resilent Graphene Nanoplatelet Resin/Adhesive: Ph.D. Thesis*. Halifax, 2015

[335] Arlt, C.: *Wirkungsweisen nanaskaliger Böhmite in einem Polymer und seinem Kohlenstofffaserverbund unter Druckbelastung*. Braunschweig, 2011

[336] Brunauer, S.; Emmett, P. H. and Teller, E.: Adsorption of Gases in Multimolecular Layers. In: *Journal of the American Chemical Society* 60 (1938),2, 309–319

[337] Scheibe, B.; Borowiak-Palen, E. and Kalenczuk, R. J.: Oxidation and reduction of multiwalled carbon nanotubes — preparation and characterization. In: *Materials Characterization* 61 (2010),2, 185–191

[338] Lehman, J. H.; Terrones, M.; Mansfield, E.; Hurst, K. E. and Meunier, V.: Evaluating the characteristics of multiwall carbon nanotubes. In: *Carbon* 49 (2011),8, 2581–2602

[339] Gojny, F. H.: *Evaluation of the potential of carbon nanotubes as nano-structured modification of (glass-fibre reinforced) epoxy-based composites: Ph.D. Thesis*. Hamburg, 2006

[340] Tuinstra, F. and Koenig, J. L.: Raman Spectrum of Graphite. In: *The Journal of Chemical Physics* 53 (1970),3, 1126–1130

[341] Cançado, L. G.; Takai, K.; Enoki, T.; Endo, M.; Kim, Y. A.; Mizusaki, H.; Jorio, A.; Coelho, L. N.; Magalhães-Paniago, R. and Pimenta, M. A.: General equation for the determination of the crystallite size La of nanographite by Raman spectroscopy. In: *Applied Physics Letters* 88 (2006),16, 163106

[342] Knight, D. S. and White, W. B.: Characterization of diamond films by Raman spectroscopy. In: *Journal of Materials Research* 4 (1989),02, 385–393

[343] Tai, F. C.; Wei, C.; Chang, S. H. and Chen, W. S.: Raman and X-ray diffraction analysis on unburned carbon powder refined from fly ash. In: *Journal of Raman Spectroscopy* 41 (2010),9, 933–937

[344] Cançado, L. G.; Jorio, A.; Ferreira, E. H. M.; Stavale, F.; Achete, C. A.; Capaz, R. B.; Moutinho, M. V. O.; Lombardo, A.; Kulmala, T. S. and Ferrari, A. C.: Quantifying defects in graphene via Raman spectroscopy at different excitation energies. In: *Nano letters* 11 (2011),8, 3190–3196

[345] Shen, J. T.; Buschhorn, S. T.; Hosson, J.de; Schulte, K. and Fiedler, B.: Pressure and temperature induced electrical resistance change in nano-carbon/epoxy composites. In: *Composites Science and Technology* 115 (2015), 1–8

[346] Meeuw, H.; Körbelin, J.; Wisniewski, V.; Nia, A.; Vázquez, A.; Lohe, M.; Feng, X. and Fiedler, B.: Carbon Nanoparticles' Impact on Processability and Physical Properties of Epoxy Resins—A Comprehensive Study Covering Rheological, Electrical, Thermo-Mechanical, and Fracture Properties (Mode I and II). In: *Polymers* 11 (2019),2, 231

[347] Meeuw, H.; Wisniewski, V. and Fiedler, B.: Frequency or Amplitude?—Rheo-Electrical Characterization of Carbon Nanoparticle Filled Epoxy Systems. In: *Polymers* 10 (2018),9, 999

[348] Meeuw, H.; Wisniewski, V. K.; Köpke, U.; Nia, A. S.; Vázquez, A. R.; Lohe, M. R.; Feng, X. and Fiedler, B.: In-line monitoring of carbon nanoparticle epoxy dispersion processes. In: *Production Engineering* 51 (2019),4, 585

[349] Meeuw, H.; Radek, M. and Fiedler, B.: Development of a colored GFRP with antistatic properties. In: *AIP Conference Proceedings* Bd. 2055, AIP, 2019 (AIP Conference Proceedings), 090007, 1–5

[350] Meeuw, H.; Körbelin, J.; Bernstorff, D.von; Augustin, T.; Liebig, W. V. and Fiedler, B.: Smart dispersion: Validation of OCT and impedance spectroscopy as solutions for in-situ dispersion analysis of CNP/EP-composites. In: *Materialia* 1 (2018), 185–197

[351] DIN EN ISO 1524: *Beschichtungsstoffe und Druckfarben – Bestimmung der Mahlfeinheit (Körnigkeit)*. Berlin: Beuth Verlag GmbH, 2013

[352] Hexion: EPIKOTE Resin MGS RIMR 135 and EPIKURE Curing Agent MGS RIMH 134–RIMH 137: Technical Data Sheet. (2006)

[353] DIN EN ISO 3915: *Messung des spezifischen elektrischen Widerstandes von leitfähigen Kunststoffen*. Berlin: Beuth Verlag GmbH, 1999

[354] ASTM D527 - 07: *Test Methods for DC Resistance or Conductance of Insulating Materials*. West Conshohocken: ASTM International, 2007

[355] Keithley Instruments: Volume and Surface Resistivity Measurements of Insulating Materials Using the Model 6517A Electrometer/High Resistance Meter. In: *Application Note Series* 314 (2001),1680

[356] Manolica, N. and Chapalo, I.: Surface resistivity measurements of electrostatic discharge protective materials for different relative humidity levels. In: *Electrotehnica, Energetica, Electronica* 57 (2011),1, 59–66

[357] Keithley Instruments: *Model 8009 Resistivity Test Fixture: Instruction Manual*. C. Cleveland, 2008

[358] Belhimria, R.; Boukheir, S.; Samir, Z.; Len, A.; Achour, M. E.; Éber, N.; Costa, L. C. and Oueriagli, A.: Fractal Approach to Alternating Current Impedance Spectroscopy Studies of Carbon Nanotubes/Epoxy Polymer Composites. In: *Applied Microscopy* 47 (2017),3, 126–130

[359] Xiao, K.; Ye, L. and Kwok, Y. S.: Effects of pre-cracking methods on fracture behaviour of an Araldite-F epoxy and its rubber-modified systems. In: *Journal of Materials Science* 33 (1998),11, 2831–2836

[360] Souza, J. M.; Yoshimura, H. N.; Peres, F. M. and Schön, C. G.: Effect of sample pre-cracking method and notch geometry in plane strain fracture toughness tests as applied to a PMMA resin. In: *Polymer Testing* 31 (2012),6, 834–840

[361] Kuppusamy, N. and Tomlinson, R. A.: Repeatable pre-cracking preparation for fracture testing of polymeric materials. In: *Engineering Fracture Mechanics* 152 (2016), 81–87

[362] Haddadi, E.; Choupani, N. and Abbasi, F.: Investigation on the Effect of Different Pre-Cracking Methods on Fracture Toughness of RT-PMMA. In: *Latin American Journal of Solids and Structures* 13 (2016),11, 2012–2026

[363] Hexion: *Product selector*. Columbus, 2016

[364] Hexion: *EPIKURE™ Curing Agent MGS RIMH 137: Safety Data Sheet*. 2017

[365] Hexion: *EPIKURE Curing Agent MGS RIMH 134: Safety Data Sheet*. 2017

[366] Burton, B.; Alexander, D.; Klein, H.; Garibay-Vasquez, A.; Pekarik, A. and Henkee, C.: *Epoxy Formulations Using JEFFAMINE Polyetheramines*. Huntsman Corporation, 2005

[367] Garibay-Vasquez, A.: *JEFFAMINE POLYETHERAMINES*. Huntsman Corporation, 2007

[368] BASF SE: *Isophorone diamine von BASF SE, Intermediates Division - Farben & Lacke*. `https://www.ulprospector.com/de/eu/Coatings/Detail/3819/109024/Isophorone-diamine`, Last checked: 17.01.2019

[369] González Garcia, F.; Soares, B. G.; Leyva, M. E. and Simões, A. Z.: Influence of aliphatic amine epoxy hardener on the adhesive properties of blends of mono-carboxyl-terminated poly(2-ethylhexyl acrylate-co-methyl methacrylate) with epoxy resin. In: *Journal of Applied Polymer Science* 114 (2010), 2762–2770

[370] European Commission - Employment, Social Affairs & Inclusion: *Recommendation from the Scientific Committee on Occupational Exposure Limits for commercial nonylphenol*. 2003

[371] Hardis, R.; Jessop, J. L.; Peters, F. E. and Kessler, M. R.: Cure kinetics characterization and monitoring of an epoxy resin using DSC, Raman spectroscopy, and DEA. In: *Composites Part A: Applied Science and Manufacturing* 49 (2013), 100–108

[372] Hamerton, I.: *Recent developments in epoxy resins*. Bd. 91. Shawbury: Rapra Technology, 1996

[373] Czymmek, K. J. and Dahms, T. E. S.: Future Directions in Advanced Mycological Microscopy. Version: 2015. In: Dahms, T. (Hrsg.): *Advanced microscopy in mycology*. Berlin: Springer, 2015, 143–162

[374] Gaukler, J. C.: *Lagerungsstabilität, Netzwerkbildung und Eigenschaften von Epoxid-Dicyandiamid-Systemen für Nanoverbundwerkstoffe: Ph.D. Thesis*. Saarbrücken, 2011

[375] Edwards, G. D.: Estimation of molecular weights of epichlorohydrin–bisphenol a polymers by gel permeation chromatography. In: *Journal of Applied Polymer Science* 9 (1965),12, 3845–3850

[376] Szesztay, M.; László-Hedvig, Z.; Tüdős, F.; Hörhold, H. H. and Klee, J.: GPC estimation of molecular mass distribution of addition polymers from bisphenol–a–diglycidyl ether and amines. In: *Angewandte Makromolekulare Chemie* 162 (1988),1, 149–162

[377] Opfermann, J.; Hörhold, H.-H.; Klee, J. and Wondraczek, R.: Zur Gelchromatographie von Additionspolymeren aus Bisphenol-A-diglycidylether und Anilin: Unvernetzte Epoxid-Amin-Additionspolymere. In: *Acta Polymerica* 36 (1985),10, 561–565

[378] Cain, M. L.: *Epoxy resins: Synthesis, applications and recent developments*. Nova Science Publishers, 2016 (Polymer science and technology)

[379] Winter, H. H.: The Solidification Rheology of Amorphous Polymers − Vitrification as Compared to Gelation. In: *Macromolecular Symposia* 374 (2017),1, 1600113

[380] Smith, I. T.: The mechanism of the crosslinking of epoxide resins by amines. In: *Polymer* 2 (1961), 95–108

[381] Duemichen, E.; Javdanitehran, M.; Erdmann, M.; Trappe, V.; Sturm, H.; Braun, U. and Ziegmann, G.: Analyzing the network formation and curing kinetics of epoxy resins by in situ near-infrared measurements with variable heating rates. In: *Thermochimica Acta* 616 (2015), 49–60

[382] Cook, W.; Mehrabi, M. and Edward, G.: Ageing and yielding in model epoxy thermosets. In: *Polymer* 40 (1999),5, 1209–1218

[383] Muc, A.; Romanowicz, P. and Chwał, M.: Description of the Resin Curing Process-Formulation and Optimization. In: *Polymers* 11 (2019),1

[384] McCoy, J. D.; Ancipink, W. B.; Clarkson, C. M.; Kropka, J. M.; Celina, M. C.; Giron, N. H.; Hailesilassie, L. and Fredj, N.: Cure mechanisms of diglycidyl ether of bisphenol A (DGEBA) epoxy with diethanolamine. In: *Polymer* 105 (2016), 243–254

[385] Shechter, L.; Wynstra, J. and Kurkjy, R. P.: Glycidyl Ether Reactions with Amines. In: *Industrial & Engineering Chemistry* 48 (1956),1, 94–97

[386] Rozenberg, B. A.: Kinetics, thermodynamics and mechanism of reactions of epoxy oligomers with amines. Version: 1986. In: Dušek, K. (Hrsg.): *Epoxy Resins and Composites II* Bd. 75. Berlin: Springer, 1986, 113–165

[387] Choi, S.; Janisse, A. P.; Liu, C. and Douglas, E. P.: Effect of water addition on the cure kinetics of an epoxy-amine thermoset. In: *Journal of Polymer Science Part A: Polymer Chemistry* 49 (2011),21, 4650–4659

[388] Ehlers, J.-E.; Rondan, N. G.; Huynh, L. K.; Pham, H.; Marks, M. and Truong, T. N.: Theoretical Study on Mechanisms of the Epoxy−Amine Curing Reaction. In: *Macromolecules* 40 (2007),12, 4370–4377

[389] Prime, R. B.: Differential scanning calorimetry of the epoxy cure reaction. In: *Polymer Engineering and Science* 13 (1973),5, 365–371

[390] Montserrat, S.: Effect of crosslinking density on $\Delta C_P(T_g)$ in an epoxy network. In: *Polymer* 36 (1995),2, 435–436

[391] Theocaris, P. S.: Viscoelastic properties of epoxy resins derived from creep and relaxation tests at different temperatures. In: *Rheologica Acta* 2 (1962),2, 92–96

[392] Lee, A. and McKenna, G.: Effect of crosslink density on physical ageing of epoxy networks. In: *Polymer* 29 (1988),10, 1812–1817

[393] Chevalier, J.; Morelle, X. P.; Camanho, P. P.; Lani, F. and Pardoen, T.: On a unique fracture micromechanism for highly cross-linked epoxy resins. In: *Journal of the Mechanics and Physics of Solids* 122 (2019), 502–519

[394] Mayr, A. E.; Cook, W. D. and Edward, G. H.: Yielding behaviour in model epoxy thermosets — I. Effect of strain rate and composition. In: *Polymer* 39 (1998),16, 3719–3724

[395] Ramsteiner, F.: An approach towards understanding model II failure of poly(methyl methacrylate). In: *Polymer* 34 (1993),2, 312–317

[396] Kwon, H. J. and Jar, P.-Y.: Fracture toughness of polymers in shear mode. In: *Polymer* 46 (2005),26, 12480–12492

[397] Benra, J. and Forero, S.: Epoxy resins reinforced with carbon nanotubes. In: *Lightweight Design worldwide* 11 (2018),1, 6–11

[398] iNanoComm: *TUBALL™ Single Wall Carbon Nanotubes*. `http://inanocomm.org/tuball/`, Last checked: 23.07.2017

[399] Yang, S.; Lohe, M. R.; Müllen, K. and Feng, X.: New-Generation Graphene from Electrochemical Approaches: Production and Applications. In: *Advanced materials (Deerfield Beach, Fla.)* 28 (2016),29, 6213–6221

[400] Alig, I.; Lellinger, D.; Engel, M.; Skipa, T. and Pötschke, P.: Destruction and formation of a conductive carbon nanotube network in polymer melts: In-line experiments. In: *Polymer* 49 (2008),7, 1902–1909

[401] Alig, I.; Skipa, T.; Lellinger, D. and Pötschke, P.: Destruction and formation of a carbon nanotube network in polymer melts: Rheology and conductivity spectroscopy. In: *Polymer* 49 (2008),16, 3524–3532

[402] Koya, P. R. and Goshu, A. T.: Generalized Mathematical Model for Biological Growths. In: *Open Journal of Modelling and Simulation* 01 (2013),04, 42–53

[403] Lenk, R. S.: *Rheologie der Kunststoffe: Mit 12 Tabellen*. München: Hanser, 1971

[404] Gómez, J.; Villaro, E.; Navas, A. and Recio, I.: Testing the influence of the temperature, RH and filler type and content on the universal power law for new reduced graphene oxide TPU composites. In: *Materials Research Express* 4 (2017),10, 105020

[405] Alig, I.; Lellinger, D.; Dudkin, S. M. and Pötschke, P.: Conductivity spectroscopy on melt processed polypropylene–multiwalled carbon nanotube composites: Recovery after shear and crystallization. In: *Polymer* 48 (2007),4, 1020–1029

[406] Zhang, J.; Mine, M.; Zhu, D. and Matsuo, M.: Electrical and dielectric behaviors and their origins in the three-dimensional polyvinyl alcohol/MWCNT composites with low percolation threshold. In: *Carbon* 47 (2009),5, 1311–1320

[407] Harrington, D. A. and van den Driessche, P.: Mechanism and equivalent circuits in electrochemical impedance spectroscopy. In: *Electrochimica Acta* 56 (2011),23, 8005–8013

[408] Han, P.-j.; Zhang, Y.-f.; Chen, F. Y. and Bai, X.-h.: Interpretation of electrochemical impedance spectroscopy (EIS) circuit model for soils. In: *Journal of Central South University* 22 (2015),11, 4318–4328

[409] Li, Y.; Zhang, H.; Porwal, H.; Huang, Z.; Bilotti, E. and Peijs, T.: Mechanical, electrical and thermal properties of in-situ exfoliated graphene/epoxy nanocomposites. In: *Composites Part A: Applied Science and Manufacturing* 95 (2017), 229–236

[410] Chen, J.; Duan, M. and Chen, G.: Continuous mechanical exfoliation of graphene sheets via three-roll mill. In: *Journal of Materials Chemistry* 22 (2012),37, 19625

[411] Kernin, A.; Wan, K.; Liu, Y.; Shi, X.; Kong, J.; Bilotti, E.; Peijs, T. and Zhang, H.: The effect of graphene network formation on the electrical, mechanical, and multifunctional properties of graphene/epoxy nanocomposites. In: *Composites Science and Technology* (2018)

[412] Paton, K. R.; Varrla, E.; Backes, C.; Smith, R. J.; Khan, U.; O'Neill, A.; Boland, C.; Lotya, M.; Istrate, O. M.; King, P.; Higgins, T.; Barwich, S.; May, P.; Puczkarski, P.; Ahmed, I.; Moebius, M.; Pettersson, H.; Long, E.; Coelho, J.; O'Brien, S. E.; McGuire, E. K.; Sanchez, B. M.; Duesberg, G. S.; McEvoy, N.; Pennycook, T. J.; Downing, C.; Crossley, A.; Nicolosi, V. and Coleman, J. N.: Scalable production of large quantities of defect-free few-layer graphene by shear exfoliation in liquids. In: *Nature materials* 13 (2014),6, 624–630

[413] Li, Y.; Zhang, H.; Bilotti, E. and Peijs, T.: Optimization of Three-Roll Mill Parameters for In-Situ Exfoliation of Graphene. In: *MRS Advances* 1 (2016),19, 1389–1394

[414] Leopold, C.; Augustin, T.; Schwebler, T.; Lehmann, J.; Liebig, W. V. and Fiedler, B.: Influence of carbon nanoparticle modification on the mechanical and electrical properties of epoxy in small volumes. In: *Journal of Colloid and Interface Science* 506 (2017), 620–632

[415] Engineers Edge: *Thermal Properties of Metals, Conductivity, Thermal Expansion, Specific Heat*. `https://www.engineersedge.com/properties_of_metals.htm`, Last checked: 24.03.2019

[416] Accuratus: *Silicon Carbide SiC Material Properties*. `https://accuratus.com/silicar.html`, Last checked: 24.03.2019

[417] Choi, W. S.; Shanmugharaj, A. M. and Ryu, S. H.: Study on the effect of phenol anchored multiwall carbon nanotube on the curing kinetics of epoxy/Novolac resins. In: *Thermochimica Acta* 506 (2010),1-2, 77–81

[418] Simpson, J. O. and Bidstrup, S. A.: Rheological and dielectric changes during isothermal epoxy-amine cure. In: *Journal of Polymer Science Part B: Polymer Physics* 33 (1995),1, 55–62

[419] Chakraborty, A. K.; Plyhm, T.; Barbezat, M.; Necola, A. and Terrasi, G. P.: Carbon nanotube (CNT)–epoxy nanocomposites: A systematic investigation of CNT dispersion. In: *Journal of Nanoparticle Research* 13 (2011),12, 6493–6506

[420] Faiella, G.; Piscitelli, F.; Lavorgna, M.; Antonucci, V. and Giordano, M.: Tuning the insulator to conductor transition in a multiwalled carbon nanotubes/epoxy composite at substatistical percolation threshold. In: *Applied Physics Letters* 95 (2009),15, 153106

[421] Pegel, S.; Pötschke, P.; Petzold, G.; Alig, I.; Dudkin, S. M. and Lellinger, D.: Dispersion, agglomeration, and network formation of multiwalled carbon nanotubes in polycarbonate melts. In: *Polymer* 49 (2008),4, 974–984

[422] Alig, I.; Skipa, T.; Lellinger, D.; Bierdel, M. and Meyer, H.: Dynamic percolation of carbon nanotube agglomerates in a polymer matrix: comparison of different model approaches. In: *physica status solidi (b)* 245 (2008),10, 2264–2267

[423] Kovacs, J. Z.; Velagala, B. S.; Schulte, K. and Bauhofer, W.: Two percolation thresholds in carbon nanotube epoxy composites. In: *Composites Science and Technology* 67 (2007),5, 922–928

[424] Sumfleth, J.; Adroher, X. C. and Schulte, K.: Synergistic effects in network formation and electrical properties of hybrid epoxy nanocomposites containing multi-wall carbon nanotubes and carbon black. In: *Journal of Materials Science* 44 (2009),12, 3241–3247

[425] Feng, C. and Jiang, L.: Micromechanics modeling of the electrical conductivity of carbon nanotube (CNT)–polymer nanocomposites. In: *Composites Part A: Applied Science and Manufacturing* 47 (2013), 143–149

[426] Seidel, G. D. and Lagoudas, D. C.: A Micromechanics Model for the Electrical Conductivity of Nanotube-Polymer Nanocomposites. In: *Journal of Composite Materials* 43 (2009),9, 917–941

[427] Seyhan, A. T.; La Vega, A.de; Tanoglu, M. and Schulte, K.: Thermal curing behavior of MWCNT modified vinyl ester-polyester resin suspensions prepared with 3-roll milling technique. In: *Journal of Polymer Science Part B: Polymer Physics* 47 (2009),15, 1511–1522

[428] Prolongo, M. G.; Salom, C.; Arribas, C.; Sánchez-Cabezudo, M.; Masegosa, R. M. and Prolongo, S. G.: Influence of graphene nanoplatelets on curing and mechanical properties of graphene/epoxy nanocomposites. In: *Journal of Thermal Analysis and Calorimetry* 125 (2016),2, 629–636

[429] Yu, J. W.; Jung, J.; Choi, Y.-M.; Choi, J. H.; Yu, J.; Lee, J. K.; You, N.-H. and Goh, M.: Enhancement of the crosslink density, glass transition temperature, and strength of epoxy resin by using functionalized graphene oxide co-curing agents. In: *Polymer Chemistry* 7 (2016),1, 36–43

[430] Seyhan, A. T.; Gojny, F. H.; Tanoğlu, M. and Schulte, K.: Rheological and dynamic-mechanical behavior of carbon nanotube/vinyl ester–polyester suspensions and their nanocomposites. In: *European Polymer Journal* 43 (2007),7, 2836–2847

[431] Spanoudakis, J. and Young, R. J.: Crack propagation in a glass particle-filled epoxy resin - Part 1: Effect of partic/e volume fraction and size. In: *Journal of Materials Science* 19 (1984),2, 487–496

[432] Spanoudakis, J. and Young, R. J.: Crack propagation in a glass particle-filled epoxy resin - Part 2: Effect of particle-matrix adhesion. In: *Journal of Materials Science* 19 (1984),2, 473–486

[433] Materials - European Conference on Composite (Hrsg.): *Proceedings of the 17th European Conference on Composite Materials: ECCM17 - 17th European Conference on Composite Materials, 26-30th June 2016, Munich, Germany*. Augsburg: MAI Carbon Cluster Management GmbH, 2016

[434] Carpinteri, A.; Valente, S.; Ferrara, G. and Melchiorrl, G.: Is mode II fracture energy a real material property? In: *Computers & Structures* 48 (1993),3, 397–413

[435] Maierhofer, J.; Kolitsch, S.; Pippan, R.; Gänser, H.-P.; Madia, M. and Zerbst, U.: The cyclic R-curve – Determination, problems, limitations and application. In: *Engineering Fracture Mechanics* 198 (2018), 45–64

[436] Isaksson, P. and Ståhle, P.: Mode II crack paths under compression in brittle solids – a theory and experimental comparison. In: *International Journal of Solids and Structures* 39 (2002),8, 2281–2297

[437] Kinloch, A. J. and Young, R. J.: *Fracture Behaviour of Polymers*. Dordrecht: Springer Netherlands, 2013

[438] Dekkers, M. E. J. and Heikens, D.: Crazing and shear deformation in glass bead-filled glassy polymers. In: *Journal of Materials Science* 20 (1985),11, 3873–3880

[439] Fiedler, B.; Hojo, M.; Ochiai, S.; Schulte, K. and Ando, M.: Failure behavior of an epoxy matrix under different kinds of static loading. In: *Composites Science and Technology* 61 (2001),11, 1615–1624

[440] Turk, M.; Hamerton, I. and Ivanov, D. S.: Ductility potential of brittle epoxies: Thermomechanical behaviour of plastically-deformed fully-cured composite resins. In: *Polymer* 120 (2017), 43–51

[441] Zike, S.; Sørensen, B. F. and Mikkelsen, L. P.: Experimental determination of the micro-scale strength and stress-strain relation of an epoxy resin. In: *Materials & Design* 98 (2016), 47–60

[442] Sui, X. M.; Tiwari, M.; Greenfeld, I.; Khalfin, R. L.; Meeuw, H.; Fiedler, B. and Wagner, H. D.: Extreme scale-dependent tensile properties of epoxy fibers. In: *Express Polymer Letters* 13 (2019),11, 993–1003

[443] Zhang, W.; Srivastava, I.; Zhu, Y.-F.; Picu, C. R. and Koratkar, N. A.: Heterogeneity in epoxy nanocomposites initiates crazing: significant improvements in fatigue resistance and toughening. In: *Small (Weinheim an der Bergstrasse, Germany)* 5 (2009),12, 1403–1407

[444] Norman, D. A. and Robertson, R. E.: Rigid-particle toughening of glassy polymers. In: *Polymer* 44 (2003),8, 2351–2362

[445] Jones, S. A. and Tomlinson, R. A.: Investigating mixed-mode (I/II) fracture in epoxies using digital image correlation: Composite GIIc performance from resin measurements. In: *Engineering Fracture Mechanics* 149 (2015), 368–374

[446] Berkei, M.: Conductive Coatings Using Carbon Nanotubes. In: *CHEManager Europe* (2011),7-8, 10

[447] Widmann, G. and Riesen, R.: *Thermoanalyse: Anwendungen, Begriffe, Methoden*. 3., durchges. Aufl. Heidelberg: Hüthig, 1990

[448] Schürmann, H.: *Konstruieren mit Faser-Kunststoff-Verbunden*. 2., bearbeitete und erweiterte Auflage. Berlin: Springer, 2007

[449] Ehrenstein, G. W.: *Polymer-Werkstoffe: Struktur - Eigenschaften - Anwendung*. 3. Aufl. München: Hanser, 2011

[450] Ehrenstein, G. W.: *Faserverbund-Kunststoffe: Werkstoffe, Verarbeitung, Eigenschaften*. 2. völlig überarb. Aufl. München and Wien: Hanser, 2006

[451] Thomas Allspach: DCPD-UP-Harze. In: *Kunststoffe* 89 (1999),11, 117–118

[452] Voss, R.: *AROPOL FS7993M-25: Technical Data Sheet*. 2003

[453] altropol: *AltroColor PU 5011 lemon yellow: Material Safety Data Sheet*. 2015

[454] Gueli, A. M.; Bonfiglio, G.; Pasquale, S. and Troja, S. O.: Effect of particle size on pigments colour. In: *Color Research & Application* 42 (2017),2, 236–243

[455] Seyhan, A. T.; Gojny, F. H.; Tanoğlu, M. and Schulte, K.: Critical aspects related to processing of carbon nanotube/unsaturated thermoset polyester nanocomposites. In: *European Polymer Journal* 43 (2007),2, 374–379

[456] Hermant, M. C.: Manipulating the percolation threshold of carbon nanotubes in polymeric composites. (2009)

[457] Sumfleth, J.: *Rheological and electrical characterisation of single- and multi-filler polymer nanocomposites: Ph.D. Thesis*. Hamburg, 2010

[458] Ma, P.-C.; Liu, M.-Y.; Zhang, H.; Wang, S.-Q.; Wang, R.; Wang, K.; Wong, Y.-K.; Tang, B.-Z.; Hong, S.-H.; Paik, K.-W. and Kim, J.-K.: Enhanced electrical conductivity of nanocomposites containing hybrid fillers of carbon nanotubes and carbon black. In: *ACS applied materials & interfaces* 1 (2009),5, 1090–1096

[459] Sumfleth, J.; Almeida Prado, L. A.; Sriyai, M. and Schulte, K.: Titania-doped multi-walled carbon nanotubes epoxy composites: Enhanced dispersion and synergistic effects in multiphase nanocomposites. In: *Polymer* 49 (2008),23, 5105–5112

[460] Sumfleth, J.; Sriyai, M.; Prado, L.; Wichmann, M. H. and Schulte, K.: Synergistic Physical Properties of Multiphase Nanocomposites with Carbon Nanotubes and Inorganic Particles. In: *MRS Proceedings* 1056 (2007), 175

[461] Sumfleth, J.; A. Prado, L. A. S.; Richau, S.; Sriyai, M. and Schulte, K.: Enhanced Dispersion of MWCNTs and Synergistic Properties in Multiphase Epoxy Nanocomposites by Incorporation of Inorganic Nanoparticles. In: *Solid State Phenomena* 151 (2009), 176–180

[462] Zhang, W.; Blackburn, R. S. and Dehghani-Sanij, A. A.: Effect of silica concentration on electrical conductivity of epoxy resin–carbon black–silica nanocomposites. In: *Scripta Materialia* 56 (2007),7, 581–584

[463] Mohri, T.; Nakahara, Y.; Zhang, W.; Kida, T.; Nakatsuji, Y. and Ikeda, I.: Study on the Adsorption Behavior of Dispersants onto Pigment Using 1H NMR Spin-Lattice Relaxation Time. In: *Journal of Oleo Science* 50 (2001),8, 623–631

[464] Evonik Industries: *AEROSIL - Fumed Silica: Technical Overview*. https://www.aerosil.com/product/aerosil/downloads/aerosil-technical-overview-de.pdf, Last checked: 13.02.2020

[465] Yue, L.; Pircheraghi, G.; Monemian, S. A. and Manas-Zloczower, I.: Epoxy composites with carbon nanotubes and graphene nanoplatelets – Dispersion and synergy effects. In: *Carbon* 78 (2014), 268–278

[466] Konishi, Y. and Cakmak, M.: Nanoparticle induced network self-assembly in polymer–carbon black composites. In: *Polymer* 47 (2006),15, 5371–5391

[467] Zhang, S. M.; Lin, L.; Deng, H.; Gao, X.; Bilotti, E.; Peijs, T.; Zhang, Q. and Fu, Q.: Synergistic effect in conductive networks constructed with carbon nanofillers in different dimensions. In: *Express Polymer Letters* 6 (2012),2, 159–168

[468] Bilotti, E.; Zhang, H.; Deng, H.; Zhang, R.; Fu, Q. and Peijs, T.: Controlling the dynamic percolation of carbon nanotube based conductive polymer composites by addition of secondary nanofillers: The effect on electrical conductivity and tuneable sensing behaviour. In: *Composites Science and Technology* 74 (2013), 85–90

[469] OCSiAl: *Recent developments in the industrial application and prospect markets of Tuball SWCNT: Oral communication on K – International Trade Fair for Plastics & Rubber*. 23.10.2019

A Programmed Applications

A.1 OCT Evaluation via Matlab

A.1.1 Main.m

```
clear all
close all

directory = 'D:\PATHNAME';
filelist=dir([directory,'/*.png']);
filelistlength = length(filelist);

for p=1:filelistlength
    close all
    clear length
    im = imread(fullfile(directory,filelist(p).name));

    I2 = imtophat(im,strel('disk',15));

    figure, imshow(I2);

    pixel_size=1;

    imshow(im);

    h = imrect(gca, [50 50 150 400]);

    position = wait(h);
    [im, rect] = imcrop(im,position);


    im_size=size(im);
    im_area = im_size(1)*im_size(2)*pixel_size^2;
    figure, imshow(im)
    name = strcat(filelist(p).name,'crop.png')
    print('-dpng',name);

    x = im
    [Level,BW] = thresh_tool(x);
    name = strcat(filelist(p).name,'heat.png');
    print('-dpng',name);
    figure, imshow(BW)

    name = strcat(filelist(p).name,'threshold.png');
    print('-dpng',name);

    cc = bwconncomp(BW, 18);

    labeled = labelmatrix(cc);
    whos labeled
    RGB_label = label2rgb(labeled, @spring, 'c', 'shuffle');
    imshow(RGB_label)
    name = strcat(filelist(p).name,'particles.png')
    print('-dpng',name);

```

```
51
52      particledata = regionprops(cc,'basic')
53      Particle_areas=[particledata.Area];
54      particle_areas = num2cell(([particledata.Area]*(pixel_size^2))');
55
56      ID  = cellstr(filelist(p).name);
57      ps = num2cell(pixel_size);
58      im_a = num2cell(im_area);
59
60  figure
61  histogram(Particle_areas)
62  title(filelist(p).name);
63
64  name = strcat(filelist(p).name,'histogramm.pdf');
65      print('-dpdf',name);
66
67  file = 'particle_data.xlsx';
68  sheet = num2str(p)
69
70
71
72  xlswrite(file,vertcat('Probennummer',ID),sheet,'A1');
73  xlswrite(file,vertcat('Pixel length',ps),sheet,'B1');
74  xlswrite(file,vertcat('Crop Flaeche',im_a),sheet,'C1');
75  xlswrite(file,vertcat('Flaeche Partikel',particle_areas),sheet,'D1');
76
77  end
78
79  close all
```

A.1.2 Thresh_tool.m

```
function [level,bw] = thresh_tool(im,cmap,defaultLevel)

error(nargchk(1,3,nargin))
error(nargoutchk(0,2,nargout))

if nargin>2
  dataType = class(im);
  switch dataType
    case 'uint8','uint16','int16'
      if defaultLevel<intmin(dataType) | defaultLevel>intmax(dataType)
        error(['Specified DEFAULTLEVEL outside class range for ' dataType])
      elseif defaultLevel<min(im(:)) | defaultLevel>max(im(:))
        error('Specified DEFAULTLEVEL outside data range for IM')
      end
    case 'double','single'

    otherwise
      error(['Unsupport image type ' dataType])
  end
end

max_colors=1000;


color_range = double(limits(im));
if isa(im,'uint8')
  color_range = [0 255];
  num_colors = 256;
  di = 1;
elseif isinteger(im)

  num_colors = diff(color_range)+1;
  if num_colors<max_colors
    di = 1;
  else
    num_colors = max_colors;
    di = diff(color_range)/(num_colors-1);
  end
else

  di = min(diff(sort(unique(im(:)))));
  num_colors = round(diff(color_range)/di)+1;
  if num_colors>max_colors
    num_colors = max_colors;
    di = diff(color_range)/(num_colors-1);
  end
end
bin_ctrs = [color_range(1):di:color_range(2)];
FmtSpec = ['%.' num2str(ceil(-log10(di))) 'f'];

h_fig = figure;
set(h_fig,'ToolBar','Figure')
if nargin>1 && isstr(cmap) && strmatch(lower(cmap),'gray')
  full_map = gray(num_colors);
elseif nargin>1 && isnumeric(cmap) && length(size(cmap))==2 && size(cmap,2)==3
  full_map = cmap;
else
  full_map = jet(num_colors);
end
```

```
setappdata(h_fig,'im',im)
setappdata(h_fig,'FmtSpec',FmtSpec)

h_ax1 = axes('unit','norm','pos',[0.05 0.35 0.4 0.60]);
rgb = im2rgb(im,full_map);
  function rgb = im2rgb(im,full_map);

    gray = imadjust(im,[],[0 1]);

    num_colors = size(full_map,1);
    ind = gray2ind(gray,num_colors);

    rgb = ind2rgb(ind,full_map);
  end

image(rgb), axis image

axis off, title('Input Image')


h_ax2 = axes('unit','norm','pos',[0.55 0.35 0.4 0.60]);
axis off
setappdata(h_fig,'h_ax2',h_ax2)

h_hist = axes('unit','norm','pos',[0.05 0.1 0.9 0.2]);
n = hist(double(im(:)),bin_ctrs);
bar(bin_ctrs,n)
axis([color_range limits(n(2:end-1))])
set(h_hist,'xtick',[],'ytick',[])
title('Intensity Distribution')

h_cbar = axes('unit','norm','pos',[0.05 0.05 0.9 0.05],'tag','thresh_tool_cbar');
subimage(color_range,[0.5 1.5],1:num_colors,full_map)
set(h_cbar,'ytick',[],'xlim',color_range)
axis normal

v=version;
if str2num(v(1:3))≥7

  linkaxes([h_ax1 h_ax2])

  linkaxes([h_hist h_cbar],'x')
end


set(h_cbar,'xtick',color_range)

if nargin>2
  my_level = defaultLevel;
else
  lo = double(color_range(1));
  hi = double(color_range(2));
  norm_im = (double(im)-lo)/(hi-lo);
  norm_level = graythresh(norm_im);
  my_level = norm_level*(hi-lo)+lo;
end
my_level = 155;

axes(h_hist)
h_lev = vline(my_level,'-');
set(h_lev,'LineWidth',2,'color',0.5*[1 1 1],'UserData',my_level)
setappdata(h_fig,'h_lev',h_lev)

```

```
move_vline(h_lev,@update_plot);

axes(h_cbar)
y_lim = get(h_cbar,'ylim');

h_text = text(my_level,mean(y_lim),'dummy','HorizontalAlignment','Center');
if nargin<2
  text_color = 0.5*[1 1 1];
else
  text_color = 'm';
end
set(h_text,'FontWeight','Bold','color',text_color,'Tag','cbar_text')
movex_text(h_text,my_level)

bw = im>my_level;
axes(h_ax2)
hold on
subimage(bw), axis off, axis ij
hold off
title('Segmented')

update_plot


h_reset = uicontrol('unit','norm','pos',[0.0 0.95 .1 .05]);
set(h_reset,'string','Reset','callback',@ResetOriginalLevel)

if nargout>0
  h_done = uicontrol('unit','norm','pos',[0.9 0.95 0.1 0.05]);
  set(h_done,'string','Done','callback','delete(gcbo)')

  set(h_fig,'WindowStyle','modal')
  waitfor(h_done)
  if ishandle(h_fig)
    h_lev = getappdata(gcf,'h_lev');
    level = mean(get(h_lev,'xdata'));
    if nargout>1
      h_im2 = findobj(h_ax2,'type','image');
      bw = logical(rgb2gray(get(h_im2,'cdata')));
    end
    delete(h_fig)
  else
    warning('THRESHTOOL:UserAborted','User Aborted - no return value')
    level = [];
  end
end
figure, imshow(rgb)
end

function ResetOriginalLevel(hObject,varargin)
h_lev = getappdata(gcf,'h_lev');
init_level = get(h_lev,'UserData');
set(h_lev,'XData',init_level*[1 1])
text_obj = findobj('Type','Text','Tag','cbar_text');
movex_text(text_obj,init_level)
update_plot
end


function update_plot
im = getappdata(gcf,'im');
h_lev = getappdata(gcf,'h_lev');
my_level = mean(get(h_lev,'xdata'));
```

```
186 h_ax2 = getappdata(gcf,'h_ax2');
187 h_im2 = findobj(h_ax2,'type','image');
188
189 bw = (im>my_level);
190 rgb_version = repmat(double(bw),[1 1 3]);
191 set(h_im2,'cdata',rgb_version)
192 end
193
194 function move_vline(handle,DoneFcn)
195
196 set(gcf,'Nextplot','Replace')
197 set(gcf,'DoubleBuffer','on')
198
199 h_ax=get(handle,'parent');
200 h_fig=get(h_ax,'parent');
201 setappdata(h_fig,'h_vline',handle)
202 if nargin<2, DoneFcn=[]; end
203 setappdata(h_fig,'DoneFcn',DoneFcn)
204 set(handle,'ButtonDownFcn',@DownFcn)
205
206   function DownFcn(hObject,eventdata,varargin)
207     set(gcf,'WindowButtonMotionFcn',@MoveFcn)
208     set(gcf,'WindowButtonUpFcn',@UpFcn)
209   end
210
211   function UpFcn(hObject,eventdata,varargin)
212     set(gcf,'WindowButtonMotionFcn',[])
213     DoneFcn=getappdata(hObject,'DoneFcn');
214     if isstr(DoneFcn)
215       eval(DoneFcn)
216     elseif isa(DoneFcn,'function_handle')
217       feval(DoneFcn)
218     end
219   end
220
221   function MoveFcn(hObject,eventdata,varargin)
222     h_vline=getappdata(hObject,'h_vline');
223     h_ax=get(h_vline,'parent');
224     cp = get(h_ax,'CurrentPoint');
225     xpos = cp(1);
226     x_range=get(h_ax,'xlim');
227     if xpos<x_range(1), xpos=x_range(1); end
228     if xpos>x_range(2), xpos=x_range(2); end
229     XData = get(h_vline,'XData');
230     XData(:)=xpos;
231     set(h_vline,'xdata',XData)
232
233     text_obj = findobj('Type','Text','Tag','cbar_text');
234     movex_text(text_obj,xpos)
235   end
236
237 end
238
239 function [x,y] = limits(a)
240
241 if nargin≠1 | nargout>2
242   error('usage: [lo,hi]=limits(a)')
243 end
244
245 siz=size(a);
246
247 if prod(siz)==1
248   result=a;
```

```
else
  result=[min(a(:)) max(a(:))];
end

if nargout==1
  x=result;
elseif nargout==2
  x=result(1);
  y=result(2);
else
  ans=result
end

end

function movex_text(h_txt,x_pos)
FmtSpec=getappdata(get(get(h_txt,'parent'),'parent'),'FmtSpec');
msg=sprintf(FmtSpec,x_pos);
pos=get(h_txt,'position');
pos(1)=x_pos;
set(h_txt,'Position',pos,'String',msg)
end


function hhh=vline(x,in1,in2)

if length(x)>1
    for I=1:length(x)
        switch nargin
        case 1
            linetype='r:';
            label='';
        case 2
            if ¬iscell(in1)
                in1={in1};
            end
            if I>length(in1)
                linetype=in1{end};
            else
                linetype=in1{I};
            end
            label='';
        case 3
            if ¬iscell(in1)
                in1={in1};
            end
            if ¬iscell(in2)
                in2={in2};
            end
            if I>length(in1)
                linetype=in1{end};
            else
                linetype=in1{I};
            end
            if I>length(in2)
                label=in2{end};
            else
                label=in2{I};
            end
        end
        h(I)=vline(x(I),linetype,label);
    end
else
```

```
312     switch nargin
313     case 1
314         linetype='r:';
315         label='';
316     case 2
317         linetype=in1;
318         label='';
319     case 3
320         linetype=in1;
321         label=in2;
322     end
323
324     g=ishold(gca);
325     hold on
326
327     y=get(gca,'ylim');
328     h=plot([x x],y,linetype);
329     if length(label)
330         xx=get(gca,'xlim');
331         xrange=xx(2)-xx(1);
332         xunit=(x-xx(1))/xrange;
333         if xunit<0.8
334             text(x+0.01*xrange,y(1)+0.1*(y(2)-y(1)),label,'color',get(h,'color'))
335         else
336             text(x-.05*xrange,y(1)+0.1*(y(2)-y(1)),label,'color',get(h,'color'))
337         end
338     end
339
340     if g==0
341     hold off
342     end
343     set(h,'tag','vline','handlevisibility','off')
344 end
345
346 if nargout
347     hhh=h;
348 end
349 end
```

B Additional Material Characterization

B.1 Additional Characterization of CNP

B.1.1 Energy Dispersive X-Ray Spectroscopy

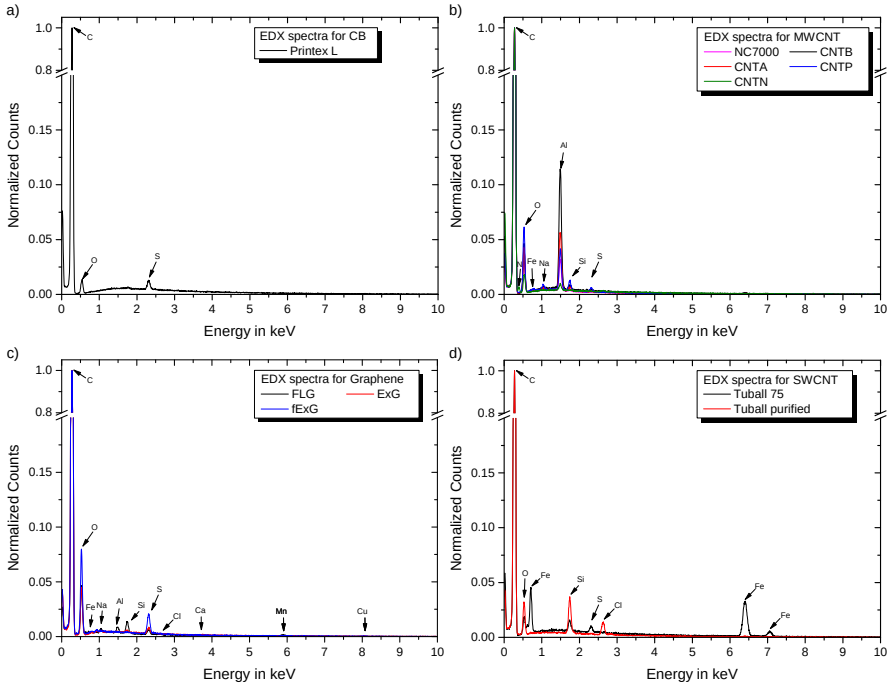


Figure B.1: EDX spectra for (**a**) CB, (**b**) MWCNT, (**c**) planar particles and (**d**) SWCNT

B.1.2 Raman Spectroscopy

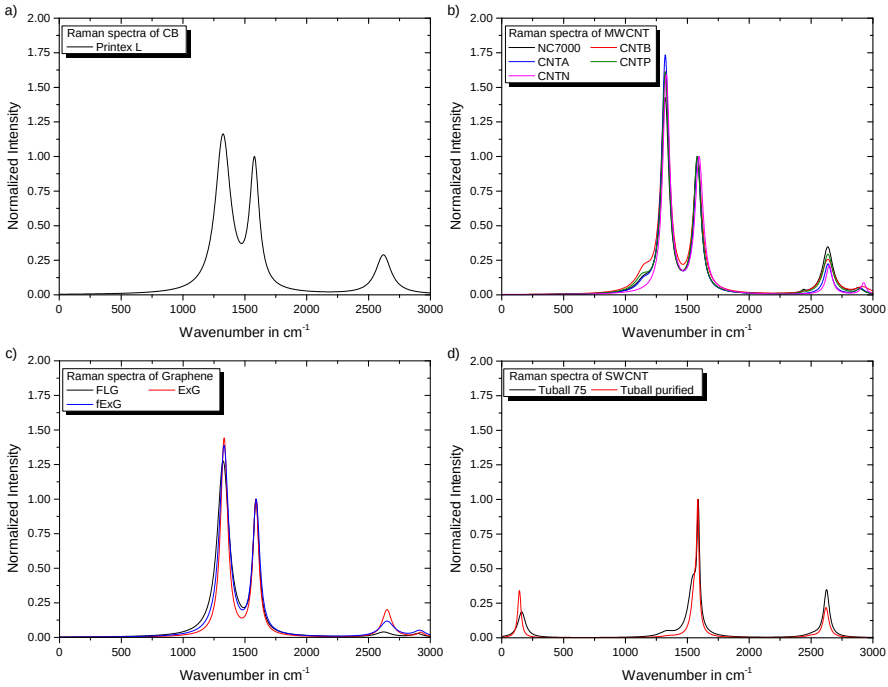


Figure B.2: Raman spectra for (**a**) CB, (**b**) MWCNT, (**c**) planar particles and (**d**) SWCNT

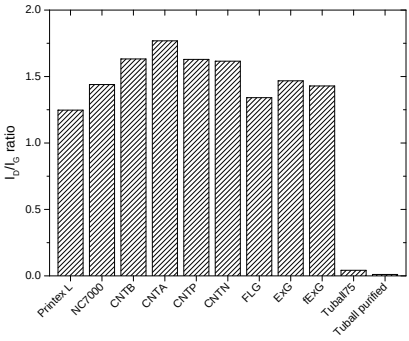


Figure B.3: Evaluation of I_D / I_G ratio

B.1.3 Thermo Gravimetric Analysis

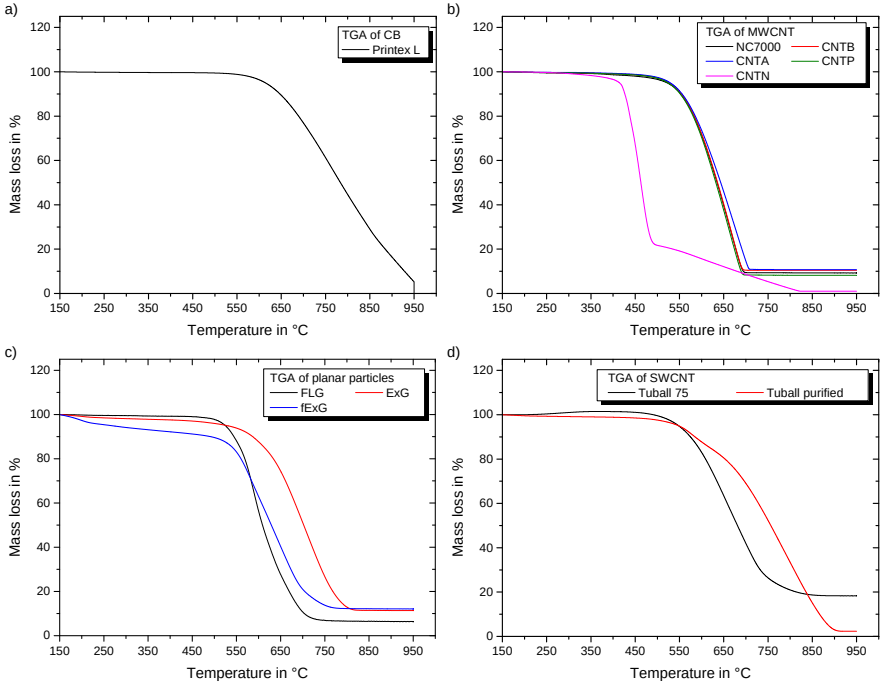


Figure B.4: TGA curves for (**a**) CB, (**b**) MWCNT, (**c**) planar particles and (**d**) SWCNT

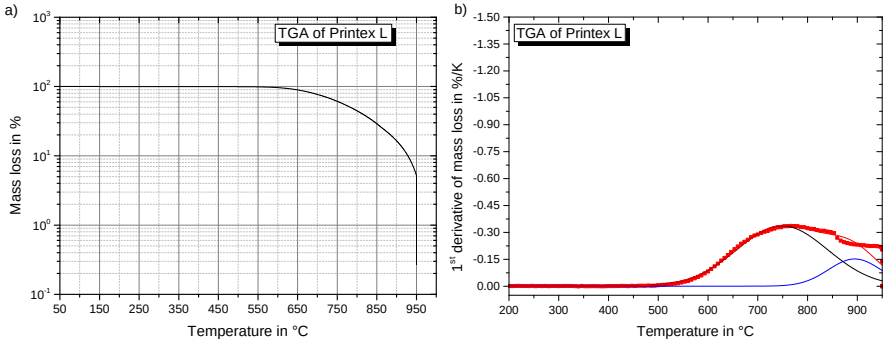


Figure B.5: TGA curve for CB (**a**) mass loss in dependency of temperature and (**b**) evaluation of decomposition peaks

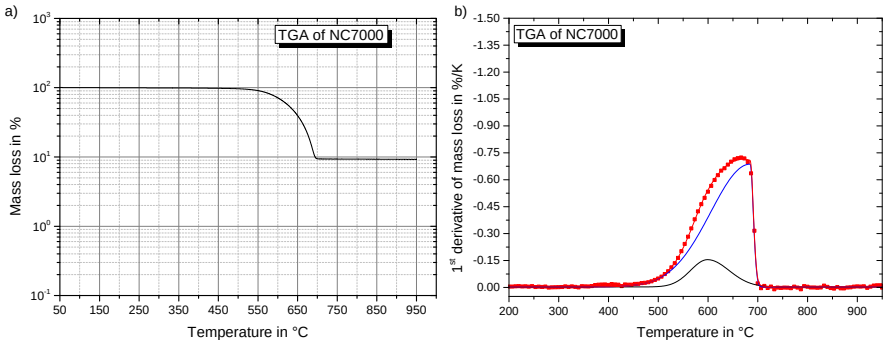


Figure B.6: TGA curve for MWCNT NC7000 (**a**) mass loss in dependency of temperature and (**b**) evaluation of decomposition peaks

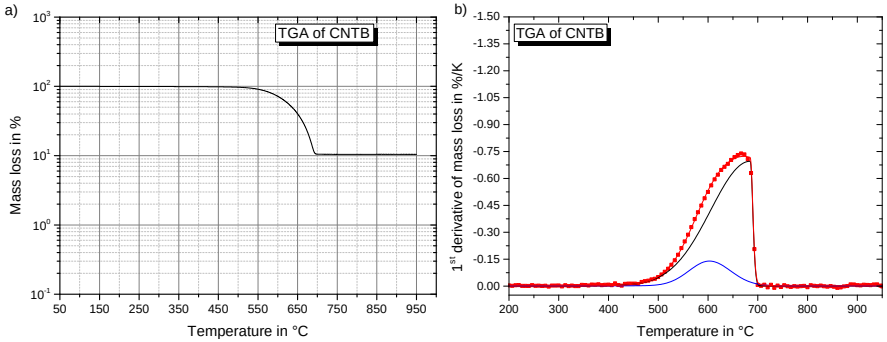


Figure B.7: TGA curve for MWCNT CNTB (**a**) mass loss in dependency of temperature and (**b**) evaluation of decomposition peaks

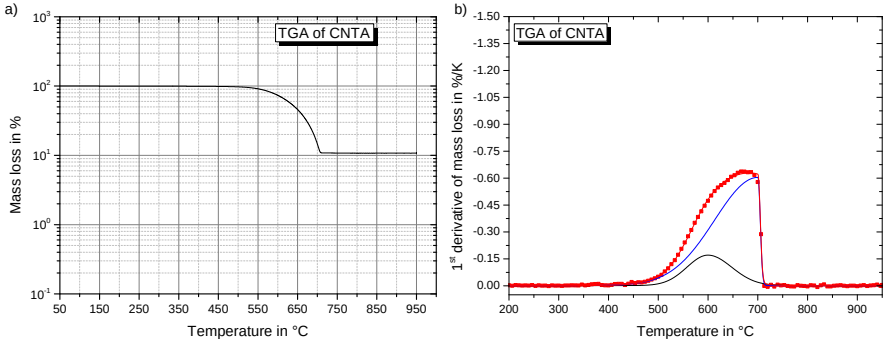


Figure B.8: TGA curve for MWCNT CNTA (**a**) mass loss in dependency of temperature and (**b**) evaluation of decomposition peaks

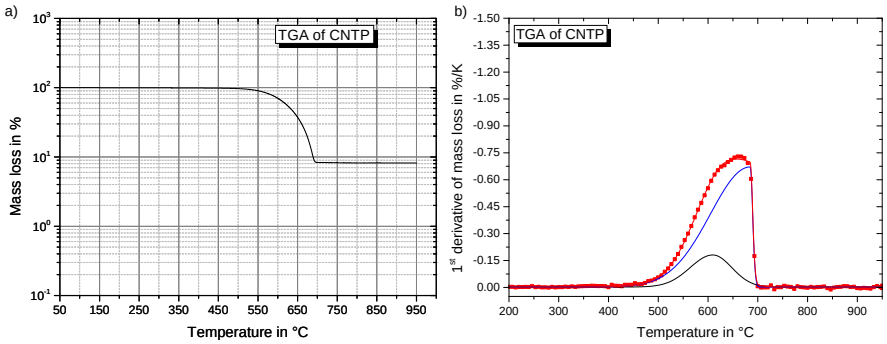


Figure B.9: TGA curve for MWCNT CNTP (**a**) mass loss in dependency of temperature and (**b**) evaluation of decomposition peaks

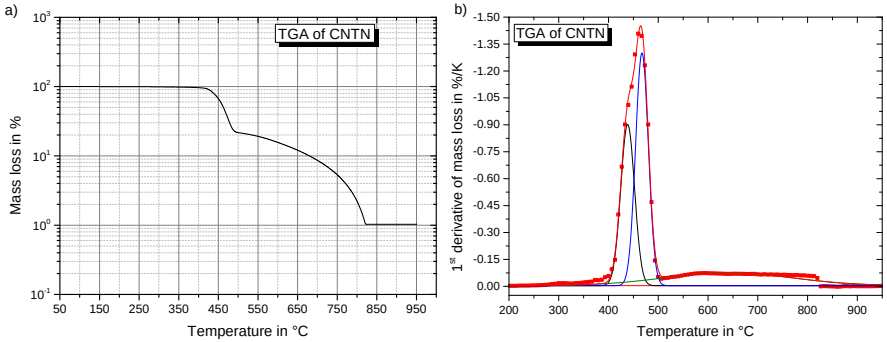


Figure B.10: TGA curve for MWCNT CNTN (**a**) mass loss in dependency of temperature and (**b**) evaluation of decomposition peaks

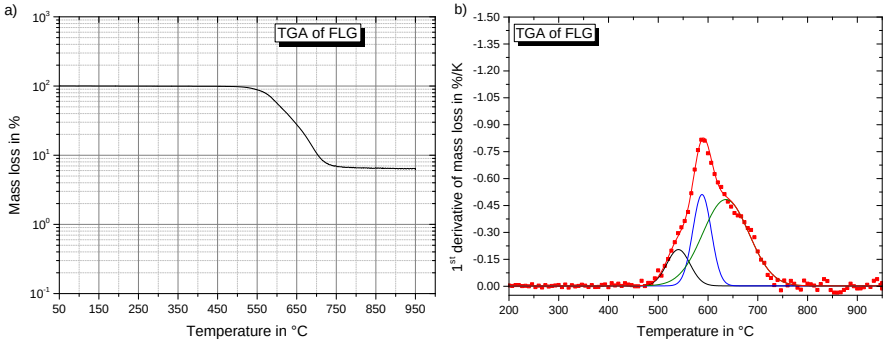


Figure B.11: TGA curve for FLG (**a**) mass loss in dependency of temperature and (**b**) evaluation of decomposition peaks

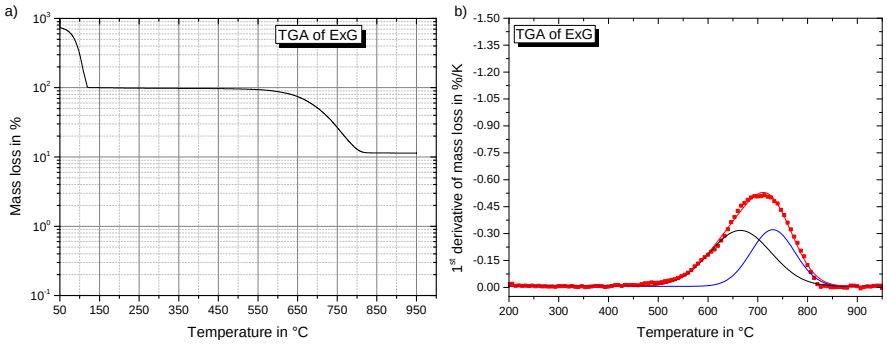


Figure B.12: TGA curve for ExG (**a**) mass loss in dependency of temperature and (**b**) evaluation of decomposition peaks

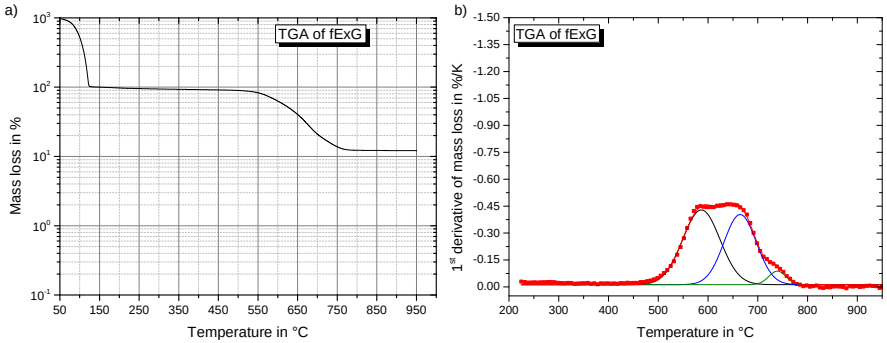


Figure B.13: TGA curve for fExG (**a**) mass loss in dependency of temperature and (**b**) evaluation of decomposition peaks

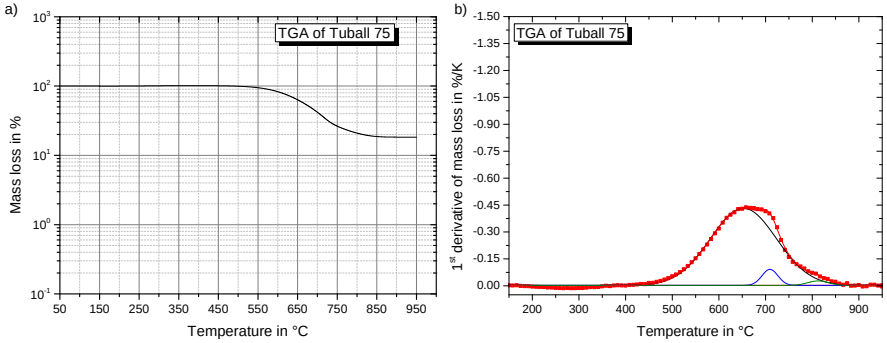


Figure B.14: TGA curve for SWCNT Tuball 75 (**a**) mass loss in dependency of temperature and (**b**) evaluation of decomposition peaks

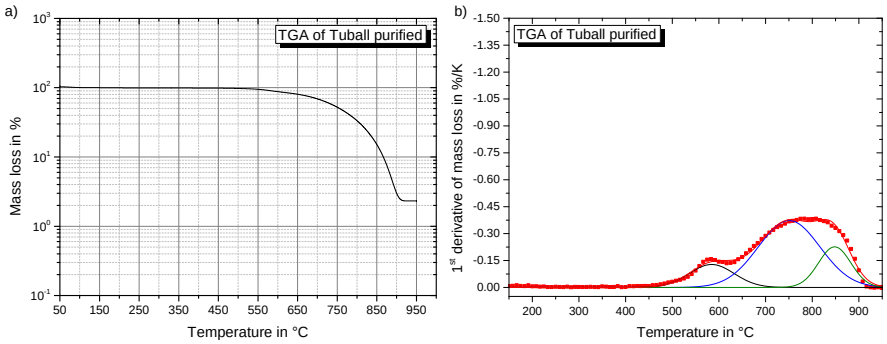


Figure B.15: TGA curve for SWCNT Tuball purified (**a**) mass loss in dependency of temperature and (**b**) evaluation of decomposition peaks

B.1.4 Scanning Electron Microscopy

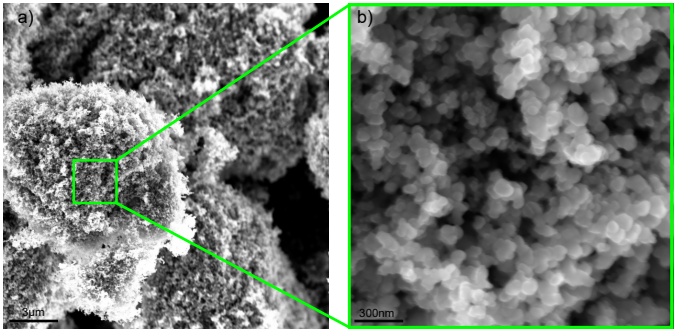


Figure B.16: SEM images for Printex L at magnifications of (**a**) 10 k and (**b**) 150 k

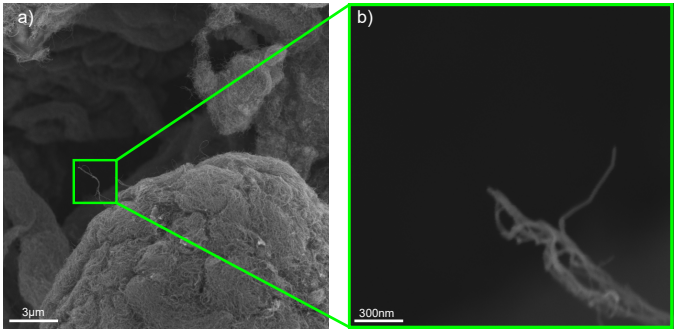


Figure B.17: SEM images for NC7000 at magnifications of (**a**) 10 k and (**b**) 150 k

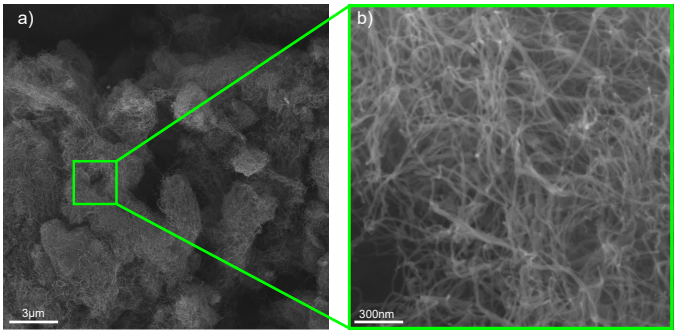


Figure B.18: SEM images for CNTB at magnifications of (**a**) 10 k and (**b**) 150 k

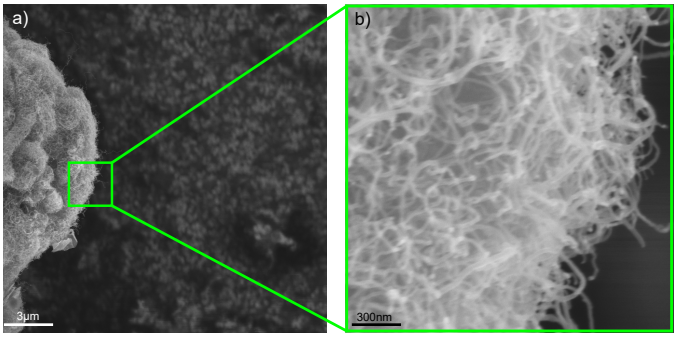


Figure B.19: SEM images for CNTA at magnifications of (**a**) 10 k and (**b**) 150 k

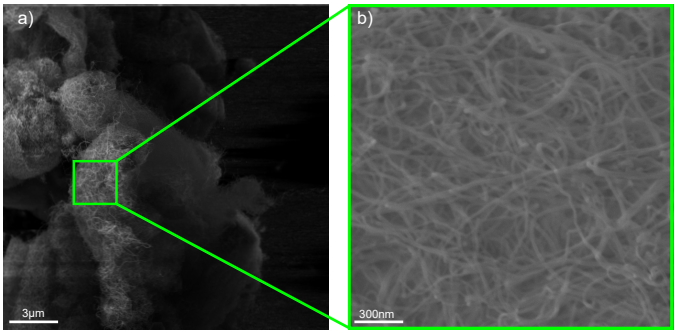


Figure B.20: SEM images for CNTP at magnifications of (**a**) 10 k and (**b**) 150 k

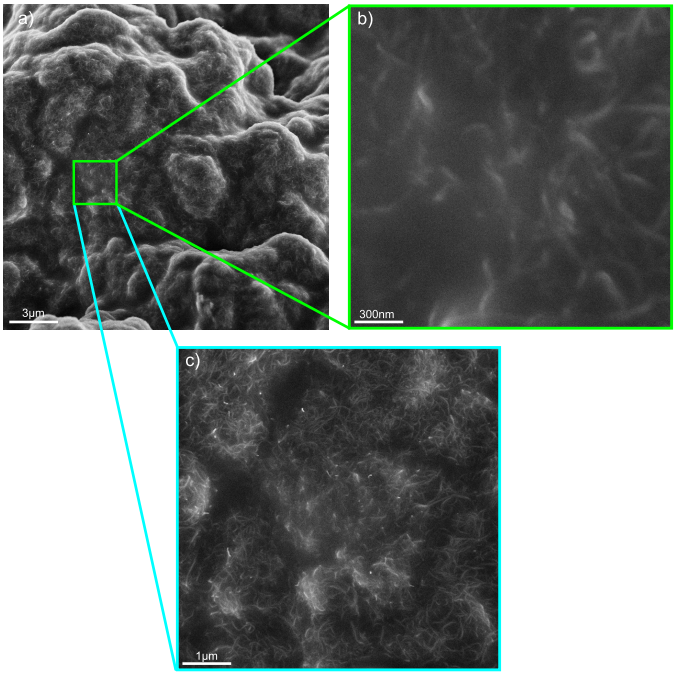


Figure B.21: SEM images for CNTN at magnifications of (**a**) 10 k, (**b**) 150 k and (**c**) 25 k

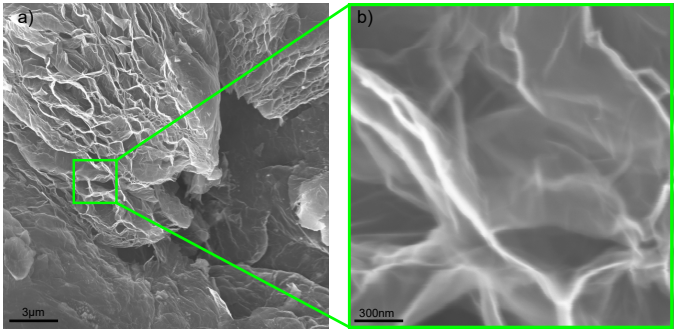


Figure B.22: SEM images for FLG at magnifications of (**a**) 10 k and (**b**) 150 k

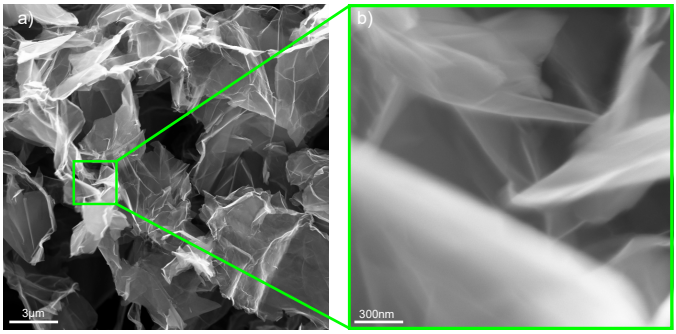


Figure B.23: SEM images for ExG at magnifications of (**a**) 10 k and (**b**) 150 k

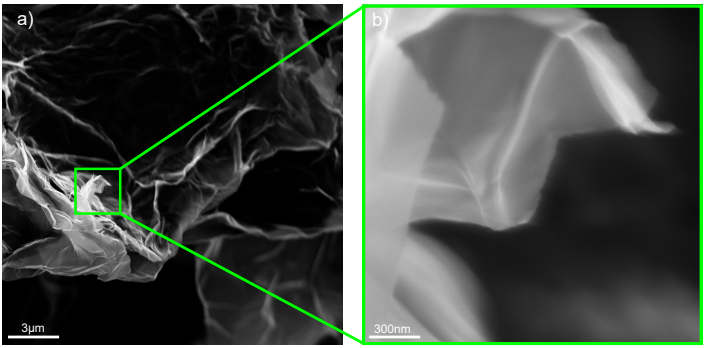


Figure B.24: SEM images for fExG at magnifications of (**a**) 10 k and (**b**) 150 k

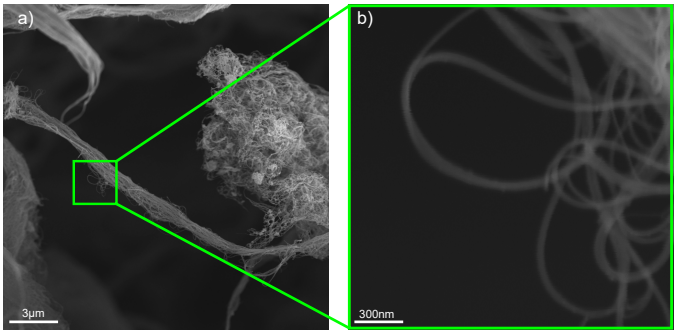


Figure B.25: SEM images for Tuball 75 at magnifications of (**a**) 10 k and (**b**) 150 k [350]

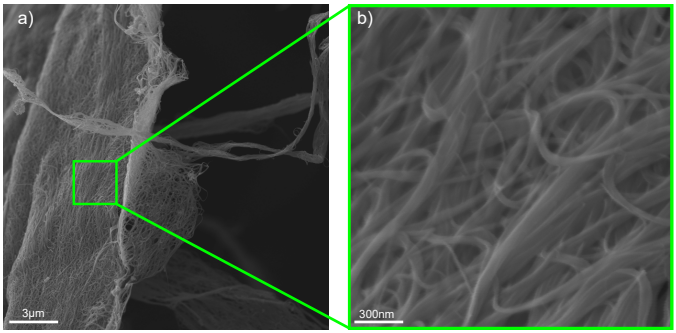


Figure B.26: SEM images for Tuball purified at magnifications of (**a**) 10 k and (**b**) 150 k

B.1.5 Transmission Electron Microscopy

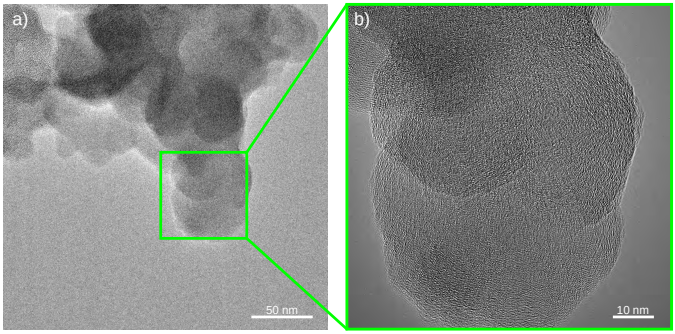


Figure B.27: TEM images for Printex L at (**a**) low magnification and (**b**) high magnification

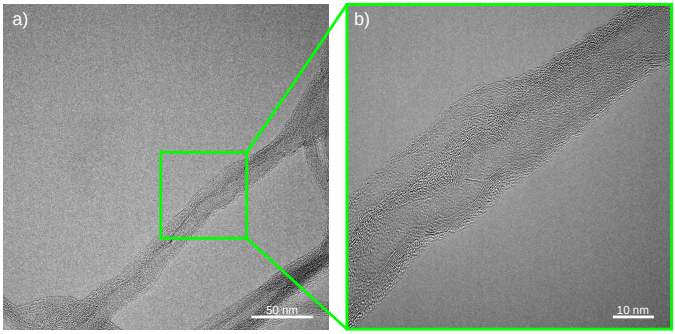


Figure B.28: TEM images for NC7000 at (**a**) low magnification and (**b**) high magnification

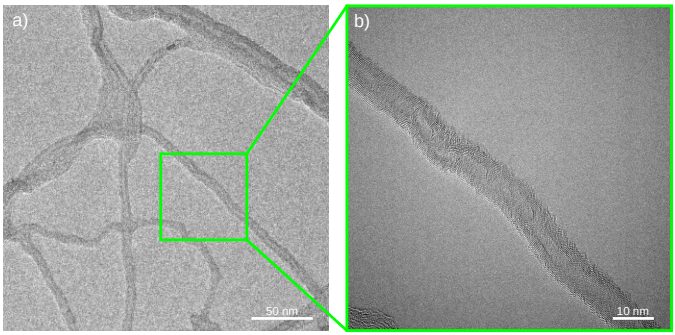


Figure B.29: TEM images for CNTB at (**a**) low magnification and (**b**) high magnification

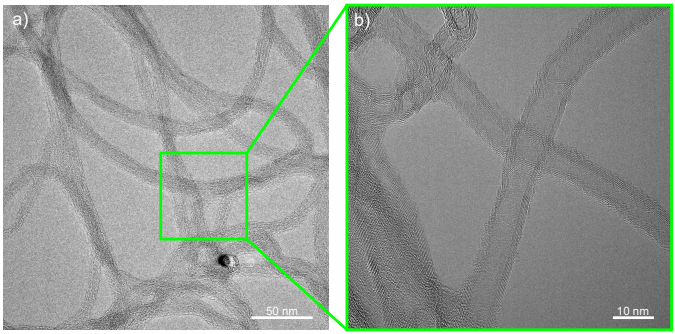


Figure B.30: TEM images for CNTA at (**a**) low magnification and (**b**) high magnification

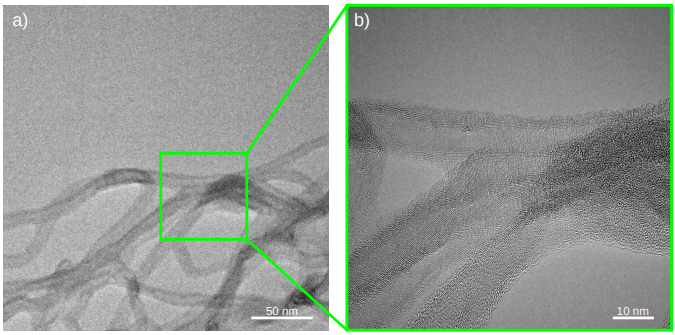


Figure B.31: TEM images for CNTP at (**a**) low magnification and (**b**) high magnification

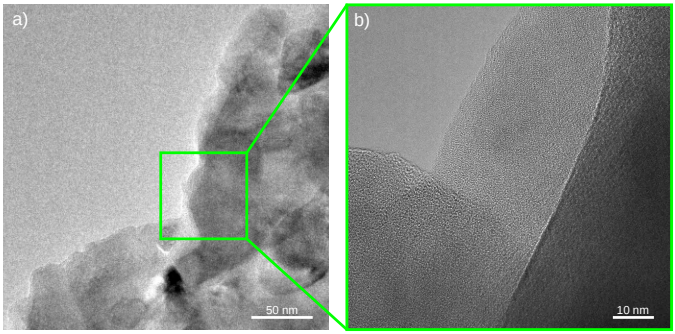


Figure B.32: TEM images for CNTN at (**a**) low magnification and (**b**) high magnification

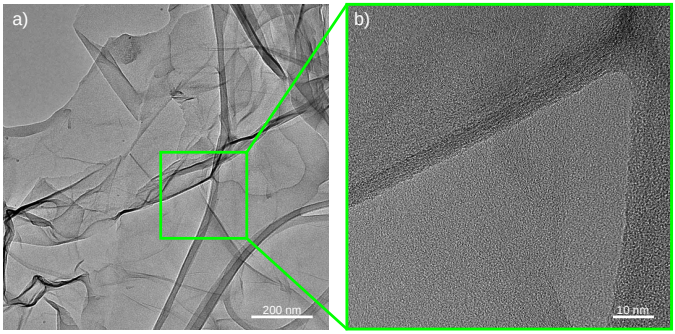


Figure B.33: TEM images for FLG at (**a**) low magnification and (**b**) high magnification

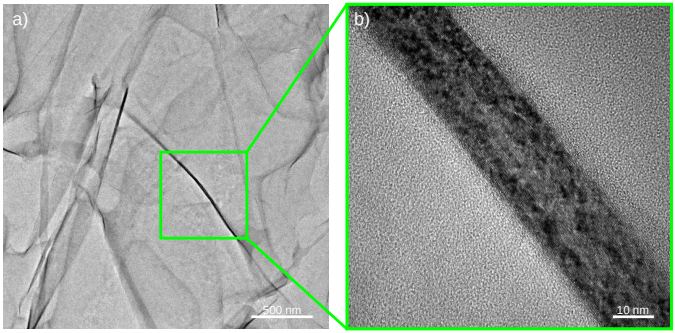


Figure B.34: TEM images for ExG at (**a**) low magnification and (**b**) high magnification

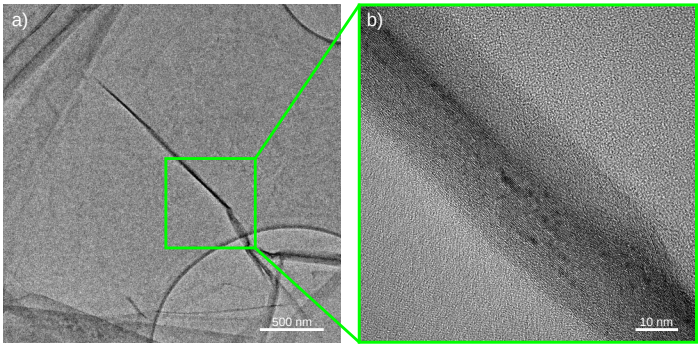


Figure B.35: TEM images for fExG at (**a**) low magnification and (**b**) high magnification

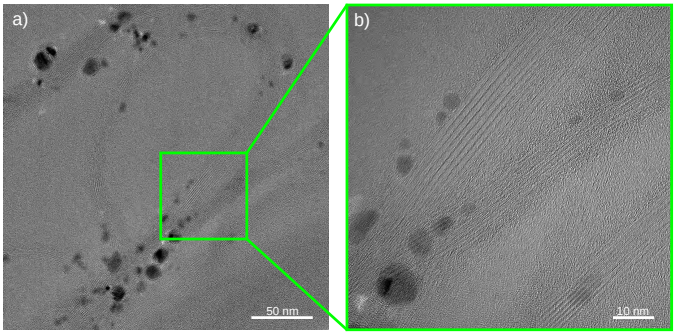


Figure B.36: TEM images for Tuball 75 at (**a**) low magnification and (**b**) high magnification [350]

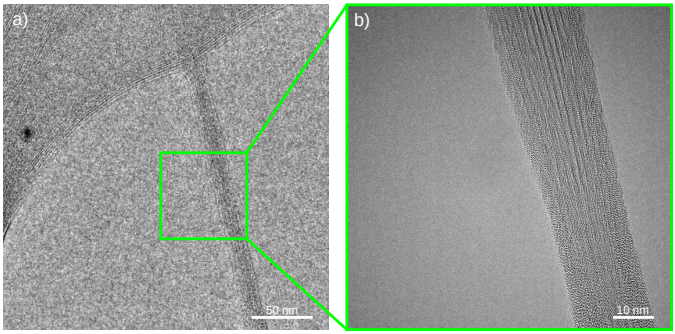


Figure B.37: TEM images for Tuball purified at (**a**) low magnification and (**b**) high magnification

B.2 Dynamic Mechanical Thermal Analysis of CNP/EP Composites

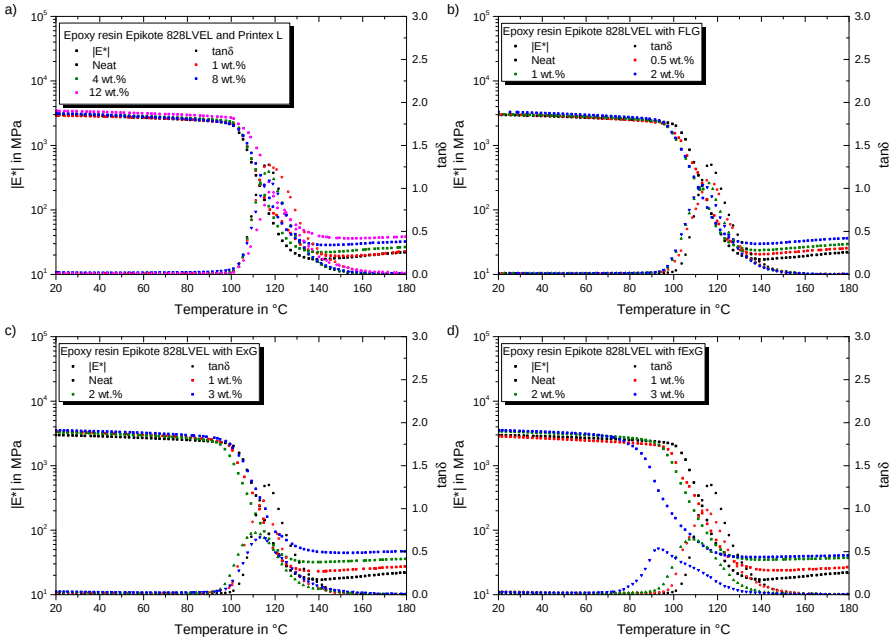


Figure B.38: DMTA curves for (**a**) Printex L, (**b**) FLG, (**c**) ExG and (**d**) fExG in Epikote 828LVEL

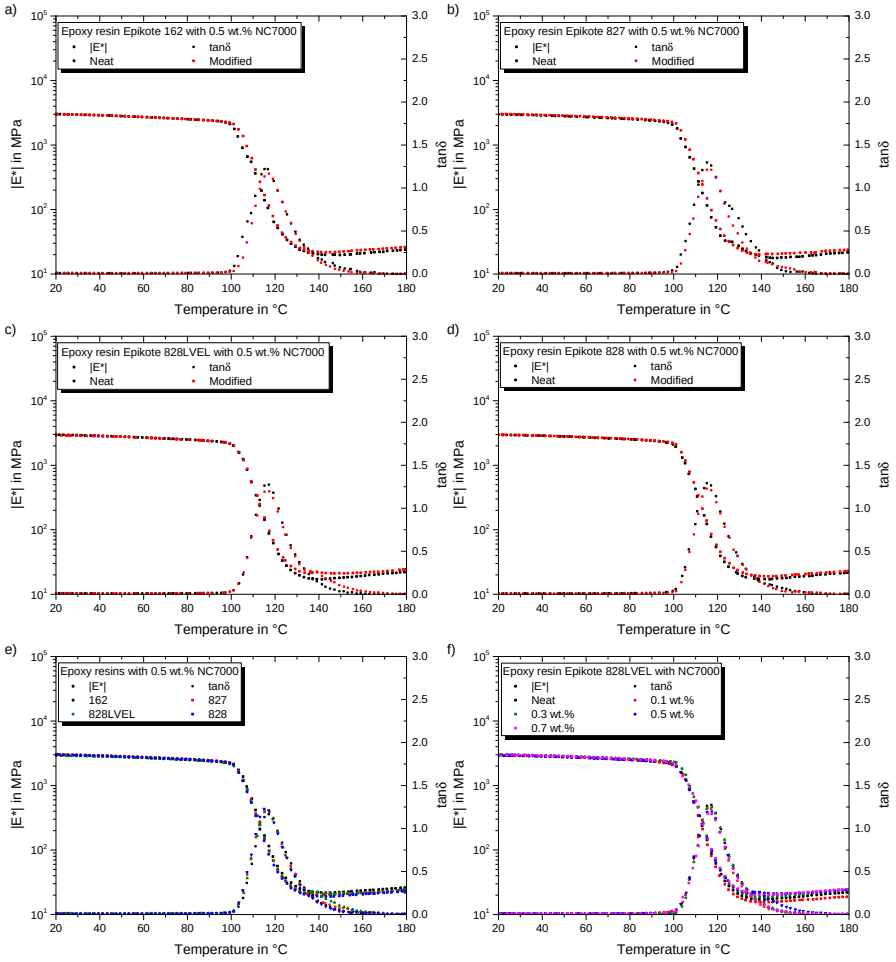


Figure B.39: DMTA curves for NC7000 modified (**a**) Epikote 162, (**b**) Epikote 827, (**c**) Epikote 828LVEL and (**d**) Epikote 828; (**e**) different MW epoxy resins and (**f**) different filler loadings in Epikote 828LVEL

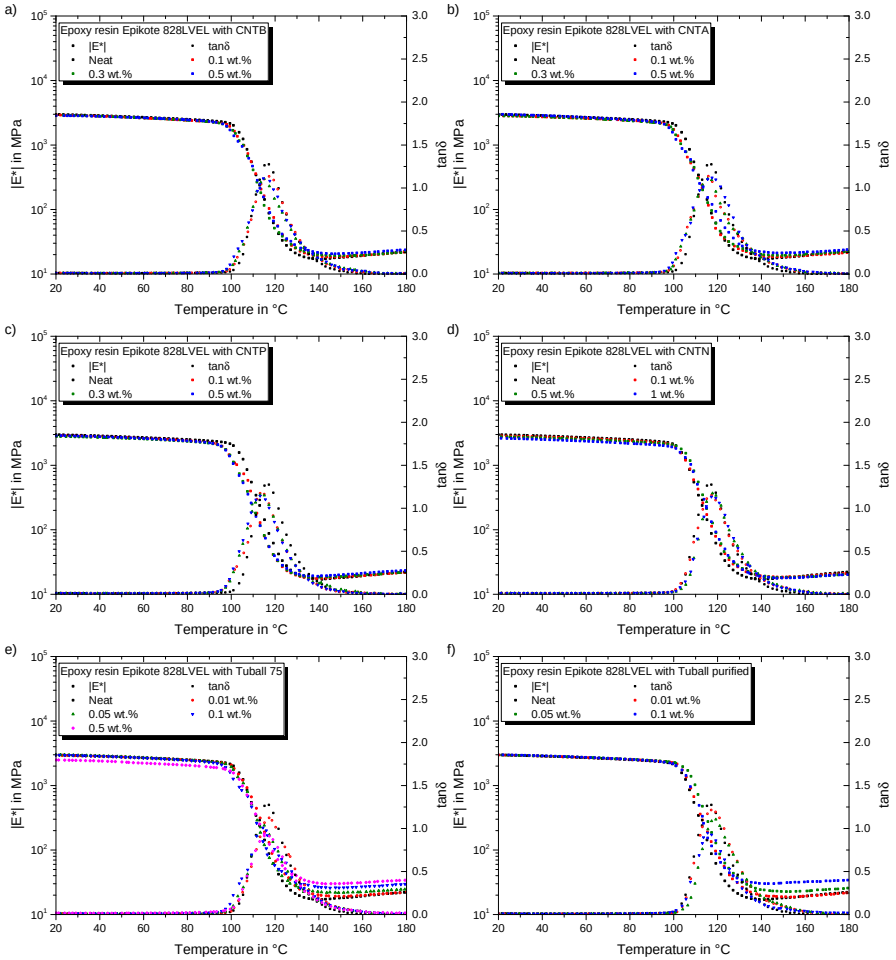


Figure B.40: DMTA curves for (**a**) CNTB, (**b**) CNTA, (**c**) CNTP, (**d**) CNTN and (**e**) Tuball 75 and (**f**) Tuball purified in Epikote 828LVEL

B.3 Final comparison of Impedance Spectroscopy Results

Figure B.41 shows the Nyquist and Bode plots for the evaluated filler concentrations. In the planes the dependency of Z' and Z'' on the frequency is given, respectively. This results are in good accordance from the derived model, see figure 6.18.

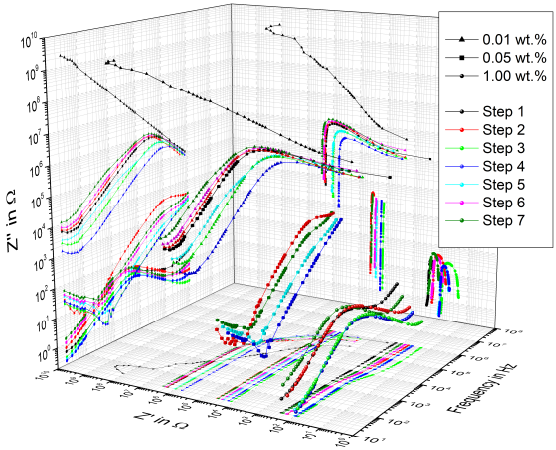


Figure B.41: Comparison of impedance spectra of all filler concentrations